INFLUENCES OF THE HEME-LYS CROSSLINK FOUND IN CYTOCHROME P460 IN HYDROXYLAMINE OXIDATION AND NITRIC OXIDE SENSITIVITY

A Dissertation

Presented to the Faculty of the Graduate School

of Cornell University

In Partial Fulfillment of the Requirements for the Degree of

Doctor of Philosophy of Chemistry and Chemical Biology

by

Avery Vilbert

August 2018

INFLUENCES OF THE HEME-LYS CROSSLINK FOUND IN CYTOCHROME P460 IN HYDROXYLAMINE OXIDATION AND NITRIC OXIDE SENSITIVITY

Avery Vilbert, Ph.D.

Cornell University 2018

Nitrous oxide (N_2O) is a greenhouse gas with a global warming potential about 300 times that of CO_2. The link between agriculture and N_2O emissions largely owes to the activity of ammonia oxidizing bacteria and archaea. These organisms mediate the first phase of nitrification, the oxidation of NH_3 to nitrite (NO_2^-). The first step from NH_3 to NO_2^- is catalyzed by the membrane bound ammonia monooxygenase (AMO), which oxidizes NH_3 to NH_2OH. Next, NH_2OH is oxidized by the multi-heme enzyme hydroxylamine oxidoreductase (HAO). This enzyme contains 8 hemes per subunit, 7 of which are coordinately saturated c-type hemes used in electron transfer. The active site of HAO is termed the P460 cofactor, which is unique heme c-type heme that features an additional cross-link to the heme center. This thesis focuses on the P460 cofactor found in cytochrome (cyt) P460. Cyt P460 is a periplasmic protein also found in *Nitrosomonas europaea,* an ammonia oxidizing bacteria that contains this unique cofactor and also exhibits NH_2OH oxidase reactivity.

First, this thesis establishes a route for N_2O emission by cyt P460 and provides a possible mechanism for oxidation of NH_2OH to N_2O by cyt P460. This mechanism necessitates a 6-coordinate (6c) $\{FeNO\}^7$ and a $\{FeNO\}^6$ as intermediates. The 5-coordinate (5c) $\{FeNO\}^7$ species had been previously shown to be inert. Next a

possible role of the cross-link is addressed when investigating the His dissociation mechanism. Treatment of Fe^{II} cyt P460 with a NO donor to form the 6c $\{FeNO\}^7$ species will slowly decay to the 5c $\{FeNO\}^7$ species with a rate constant of $k_{His\text{-}off}$ = $2.90 \times 10^{-3}\ s^{-1}$. However, removal of the cross-link restores rapid 6c to 5c conversion that is also NO dependent ($k_{His\text{-}off(NO)}$ = 790 $M^{-1}s^{-1}$). This suggests, at least one function of the cross-link is to kinetically bypass the production of the off-pathway 5c $\{FeNO\}^7$ intermediate during turnover by protecting the cofactor from deactivation by NO thereby allowing for the oxidation of the 6c $\{FeNO\}^7$ to the critical $\{FeNO\}^6$ species for N_2O production.

The next two chapters investigate how the cross-link aids in activating the heme towards NH_2OH oxidation. The previous chapter touches on the fact that the cross-link deficient variant is does not exhibit NH_2OH oxidase activity. The degree of heme ruffling has been proposed to direct the reactivity of the P460 cofactor. Therefore, chapter 4 addresses if the cross-link deficient variants lose NH_2OH oxidase activity due to the formation of a more planar heme site. Chapter 5 further analyzes the differences in reactivity of the cross-link deficient variant compared to WT cyt P460. This analysis demonstrates that the cross-link generates a radically different heme center that seems to be important in directing its ability to carry out direct substrate bound oxidation.

BIOGRAPHICAL SKETCH

Avery Christmastree Vilbert was born in Wilmington, DE on Christmas day. She spent her first couple of years living outside Philadelphia, until moving up to Plattsburgh, NY at the age of 4. In Plattsburgh, NY she enjoyed hiking and fishing in the Adirondacks with her dad. mom and sister. She also loved to play soccer and basketball with her friends. Avery also enjoyed visiting Montreal with her family on the weekends to grab cheeses and sausages to bring back home with her to Plattsburgh.

For college, she moved back to Philadelphia and attended St. Joseph's University. In Philadelphia, Avery enjoyed eating cheesesteaks and cheese fries while attending Big Five, Flyers, Phillies or Eagles games in the city. At St. Joseph's University she discovered her love for chemistry while working in a research lab under Dr. Mark Reynolds. The research focused on a heme protein called FixL, which is an oxygen sensor protein that acts as a kinase to phosphorylate FixJ to activate transcription of nitrogen fixation genes. Avery graduated St. Joseph's University and attended Cornell University for a graduate program in Chemistry and Chemical Biology in Ithaca, NY. There she worked on another heme protein involved in the nitrogen cycle called cytochrome P460.

This is dedicated to my Mom, Dad, my sister Lauren and my cat Bagheera

ACKNOWLEDGMENTS

First, I would like to thank my committee members Brian Crane and Frank Schoeder for being so helpful throughout my years here at Cornell.

I want to extend a special thanks to my advisor Kyle Lancaster and the Lancaster group for understanding the true meaning of a work hard play hard mentality. All of you have made my time here at Cornell fun and enjoyable. Special shout-out to Jon Caranto who has helped me out a lot with this project. Also, I would like to thank Jon and Rich Walroth for always being down to get off topic on Friday afternoons before going to the Barn to get beers.

Next, I would like to thank Kyle Mack, James Lukens and Anton Chavez for our game and GOT nights that were always accompanied by lots of great wine and food. Thanks for always being down for shenanigans.

Mike Lynch, you have been the Jesus to my Mary, my yin to my yang, thanks for all the great low-key wine nights and constant dance parties.

Thanks to my Mom and my Dad. You have always been here for me to support me throughout this long journey, thanks for always coming down to Cornell when I need a good day off for a trip to the wineries. I have learned a lot about balancing hard work and enjoying downtime from you guys, love you!

Special thanks to my sister Lauren, you've been my best friend since day 1 and I truly look up to you and your strength. You will always be the Paris to my Nicole, love you Laur!

Last but definitely not least, I would like to thank Spencer Palmerlee Heins, you have been my rock for these years at Cornell. I am so grateful to have you in my life. There is no one in the world who I would rather spend my time eating wheels of cheese and drinking great wine with. I love you and can't wait to start the next chapter of our lives together.

TABLE OF CONTENTS

LIST OF FIGURES

FIGURES IN APPENDIX

LIST OF TABLES

LIST OF SCHEMES

LIST OF ABBREVIATIONS

AOB = ammonia oxidizing bacteria

AOA = ammonia oxidizing archaea

AMO = ammonia monooxygenase

HAO = hydroxylamine oxidoreductase

Cyt P460 = cytochrome P460

K70Y = lysine 70 to tyrosine variant of cytochrome P460

K70A = lysine 70 to alanine variant of cytochrome P460

NSD = normal-coordinate structural decomposition

CHAPTER 1

INTRODUCTION

Ammonia Oxidizing Bacteria

Microorganisms have developed a wide range of interesting protein machinery in order to obtain energy from many diverse sources in the biosphere.[1] Utilizing either energy driven from light or oxidation of chemical compounds, microorganisms' enzymatic machinery are platforms for the study for interesting biological transformations.[2] Organisms termed chemolithotrophs have developed specific machinery in order to drive the oxidation of a variety of inorganic substrates for cell biosynthesis and maintenance. This thesis focuses on the unique machinery of a type of chemolithotroph that obtains energy for cellular processes via the oxidation of ammonia (NH_3).

Ammonia oxidizing bacteria (AOB), and archaea (AOA) as well as nitrite oxidizing bacteria comprise the organisms that drive nitrification.[3,4] AOB and AOA perform the first step of nitrification which is the oxidation of NH_3 to nitrite (NO_2^-). The second step of nitrification is the 2-electron oxidation of NO_2^- to nitrate (NO_3^-). Recently, organisms have been discovered that can perform the 8-electron oxidization of NH_3 to NO_3^-; these organisms are termed "complete NH_3-oxidizing" or comammox bacteria.[3,5] Nitrification is an important component of the biogeochemical nitrogen cycle for the conversion of fixed nitrogen into more readily assimilated oxyanions, but nitrification promotes deleterious environmental phenomena including greenhouse gas emission and formation of algal blooms.[6] The increase in the world population has led to a need for the increase of NH_3 based fertilizers. AOA and AOB thus have increased feedstocks for the production of NO_2^-/NO_3^-, which easily runoff into lakes, streams and rivers. The runoff into the water systems consequently produce

algal blooms and eventually "dead zones" where the depletion of O_2 results in an environment incapable of supporting marine organisms.[7]

The environmental relevance of AOB make these organisms an important topic of study. A key knowledge gap persists: AOB metabolic machinery are still yet to be fully characterized (Fig. 1). The first step of the ammonia oxidizing pathway requires the input of 2-electrons and is catalyzed by ammonia monooxygenase (AMO). It is proposed that AMO uses Cu and O_2 to activate the strong 107 kcal/mol N-H bond of NH_3 resulting in hydroxylamine (NH_2OH).[8] AMO is a transmembrane protein belonging to the family of copper membrane monooxygenases (CuMMOs).[9] The enzyme particulate methane monooxygenase (pMMO) that oxidizes CH_4 to CH_3OH is the only CuMMO that has been structurally characterized.[10] The first energy generating step of this process is the second step of nitrification, which oxidizes NH_2OH to its proposed product NO_2^- via the multiheme enzyme hydroxylamine oxidoreductase (Fig. 1).[11] This enzyme is homotrimeric and contains 8 hemes per subunit, 7 of which are coordinatively saturated c-type hemes used in electron transfer and the final heme is the active site, P460.[12]

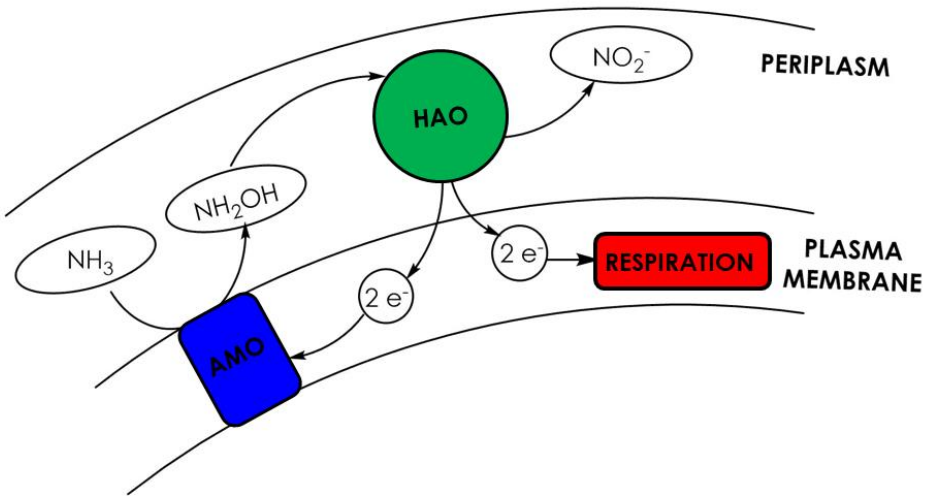

Scheme 1.1. Schematic of the key enzymes involved in bacterial nitrification, ammonia monooxygenase (AMO) and hydroxylamine oxidoreductase (HAO) are labeled above.

The mechanism of NH_2OH oxidation by this unique heme cofactor is the focus of this study. Precise control over each intermediate in this metabolic step is necessary due to the production of highly reactive and cytotoxic intermediates (e.g NH_2OH, HNO, NO). Therefore, extensive studies on this process are necessary in order to understand how these organisms are able to derive energy in a stepwise fashion from these reactive intermediates. This thesis focuses on the unique P460 active site that is necessary for NH_2OH oxidation and discusses how organisms modify the simple heme cofactor to perform a multitude of functions.

Brief overview of porphyrins and their derivatives found in proteins

The macrocyclic tetrapyrroles are found in a wide variety of proteins and can be either metal free as in pheophrytins, biosynthetic intermediates and catabolites or contain Fe as in hemes, Mg as in chlorophylls or Co as in vitamin B_{12}.[13] These biological macrocyclic tetrapyrroles are vital cofactors for a wide range of biological functions. The function of heme proteins wildly varies from binding of small diatomic ligands (e.g NO or O_2) for transport or storage to electron transfer and catalysis.[14] This study seeks to understand the role of a unique heme cross-link modification on its reactivity in the nitrification pathway.

Throughout decades of study of heme proteins, extensive effort has focused on understanding the structural mechanisms that control their varied biological functions.[15] There are a variety of modes that control heme reactivity including the interaction of the protein scaffold on the heme center, as well as, directly modulating the properties of the Fe porphyrin cofactor to yield a particular function.[16] There are a wide range of Fe porphyrins present in heme proteins including heme *a, b, c, d, d_1, o,* and P460.[14] The presence of a particular heme site is essential for a specific function. These heme sites differ from one another either by their peripheral substituents or the degree of conjugation about the porphyrin ring.[17]

The simplest heme is heme *b* (or Fe protoporphyrin IX) and is found in globins, nitrophorins, catalases, peroxidases and nitric oxide synthases (Fig. 2a).[18] These hemes are noncovalently attached to the protein scaffold. However, there are hemes that are covalently attached to proteins via thioether linkages that are termed hemes *c* (Fig. 2b). Heme *c* covalently attaches to the protein via an interaction between sulfhydryl groups of Cys residues and the vinyl groups on the heme. The typical heme-binding motif is the CXXCH.[19] However, attachment of the heme to an (A/F)XXCH motif has also been discovered.[17] The heme protein hydrazine synthase from an annamox bacterium has recently shown through X-ray crystal structure that the heme termed heme-γI has the typical two thioether bonds but it also displays an additional attachment from a nearby Cys residue to the C1 porphyrin methyl group.[20] This site is believed to be the active site of the enzyme that catalyzes the reduction of nitric oxide (NO) to hydroxylamine (NH_2OH).[21]

Tetrapyroles also can differ from one another from the conjugation of the porphyrin ring. These heme derivatives are essential in light harvesting in photosynthetic organisms as well as in the sulfur assimilation pathway. Algae and higher plants utilize chlorophylls, which are green Mg (II) 2,3-dihydroporphyrins (chlorins) whereas purple bacteria utilize bacteriochlorins such as bacteriochlorophyll a. Siroheme is an isobacteriochlorin that is found in sulfite reductases (SiRs) and the related nitrite reductases (NiRs) (Fig. 2c).[22] These enzymes couple the unique siroheme to an iron-sulfur cluster to produce the active site that is essential in performing the 6-electron reduction of sulfite to sulfide or NO_2^- to NH_3.[23]

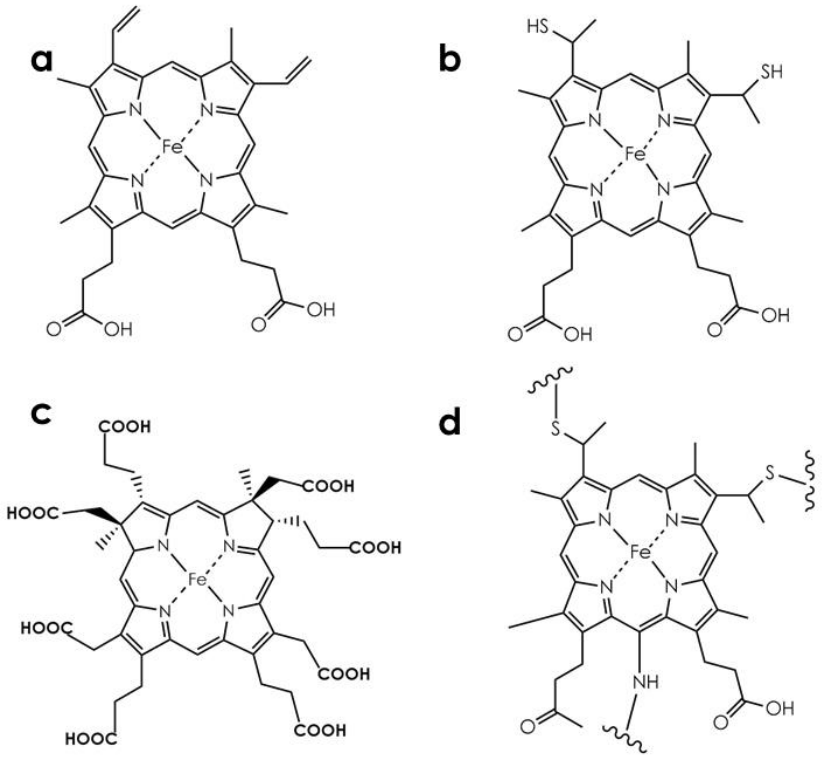

Figure 1.1. Representations of different heme centers in biology heme *b* (a), heme *c* (b), siroheme (c) and P460 (d) from cytochrome P460.

Each perturbation of the tetrapyrrole structure seems to be important in directing biological function. This study seeks to understand the biological function of the unique P460 heme site that is found in a wide variety of bacteria (e.g nitrifying, methanotrophs, annamox). This heme derivative is a *c*-type heme with an additional covalent attachment to the heme center. The P460 cofactor is named for its characteristics Soret peak in the Fe^{II} state.[24] To date there are two different type of P460 heme centers, one that has a Lys-heme cross-link to the meso carbon between the propionate groups[25] (Fig. 3d) and the other has two additional covalent attachments of a Tyr between the thiol linkages.[12] The Tyr $C\varepsilon_1$ and phenolate O cross-

link with the *c*-heme at the 5′ meso carbon and the adjacent pyrrole α-carbon, respectively (Fig. 3c).[12] The heme-Lys cross-link is found in the 36-kDa homodimeric protein cytochrome P460 (Fig. 3b).[26] This protein is found in the periplasm of the nitrifying bacteria *Nitrosomonas europaea* but has also been identified in methanotrophs.[27] The heme-Tyr cross-link belongs to the metabolic enzyme HAO in nitrifying organisms (Fig. 3a). HAO is a member of the octaheme oxidoreductases and a HAO like enzyme has also been identified in anaerobic ammonia oxidizing bacteria (annamox).[28]

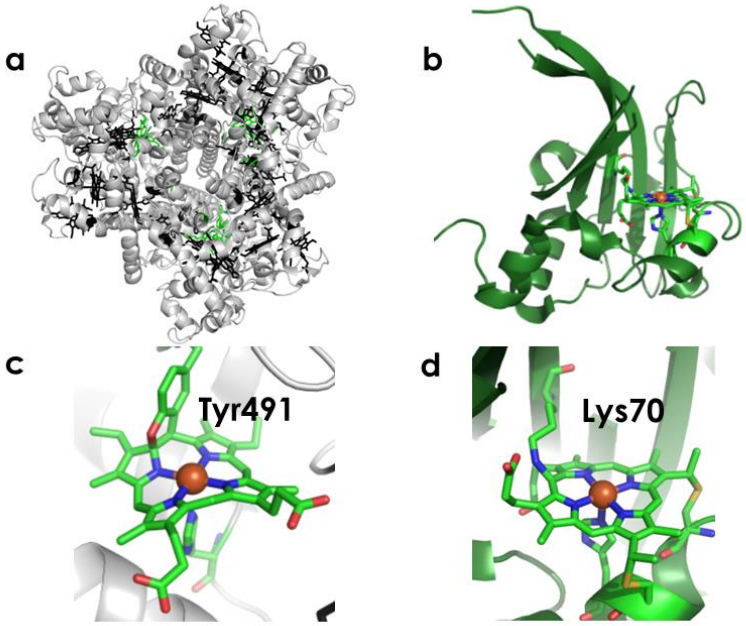

Figure 2.2. X-ray crystal structure of *N. europaea* HAO (a) and cyt P460 (b) and their respective cofactors (c) and (d). PDBID: 1FGJ, 2JE3.

Outline of thesis

This thesis investigates the role of covalent heme modifications in the oxidation of NH_2OH. The first chapter examines the production of N_2O under anaerobic conditions via the oxidation of NH_2OH by cyt P460 *N. europaea*.[29] Under

aerobic conditions, cyt P460 *N. europaea* only produced sub stochiometric amounts of NO_2^-. This is in direct contrast to previous literature[25,30,31], which stated the oxidation of NH_2OH by cyt P460 resulted in the production of NO_2^-. This chapter also discusses how the discovery that cyt P460 does not oxidize NH_2OH to NO_2^- prompted further examination on the product of NH_2OH oxidation by HAO.[32]

The next chapter begins with identification of the 6-coordinate (6c) $\{FeNO\}^7$ species, a key intermediate in the NH_2OH oxidation pathway of cyt P460.[33] This key intermediate also led to further discussion on the role of the cross-link in catalysis. The mechanism for N_2O production by cyt P460 necessitates a 6c $\{FeNO\}^7$ and a $\{FeNO\}^6$ as intermediates. The 5-coordinate (5c) $\{FeNO\}^7$ species was shown to be catalytically incompetent.[29] Treatment of Fe^{II} cyt P460 with a NO donor forms the 6c $\{FeNO\}^7$ species that will slowly decay to the 5c $\{FeNO\}^7$ species with a rate constant of $k_{His\text{-}off} = 2.90 \times 10^{-3}\ s^{-1}$. However, removal of the cross-link now generates a fast 6c to 5c conversion that is now NO dependent ($k_{His\text{-}off(NO)} = 790\ M^{-1}s^{-1}$). The dependence on NO for His dissociation after the formation of the $\{FeNO\}^7$ species is similar to other heme NO signaling proteins.[34] Therefore, the presence of the cross-link is necessary in order to avoid the 5c $\{FeNO\}^7$ dead end species.[33]

However, the cross-link deficient variant does not exhibit NH_2OH oxidase activity. Therefore, the presence of the cross-link must be important in activating the heme towards NH_2OH oxidation, this question is addressed in the next two chapters of the thesis. Chapter 4 first analyzes whether the difference in reactivity comes from the degree of ruffling in the P460 center. The degree of heme ruffling has been proposed to direct the reactivity of the P460 cofactor.[35] The degree of ruffling has been shown to modulate reduction potential, where a more ruffled heme exhibits a lower more negative reduction potential.[35] Ruffling has also been proposed to increase the stability of the $\{FeNO\}^6$.[36] Chapter 4 therefore addresses if the cross-link deficient variants

lose NH_2OH oxidase activity due to the formation of a more planar heme site. Chapter 5 further examines the differences in reactivity of the cross-link deficient variant compared to wild-type (WT) cyt P460. This analysis suggests that the role of the cross-link may be to generate a radically different heme center that is important in directing its ability to carry out direct substrate bound oxidation.

REFERENCES

1. Zannoni, D. *Respiration in Archaea and Bacteria: Diversity of Prokaryotic Respiratory Systems*. *Advances in Photosynthesis and Respiration* **16,** (2005).
2. Pace, N. R. A Molecular View of Microbial Diversity and the Biosphere. *Science (80-.).* **276,** 734 LP-740 (1997).
3. Lancaster, K. M., Caranto, J. D., Majer, S. H. & Smith, M. A. Alternative Bioenergy: Updates to and Challenges in Nitrification Metalloenzymology. *Joule* **2,** 421–441 (2018).
4. Klotz, M. G. & Stein, L. Y. Nitrifier genomics and evolution of the nitrogen cycle. *FEMS Microbiol. Lett.* **278,** 146–156 (2008).
5. Van Kessel, M. A. H. J. *et al.* Complete nitrification by a single microorganism. *Nature* **528,** 555–559 (2015).
6. Reay, D. S. *et al.* Global agriculture and nitrous oxide emissions. *Nat. Clim. Chang.* **2,** 410–416 (2012).
7. Conrad, R. Soil microorganisms as controllers of atmospheric trace gases (H2, CO, CH4, OCS, N2O, and NO). *Microbiol. Rev.* **60,** 609–40 (1996).
8. Ensign, S. A., Hyman, M. R. & Arp, D. J. In vitro activation of ammonia monooxygenase from Nitrosomonas europaea by copper. *J. Bacteriol.* **175,** 1971–1980 (1993).
9. Coleman, N. V. *et al.* Hydrocarbon monooxygenase in Mycobacterium: Recombinant expression of a member of the ammonia monooxygenase superfamily. *ISME J.* **6,** 171–182 (2012).
10. Lieberman, R. L. & Rosenzweig, A. C. Crystal structure of a membrane-bound metalloenzyme that catalyses the biological oxidation of methane. *Nature* **434,** 177–182 (2005).
11. Arp, D. J., Sayavedra-Soto, L. A. & Hommes, N. G. Molecular biology and biochemistry of ammonia oxidation by Nitrosomonas europaea. *Arch. Microbiol.* **178,** 250–255 (2002).
12. Cedervall, P., Hooper, A. B. & Wilmot, C. M. Structural studies of hydroxylamine oxidoreductase reveal a unique heme cofactor and a previously unidentified interaction partner. *Biochemistry* **52,** 6211–6218 (2013).
13. Warren, M. J. *Tetrapyrroles Birth , Life and Death*.
14. Poulton, R. *et al.* NIH Public Access. **360,** 1640–1645 (2013).
15. Jentzen, W., Ma, J.-G. & Shelnutt, J. A. Conservation of the Conformation of the Porphyrin Macrocycle in Hemoproteins. *Biophys. J.* **74,** 753–763 (1998).
16. A. Shelnutt, J. *et al.* Nonplanar porphyrins and their significance in proteins. *Chem. Soc. Rev.* **27,** 31 (1998).
17. Lin, Y. W. Structure and function of heme proteins regulated by diverse post-translational modifications. *Arch. Biochem. Biophys.* **641,** 1–30 (2018).
18. Bertini, I. & Gray, H. B. *Bioinorganic chemistry*.
19. Cowley, A. B., Lukat-Rodgers, G. S., Rodgers, K. R. & Benson, D. R. A Possible Role for the Covalent Heme-Protein Linkage in Cytochrome c Revealed via Comparison of N-Acetylmicroperoxidase-8 and a Synthetic, Monohistidine-Coordinated Heme Peptide. *Biochemistry* **43,** 1656–1666 (2004).
20. Dietl, A. *et al.* The inner workings of the hydrazine synthase multiprotein complex. *Nature* **527,** 394–397 (2015).
21. Kartal, B. *et al.* Molecular mechanism of anaerobic ammonium oxidation. *Nature* **479,** 127–130 (2011).

22. Stroupe, M. E. & Getzoff, E. D. The Role of Siroheme in Sulfite and Nitrite Reduetases. (2009).
23. Exchange, E. L., Crane, B. R., Siegel, L. M., Getzoff, E. D. & Carolina, N. Structures of the Siroheme- and Fe 4 S 4 -Containing Active Center of Sulfite Reductase in Different States of Oxidation : Heme Activation via Reduction-Gated. **1,** 12101–12119 (1997).
24. Collins, M. J., Arciero, D. M. & Hooper, A. B. Optical spectropotentiometric resolution of the hemes of hydroxylamine oxidoreductase. Heme quantitation and pH dependence of E(m). *J. Biol. Chem.* **268,** 14655–14662 (1993).
25. Pearson, A. R. *et al.* The crystal structure of cytochrome P460 of Nitrosomonas europaea reveals a novel cytochrome fold and heme - Protein cross-link. *Biochemistry* **46,** 8340–8349 (2007).
26. Elmore, B. O., Bergmann, D. J., Klotz, M. G. & Hooper, A. B. Cytochromes P460 and c′-beta; A new family of high-spin cytochromes c. *FEBS Lett.* **581,** 911–916 (2007).
27. Bergmann, D. J., Zahn, J. A., Hooper, A. B. & DiSpirito, A. A. Cytochrome P460 genes from the methanotroph Methylococcus capsulatus bath. *J. Bacteriol.* **180,** 6440–6445 (1998).
28. Maalcke, W. J. *et al.* Structural basis of biological no generation by octaheme oxidoreductases. *J. Biol. Chem.* **289,** 1228–1242 (2014).
29. Caranto, J. D., Vilbert, A. C. & Lancaster, K. M. Nitrosomonas europaea cytochrome P460 is a direct link between nitrification and nitrous oxide emission. (2016). doi:10.1073/pnas.1611051113
30. Numata, M., Saito, T., Yamazaki, T., Fukumori, Y. & Yamanaka, T. Cytochrome P-460 of Nitrosomonas europaea: Further purification and further characterization. *J. Biochem.* **108,** 1016–1021 (1990).
31. Fernández, M. L., Estrin, D. A. & Bari, S. E. Theoretical insight into the hydroxylamine oxidoreductase mechanism. *J. Inorg. Biochem.* **102,** 1523–1530 (2008).
32. Caranto, J. D. & Lancaster, K. M. Nitric oxide is an obligate bacterial nitrification intermediate produced by hydroxylamine oxidoreductase. *Proc. Natl. Acad. Sci.* 201704504 (2017). doi:10.1073/pnas.1704504114
33. Vilbert, A. C., Caranto, J. D. & Lancaster, K. M. Influences of the heme-lysine crosslink in cytochrome P460 over redox catalysis and nitric oxide sensitivity. *Chem. Sci.* **9,** 368–379 (2018).
34. Derbyshire, E. R. & Marletta, M. A. Structure and Regulation of Soluble Guanylate Cyclase. *Annu. Rev. Biochem.* **81,** 533–559 (2012).
35. Liptak, M. D., Wen, X. & Bren, K. L. NMR and DFT investigation of heme ruffling: Functional implications for cytochrome c. *J. Am. Chem. Soc.* **132,** 9753–9763 (2010).
36. Walker, F. A. Nitric oxide interaction with insect nitrophorins and thoughts on the electron configuration of the {FeNO}6complex. *J. Inorg. Biochem.* **99,** 216–236 (2005).

CHAPTER 2

NITROSOMONAS EUROPAEA CYTOCHROME P460 IS A DIRECT LINK BETWEEN NITRIFICATION AND NITROUS OXIDE EMISSION

Reproduced in part from:

"*Nitrosomonas europaea* cytochrome P460 is a direct link between nitrification and nitrous oxide emission"

Jonathan D. Caranto, Avery C. Vilbert and Kyle M. Lancaster

Proceedings of the National Academy of Sciences. **2016** 113, 14704-14709.

https://doi.org/10.1073/pnas.1611051113

I gratefully acknowledge Dr. Jon D. Caranto for his help on the gas chromatography experiments for stoichiometry of NH_2OH to N_2O. As well as his work on the steady state experiments and deriving the rate equation for the cyt P460 minimal mechanism. I would also like to thank Prof. Kyle Lancaster on his guidance throughout this project.

Introduction

Nitrous oxide (N_2O) participates in ozone-layer depletion and possesses a global warming potential nearly 300 times greater than that of CO_2.[1] Atmospheric N_2O concentrations have increased approximately 120% since the pre-industrial era, largely due to the widespread use of fertilizers required to produce sustenance for humans and livestock.[2] Agricultural soils account for an estimated 60–75% of global N_2O emissions, a by-product of microbial transformations of fertilizer components including ammonia (NH_3) and nitrate (NO_3^-). The nitrification pathway oxidizes NH_3 to NO_3^- and produces

N_2O as a by-product.[3,4] Nitrification occurs in two steps, both of which are mediated by autotrophic microorganisms: NH_3-oxidizing bacteria (AOB) or archaea (AOA) oxidize NH_3 to nitrite (NO_2^-), which nitrite-oxidizing bacteria subsequently oxidize to NO_3^-. NH_3-oxidizing microbes contribute substantially to global N_2O emission while NO_2^--oxidizing bacteria produce negligible N_2O.[5] The source of N_2O is unclear, but is proposed to result as an adventitious by-product of the nitrification pathway or as a product of the nitrifier denitrification pathway.[2,6,7]

The biochemical oxidation of NH_3 to NO_2^-occurs in two steps.[8] The first step is catalyzed by the membrane-bound NH_3 monooxygenase, which uses Cu and dioxygen (O_2) to hydroxylate NH_3 to hydroxylamine (NH_2OH). In the second step, NH_2OH is oxidized by four-electrons to NO_2^- by hydroxylamine oxidoreductase (HAO). HAO is a multi-heme enzyme with eight c-type hemes per subunit: Seven are electron transfer cofactors and the eighth is the so-called cytochrome P460 active site that contains a unique tyrosine crosslink to the heme ring (Fig. 1b). The ferrous form of this "P460" cofactor is characterized by its eponymous 460 nm Soret absorption. The enzyme (or enzymes) that AOA use to oxidize NH_2OH are currently unknown.[9,10]

AOB also possess machinery for nitrifier denitrification that reduces NO_2^- to N_2O via a nitric oxide (NO) intermediate.[3,11] The archetypal AOB *Nitrosomonas europaea* possesses genes for a copper-containing nitrite reductase (NirK) and a membrane-bound heme-containing NO reductase (NorB). NirK reduces NO_2^- by one electron to NO while NorB catalyzes the 2-electron reduction of 2 NO to N_2O. In contrast to the O_2-dependent nitrification pathway, nitrifier denitrification is

upregulated in microaerobic or anaerobic conditions. The production of N_2O and NO by AOB increases at low O_2 concentration. [12] However, nitrifier denitrification does not account for total N_2O emission because N_2O is also producecd under aerobic conditions as well.

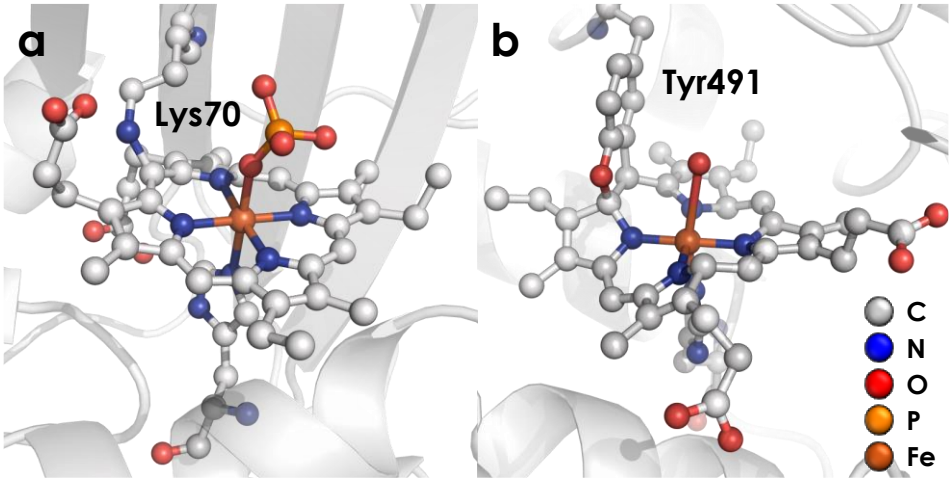

Figure 2.2. Fe^{III} P460 cofactors in cyt P460 (a) (Protein Data Bank (PDB) 2JE2) and HAO (b) (PDB 4FAS)

Under aerobic conditions, N_2O is proposed to result from incomplete oxidation of NH_2OH to either nitroxyl (HNO) or NO.[7,13] Two equiv. HNO rapidly reacts to form N_2O, while NO is proposed to be reduced by an NO reductase. In support of these proposals, both NO and N_2O have been observed to form during steady-state turnover of purified HAO under aerobic conditions.[14] NorB could facilitate the reduction of NO to N_2O. However, AOB still produces N_2O at atmospheric O_2 tension with a NorB knockout strain which is consistent with an alternate N_2O production pathway.[15]

This study demonstrates that there is a direct enzymatic pathway from NH_2OH to N_2O by the constitutively expressed cytochrome (cyt) P460 from *N. europaea.* Cyt

P460 is a 36 kDa homodimeric protein in which each subunit bears a mono-His *c*-heme with an N–C cross-link from the 13′ meso-carbon to the amine of Lys70 (Fig. 1a).[16] This cross-link necessarily influences electronic structure through the disruption of porphyrin π-conjugation. Moreover, the heme P460 macrocycle exhibits significant ruffling, a common distortion mode for *c*-type heme.[17,18] An analogous P460 center is found in HAO, however, the P460 center in HAO has two crosslinks to the heme center one at the 5′ mesocarbon and the other at an adjacent pyrrole α-carbon. The presence of the P460 cofactor has been implemented in NH_2OH oxidation. [16,19,20]

Studies of purified HAO, HAO analogs and cytochrome (cyt) P460 demonstrated that the product of NH_2OH oxidation by this P460 active site remains a subject of debate. Therefore, not only does this study show that there is a direct route to N_2O emission from NH_2OH, but it also ignited further discussion on the product of NH_2OH oxidation by the metabolic enzyme HAO. Cyt P460 was previously reported to exhibit NH_2OH oxidase activity via the production of NO_2^-.[21] However, *Methylococcus capsulatus* (Bath) cyt P460 was reported to yield a NH_2OH:NO_2^- ratio of 1:0.85 and thus never achieving full conversion to NO_2^-suggesting the remaining NH_2OH is transformed to a second product. An HAO-like protein from the anaerobic NH_3-oxidizing microorganism, *Kuenenia stuttgartiensis*, was shown to oxidize NH_2OH to NO instead of NO_2^-. [22] Likewise, *N. europeae* HAO was found to produce a mixed bag of N-oxides under anaerobic conditions.[14] Investigation of the NH_2OH oxidation pathway by cyt P460 is ideal due to the lack of electron-transfer cytochrome c sites, which occludes spectroscopic data of the active site. This study demonstrated that the

production of N_2O by cyt P460 undergoes a direct oxidation of the substrate bound NH_2OH that proceeds to a three-electron oxidized intermediate. Identification of this latter species is shown to be an iron-nitrosyl species that reacts with NH_2OH to form N_2O in the rate-determining step. This study also comments on how the identification of the NH_2OH oxidation pathway by cyt P460 paved the way for the discovery of NO as the product of NH_2OH oxidation by HAO.[23]

Exclusive Conversion of Hydroxylamine to N_2O by Cyt P460 under Anaerobic Conditions

Consistent with previous studies, under aerobic conditions *Nitrosomonas europea* cyt P460 reacts with NH_2OH in the presence of the oxidant phenazine methosulfate (PMS) to form NO_2^- as detected by Griess diazotization assays.[16] However, as with *M. capsulatus* (Bath) cyt P460, stoichiometric oxidation of NH_2OH to NO_2^- was not observed. The maximum stoichiometry achieved for the oxidation of NH_2OH by *N. europaea* cyt P460 was 0.7 mol NO_2^- per mol NH_2OH (Table 1). Gas chromatography (GC) analysis revealed that the remainder of the NH_2OH was converted to N_2O.

Table 2.1. Oxidation of NH_2OH by cyt P460 under aerobic conditions[a]

$[NH_2OH]_0$ (μM)	$[N_2O]$ (μM)	$[NO_2^-]$ (μM)	Total NH_2OH consumed (μM)	% converted to N_2O	% converted to NO_2^-
100	15	61	91	33	67
500	104	259	467	45	55
1000	227	515	969	47	53

[a]Reaction conditions were 5 μM cyt P460, 1 mM PMS in 50 mM phosphate, pH 8.0 at 37 °C

Similar experiments were performed under anaerobic conditions to determine whether NH_2OH could be stoichiometrically converted to a single product. Under these

conditions, GC analysis (Fig. 2) revealed that cyt P460 catalyzes oxidant-driven ($[Ru(NH_3)_6]Cl_3$, horse-heart cyt *c*, or PMS), selective N_2O production from NH_2OH. Reaction stoichiometries were established by monitoring the amount of N_2O produced under various NH_2OH (Fig. 3a) or oxidant concentrations (Fig. 3b). Our results showed that the reaction requires 2 equiv. NH_2OH 4 equiv. of oxidant to produce 1 equiv. of N_2O (Equation 1):

$$2\ NH_2OH \rightarrow N_2O + H_2O + 4\ e^- + 4\ H^+ \quad (1)$$

Only trace N_2O is formed in the absence of either enzyme or oxidant (Fig. 2). No NO_2^- could be detected when cyt P460 was treated with NH_2OH and PMS under anaerobic conditions.

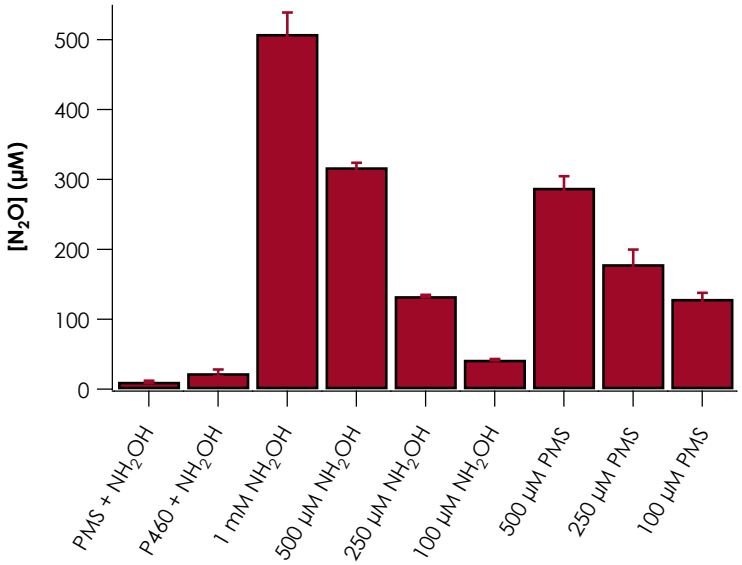

Figure 2.3. N_2O production by cytochrome (cyt) P460 under varying NH_2OH and oxidant concentrations as monitored with gas chromatography. Data points are averages of triplicate reactions of 5 μM ferric cyt

P460 in anaerobic 50 mM 4-(2-hydroxyethyl)-1-piperazine-ethanesulphonic acid, pH 8.0, at room temperature overnight. Error bars represent 1 standard deviation of three trials.

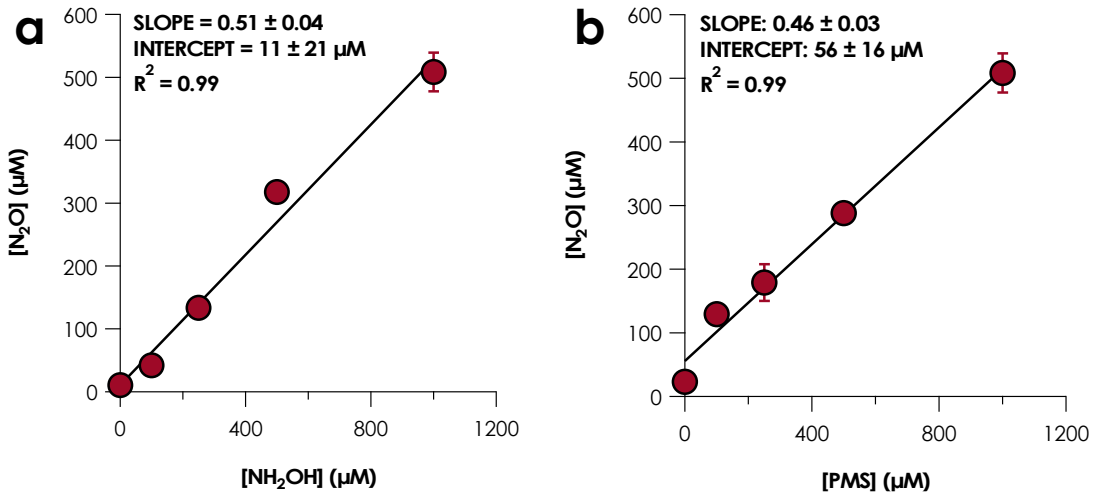

Figure 2.4. Stoichiometry of nitrous oxide (N_2O) production by cyt P460 determined with gas chromatography. Data points are averages of triplicate trials with 5 µM ferric cyt P460 in anaerobic 50 mM 4-(2-hydroxyethyl)-1-piperazine-ethanesulphonic acid (HEPES), pH 8.0, at room temperature overnight. Error bars represent 1 standard deviation of three trials. In (a), the concentration of phenazine methosulfate (PMS) is held at 1.0 mM while the hydroxylamine (NH_2OH) concentration is varied; in (b), the NH_2OH concentration is held at 1.0 mM while PMS concentration varies.

Steady-State Kinetics

Steady-state cyt P460 activity assays were performed under anaerobic conditions using a reported 2,6-dichlorophenolindophenol (DCPIP)/PMS coupled assay.[21] The activity was monitored with UV/visible (UV/vis) absorption spectroscopy by following the decay of the DCPIP absorbance at 605 nm. Under steady-state conditions, 2 equivalents of DCPIP were reduced for each equivalent of N_2O produced as monitored by a N_2O-selective electrode (Fig. 4). This stoichiometry is consistent with Equation 1 since DCPIP is a two-electron oxidant, therefore this assay provides a convenient means of measuring steady-state N_2O production by cyt P460.

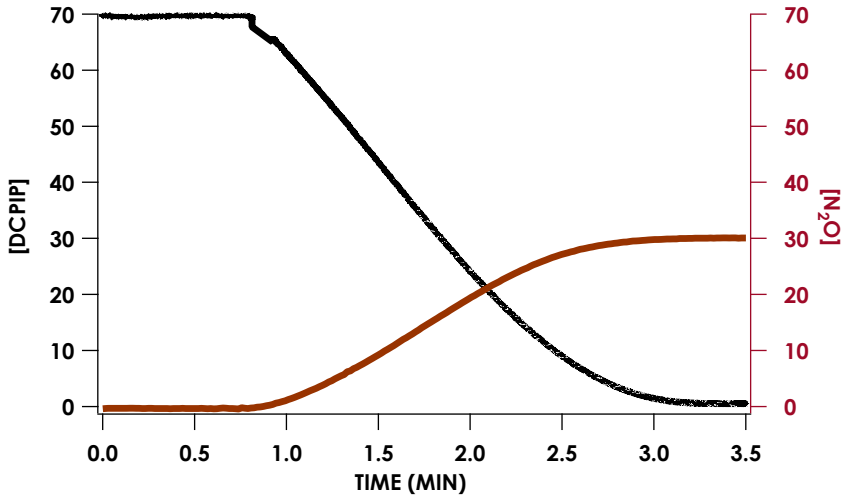

Figure 2.5. Representative time courses of 2,6-dichlorophenolindophenol (DCPIP) consumption (black trace) and N_2O production (red trace) during the reaction of 1 µM cyt P460 with 5 mM NH_2OH and 70 µM DCPIP in anaerobic 50 mM phosphate, pH 8.0, at 25 °C. Consumption of DCPIP was monitored by its absorbance at 605 nm. N_2O production was measured with an N_2O-selective electrode. Initial rates were measured through fitting to a linear equation. Initial rates showed a DCPIP consumption rate of 40 µM min^{-1} and an N_2O production rate of 20 µM min^{-1}. Experiment conducted by J.D.C.

Steady-state activities of cyt P460 have been reported previously,[16,21] but no studies have presented steady-state activity plots. The steady-state activity plot (Fig. 5) shows non-saturating, linear behavior from 0.05 to 20 mM NH_2OH that spans turnover frequencies of 0.3 to 80 µM DCPIP consumed•min^{-1}•µM enzyme^{-1}. This non-saturating behavior precludes determination of k_{cat} or K_M, but the slope of this linear region suggests a k_{cat}/K_M of at least 5000 M^{-1} min^{-1} (26). However, the following characterization of pathway intermediates suggests a multistep reaction mechanism that is inconsistent with classical Michaelis–Menten kinetics (*vide infra*).

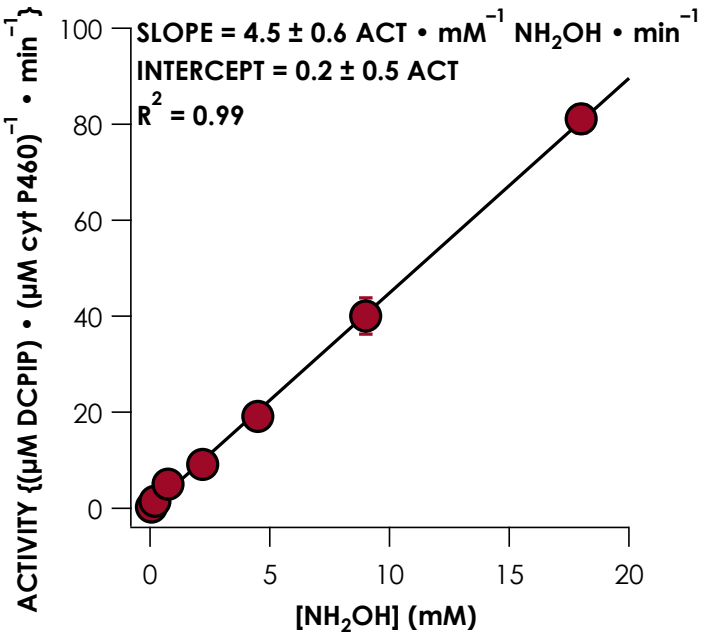

Figure 2.6. Steady-state hydroxylamine oxidase activity plot for cyt P460. The assay conditions were 1 μM cyt P460, 6 μM PMS, and 100 μM 2,6-dichlorophenolindophenol with various NH_2OH concentrations in anaerobic 50 mM HEPES, pH 8.0, at 25 °C. Each data point is the average of three trials with error bars representing 1 standard deviation. The black trace is a linear regression fit to the data. Experiment conducted by J.D.C.

Characterization of Cyt P460 Fe^{III}-NH_2OH

Recombinant expression and purification of cyt P460 was previously achieved by Elmore and co-workers.[16] This method yields an emerald green protein with UV/vis absorption and electron paramagnetic resonance (EPR) spectra consistent with those previously reported for the enzyme isolated from *N. europaea*.[16,24] The absorption spectrum of the as-isolated cyt P460 has a Soret λ_{max} at 440 nm with a shoulder at 414 nm and Q-band maxima at 570 nm and 627 nm (Fig. 6a). The corresponding EPR spectrum (Fig. 6b) is characteristic of an $S = {}^5/_2$ Fe^{III}, with g values of 6.57, 5.09, and 1.97 ($^E/_D = 0.03$).

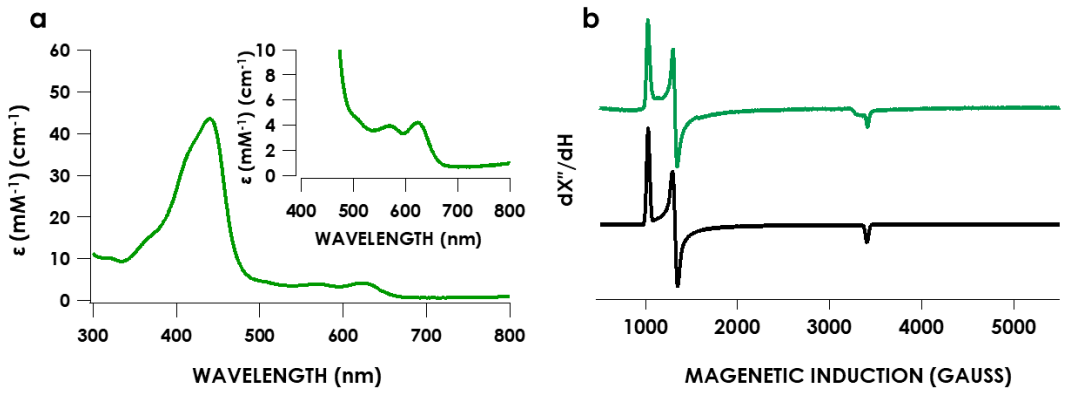

Figure 2.7 UV/vis absorption spectrum (a) and Electron paramagnetic spectrum (b) of cyt P460 Fe^{III}. Black trace is the simulated spectrum with parameters listed in Table (appendix).

The crystal structure of the as-isolated cyt P460 (see Fig. 1a) shows a phosphate-ligated Fe center.[16] It is still unclear if the distal position of cyt P460 *N. europaea* is occupied with a water molecule in noncoordinating buffer. A Cyt P460 from the organism *Nitrosomonas* sp. AL212was crystalized and diffracted to 1.45 Å resolution.[25] This cyt P460 also exhibited a high spin $S = {}^5/_2$ Fe^{III} EPR signal with similar g-values as *N. europaea* cyt P460. According to the crystal structure of cyt P460 AL212, the P460 heme lacked a ligand in the distal coordination site, suggesting that as-isolated Fe^{III} cyt P460 is 5-coordinate rather than 6-coordinate with a bound water. However, cyt P460 AL212 also lacks a glutamate residue above the heme pocket. In the previously characterized crystal structure of *N. europaea* this amino acid was shown to H-bond with the bound phosphate. This amino acid has also been shown to be important in the catalysis of NH_2OH oxidation. The UV/vis absorption spectrum of cyt P460 Al212 exhibits a more pronounced shoulder at 414 nm than *N. europaea* cyt P460. The split Soret has been shown to be due to the non-degenerate e_g set according to the 4-orbital model of the porphyrin electronic structure and therefore linked to the symmetry of the porphyrin. Mutation of the alanine residue to a glutamate residue in cyt P460 AL212

decreases the shoulder at 414 nm with a more pronounced absorbance at 440 nm more consistent with cyt P460 *N. europaea.* This decrease in the shoulder at 414 nm could be a result of increase in symmetry going from the 5-coordinate cyt P460 AL212 to the 6-coordinate cyt P460 with a bound water. Therefore, it is speculated that in *N. europaea* cyt P460 a water molecule is bound at distal site similar to HAO[20] (Fig. 1b) and held in place via the H-bonding interaction from the glutamate residue. However, without a crystal structure of *N.europaea* cyt P460 in a non-coordinating buffer, it remains unknown if the Fe^{III} as isolated species is 6-coordinate.

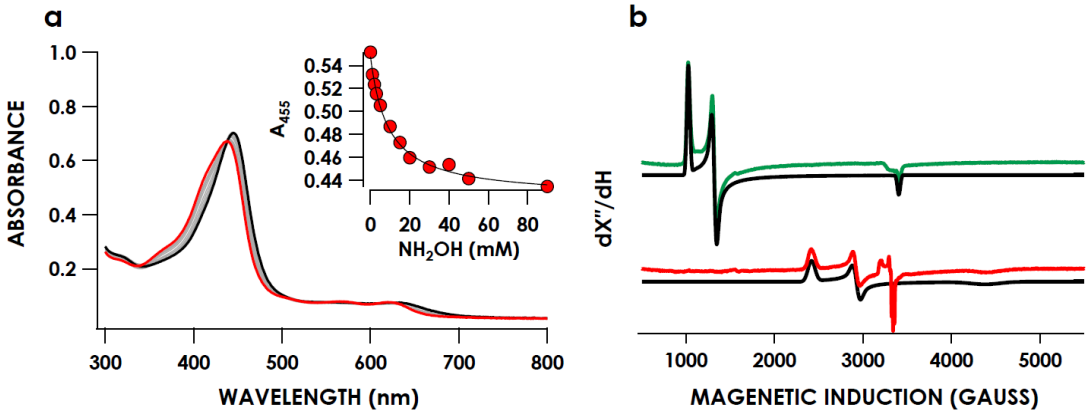

Figure 2.8. Cyt P460 and NH_2OH titration curve as monitored by (a) UV/visible (UV/vis) absorption spectroscopy. UV/vis traces of 12 µM cyt P460 titrated against various amounts of NH_2OH in anaerobic 50 mM phosphate, pH 8.0, at room temperature. Inset shows a plot of $A_{414\text{-nm}}$ versus NH_2OH concentration. This was fit to the following hyperbolic equation: $\boldsymbol{A_{414-nm}} = \frac{\Delta A_{414}[NH_2OH]_0}{K_d + [NH_2OH]_0}$. EPR spectra of 170 µM cyt P460 (Fe^{III}-aquo) in green and of 170 µM cyt P460 with 50mM NH_2OH (red) in anaerobic 50 mM phosphate, pH 8.0. The spectra were collected at 10 K and a microwave power of 6 µW. The spectra shown in black are the simulated spectra. Black trace is the simulated spectrum with parameters listed in Table (appendix).

The addition of NH_2OH to Fe^{III} cyt P460 produces a species with a UV/vis absorption spectrum distinct from that of the resting oxidized species. Within the time of manual mixing, the 414 nm shoulder of the Fe^{III} spectrum disappears concomitantly

with a shift in the Soret to 445 nm and broadening of the Q-bands. This putative NH_2OH binding was analyzed more clearly by monitoring changes in the UV/vis absorption spectrum during the titration of cyt P460 with NH_2OH. The resulting series of spectra (Fig. 7a) showed an isosbestic point at 438 nm, which suggested a one-step conversion from the resting to the Fe^{III}-NH_2OH species. The NH_2OH dissociation constant [$K_{d(NH_2OH)}$] was determined by plotting the absorption at 414 nm (A_{414}) against NH_2OH concentration (Fig. 7a, inset). This absorption decreased as NH_2OH concentration increased. Fitting the data to a hyperbolic binding curve resulted in a $K_{d(NH_2OH)}$ of 9 ± 1 mM (Fig. 7a, inset).

The EPR spectrum of Fe^{III} cyt P460 treated with 100 mM NH_2OH showed the complete disappearance of the Fe^{III} $S = {}^5/_2$ signal and the appearance of two rhombic $S = {}^1/_2$ EPR signals (Fig. 7b). The first signal had g-values of 2.75, 2.28, and 1.54 and was consistent with a highly anisotropic low-spin Fe^{III}.[26] EPR spectra of cyt P460 treated with increasing concentrations of NH_2OH verified the $K_{d(NH_2OH)}$ value determined with UV/vis spectrometry. The conversion from high-spin to low-spin Fe^{III} supports the conclusion that NH_2OH binds to the iron center. Therefore, this new S = ½ species was assigned as an Fe^{III}-NH_2OH complex.

The EPR spectrum of Fe^{III} cyt P460 treated with 100 mM NH_2OH (see Fig. 7b) showed a second rhombic $S = {}^1/_2$ signal with g-values of 2.10, 2.02, and 2.01 and ^{14}N hyperfine coupling with values of 50 MHz, 57 MHz, and 45 MHz. This signal represented less than 5% of the total spin and was consistent with a 5-coordinate heme ferrous-nitrosyl species[27] ($\{FeNO\}^7$ in Enemark–Feltham notation[28]). This species was

also generated independently by treating cyt P460 with disodium diazen-1-ium-1,2,2 triolate ($Na_2N_2O_3$, Angeli's salt), a nitroxyl (HNO) donor. The resulting $\{FeNO\}^7$ was stable to treatment with both NH_2OH and oxidant (Fig. 8). This low yield and lack of reactivity suggest that the species is a dead-end product, outside the productive N_2O-generating cyt P460 pathway. The presence of the $\{FeNO\}^7$ species in the absence of air, oxidant or NO is puzzling. One possibility is that the samples are exposed to a small amount of air during freezing, which oxidizes the Fe^{III}-NH_2OH species to $\{FeNO\}^7$. Experiments by Hendrich and coworkers[29] on HAO also found a similar 5-coordinate $\{FeNO\}^7$ EPR signal when HAO is treated with NH_2OH.

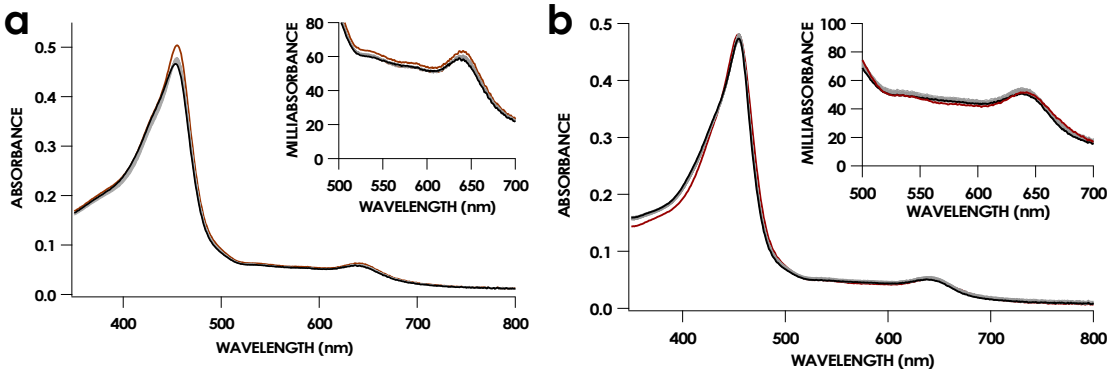

Figure 2.9. UV/vis absorption spectrum of 10 µM cyt P460 incubated with 50 µM Angeli's salt for 30 min and then reacted with either (a) NH_2OH or (b) $[Ru(NH3)_6]Cl_3$. All reactions were performed in anaerobic 200 mM HEPES, pH 8.0, at room temperature.

Observation and Characterization of an Intermediate in NH_2OH Oxidation

The addition of the oxidant $[Ru(NH_3)_6]Cl_3$ to Fe^{III}-NH_2OH under anaerobic conditions results in the formation of a new species with a Soret band maximum at 455 nm. Cyt P460 (10µM) was pre-incubated with 6 mM NH_2OH to form the Fe^{III}-NH_2OH adduct. The addition of 200 µM $[Ru(NH_3)_6]Cl_3$ initiated a reaction that was monitored

with UV/vis absorption spectroscopy. The resulting spectral time course of 20 min showed two phases. The first phase featured the accumulation of a new species within 2 min. The absorption spectrum of the new species exhibits an intense and sharp Soret band centered at 455 nm with Q-bands at 554 nm, 603 nm, and 652 nm (Fig. 9). Several isosbestic points apparent in the spectral time course indicated a one-step transition from Fe^{III}-NH_2OH to this new species. The second phase featured the decay of the new species to Fe^{III}-NH_2OH. The spectral time course of this phase also exhibited several isosbestic points. The complete time course strongly suggested the accumulation and decay of an intermediate on the cyt P460 pathway. This putative intermediate is referred to as the 455 nm intermediate owing to its Soret absorption maximum.

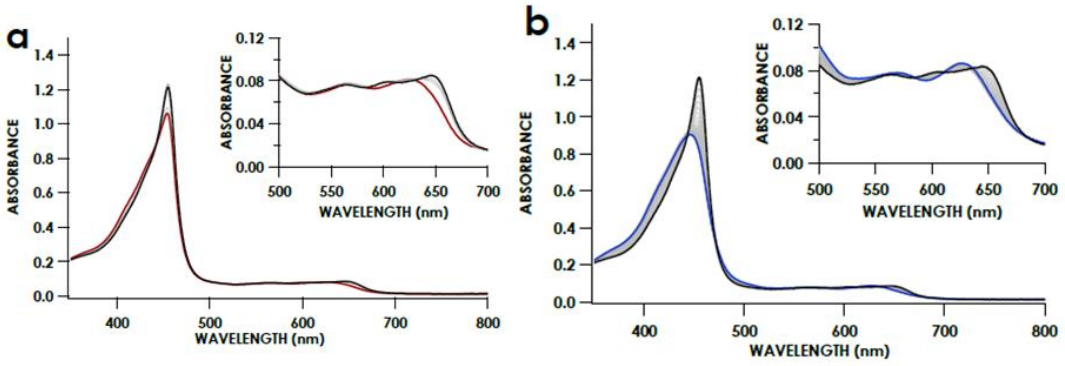

Figure 2.10. Representative UV/vis absorption spectral time courses of the (a) accumulation and (b) decay of the 455 nm intermediate during the reaction of 10 µM cyt P460, 80 µM $Ru(NH_3)_6Cl_3$, and 6 mM NH_2OH in 50 mM HEPES, pH 8.0, at room temperature. The reaction was initiated by the addition of $Ru(NH_3)_6Cl_3$. The red trace in panel (a) is the UV/vis spectrum collected immediately after the addition of NH_2OH, and the black trace is the accumulated 455-nm intermediate. The blue trace in panel (b) is the spectrum of the decay product. The insets in both figures highlight the Q-band region.

Monitoring the reaction kinetics for the formation and decay of the 455-intermediate with respect to NH_2OH produced an interesting result. As expected there was a dependence on NH_2OH for the formation of the 455 nm intermediate indicative

of the reaction requiring NH_2OH. More interestingly, however, there was also a dependence on NH_2OH for the decay of the 455 nm intermediate. The formation and decay of the 455 nm intermediate produced a double exponential curve (Fig. 10a). The sum of two exponentials were fit to the $A_{455\text{-nm}}$ traces providing observed rate constants (k_{obs}) for both the formation [$k_{obs(1)}$] and decay [$k_{obs(2)}$] of the 455 nm species. At higher NH_2OH concentrations, $k_{obs(1)}$ was too fast to fit accurately but qualitatively appeared to increase with increasing NH_2OH concentration. The $k_{obs(2)}$ parameter showed a linear dependence on NH_2OH consistent with a bimolecular reaction between NH_2OH and the 455 nm intermediate. A linear regression fit to a plot of k_{obs} versus NH_2OH concentration provided an apparent second-order rate constant of 0.07 mM^{-1} min^{-1} (Fig. 10b).

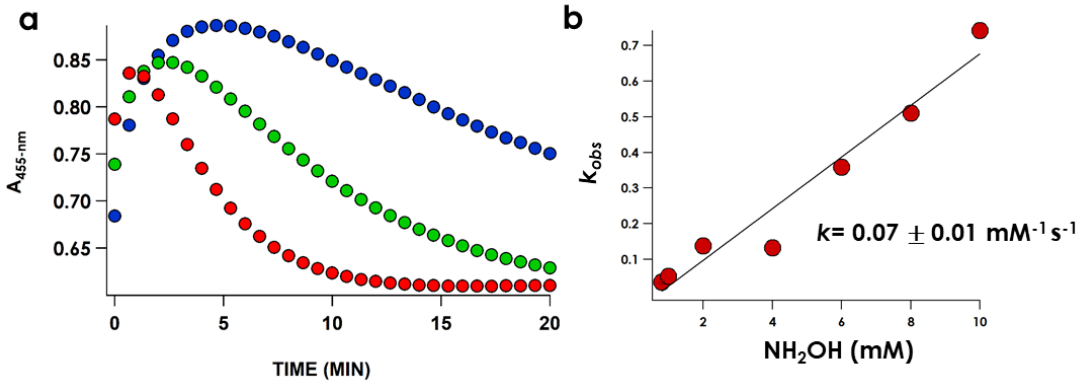

Figure 2.11. (a) Representative $A_{455\text{-nm}}$ traces monitoring the reaction of cyt P460 (10 µM), and $Ru(NH_3)_6Cl_3$ (100 µM) vs. 1 mM (blue), 2 mM (green) and 6 mM (red) NH_2OH concentrations. (b) Plot of k_{obs2} determined by fitting Equation S1 to traces in panel a vs. NH_2OH concentration.

If the decay of the 455 nm intermediate is dependent on NH_2OH, then under limiting NH_2OH concentrations a long-lived 455 nm species can be produced. Using DPCIP as the oxidant (Fig. 11), the formation of the 455 nm intermediate was complete

in the time of mixing and its concentration persisted for 1 min—until DCPIP was completely consumed—at which point the 455 nm absorbance slowly decreased. The addition of 10 mM NH_2OH after DCPIP was consumed hastened the decay of the 455 nm intermediate (Fig. 11). The spectral time course of the decay phase showed an isosbestic point at 445 nm consistent with direct conversion of the intermediate to a single species. Comparison of the final decay product spectrum with that of as-isolated cyt P460 mixed with 10 mM NH_2OH confirmed that the decay product was Fe^{III}-NH_2OH. The persistence of the 455 nm intermediate in the presence of excess oxidant suggests that under turnover conditions, the decay of the intermediate is the rate-determining step. The apparent increase in the intermediate decay rate at higher NH_2OH concentrations is consistent with a bimolecular reaction between the intermediate and NH_2OH.

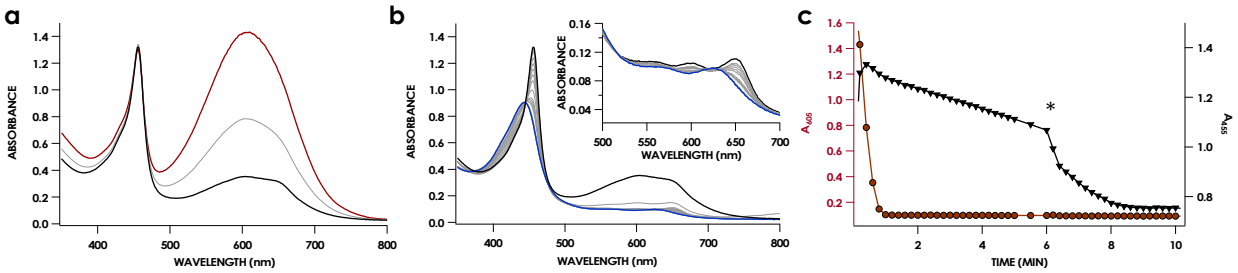

Figure 2.12. Representative spectral time courses of the (a) accumulation and (b) decay of the 455 nm intermediate during the reaction of 12 µM cyt P460 with 1 mM NH_2OH using 70 µM DCPIP as the oxidant in 50 mM phosphate, pH 8.0, at room temperature. The reaction was initiated by the addition of 1 mM NH_2OH. Part (b) shows a representative spectral time course of the decay of the 455 nm intermediate before and after adding another 10 mM NH_2OH. In kinetic traces of the decay of the 455 nm intermediate, black is the accumulated intermediate and blue is the final decay product. The inset highlights the Q-band region. (c) Representative 455 and 605 nm traces following the accumulation and decay of the 455 nm intermediate (red trace) and the consumption of DCPIP (black trace). The asterisk indicates the addition of 10 mM NH_2OH to the 455 nm intermediate once the DCPIP has been exhausted. Experiment conducted by J.D.C.

The 455 nm intermediate was trapped by freezing the reaction of 170 μM cyt P460 with 2 mM NH_2OH and 2 mM DCPIP within 1 minute. The spectrum of the resulting sample showed neither the $S = {}^5/_2$ nor the $S = ½$ signals associated with Fe^{III} or Fe^{III}-NH_2OH, respectively (Fig. 12a). The absence of these signals strongly suggested that the protein was converted to the 455 nm intermediate or another partially oxidized EPR-silent species. The only EPR signal observed in this sample was an $S = ½$ with hyperfine structure that we attributed to Mn^{2+} contamination in the protein sample. The lack of an iron-based EPR signal implied that the 455 nm intermediate is a diamagnetic or non-Kramers (integer spin greater than 0) species.

To identify the decay product of this reaction, an EPR spectrum was obtained after treating 150 μM cyt P460 with 45 mM NH_2OH and 2 mM DCPIP for 10 min at room temperature. The EPR spectrum of this sample lacked any $S = {}^5/_2$ signal but showed 80 μM of the Fe^{III}-NH_2OH signal and 70 μM of the $\{FeNO\}^7$ signal (Fig. 12a). The combined spin quantities accounted for all of the Fe centers in this sample, which indicated quantitative conversion of the protein to either Fe^{III}-NH_2OH or $\{FeNO\}^7$. Together with the above EPR result, this suggests that the 455 nm intermediate is a perpendicular-mode X-band EPR-silent species, and its decay products comprise a combination of both the Fe^{III}-NH_2OH and the unreactive $\{FeNO\}^7$ species.

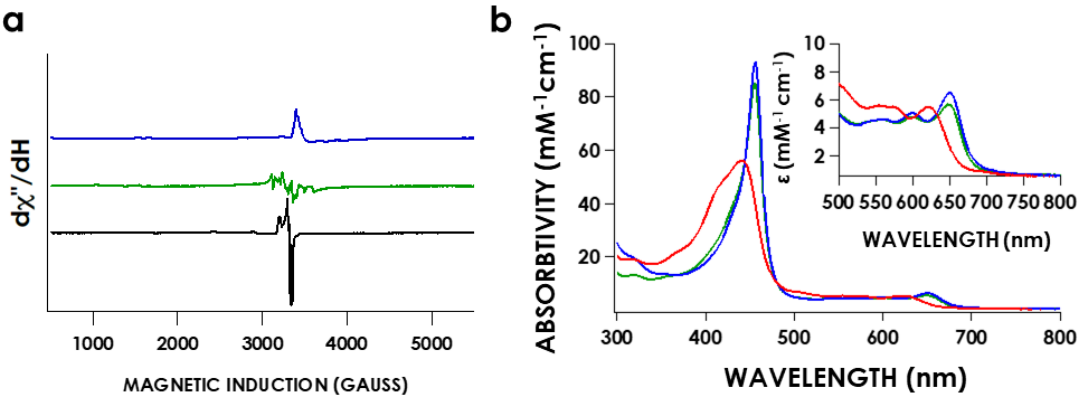

Figure 2.13. Electron paramagnetic resonance spectra (a) of 170 μM cyt P460 treated with 2mM Proli-NONOate (blue trace), with 2 mM NH_2OH and 2 mM DCPIP (green trace) and with 45 mM NH_2OH and 2 mM DCPIP and incubated for 10 min (black trace). Spectra were collected at 10 K and 633 μW or at 20 K and 63 μW**.** UV/vis absorption spectra (b) of Fe^{III} cyt P460 (red trace), $\{Fe\text{-}NO\}^6$ cyt P460 generated via treatment with PROLI-NONOate (blue) or oxidation of Fe^{III}-NH_2OH (green). The inset magnifies the Q-bands.

Identification of the 455 nm Intermediate as an {FeNO}^{6} Species

The requirement for oxidant to form the 455 nm intermediate suggested that the species is an oxidized form of Fe^{III}-NH_2OH. Bari and co-workers[30] proposed several oxidized species for the mechanism of HAO, including $\{FeNO\}^7$, $\{FeNO\}^6$, and an Fe^{II}-ONOH species. Other possibilities include the one-electron oxidized ferric NH_2OH radical (Fe^{III}-$^{\bullet}NH_2OH$), which has been proposed as an intermediate in the enzymatic pathway of P450 NO reductase[31,32]. Another possibility is Fe^{II}-HNO, which has been characterized in only one biological system, the myoglobin–HNO complex[33,34]. Finally,

because N_2O is the product of cyt P460 under these conditions, another possibility is that the 455 nm intermediate is an Fe–N_2O complex.

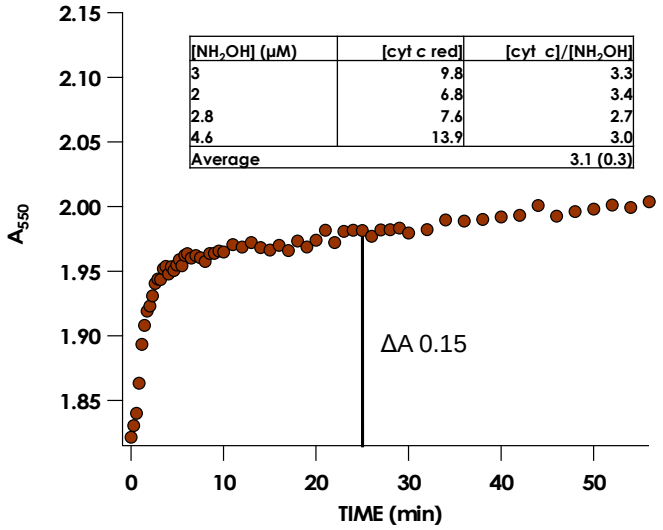

Figure 2.14. A 550 nm trace monitoring the reduction of cyt c in the presence of NH_2OH at sub-stoichiometric concentrations relative to cyt P460. Final reaction conditions: 15 μM cyt P460, 23 μM cyt c in phosphate, pH 8.0 at room temperature. The reaction was initiated by adding 2.8 μM NH_2OH. Experiment conducted by J.D.C.

The number of oxidizing equivalents required to convert Fe^{III}-NH_2OH to the 455 nm intermediate was determined by treating sub-stoichiometric NH_2OH with excess cyt P460 and cyt *c*. The reduction of cyt *c* was monitored by the increase in absorption at 550 nm (ε_{550} = 19,600 $M^{-1}cm^{-1}$,[35] (Fig. 13). These experiments showed that 3 electrons are required to oxidize Fe^{III}-NH_2OH to the 455 nm intermediate, which suggested an $\{FeNO\}^6$ or Fe^{II}-ONOH species.[28] Supporting this assignment, Fe^{III} cyt P460 treated with NO produced an EPR-silent species (see Fig. 12a) with a UV/vis absorption spectrum identical to that of the 455 nm intermediate (see Fig. 12b). This 455 nm intermediate was therefore assigned as an $\{FeNO\}^6$. The $\{FeNO\}^6$ intermediate

generated from the reaction of Fe^{III} cyt P460 and NO was stable for at least 1 h and stable towards excess DCPIP (Fig. 14). This stability is inconsistent with the hypothesis that the hydrolysis of an $\{FeNO\}^6$ P460 center forms an Fe^{II}-ONOH adduct poised for proton-coupled, one-electron oxidation to NO_2^-.[30] Additionally, cyt P460 does not produce NO_2^- under anaerobic conditions.

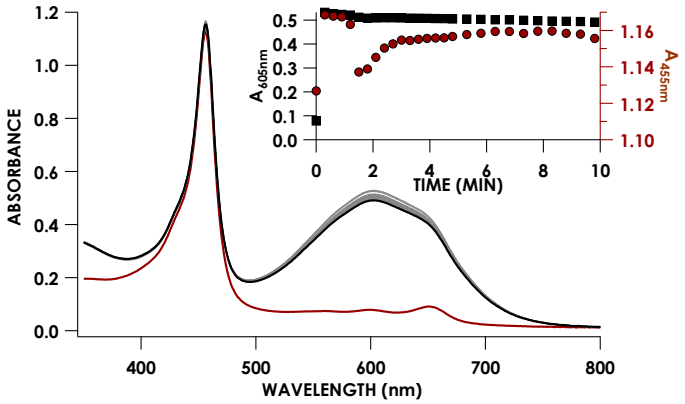

Figure 2.15. Stability of $\{FeNO\}^6$ against DCPIP. P460 (16 µM) and 1 equivalent of NO were first reacted to generate the $\{FeNO\}^6$ species (red trace). Then 30 µM DCPIP was added. The inset single-wavelength traces follow the absorbance at 605 nm for DCPIP (black squares) and the absorbance of the 455 nm intermediate (red circles).

The stability of the $\{FeNO\}^6$ intermediate in the absence of NH_2OH and the NH_2OH-concentration dependence of its decay suggested that $\{FeNO\}^6$ reacts with NH_2OH to form N_2O. Experiments with a 'shunted' $\{FeNO\}^6$ were monitored to confirm this reactivity of the $\{FeNO\}^6$ and NH_2OH. The $\{FeNO\}^6$ species could be directly formed by adding 2 equivalents of NO (as either gas or a NONOate) to cyt P460. The addition of 2 mM NH_2OH resulted in the decay of the 455 nm species to Fe^{III}-NH_2OH (Fig. 15a). Consumption of $\{FeNO\}^6$ generated in this manner exhibited

the same dependence on NH_2OH concentration, 0.06 ± 0.01 mM^{-1} min^{-1}, as the $\{FeNO\}^6$ that accumulated under turnover conditions (Fig. 15b).

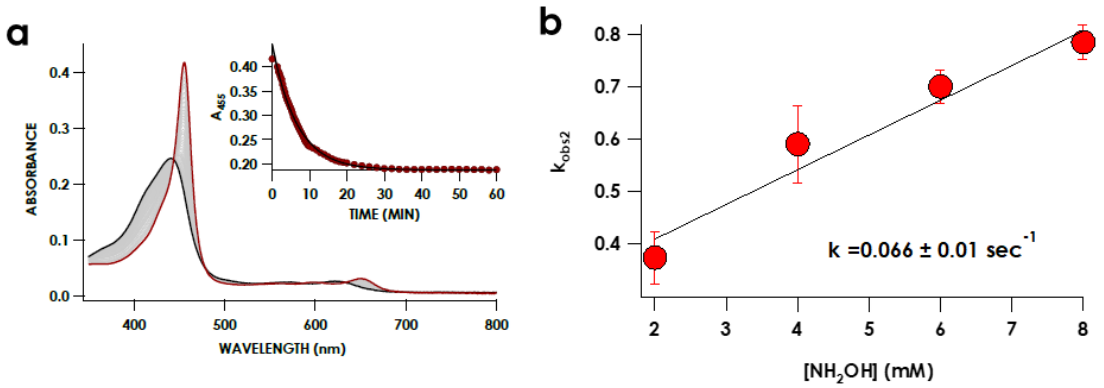

Figure 2.16. Reaction of $\{FeNO\}^6$ formed via the NO shunt with NH_2OH. The $\{FeNO\}^6$ species was formed with 5 µM cyt P460 and 16 µM PROLI-NONOate in 200 mM HEPES, pH 8.0. The decay of $\{FeNO\}^6$ was initiated by addition of a final concentration of 2 mM NH_2OH and followed by observing the decay of the 455 nm Soret peak. (a) UV/vis absorption spectra time course of decay of the 455 nm (red) Soret peak to the Fe^{III}-NH_2OH adduct (black). Inset shows the $A_{455\text{-nm}}$ trace. (b) pseudo-first order plot of the reaction of 5 µM cyt P460 and 16 µM PROLI-NONOate in 200 mM HEPES, pH 8.0 with varying NH_2OH concentrations. Experiments were performed at 25 °Cat pH 8.0.

To determine if this was the N_2O production step of this pathway, cyt P460 was treated with varying concentrations of PROLI-NONOate and excess NH_2OH, and the amount of N_2O produced under these conditions was monitored by GC/MS. The results indicated a clear 1:1 stoichiometry of N_2O produced versus NO added (Fig. 16a). Furthermore, the addition of NO to NH_2OH in the absence of cyt P460 showed no evidence of N_2O production. This result was consistent with NO binding to cyt P460 to form the $\{FeNO\}^6$ intermediate, which then reacts with NH_2OH to form N_2O. The same experiment was performed with NO and isotopically labeled $^{15}NH_2OH$. The production of 95% mixed isotope product via the mass shift from 44 amu to 45 amu (Fig. 16b) in

the presence of cyt P460 clearly showed that N_2O is produced via the reaction between the $\{FeNO\}^6$ species and NH_2OH.

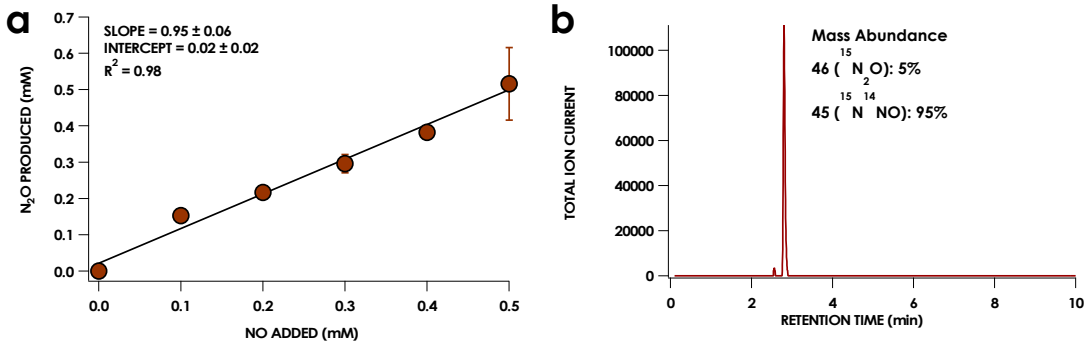

Figure 2.17. Gas chromatography–mass spectroscopy (GC–MS) analysis of $\{FeNO\}^6$ shunt experiments with the addition of 10 mM NH2OH. The $\{FeNO\}^6$ was generated by using 5 μM cyt P460 and varying amounts of PROLI-NONOATE. The reaction was initiated with the addition of 10 mM NH_2OH. (a) Stoichiometry results of the GC–MS analysis showing a 1:1 ratio of added NO to produced N_2O. (b) MS chromatogram showing that the reaction of $^{15}NH_2OH$ with $\{FeNO\}^6$ (P460 and ^{14}NO) produces only mixed-isotope N_2O.

Proposed Mechanism for N_2O Formation from NH_2OH by Cyt P460

Given the results above, a mechanism in Scheme 1 was proposed for the NH_2OH oxidase activity of cyt P460. The catalytic cycle initiates from the resting Fe^{III} ($S = {}^5/_2$) state, which binds NH_2OH to form an S = ½ Fe^{III}-NH_2OH intermediate that is stable in the absence of oxidant. In the presence of oxidant, Fe^{III}-NH_2OH is rapidly oxidized by three electrons to the EPR-silent $\{FeNO\}^6$, which undergoes nucleophilic attack by a second equivalent of NH_2OH, yielding N_2O and H_2O. Production of N_2O yields an Fe^{II} species that is rapidly oxidized to return the cycle to Fe^{III}.

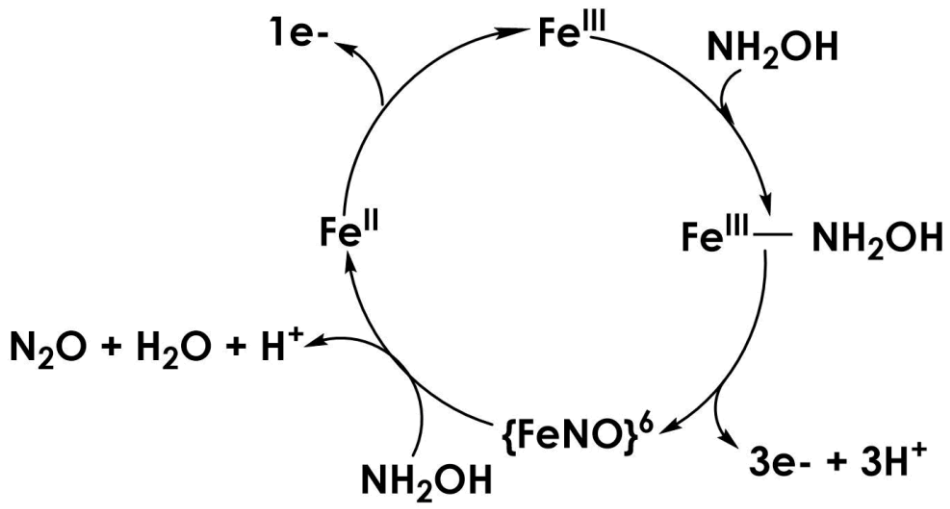

Scheme 2.1. Minimal mechanism of NH_2OH oxidation by cyt P460.

Several other intermediates are envisioned between the conversion of Fe^{III} to $\{FeNO\}^6$. Both one-electron ($K_3[Fe(CN)_6]$, Cu^{II}-azurin, and $[Ru(NH_3)_6]Cl_3$) and two-electron oxidants (DCPIP and PMS) can access $\{FeNO\}^6$, which suggests that rapid, subsequent one-electron oxidation steps occur in the transition from Fe^{III}-NH_2OH to $\{FeNO\}^6$. Although an $\{FeNO\}^7$ appeared under certain conditions (i.e., after complete consumption of oxidant), this was not a catalytically competent intermediate. The EPR spectrum of this species is consistent with a 5-coordinate $\{FeNO\}^7$ leaving the possibility that a 6-coordinate $\{FeNO\}^7$ is on the reaction pathway (see Ch. 3).[27,36] Possible one-electron oxidized intermediates include Fe^{III}-$^{\bullet}NH_2OH$ or an $\{Fe(H)NO\}^8$. However, there has been no evidence in these experiments of any other species formed prior to $\{FeNO\}^7$.

The rate-determining step of the anaerobic cyt P460 cycle is the bimolecular reaction of NH_2OH with $\{FeNO\}^6$, which results in N_2O formation. The UV/vis absorption spectral features of Fe^{III} reacted with NO are identical to those exhibited for the intermediate formed using NH_2OH and oxidant (Fig. 12b). Combined with the lack of Fe-based EPR signals in these samples, the data suggest that under both conditions all active sites are quantitatively converted to this species. This quantitative accumulation suggests that its decay upon nucleophilic attack by NH_2OH is the rate-determining step of the catalytic cycle. There is precedent for NH_2OH reacting with $[Fe(CN)_5(NO)]^{2-}$—a classic example of $\{FeNO\}^6$—to form N_2O with stoichiometry matching that proposed above for cyt P460.[37]

We propose that NH_2OH reacts with $\{FeNO\}^6$ to form an Fe^{II} species based on the precedent that $[Fe(CN)_5NO]^{2-}$ reacts with NH_2OH to form $[Fe(CN)_5(OH_2)]^{3-}$. Oxidation of the Fe^{II} species then returns the enzyme to the Fe^{III} resting form. However, the characteristic 463 nm UV/vis absorption peak of reduced cyt P460 was never observed in our experiments as an intermediate or an end product. The Fe^{II} cyt P460 is expected to rapidly react with other species present during turnover (oxidant, NH_2OH or NO [See below]), thereby, precluding its observation. The reaction of Fe^{II} cyt P460 with NO produces the same inactive $\{FeNO\}^7$ species as observed when Fe^{III} reacts with HNO (Fig. 8). Fe^{II} cyt P460 reacts with NH_2OH to form Fe^{III} via an intermediate with a UV/vis absorption feature at 663 nm that has not been observed in any of our other experiments (Fig. 17). This 663 nm intermediate forms and disappears within 3 s and therefore, assignment of this intermediate will require rapid-mixing techniques. Most importantly, the reaction of Fe^{II} with NH_2OH does not inactivate the enzyme.

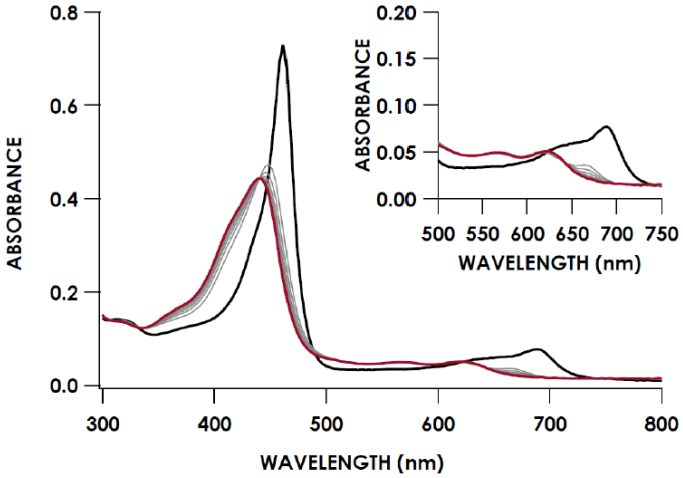

Figure 2.18. UV/vis absorption spectral time course of 30 μM Fe^{II} cyt P460 mixed with 10mM NH_2OH in anaerobic 50 mM sodium phosphate, pH 8.0 at 25°C. The black spectrum is the spectrum of the Fe^{II} cyt P460 before adding NH_2OH. Grey traces are collected every 0.3 seconds after NH_2OH addition. The red spectrum is the final spectrum at 3.0 seconds. Experiment conducted by J.D.C

Single wavelength (463-nm) stopped-flow UV/vis absorption spectroscopy provided insight into why inactivation of the enzyme by NO is avoided during turnover (Fig. 18). The kinetics of the Fe^{II} cyt P460 reaction with $[Ru(NH_3)_6]Cl_3$), NH_2OH or NO were measured. The oxidant, $[Ru(NH_3)_6]Cl_3$, completely oxidized Fe^{II} cyt P460 to Fe^{III} within the time of mixing (< 3 ms) placing a lower limit on k_{obs} of 1100 s^{-1}. The reactions with NH_2OH and NO exhibit k_{obs} of 1.3 and 2.8 s^{-1}, respectively. These results indicate that oxidation of Fe^{II} to Fe^{III} is much faster than the other two reactions, thereby avoiding the inactive $\{FeNO\}^7$ species. After the oxidant is completely consumed, Fe^{II} will react with either NH_2OH or NO. The reaction of NH_2OH will form the Fe^{III} resting species, or in the case of high NH_2OH concentration, Fe^{III}-NH_2OH, whereas the reaction with NO results in the inactive $\{FeNO\}^7$. Thus, this accounts for the products observed in EPR spectrum of 455-nm intermediate decay sample (Fig. 12a).

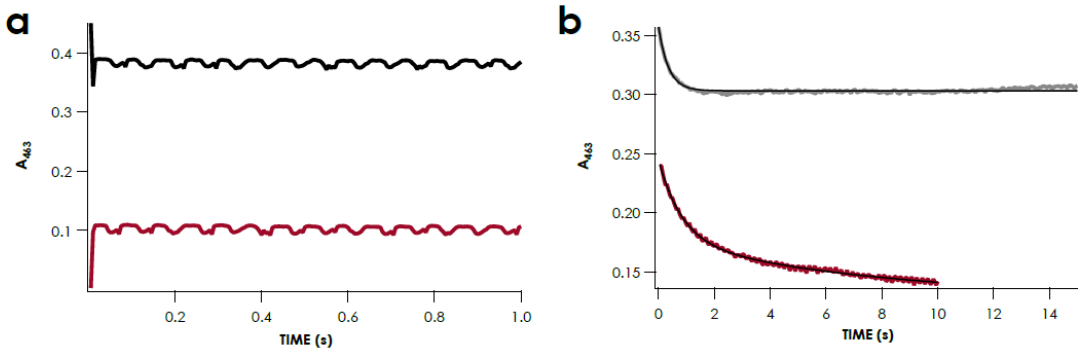

Figure 2.19. Single-wavelength (463 nm) stopped-flow time courses of Fe^{II} cyt P460 (a) before (black trace) and adter (red trace) mixing with 1 mM $[Ru(NH_3)_6Cl_3$ and (b) after mixing with 1mM NO (gray trace) or 2 mM NH_2OH (red trace). Fits to the data are shown in black. Conditions after mixing were 7 µM cyt P460 in anaerobic 50mM sodium phosphate, pH 8.0 at 25°C. Experiment conducted by J.D.C.

To account for the linear behavior observed in the steady-state activity plot (see Fig. 5), the King–Altman method[38] was used to derive a steady-state equation based on the minimal mechanism shown in Scheme 1. In this simplified model, NH_2OH binding was treated as reversible, with association (k_1) and dissociation (k_{-1}) rate constants. Both the Fe^{III}-NH_2OH oxidation (k_2) and the subsequent $\{FeNO\}^6$ reaction with NH_2OH (k_3) were assumed to be irreversible. The resulting model (Equations 2–4) indicated that k_2[ox] influences both k_{cat} and K_m.

$$\frac{velocity}{[\text{cyt P460}]_0} = \frac{k_2[\text{ox}][\text{NH}_2\text{OH}]_0}{K_m + [\text{NH}_2\text{OH}]_0} \quad (2)$$

$$K_m = \frac{k_{-1}k_3 + k_2[\text{ox}](k_1 + k_3)}{k_1 k_3} \quad (3)$$

$$k_{cat} = k_2[\text{ox}] \quad (4)$$

There are two limiting regimes of the derived steady-state model in which either $k_{-1}k_3$ or k_2[ox]($k_1 + k_3$) dominates the numerator of the K_m term. In the first limit, K_m should resemble $K_{d(NH_2OH)}$, which we measured to be 9 mM. The steady-state activity plot lacks any clear curvature despite the inclusion of activity measurements up to 20 mM NH_2OH.

This result suggested that the second regime, which is highly dependent on k_2[ox], contributed substantially under these assay conditions, thereby increasing the observed K_m. Currently, an estimate of only one rate constant (k_3, 0.07 $mM^{-1}min^{-1}$) and lack evidence that Fe^{III}-NH_2OH oxidation or the $\{FeNO\}^6$ reaction with NH_2OH are irreversible. For now, the absence of saturation in the steady-state activity plot is attributed to a large K_m, which suggests a large second-order rate constant for Fe^{III}-NH_2OH oxidation.

The kinetic model suggests that the physiological rate of N_2O generation by cyt P460 is influenced by physiological NH_2OH concentration, oxidant concentration, and the rate of electron transfer between Fe^{III}-NH_2OH and the oxidant. *N. europaea* can tolerate at least 10 mM NH_2OH without showing inhibited O_2 uptake.[39] Under steady-state conditions, the rate of N_2O production is estimated at 10 mM NH_2OH to be 23 μM N_2O μM $enzyme^{-1}$ min^{-1}. The properties of the oxidant, including its reduction potential, heavily influence k_2 and, by extension, the rate at which N_2O is produced by cyt P460. The identity of the native electron transfer partner is unknown and therefore the true physiological rate remains undetermined. Future kinetic studies will provide further insights into the effects oxidant reduction potential, pH, and other conditions may have on the physiological rate of N_2O production.

The observation that NO binding accesses a shunt in the cyt P460 catalytic pathway provides evidence for the hypothesis that cyt P460 contributes to NO detoxification in the cell.[2] Furthermore, if NO binding is reversible, there may be an alternate cyt P460 NH_2OH-oxidation pathway that results in NO as the product. At low

NH_2OH concentrations, at which the bimolecular reaction with $\{FeNO\}^6$ would be slow, NO dissociation may outpace N_2O formation.

This alternate NO formation pathway is also likely responsible for the observation of NO_2^- formation under aerobic conditions since NO reacts with O_2 in aqueous solution to form NO_2^-. To test this hypothesis, $\{FeNO\}^6$ was generated by allowing Fe^{III} to react with one equivalent of NO generated from PROLI-NONOate. Exposure of the resulting $\{FeNO\}^6$ species to aerobic conditions results in the enzyme returning to Fe^{III} and generation of NO_2^- (Fig. 19). Therefore, under aerobic conditions production of NO_2^- is not directly formed by cyt P460 but is a by-product resulting from NO dissociation from the $\{FeNO\}^6$ intermediate. A detailed kinetic analysis will be performed in a future study to determine the partitioning between the NO_2^- and N_2O forming pathways.

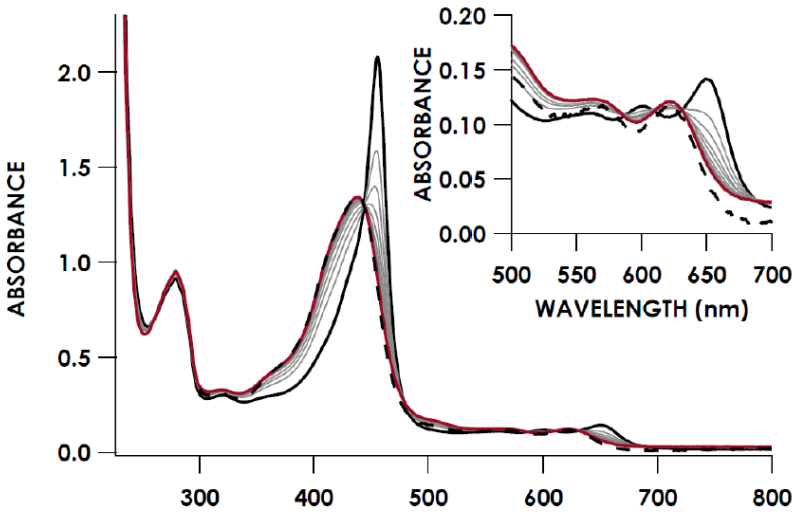

Figure 2.20. UV/vis absorption spectral time course over 24 mins of Fe^{III} cyt P460 (30 μM) with 1 equiv. NO that had been exposed to air in 50 mM sodium phosphate, pH 8.0 at 25 °C. Inset shows expanded Q-band region. The initial spectrum is shown in black of the $\{FeNO\}^6$ species generated from the addition of 0.5 equivalents of PROLI-NONOate to Fe^{III} cyt P460. Grey traces are collected in 2-minute increments after exposure to air and the red spectrum is the final spectrum after 24 minutes. The dashed line is Fe^{III} cyt P460 (30 μM) for comparison.

A previous report showed that cell free extracts of *N. europaea* oxidize NH_2OH to N_2O and NO without any formation of NO_2^-.[40] Furthermore, purified HAO was shown to react with NH_2OH and PMS or DCPIP under aerobic conditions to form a mixture of products including NO, N_2O, NO_2^- and NO_3^-.[14]Additionally, a stable $\{FeNO\}^6$ species on the P460 cofactor of HAO was observed after Fe^{III} was allowed to react with NO in the absence of NH_2OH.[29] Given the results from the oxidation of NH_2OH by cyt P460 and the evidence above, the biochemistry of HAO was revisited (see below) to determine if NO_2^- is indeed its terminal, enzymatic product.[22]

Outlook: Environmental Consequences?

AOB are major contributors to N_2O emissions from wastewater treatment plants (WWTPs), at which *N. europaea* is the dominant AOB species.[41] There are two proposed methods for N_2O emission from AOB, the first is as a product in the nitrifier denitrification pathway and the second is as a by-product in incomplete NH_2OH oxidation. The direct mechanism of NH_2OH oxidation to N_2O, although largely unknown, has been linked to incomplete NH_2OH oxidation by HAO. The results of our study demonstrate that the constitutively expressed cytochrome P460 is a direct link between NH_2OH oxidation and the emission of N_2O from *N. europaea*. This study establishes an alternative oxidative route to the production of N_2O from NH_2OH by cyt P460. A strict stoichiometry of 2 equivalents of NH_2OH and 4 oxidizing equivalents to produce 1 equivalent of N_2O was established through GC and kinetic analysis. Due to the reactivity of NH_2OH with biological electrophiles, *N. europaea* must have evolved methods for detoxification to deal with high NH_2OH concentrations. Previously, cyt P460 was thought to have a role in NH_2OH detoxification through the oxidation of NH_2OH and NO to NO_2^-.[19] However, the results suggested herein an alternative role in NH_2OH detoxification through the production of N_2O.[2]

The production of N_2O from NH_2OH oxidation by cyt P460 was demonstrated under anaerobic conditions, thereby establishing a direct enzymatic link between nitrification and N_2O formation via NH_2OH. The identification of this source of N_2O emission helps to explain the production of N_2O in WWTP under conditions of low dissolved O_2 concentrations and high NH_3 concentrations; conditions where the nitrifier denitrification pathway would not dominate.[3] The influx of high

concentrations of NH_3 in WWTPs causes an increase in NH_3 oxidation rates, which in turn increases intracellular NH_2OH concentration.[42] Studies using activated sludge from WWTPs with high concentrations of NH_3 have shown that transitioning from an aerobic to an anoxic environment increases the amount of N_2O released. Isotopic labeling studies show that the N_2O produced under these conditions originates from the NH_2OH oxidation pathway rather than the nitrifier denitrification pathway.[12] This study pinpoints direct N_2O production via the NH_2OH oxidation pathway. Identifying the chemical source of this emission should aid in the design and operation of WWTPs with curtailed N_2O emission. The influx of NH_4^+ to high concentrations in WWTPs and the accumulation of intracellular NH_2OH by AOB suggest that cyt P460 has a role in the detoxification of excess cellular NH_2OH and therefore a role in the emission of N_2O by AOB.

Hydroxylamine Oxidoreductase oxidizes NH_2OH to NO, and not NO_2^-

Exclusive production of N_2O by cyt P460 prompted the reinvestigation of NH_2OH oxidation by HAO. Previous reports of the oxidation of NH_2OH by HAO showed similar inconsistencies as seen with cyt P460. Reminiscent of the reports of cyt P460, under aerobic conditions, purified HAO does not stoichiometrically produce NO_2^- from the oxidation of NH_2OH.[43] Furthermore, under anaerobic conditions, HAO did not product NO_2^- but instead the products were a mixture of both NO and N_2O.[14] The production of these species was attributed to incomplete NH_2OH oxidation and production of NO and HNO, where HNO will then rapidly dimerize to produce N_2O. These results suggested that O_2 is necessary for the oxidation of NH_2OH to NO_2^- via purified HAO.

Whole cell oxygen-isotope-labeling studies of AOB determined that one O from NO_2^- originated from O_2 via the O_2 dependent AMO oxidation step and the other O from H_2O.[44] This disagrees with the above purified HAO results, where there was no formation of NO_2^- anaerobically. In terms of the metabolism of AOB, it would be disadvantageous for AOB to have another O_2 dependent oxidation step. In an O_2 dependent NH_2OH oxidation step those electrons released from NH_2OH would be scavenged by the O_2 prior to transfer to the electron transport chain. Therefore, an O_2 dependent NH_2OH oxidation step would not be beneficial to the cell and necessities that this oxidation process has a different product.

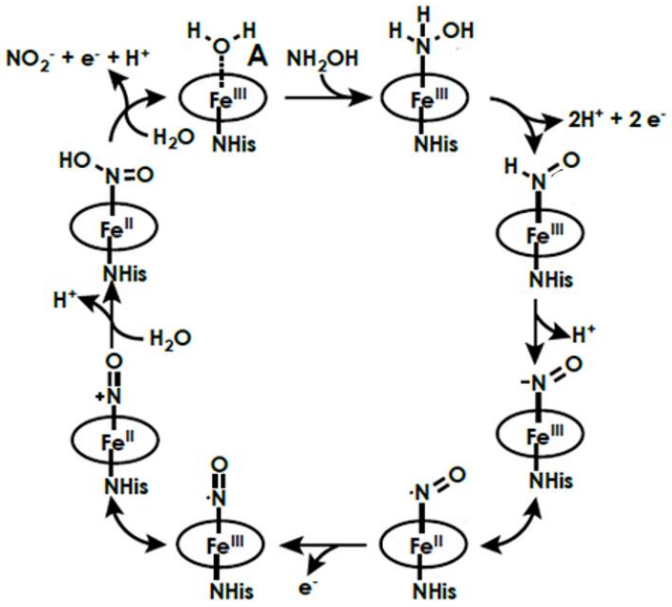

Scheme 2.2. Theoretical mechanism of NH_2OH oxidation by HAO adapted from reference 10.

Caranto et al [23] confirmed the product distribution of NH_2OH oxidation in either aerobic or anaerobic conditions with purified HAO. Under aerobic conditions,

the oxidation of NH_2OH by HAO produces a mixture of NO_2^- and NO_3^-, whereas, under anaerobic conditions, neither NO_2^- nor NO_3^- are produced. In either case, the presence of both HAO and PMS are necessary for the oxidation of NH_2OH. In the absence of HAO, less than 5% of the NH_2OH was consumed whereas in absence of oxidant PMS, only about 15% of the NH_2OH was consumed.[23] The inconsistent and low yield of NO_2^- production by HAO under either anaerobic or aerobic conditions strongly suggest that NO_2^- is not the product of NH_2OH oxidation

Similarities can be drawn between HAO and cyt P460 by examining the mechanism of NH_2OH oxidation. The theoretical mechanism of HAO calculated by Bari[30] (scheme 2) also invokes similar $\{FeNO\}^x$ species as was seen with the cyt P460.[45] According to Bari et al, NH_2OH binds to the P460 center and proceeds through both $\{FeNO\}^7$ and $\{FeNO\}^6$ intermediates. The production of NO_2^- results from attack of a water molecule to the $\{FeNO\}^6$ species. Therefore, like cyt P460[45] the pathway proceeds via $\{FeNO\}^7$ and $\{FeNO\}^6$ intermediates and generates product via nucleophilic attack to the $\{FeNO\}^6$. Caranto et al[23] demonstrated that HAO does not produce NO_2^- anaerobically, hence attack of a H_2O molecule to the $\{FeNO\}^6$ to produce NO_2^- is not operative.

Nevertheless, parallels can still be drawn, in limiting NH_2OH concentrations, the $\{FeNO\}^6$ cannot react further with NH_2OH to produce N_2O suggesting that NO production would outcompete N_2O production. In addition, NO is a reactive species that has been shown to produce N_2O, NO_2^- and NO_3^- non-enzymatically.[4] The mixture of products of NH_2OH oxidation by HAO and the parallels from the cyt P460

mechanism suggest that NO could be the product of this pathway. Under this scheme, the production of NO_2^- aerobically results from the rapid reaction of NO and O_2.[46] Production of NO from an octaheme oxidoreductase has been previously seen from a homologous octaheme oxidoreductase, Kutsc1061, from the annamox bacterium *Kuenia stuttgartiensis*. Kartel et al[22] demonstrated that purified Kutsc1061 performed stoichiometrically the 3-electron oxidation of NH_2OH to NO and not NO_2^-. This gave further evidence that NO could be the oxidation product of NH_2OH by HAO.

A NO sequestering assay was used to definitively determine that NO is the final product of this oxidation. Under anaerobic conditions the catalase assay was employed to scavenge NO production by HAO.[23] Upon binding NO (k_{on} = 1.3 x 10^7 M^{-1} s^{-1}), catalase exhibits a shift in the Soret max to 433 nm with well-resolved q band features at 542 and 579 nm.[47] Using the change in the Soret max to 433 nm ($\Delta\varepsilon$ = 47.9 mM^{-1} cm^{-1}), Caranto et al demonstrated that 88-100% of the NH_2OH was converted to NO by HAO under anaerobic conditions. Concomitantly, following the reduction of either DCPIP at 605nm or horse heart cyt c at 550 nm, the stoichiometry of oxidant consumed per NH_2OH was determined. It was found that 1.5-1.7 mol of DCPIP or 2.8-3.0 mol of cyt c were reduced per mol of NH_2OH. These data are consistent with a 3-electron oxidation of NH_2OH to NO by HAO.

Under the current hypothesis production of NO_2^- results from the non-enzymatic reaction of NO with O_2 rather than an enzyme bound O_2 dependent pathway. Ferrous-O_2 Hb (oxyHb) was used to scavenge the NO in aerobic conditions. The reaction of NO and oxyHb produces ferric Hb (metHb) and NO_3^-.[48] The shift in the Soret max from oxyHb to metHb (401 nm to 421 nm, respectively) was used to

quantify the conversion of oxyHb to metHb thereby indirectly, quantifying the production of NO. In the presence of HAO, oxidant and NH_2OH, the absorbance at 421 nm of metHb increased within 30 s of initiating the reaction consistent with production of NO. Caranto et al demonstrated that approximately 75% of the NH_2OH was converted to NO and that there was a 66-75% decrease in NO_2^- production in the presence of the NO scavenger. The stoichiometry of the oxidant consumed per NH_2OH was again consistent with the 3-electron oxidation of NH_2OH.

Reevaluating previous reports of the activity of HAO and drawing parallels from the reactivity seen in cyt P460 allowed for a more detailed look on the metabolic enzyme HAO. Both enzymes reported inconsistencies with the production of NO_2^-. Upon further investigation, neither cyt P460 nor HAO could produce NO_2^- anaerobically or stoichiometrically produce NO_2^- under aerobic conditions. Indicating that NO_2^- is not the enzymatic product in either enzyme. It could be envisioned that the mechanism of HAO is similar to that of cyt P460 where both undergo analogous intermediates but diverge at the $\{FeNO\}^6$ species. In cyt P460, this $\{FeNO\}^6$ species reacts further with additional NH_2OH to produce N_2O, whereas, in HAO the $\{FeNO\}^6$ rapidly dissociates its bound NO. Indeed, this was seen in previous experiments with Pacheo and coworkers[49] where they were not able to isolate the $\{FeNO\}^6$ species. Similar results were also seen by Caranto et al with purified HAO. This divergence in reactivity of the $\{FeNO\}^6$ species will be further discussed in chapter 5.

These results revised the nitrification pathway necessitating that NO is an obligate metabolic intermediate and consequently, prompted reexamination of the metabolic AOB pathway. These organisms stoichiometrically perform the 4-electron oxidation of NH_3 to NO_2^- with only minor production of other N-oxide species suggesting that the production of NO_2^- is an enzymatic process.[15] Furthermore, the pathway initiates with the input of 2 electrons to AMO for the initial NH_3 oxidation step. If the pathway terminated at the oxidation of NH_2OH to NO only a net of 1 electron would be transferred to the electron transport chain for cellular respiration. Also, as discussed previously, one O from NO_2^- originates from H_2O and the other from O_2 from oxidation of NH_3 by AMO.[44] This excludes the possibility of non-enzymatic production of NO_2^- via the reaction of O_2 and NO. These results suggest that NO is oxidized to NO_2^- via an unknown metabolic enzyme (scheme 3). Current work in the lab seems to suggest a possible Cu enzyme for the last step of the AOB metabolic pathway.[4]

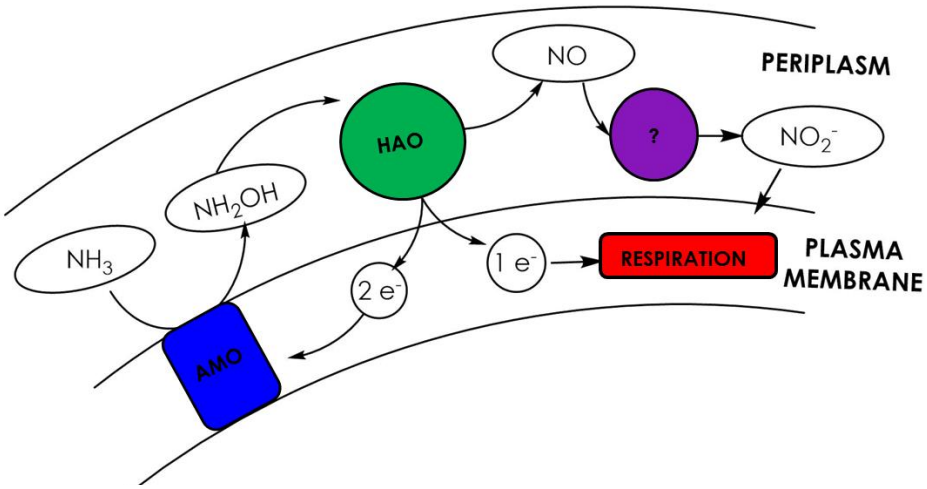

Scheme 2.3. Modified scheme of bacterial ammonia oxidation now including NO as the product of NH_2OH oxidation by HAO and the purposed enzymatic formation of NO_2^- by an metabolic unknown enzyme (?).

Experimental

General Considerations.

Milli-Q water (18.2 MΩ; Millipore) was used in the preparation of all buffers and solutions. 1-(Hydroxyl-NNO-azoxy)-L-proline, disodium salt (PROLI-NONOate), and disodium diazen-1-ium-1,2,2 triolate (Angeli's salt) were purchased from Cayman Chemicals. Hydroxylamine hydrochloride ($NH_2OH \bullet HCl$) was purchased from Sigma-Aldrich. A stock solution of PROLI-NONOate was prepared by dissolving 10 mg of PROLI-NONOate in 0.01 M NaOH. The concentration was measured spectrophotometrically ($\varepsilon_{252nm} = 8400\ M^{-1}\ cm^{-1}$). Nitric oxide (NO) release from PROLI-NONOATE was quantified by using Fe^{II}EDTA to form the resulting FeEDTA-NO complex ($\varepsilon_{440} = 900\ M^{-1}\ cm^{-1}$; EDTA = ethylenediaminetetraacetic acid) (1). A stock solution of Angeli's salt was prepared by dissolving Angeli's salt in 0.01 M NaOH. The concentration of the salt was measured spectrophotometrically ($\varepsilon_{237nm} = 6100\ M^{-1}\ cm^{-1}$) (2). All reactions were prepared in an anaerobic chamber (Coy) with buffers deoxygenated via bubbling with N_2 for at least 30 min. All UV/visible (UV/vis) absorption spectra measurements were performed with a Cary 60 UV/vis spectrometer. All other chemicals were purchased from VWR International and used as obtained.

Protein Expression and Purification.

A gene encoding *Nitrosomonas europaea* cytochrome (cyt) P460 was codon-optimized for *Escherichia coli*, synthesized, and cloned into the pET22b (+) vector by GenScript, Inc. Cyt P460 was expressed and purified as described by Elmore and colleagues (3) with slight modification. The expression plasmid and pEC86 containing the cyt c maturation genes ccmABCDEFGH (4) (provided by H. B. Gray) were co-transformed into *E. coli* strain BL21(DE3) with selection on lysogeny broth plates supplemented with 100 μg mL^{-1} each ampicillin and chloramphenicol. A single colony each was used to inoculate two 3 mL lysogeny broth starter cultures containing 100 μg mL^{-1} ampicillin and chloramphenicol. These starter cultures were incubated with shaking at 37 °C for 6 h and used to inoculate two 6 L culture flasks containing 2.5 L Terrific Broth medium and 0.5% glycerol (0.1% inoculum). The cultures were grown at 30 °C until the optical density at 600 nm reached 0.7, at which point expression was induced by adding isopropyl β-D-1-thiogalactopyranoside to a final concentration of 0.4 mM. The cells were harvested via centrifugation 6 to 8 h post-induction and yielded a green cell pellet. The cells were then lysed with sonication in 20 mM Tris (pH 8.0) containing 150 mM NaCl and 0.01% Triton X. The green lysate was clarified via centrifugation for 45 min at 35,000 × *g* relative centrifugal force. The supernatant was applied to a HiTrap Q HP nickel affinity column (GE Lifesciences), washed with 20 mM Tris (pH 8.0) containing 150 mM NaCl, and eluted with 20 mM Tris (pH 8.0) containing 150 mM NaCl and 330 mM imidazole. The fractions containing cyt P460 were pooled and concentrated and then purified to homogeneity by using a HiLoad Superdex 75 size-exclusion column equilibrated with a running buffer of 50 mM

morpholinepropanesulfonic acid (pH 7.2) containing 150 mM NaCl. Protein purity was evaluated with sodium dodecyl sulfate polyacrylamide gel electrophoresis. Typical purifications yielded Reinheitszahl values (R_z, or the purity ratio of $A_{440\ nm}/A_{280\ nm}$) of ca. 1.5.

Steady-State Activity Assays.

All assays were performed in septum-sealed cuvettes flushed with N_2 gas. NH_2OH • HCl (69 mg; 1 mmol) was equilibrated in an anaerobic environment overnight and then dissolved in 1 mL of deoxygenated water to yield a 1 M solution. This solution was serially diluted 20,000-fold in anaerobic water and assayed with the method of Frear and Burrell (5) for accurate determination of the stock NH_2OH concentration. Final concentrations of 50 µM 2,6-dichlorophenolindophenol (DCPIP), 6 µM phenazine methosulfate, and 1 µM cyt P460 were added to 2 mL of deoxygenated 50 mM phosphate (pH 8.0). The reaction was initiated by adding an appropriate volume of the NH_2OH stock solution to the reaction mixture through the septum with a Hamilton syringe. The reaction was monitored with the absorption of DCPIP at 605 nm. The rate of the first 10% of the total oxidant consumption was determined through linear regression by using Igor Pro version 6.37 (WaveMetrics). This rate was converted to the rate of oxidant consumed by using $\varepsilon_{605\ nm} = 20.6\ mM^{-1}cm^{-1}$ (6). At least three trials for each NH_2OH concentration were averaged and the standard deviations plotted. The initial rates were plotted versus NH_2OH concentration, and the resulting plot was fit using linear regression.

Pseudo First-Order Kinetics Measurements.

All reactions were prepared in an anaerobic chamber (Coy) with deoxygenated solutions. Solutions of NH_2OH • HCl were prepared as described above. Stock solutions of $[Ru(NH_3)_6]Cl_3$ were prepared anaerobically by equilibrating 62 mg of $Ru(NH_3)_6Cl_3$ in the anaerobic chamber overnight. $[Ru(NH_3)_6]Cl_3$ was then dissolved in 1 mL of deoxygenated water to generate a 200 mM deoxygenated solution. The dependence of NH_2OH on the reaction was measured by monitoring the absorbance of the 455 nm intermediate. Cyt P460 (10 µM) and $[Ru(NH_3)_6]Cl_3$ (50 µM) were combined with 2 mL of deoxygenated 50 mM 4-(2-hydroxyethyl)-1-piperazine-ethanesulphonic acid (HEPES) buffer (pH 8.0) in an anaerobic cuvette. The reaction was initiated by using a Hamilton syringe to add the appropriate volume of NH_2OH • HCl to the septum on the cuvette. Measurements were carried out from 0.2 mM to 10 mM NH_2OH. The formation and decay of the 455 nm intermediate were monitored with full-wavelength kinetic UV/vis absorption scans at intervals of 0.5 min for 0 to 10 min, 1 min from 10 to 20 min, and 2 min from 20 to 40 min. The kinetic traces were fit to the sum of two exponentials with 6.37 IGOR Pro (WaveMetrics):

$$\text{Equation S1} \quad A_0 + A_1{}^{-invTau_1 * x} + A_2{}^{-invTau_2 * x}$$

The fits provided observed rate constants (k_{obs}) for each NH_2OH concentration ($k_{obs} = k[NH_2OH]$). The plot of the slower of the two k_{obs} versus NH_2OH concentration was fit to a linear equation in IGOR Pro.

Generation of {FeNO}^{6}

All reactions were prepared in an anaerobic chamber (Coy) by using deoxygenated solutions. The {FeNO}^{6} species were prepared with PROLI-NONOate. Stock solutions of PROLI-NONOate and NO release quantification were prepared as described above. Cyt P460 (10 μM) was combined with 2 mL of deoxygenated 200 mM HEPES buffer (pH 8.0) in an anaerobic cuvette. The {FeNO}^{6} species was generated by using a gas-tight Hamilton syringe and titrating 5 μM additions of PROLI-NONOATE to the cuvette until a 1 mol equivalent of the 455 nm species was reached. The titration was monitored with UV/vis spectroscopy. The reaction between the 455 nm shunted {FeNO}^{6} species and NH_2OH was initiated by using a gas-tight Hamilton syringe and adding 2 mM NH_2OH to the cuvette containing the {FeNO}^{6} species. Full-wavelength UV/vis kinetic traces were measured at intervals of 0.5 min for 10 min, 1 min for 20 min, and 2 min for 40 min.

Pseudo first order kinetic data for reaction of shunted {FeNO}^{6} with NH_2OH

The {FeNO}^{6} species was prepared as stated above. Cyt P460 (30μM) and 1 equivalent of PROLI-NONOATE (60μM NO) were combined with 2mL of deoxygenated 200mM HEPES buffer (pH 8.0) in the coy chamber in an aerobic cuvette. The reaction between the shunted {FeNO}^{6} and NH_2OH was initiated by using a gas-tight Hamilton syringe and adding the appropriate volume of NH_2OH•Cl to the anaerobic cuvette. Measurements were carried out between 2 mM and 8 mM NH_2OH. The dependence of NH_2OH on the shunted {FeNO}^{6} was measured by monitoring the absorbance at 455nm. The decay of the {FeNO}^{6} species was

monitored with full-wavelength kinetic UV/vis absorption scans at intervals of 0.5 min for 10min, 1 min for 20 min and 2 min for 40 min. The decay traces were fit to a single exponential (equation S1) with 6.37 IGOR Pro (WaveMetrics). Observed rate constants (k_{obs}) from the provided fits for each concentration of NH_2OH ($k_{obs} = k[NH_2OH]$) were then plotted against NH_2OH concentration. The k_{obs} versus NH_2OH concentration plot was then fit by linear regression in IGOR Pro.

Generation of the {FeNO}^{7}

All reactions were prepared in an anaerobic chamber with deoxygenated solutions. The $\{FeNO\}^7$ species was prepared with Angeli's salt. Stock solutions of the salt were prepared as described above. Cyt P460 (10 µM) was combined with 2 mL of deoxygenated 200 mM HEPES buffer (pH 8.0) in an anaerobic cuvette. Cyt P460 (10µM) was incubated with 50 µM Angeli's salt to generate the $\{FeNO\}^7$ species. Stock solutions of $[Ru(NH_3)_6]Cl_3$ and NH_2OH were prepared as described above. $[Ru(NH_3)_6]Cl_3$ (100 µM) was added to the $\{FeNO\}^7$and monitored with kinetic UV/vis scans (200 to 800 nm) at intervals of 0.5 min for 10 min and 1 min for 20 min. The reactivity of $\{FeNO\}^7$ with NH_2OH was also measured. The $\{FeNO\}^7$ species was generated as described above, and the reaction was initiated with 10 mM NH_2OH. The reaction was monitored with kinetic UV/vis scans (200 to 800 nm) at intervals of 0.5 min for 10 min and 1 min for 20 min.

Measurement of N_2O

All reactions were prepared in an anaerobic chamber (Coy) with deoxygenated solutions and sealed in 5 mL headspace gas chromatography (GC) vials (Wheaton). The concentration of formed N_2O was analyzed with GC (Agilent) or GC–mass spectroscopy (GC–MS; JEOL GC-MATE II), or an N_2O microsensor housed within a septum-piercing needle (Unisense). The N_2O concentration was measured in the headspace of solutions containing 5 μM cyt P460, 1 mM phenazine methosulfate (PMS), and various amounts of NH_2OH. The headspace was measured with GC analysis using a Supel-Q PLOT column (30 mm × 0.32 mm). The concentration of N_2O formed during the $\{FeNO\}^6$ shunted experiments was measured with GC–MS using an RT Q bond column. Samples (500 μL) were prepped in a Coy chamber with 1.5 mL headspace vials (Agilent). The $\{FeNO\}^6$ was generated by incubating 5 μM P460 and various amounts of PROLI-NONOATE. The reaction was initiated by adding 10 mM $^{14}NH_2OH$ or $^{15}NH_2OH$ and was allowed to react in the Coy chamber for 2 h. After 2 h, the reaction was quenched with 1 M phosphoric acid.

Electron Paramagnetic Resonance (EPR)

All samples were prepared in an anaerobic chamber (Coy) with deoxygenated solutions. The protein concentration used was 0.3 mM in 200 mM HEPES (pH 8.0) with 25% (v/v) glycerol. The EPR spectra were recorded at X-band (9.40 GHz) on a Bruker Elexsys-II spectrometer equipped with a liquid He cryostat maintained at 10 or 20 K. EPR data were simulated, and spin concentrations were determined by using SpinCount (7).

Measurement of k_{obs} for oxidation of Fe^{II}-cyt P460 by stopped-flow spectrophotometry

As isolated cyt P460 was treated with 0.5 equivalents of $Na_2S_2O_4$ (dithionite) resulting in Fe^{II}-cyt P460. The stopped-flow experiments were performed in a Bio-Logic SFM-400 and monitored with a photomultiplier tube (Bio-Logic Science Instruments SAS). O_2 in the mixing circuit was scavenged by treatment with 10 mM $Na_2S_2O_4$ for one hour. Excess $Na_2S_2O_4$ was then washed with 4x5 ml of degassed 50 mM phosphate, pH 8.0 or degassed water. Ninety micromolar of Fe^{II}-cyt P460 in degassed 50 mM phosphate, pH 8.0 was anaerobically loaded into the stopped-flow mixing circuit and mixed 1:1 (v/v) with either 2 mM $[Ru(NH_3)_6]Cl_3$ or 4 mM NH_2OH in degassed water. The Fe^{II}-cyt P460 vs. 1 mM NO was performed as a sequential mixing experiment where a 4 mM stock solution of PROLI-NONOate prepared in 10 mM NaOH as described above was pre-mixed 1:1 (v/v) with 250 mM phosphate, pH 8.0 and allowed to decay in the delay line for 30 seconds. The resulting 2 mM NO solution was then mixed 1:1 (v/v) against 90 µM of Fe^{II}-cyt P460 in second mixing step. For all experiments, the consumption of Fe^{II}-cyt P460 was monitored by the loss of the 463-nm absorption band assigned to the Soret peak of Fe^{II}-cyt P460. All experiments were performed at room temperature.

REFERENCES

1. Ravishankara, A. R., Daniel, J. S. & Portmann, R. W. Nitrous Oxide (N₂O): The Dominant Ozone-Depleting Substance Emitted in the 21st Century. *Science (80-.).* **326,** 123 LP-125 (2009).
2. Stein, L. Y. Surveying N2O-producing pathways in bacteria. *Methods Enzymol.* **486,** 131–152 (2010).
3. Khalil, K., Mary, B. & Renault, P. Nitrous oxide production by nitrification and denitrification in soil aggregates as affected by O2concentration. *Soil Biol. Biochem.* **36,** 687–699 (2004).
4. Lancaster, K. M., Caranto, J. D., Majer, S. H. & Smith, M. A. Alternative Bioenergy: Updates to and Challenges in Nitrification Metalloenzymology. *Joule* **2,** 421–441 (2018).
5. Goreau, T. J. *et al.* Production of N02- and N20 by Nitrifying Bacteria at Reduced Concentrations of Oxygen L ; i-. **40,** 526–532 (1980).
6. Wunderlin, P., Mohn, J., Joss, A., Emmenegger, L. & Siegrist, H. Mechanisms of N2O production in biological wastewater treatment under nitrifying and denitrifying conditions. *Water Res.* **46,** 1027–1037 (2012).
7. Perez-Garcia, O., Villas-Boas, S. G., Swift, S., Chandran, K. & Singhal, N. Clarifying the regulation of NO/N2O production in Nitrosomonas europaea during anoxic-oxic transition via flux balance analysis of a metabolic network model. *Water Res.* **60,** 267–277 (2014).
8. Hooper, A. B., Vannelli, T., Bergmann, D. J. & Arciero, D. M. Enzymology of the oxidationof ammonia to nitrate by bacteria. *Antonie Van Leeuwenhoek* **71,** 59–67 (1997).
9. Stahl, D. A. & de la Torre, J. R. Physiology and Diversity of Ammonia-Oxidizing Archaea. *Annu. Rev. Microbiol.* **66,** 83–101 (2012).
10. Bartossek, R., Spang, A., Weidler, G., Lanzen, A. & Schleper, C. Metagenomic analysis of ammonia-oxidizing archaea affiliated with the soil group. *Front. Microbiol.* **3,** (2012).
11. Wasser, I. M., de Vries, S., Moënne-Loccoz, P., Schröder, I. & Karlin, K. D. Nitric Oxide in Biological Denitrification: Fe/Cu Metalloenzyme and Metal Complex NOx Redox Chemistry. *Chem. Rev.* **102,** 1201–1234 (2002).
12. Law, Y., Ni, B. J., Lant, P. & Yuan, Z. N 2O production rate of an enriched ammonia-oxidising bacteria culture exponentially correlates to its ammonia oxidation rate. *Water Res.* **46,** 3409–3419 (2012).
13. Sabba, F., Picioreanu, C., Pérez, J. & Nerenberg, R. Hydroxylamine diffusion can enhance N2O emissions in nitrifying biofilms: A modeling study. *Environ. Sci. Technol.* **49,** 1486–1494 (2015).
14. Hooper, A. B. & Terry, K. R. Hydroxylamine oxidoreductase of Nitrosomonas. Production of nitric oxide from hydroxylamine. *BBA - Enzymol.* **571,** 12–20 (1979).
15. Kozlowski, J. A., Price, J. & Stein, L. Y. Revision of N2O-producing pathways in the ammonia-oxidizing bacterium Nitrosomonas europaea ATCC 19718. *Appl. Environ. Microbiol.* **80,** 4930–4935 (2014).
16. Pearson, A. R. *et al.* The crystal structure of cytochrome P460 of Nitrosomonas europaea reveals a novel cytochrome fold and heme - Protein cross-link. *Biochemistry* **46,** 8340–8349 (2007).
17. Walker, F. A. Magnetic spectroscopic (EPR, ESEEM, Mössbauer, MCD and NMR) studies of low-spin ferriheme centers and their corresponding heme

proteins. *Coord. Chem. Rev.* **185–186,** 471–534 (1999).
18. Liptak, M. D., Wen, X. & Bren, K. L. NMR and DFT investigation of heme ruffling: Functional implications for cytochrome c. *J. Am. Chem. Soc.* **132,** 9753–9763 (2010).
19. Elmore, B. O., Bergmann, D. J., Klotz, M. G. & Hooper, A. B. Cytochromes P460 and c′-beta; A new family of high-spin cytochromes c. *FEBS Lett.* **581,** 911–916 (2007).
20. Cedervall, P., Hooper, A. B. & Wilmot, C. M. Structural studies of hydroxylamine oxidoreductase reveal a unique heme cofactor and a previously unidentified interaction partner. *Biochemistry* **52,** 6211–6218 (2013).
21. Numata, M., Saito, T., Yamazaki, T., Fukumori, Y. & Yamanaka, T. Cytochrome P-460 of Nitrosomonas europaea: Further purification and further characterization. *J. Biochem.* **108,** 1016–1021 (1990).
22. Maalcke, W. J. *et al.* Structural basis of biological no generation by octaheme oxidoreductases. *J. Biol. Chem.* **289,** 1228–1242 (2014).
23. Caranto, J. D. & Lancaster, K. M. Nitric oxide is an obligate bacterial nitrification intermediate produced by hydroxylamine oxidoreductase. *Proc. Natl. Acad. Sci.* 201704504 (2017). doi:10.1073/pnas.1704504114
24. Andersson, K. K., Kent, T. A. & Lipscomb, J. D. Mossbauer, EPR, and optical studies of the P-460 center of hydroxylamine oxidoreductase from Nitrosomonas. A ferrous heme with an unusually large quadrupole splitting. *J. Biol. Chem.* **259,** 6833–6840 (1984).
25. Smith, M. A. & Lancaster, K. M. The Eponymous Cofactors in Cytochrome P460s from Ammonia-Oxidizing Bacteria Are Iron Porphyrinoids Whose Macrocycles Are Dibasic. *Biochemistry* **57,** 334–343 (2018).
26. Zoppellaro, G. *et al.* Modulation of the Ligand-Field Anisotropy in a Series of Ferric Low-Spin Cytochrome c Mutants derived from Pseudomonas aeruginosa Cytochrome c -551 and Nitrosomonas europaea Cytochrome c -552: A Nuclear Magnetic Resonance and Electron Paramagnetic Resonan. *J. Am. Chem. Soc.* **130,** 15348–15360 (2008).
27. Goodrich, L. E., Paulat, F., Praneeth, V. K. K. & Lehnert, N. Electronic structure of heme-nitrosyls and its significance for nitric oxide reactivity, sensing, transport, and toxicity in biological systems. *Inorg. Chem.* **49,** 6293–6316 (2010).
28. Enemark, J. H. & Feltham, R. D. Principles of structure, bonding, and reactivity for metal nitrosyl complexes. *Coord. Chem. Rev.* **13,** 339–406 (1974).
29. Hendrich, M. P., Upadhyay, A. K., Riga, J., Arciero, D. M. & Hooper, A. B. Spectroscopic characterization of the NO adduct of hydroxylamine oxidoreductase. *Biochemistry* **41,** 4603–4611 (2002).
30. Fernández, M. L., Estrin, D. A. & Bari, S. E. Theoretical insight into the hydroxylamine oxidoreductase mechanism. *J. Inorg. Biochem.* **102,** 1523–1530 (2008).
31. Nicolai, L., K., P. V. K. & Florian, P. Electronic structure of iron(II)–porphyrin nitroxyl complexes: Molecular mechanism of fungal nitric oxide reductase (P450nor). *J. Comput. Chem.* **27,** 1338–1351 (2006).
32. Daiber, A. *et al.* Isotope effects and intermediates in the reduction of NO by P450NOR. *J. Inorg. Biochem.* **88,** 343–352 (2002).
33. Kumar, M. R., Fukuto, J. M., Miranda, K. M. & Farmer, P. J. Reactions of HNO with heme proteins: new routes to HNO-heme complexes and insight into physiological effects. *Inorg. Chem.* **49,** 6283–6292 (2010).
34. Lin, R. & Farmer, P. J. The HNO Adduct of Myoglobin: Synthesis and Characterization. *J. Am. Chem. Soc.* **122,** 2393–2394 (2000).

35. Yonetani, T. Studies on Cytochrome c Peroxidase : II. STOICHIOMETRY BETWEEN ENZYME, H2O2, AND FERROCYTOCHROME c AND ENZYMIC DETERMINATION OF EXTINCTION COEFFICIENTS OF CYTOCHROME c . *J. Biol. Chem.* **240,** 4509–4514 (1965).
36. Vilbert, A. C., Caranto, J. D. & Lancaster, K. M. Influences of the heme-lysine crosslink in cytochrome P460 over redox catalysis and nitric oxide sensitivity. *Chem. Sci.* **00,** 1–12 (2018).
37. Wolfe, S. K., Andrade, C. & Swinehart, J. H. Kinetic studies of the pentacyanonitrosylferrate(2-) azide and -hydroxylamine reactions. *Inorg. Chem.* **13,** 2567–2572 (1974).
38. King, E. L. & Altman, C. A Schematic Method of Deriving the Rate Laws for Enzyme-Catalyzed Reactions. *J. Phys. Chem.* **60,** 1375–1378 (1956).
39. Böttcher, B. & Koops, H. P. Growth of lithotrophic ammonia-oxidizing bacteria on hydroxylamine. *FEMS Microbiol. Lett.* **122,** 263–266 (1994).
40. Ritchie, G. A. F. & Nicholas, D. J. Identification of the sources of nitrous oxide produced by oxidative and reductive processes in Nitrosomonas europaea. *Biochem. J.* **126,** 1181–1191 (1972).
41. Gao, J., Luo, X., Wu, G., Li, T. & Peng, Y. Abundance and diversity based on amoA genes of ammonia-oxidizing archaea and bacteria in ten wastewater treatment systems. *Appl. Microbiol. Biotechnol.* **98,** 3339–3354 (2014).
42. Ni, B. J., Peng, L., Law, Y., Guo, J. & Yuan, Z. Modeling of nitrous oxide production by autotrophic ammonia-oxidizing bacteria with multiple production pathways. *Environ. Sci. Technol.* **48,** 3916–3924 (2014).
43. Hooper, A. B. & Balny, C. Reaction of oxygen with hydroxylamine oxidoreductase of Nitrosomonas. Fast kinetics. *FEBS Lett.* **144,** 299–303 (1982).
44. Andersson, K. K. & Hooper, A. B. O_2 and H_2O are each the source of one O in NO_2^- produced from NH_3 by Nitrosomonas: \dN-NMR evidence. *FEBS Lett.* **164,** 236–240 (1983).
45. Caranto, J. D., Vilbert, A. C. & Lancaster, K. M. Nitrosomonas europaea cytochrome P460 is a direct link between nitrification and nitrous oxide emission. (2016). doi:10.1073/pnas.1611051113
46. Ignarro, L. J., Fukuto, J. M., Griscavage, J. M., Rogers, N. E. & Byrns, R. E. Oxidation of nitric oxide in aqueous solution to nitrite but not nitrate: comparison with enzymatically formed nitric oxide from L-arginine. *Proc. Natl. Acad. Sci. U. S. A.* **90,** 8103–8107 (1993).
47. Pacheco, A. A., McGarry, J., Kostera, J. & Corona, A. *Techniques for investigating hydroxylamine disproportionation by hydroxylamine oxidoreductases*. *Methods in Enzymology* **486,** (Elsevier Inc., 2010).
48. Kostera, J., McGarry, J. & Pacheco, A. A. Enzymatic interconversion of ammonia and nitrite: The right tool for the job. *Biochemistry* **49,** 8546–8553 (2010).
49. Cabail, M. Z. & Pacheco, A. A. Selective One-Electron Reduction of Nitrosomonas europaea Hydroxylamine Oxidoreductase with Nitric Oxide Selective One-Electron Reduction of Nitrosomonas europaea Hydroxylamine Oxidoreductase with Nitric Oxide. *Biochemistry* **42,** 2002–2004 (2003).

APPENDIX

Appendix 1.1 Spin Hamiltonian Parameters of Cyt P460 species from SpinCount Simulations (black traces).

Species	g_x (σg_x)	g_y (σg_y)	g_z (σg_z)	A_x (MHz)	A_y (MHz)	A_z (MHz)	E/D
Fe^{III}	1.92	1.96	2	—	—	—	0.03
Fe^{III}–NH_2OH	1.52 (0.06)	2.29 (0.03)	2.78 (0.05)	—	—	—	—
$\{FeNO\}^7$	2.012 (0.0002)	2.026 (0.003)	2.098 (0.0002)	50	57	45	—

CHAPTER 3

INFLUENCES OF THE HEME-LYSINE CROSS-LINK IN CYTOCHROME P460 OVER REDOX CATALYSIS

Reproduced in part from:

"Influences of the heme-lysine cross-link in cytochrome P460 over redox catalysis and nitric oxide sensitivity"

Avery C. Vilbert Jonathan D. Caranto and Kyle M. Lancaster

Chemical Science. **2018**, 9, 368-379. DOI: 10.1039/C7SC03450D

Introduction

Ammonia (NH_3)-oxidizing bacteria (AOB) derive energy for life from nitrification: the proton-coupled multi-electron oxidation of NH_3 to nitrite (NO_2^-).[1] Nitrification begins with the oxidation of NH_3 to hydroxylamine (NH_2OH) by the integral membrane enzyme ammonia monooxygenase. NH_2OH is then oxidized to nitric oxide (NO) by the multi-heme enzyme hydroxylamine oxidoreductase (HAO) to establish net electron flow.[2] The means through which NO is oxidized to NO_2^- are unknown. Detailed mechanistic understanding of controlled NH_2OH oxidation is vital to the understanding of how nature uses NH_3 as fuel.

HAO is a homotrimer of octaheme subunits.[3] Seven of the hemes in each subunit are coordinatively saturated *c*-type hemes that mediate electron transfer. The remaining heme, also a *c*-type heme, is the site of NH_2OH oxidation. This heme is called the heme P460 center because it has a characteristic Fe^{II} Soret absorption

maximum at 463 nm.[4] HAO heme P460 cofactors are unique in that they feature two cross-links with a tyrosine (Tyr) side chain (**Fig. 1a,b**). The Tyr $C\varepsilon_1$ and phenolate O cross-link with the *c*-heme at the 5′ meso carbon and the adjacent pyrrole α-carbon, respectively.[3] These attachments disrupt the π conjugation of the porphyrin ring and distort the planarity of the heme, resulting in a ruffled heme structure. P460 cofactors are found within enzymes from other bacteria as well, including methanotrophs[5] and anaerobic NH_3 oxidizers (anammox).[6] The anammox bacterium *Kuenenia stuttgartiensis* contains at least 10 P460-containing HAO paralogs, at least two of which exhibit hydroxylamine or hydrazine oxidoreductase activity.[7] Thus, the presence of P460 cofactors appears to be a hallmark of N-oxidation functionality.[8] However, the characteristics that make this cofactor suitable for such reactions remain unknown.

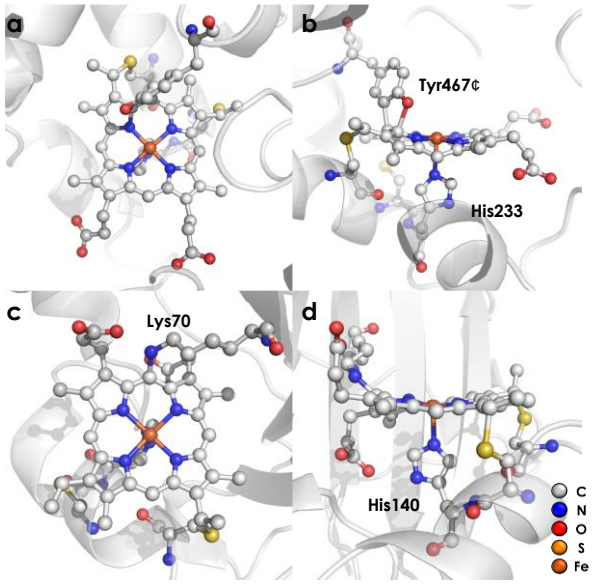

Figure 3.21. Views of the top (a) and side (b) of the *Nitrosomonas europaea* HAO heme P460 cofactor (2.1 Å resolution X-ray crystal structure, PDBID 4FAS) and the top (c) and side (d) of the *N. europaea* cytochrome (cyt) P460 heme P460 cofactor (1.8 Å resolution X-ray crystal structure, PDBID 2JE3). Both cofactors are *c*-heme cofactors with additional covalent amino acid side chain attachments. In HAO, Tyr467 from a neighboring subunit cross-links via the Cε at the 5′ meso carbon of the porphyrin and via the phenolate O at the neighboring pyrrole α-carbon. In cyt P460, the Lys70 amine N cross-links to the 13′ meso carbon.

Detailed understanding of NH_2OH oxidation by heme P460 centers is necessary to establish a link between the properties of this unique cofactor and its reactivity. However, spectroscopic probing of reaction intermediates at the 3 HAO heme P460 cofactor is occluded by the signals of the 21-electron transfer hemes. To overcome this challenge, we have explored the NH_2OH oxidation mechanism of cytochrome (cyt) P460, a soluble, dimeric mono-heme enzyme found in the periplasms of AOB.[8] In contrast to HAO, cyt P460 cofactors feature a Lys side chain amine covalently attached to the 13′ meso C of the *c*-heme (Fig. 1c,d).[9] Despite this

substitution, the UV/visible (UV/vis) absorption and ^{57}Fe Mössbauer properties characteristic of Fe^{II} heme P460 are preserved.[10] Cyt P460 had previously been reported to oxidize NH_2OH to NO_2^-.[11] However, we recently showed that cyt P460 oxidizes NH_2OH selectively to nitrous oxide (N_2O), not NO_2^-, under anaerobic conditions.[12] In our reported working mechanism (Fig. 2), Fe^{III} cyt P460 binds NH_2OH to form a stable Fe^{III}-NH_2OH adduct. This species then undergoes 3-electron oxidation to an $\{FeNO\}^6$ intermediate (Enemark-Feltham[13] notation denoting either Fe^{III}-$NO^{\bullet}$, Fe^{II}-NO^+, or Fe^{IV}-NO^-). Nucleophilic attack on this $\{FeNO\}^6$ intermediate by a second equivalent of NH_2OH produces N_2O. Consequently, each NH_2OH is oxidized by 2 electrons. Accounting for 2-electrons recycled to NH_3 monooxygenase for turnover,[14] such a cycle does not generate net cellular reducing equivalents for AOB.

The aforementioned reactivity prompted our reevaluation of the bacterial nitrification pathway. We noted that NO_2^- was among the products of cyt P460 reactivity with NH_2OH when the reactions were carried out aerobically.[12] However, NO_2^- concentrations were never stoichiometric with NH_2OH input, likely owing to competition with the reaction producing N_2O. We hypothesized that this NO_2^- was produced as a result of the non-enzymatic reaction of aqueous NO with O_2,[15] implying that P460-driven NH_2OH oxidation terminates at the $\{FeNO\}^6$ intermediate. If NO loss could outcompete the reaction of this intermediate with NH_2OH, the 3-electron oxidation of NH_2OH would be assured and, thus, establish a net electron flow for

AOB. Subsequent experiments confirmed that this outcome indeed occurs with HAO: NH_2OH is enzymatically oxidized by 3 electrons to NO and then swiftly released.[2]

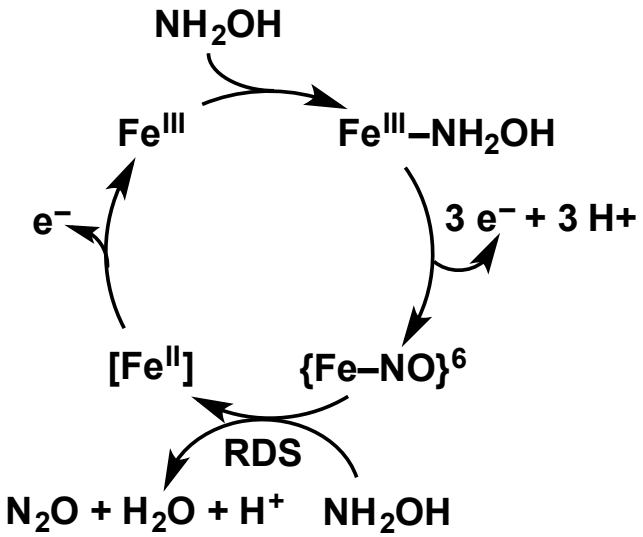

Figure 3.22. Working mechanism of the cyt P460 driven oxidation of NH_2OH and formation of N_2O. Adapted from Ref 11.

Thus, rapid access to the $\{FeNO\}^6$ intermediate is essential for the N_2O-generating mechanism of cyt P460 and the NO-generating mechanism of both cyt P460 and HAO. However, concerted biological 3-electron oxidation is unlikely. Moreover, the cyt P460 $\{FeNO\}^6$ species is formed with either 1- or 2-electron oxidants.[12] These observations strongly suggest that the oxidation of Fe^{III}-NH_2OH to the $\{FeNO\}^6$ intermediate occurs via sequential 1- or 2-electron steps, or both. Proposed intermediates include a 1-electron-oxidized Fe^{III}-NH_2OH radical (Fe^{III}-$NH_2O^{\bullet}$) and a 2-electron-oxidized species formulated either as a ferric nitroxyl (Fe^{III}-HNO) or its conjugate base $\{FeNO\}^7$.[16] However, no evidence for these intermediates has been provided. Electron paramagnetic resonance (EPR) spectroscopy provided evidence for a minor 5-coordinate (5c) $\{FeNO\}^7$ species formed either when preparing

Fe^{III}-NH_2OH samples or following complete oxidant consumption after multiple turnovers of cyt P460.[12] This species was shown to be off-pathway. Hendrich and co-workers[16] observed a similar off-pathway 5c $\{FeNO\}^7$ species with EPR spectroscopy when fully reduced HAO was allowed to react with NH_2OH.

Herein, we report the characterization of a 6-coordinate (6c) $\{FeNO\}^7$ intermediate in *N. europaea* cyt P460 that is on-pathway and precedes the formation of the critical $\{FeNO\}^6$ species. This 6c $\{FeNO\}^7$ intermediate slowly decays in a NO-independent manner to the off-pathway 5c $\{FeNO\}^7$ species. This conversion represents dissociation of the axial His140. Kinetic studies of a 13′ cross-link-deficient cyt P460 variant (Lys70Tyr cyt P460) revealed that at least one function of this cross-link is to kinetically bypass the production of the off-pathway 5c $\{FeNO\}^7$ intermediate during turnover by protecting the cofactor from deactivation by NO. The rate of 6c-to-5c conversion in the Lys70Tyr cyt P460 $\{FeNO\}^7$ is accelerated by several orders of magnitude compared with the wild-type (WT) protein due to the mechanistic participation of excess NO. This rapid, NO-dependent 6c-to-5c $\{FeNO\}^7$ conversion is reminiscent of the activation mechanism for heme-NO/O_2 (H-NOX) binding proteins including soluble guanylate cyclase (sGC).[17]

Results

Identification of a cyt P460 6-coordinate $\{FeNO\}^7$ species

In our previous study,[12] we generated an off-pathway 5c $\{FeNO\}^7$ species. This species was generated via the treatment of Fe^{III} cyt P460 with the HNO donor disodium diazen-1-ium-1,2,2 triolate ($Na_2N_2O_3$). One mole of $Na_2N_2O_3$ liberates 1 mol

of HNO with a half-life of 2 min when in room temperature pH 8.0 buffer. Hereafter, all HNO concentrations are expressed as the nominal final concentration expected from this $Na_2N_2O_3$ decomposition. In the present work, monitoring of the UV/vis absorption spectral time course immediately after the treatment of 15 μM Fe^{III} cyt P460 with 100 μM HNO revealed a previously uncharacterized species. The new species forms within 2 min and exhibits a UV/vis absorption spectrum with a Soret maximum at 452 nm and Q-band maxima at 550, 608, and 665 nm (Fig. 3). This species decays within 15 min, resulting in a UV/vis absorption spectrum with a Soret maximum at 455 nm and Q-band maxima at 535, 584, and 642 nm. These absorption features correspond to the aforementioned 5c $\{FeNO\}^7$ species.[12] A similar spectral time course was observed when 15 μM Fe^{II} cyt P460 was treated with 100 μM NO generated by Proli-NONOate at pH 8.0. One mole of Proli-NONOate liberates 2 mol of NO with a half-life of 2 s in room temperature pH 8.0 buffer. Hereafter, all NO concentrations are expressed as the nominal final concentration expected from this Proli-NONOate decomposition. Isosbestic points observed in these spectral time courses at 430, 556, 600, 610, and 652 nm indicate a one-step conversion between the two species. Together, the data suggest that an uncharacterized species forms and slowly decays to the 5c $\{FeNO\}^7$ species.

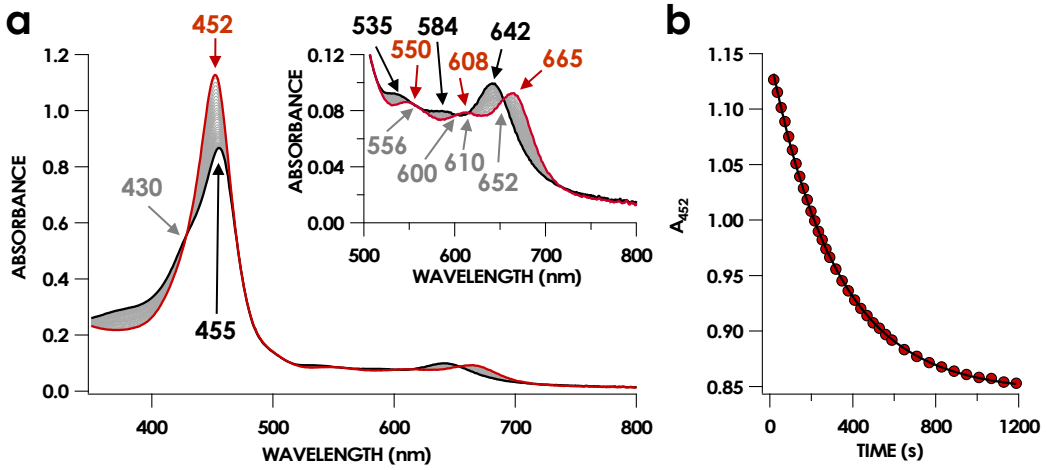

Figure 3.23. The 20 min UV/vis absorption (a) full-spectral and (b) single-wavelength (452 nm) time courses of the reaction of 15 μM Fe^{III} cyt P460 and 600 μM HNO in 200 mM HEPES buffer (pH 8.0). In (a), the solid red trace corresponds to the time point spectrum collected immediately after mixing and represents the 6c WT cyt P460 $\{FeNO\}^7$ species. The solid black trace is the spectrum collected after 20 min and represents the 5c WT cyt P460 $\{FeNO\}^7$ species. Grey spectra were collected in 30 s increments. The inset highlights the time course in the Q-band region. Absorption maxima in nanometers are labeled with colors corresponding to each species. Isosbestic points are labeled in gray. In (b), the black trace is a single exponential ($\boldsymbol{A_{452} = y_0 + A * e^{-k_{obs}*t}}$) fit to the data, yielding k_{obs} = 3.15×10^{-3} s^{-1}.

The spin state of this new species was characterized with continuous-wave X-band EPR (Fig. 4**)**. Samples were prepared by treating 150 μM cyt P460 with 750 μM HNO in pH 8.0 buffer at 25 °C. The samples were frozen with liquid N_2 within 3 min of mixing. The resulting EPR spectrum was consistent with an S = ½, 6c heme $\{FeNO\}^7$ species: the simulated g-values were 2.10, 2.01, and 1.98 with corresponding ^{14}N hyperfine values of 37, 55, and 40 MHz, respectively.[21] The sample under the same reaction condition but frozen after 1 h had a distinct EPR spectrum with simulated g-values of 2.10, 2.03, and 2.01 and corresponding ^{14}N hyperfine values of 50, 57, and 45 MHz, respectively. These parameters match those previously reported for the off-pathway 5c $\{FeNO\}^7$ intermediate.[12] Typically, 6c $\{FeNO\}^7$ complexes exhibit a 9-line superhyperfine splitting from the bound NO and the axially bound

N(His). The lack of a 9-line hyperfine ^{14}N from the bound Fe-N(His) could indicate either a weak Fe–N(His) bond or a large degree of disorder of the bound His.[17] However, more in depth EPR spectroscopies such as ENDOR would need to be attained in order to determine the degree Fe-N(His) hyperfine, which is outside the scope of this paper.

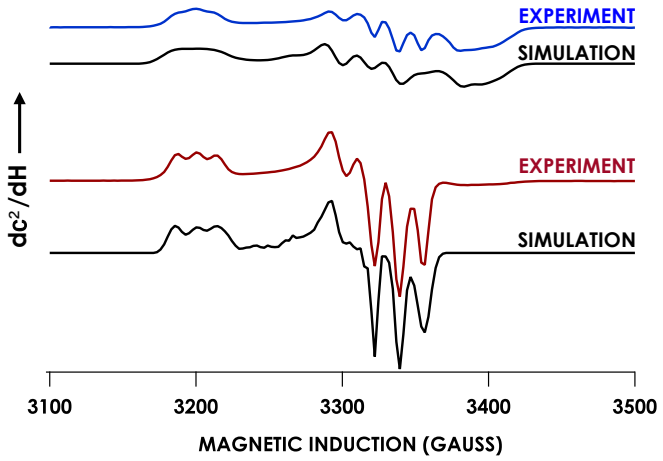

Figure 3.24. Continuous-wave X-band (9.40 GHz) EPR spectra of 200 µM Fe^{III} cyt P460 treated with 1 mM HNO in 200 mM HEPES buffer (pH 8.0) at room temperature and allowed to mature for 3 min (blue) or 30 min (red) before freezing. Measurements were obtained at 12 K with 63 µW microwave power. SpinCount simulations are shown in black for each spectrum. Spin Hamiltonian parameters for the blue spectrum, corresponding to the WT cyt P460 6c $\{FeNO\}^7$ species, are (g_1, g_2, g_3) = (2.10, 2.01, 1.98) and (^{14}N A_1, A_2, A_3) = (37, 55, 40 MHz). Parameters for the red spectrum, corresponding to the WT cyt P460 5c $\{FeNO\}^7$ species are (g_1, g_2, g_3) = (2.10, 2.03, 2.01) and (^{14}N A_1, A_2, A_3) = (50, 57, 45 MHz).

To further characterize this species Fe K-edge XAS data was obtained for both of these species. The Fe-K edge absorption near-edge regions of both the 6c and 5c $\{FeNO\}^7$ species are shown in Fig. 5. The pre-edge feature near 7113 eV is conventionally assigned as a quadrupole-allowed Fe 1s → 3d transition that can gain intensity via an electric dipole mechanism.[18] This feature appears at 7113.3 eV in the

spectrum of the initially formed 6c $\{FeNO\}^7$ intermediate. The feature exhibits significantly higher intensity in the 5c $\{FeNO\}^7$ spectrum, and this intensity increase is consistent with decreased centrosymmetry at Fe: as the coordination number decreases, the attendant diminished centrosymmetry confers dipole allowedness to the 1s → 3d transition and a corresponding increase in pre-edge intensity.

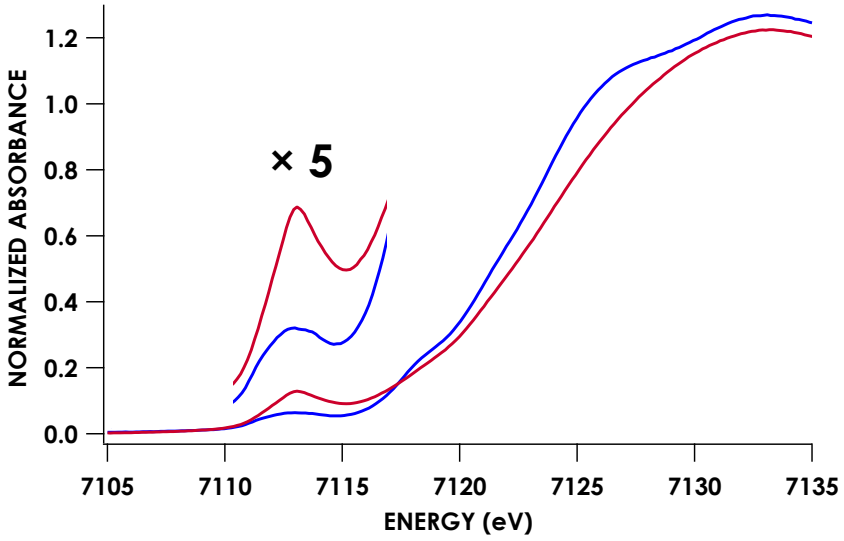

Figure 3.25. Fe K-edge XAS data obtained at 10 K for 1 mM WT cyt P460 6c (blue) and 5c (red) $\{FeNO\}^7$ species in glassed 200 mM HEPES buffer (pH 8.0) containing 25% v/v glycerol. Note the 1s → 3d pre-edge feature at 7113.3 eV.

Fits of the EXAFS region from k values of 2–14 $Å^{-1}$, where k is the photoelectron wave number, for the WT 6c and 5c $\{FeNO\}^7$ species give short Fe–N scatters assignable to Fe-NO at 1.86 Å and 1.74 Å, respectively (Fig. 6 and Table 1). These distances are consistent with typical Fe–NO bond lengths in 6c and 5c heme $\{FeNO\}^7$ species, respectively.[19] The data resolution precluded the fitting of an Fe–N(His) scattering path in the 6c $\{FeNO\}^7$ species independent from the Fe–N(heme) paths. However, the EXAFS were best fit for this species with 5 rather than 4 Fe-N

scatters at 2.04 Å. Moreover, we could reliably fit the axial His of the 5c $\{FeNO\}^7$ intermediate at a distance 2.53 Å, which is well outside the range of coordination.

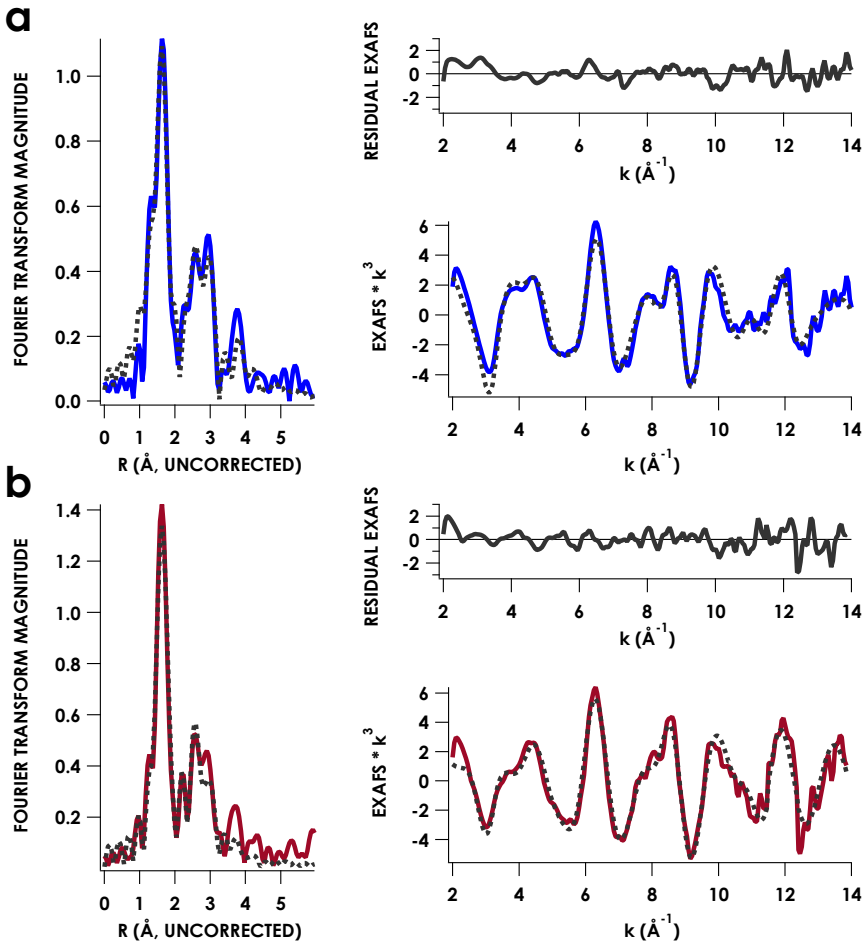

Figure 3.26. Fe K-edge EXAFS data obtained at 10 K for the 6c (a) and 5c (b) cyt P460 $\{FeNO\}^7$ intermediates in glassed 200 mM HEPES buffer (pH 8.0) containing 25% v/v glycerol. Experimental data are plotted as solid lines; fits are dotted lines.

The combined UV/vis absorption, EPR, and X-ray absorption data reveal that Fe^{III} cyt P460 reacts with HNO to accumulate a 6c $\{FeNO\}^7$ species, which subsequently decays to a 5c $\{FeNO\}^7$ form within 30 min. The simplest interpretation of this data is that the conversion results from the dissociation of the axial His140.

Dissociation of the ligand trans to the NO is frequently observed for heme $\{FeNO\}^7$ species and is attributed to the *trans* influence of NO.[20–22]

Table 3.1 Best Fits to Fe K-Edge EXAFS Data Obtained for WT Cyt P460 5c, 6c $\{FeNO\}^7$ and K70Y 5c $\{FeNO^7\}$.[a]

	Scattering Path	Coordination Number	R(Å)	ΔR(Å)	σ^2	$\Delta\sigma^2$	F (%)
WT 6c $\{FeNO\}^7$	Fe–N(pyrrole)	5	2.037	0.002	0.00504	0.00023	29.5
	Fe–N(NO)	1	1.858	0.012	0.00739	0.00153	
WT 5c $\{FeNO\}^7$	Fe–N(pyrrole)	4	2.021	0.002	0.00271	0.000152	30.3
	Fe–N(NO)	0.75	1.735	0.023	0.01294	0.00363	
	Fe–N(His)	1	2.525	0.012	0.00381	0.00131	
K70Y 5c $\{FeNO\}^7$	Fe–N(pyrrole)	4	1.991	0.003	0.00275	0.00022	35.7
	Fe–N(NO)	1	1.805	0.014	0.00693	0.00177	
	Fe–N(His)	1	2.483	0.012	0.00259	0.00122	

[a]EXAFS data were fit in OPT using paths calculated by FEFF7. Coordination numbers were held constant, whereas distances (R) and Debye-Waller factors (σ^2) were allowed to float. Errors in coordination numbers are estimated to be on the order of 25%. Fits were performed over the entire Fourier transform window (0–6.0 Å). Goodness of fit was measured with F, which was defined as $[(\sum_i^n [k_i^3(\mathrm{EXAFS_{obs}} - \mathrm{EXAFS_{calc}})_i])^2 / n]^{1/2}$.

Table 3.2 EXAFS simulations for cyt P460 6c {FeNO}^{7} EXAFS data were fit with EXAFSPAK using paths calculated by FEFF7. Distance and Debye-Waller factors were allowed to float while, coordination numbers were held constant. Goodness of fit is determined by F, defined as $[(\sum_i^n [k_i^3(\mathrm{EXAFS}_{\mathrm{obs}} - \mathrm{EXAFS}_{\mathrm{calc}})_i])^2 / n]^{1/2}$. Fe-$N_p$ denotes the pyrrole nitrogens of the porphyrin, Fe-C_α denotes the α carbons of the porphyrin, Fe-C_{meso} denotes the meso carbons of the porphyrin and Fe-C_β denotes the β carbons of the porphyrin.

Fit	Path	Coordination #	R(Å)	±	σ^2	±	E_0	F
1	Fe-N_p	5	2.038	0.0047	0.0062	0.0004	3.89	60.40%
2	Fe-N_p	5	2.029	0.0056	0.0049	0.0004	5.15	
	Fe-NO	1	1.849	0.0185	0.0054	0.0021		58.99%
3	Fe-N_p	5	2.043	0.0028	0.0060	0.0003	5.63	
	Fe-NO	1	1.647	0.0307	0.0252	0.0070		
	Fe-C_α	8	3.041	0.0051	0.0053	0.0005		43.02%
4	Fe-N_p	5	2.044	0.0023	0.0061	0.0002	5.93	
	Fe-NO	1	1.650	0.0270	0.0266	0.0059		
	Fe-C_α	8	3.042	0.0045	0.0058	0.0004		
	Fe-C_{meso}	4	3.376	0.0045	0.0058	0.0004		33.05%
5	Fe-N_p	5	2.037	0.0027	0.0048	0.0003	4.92	
	Fe-C_α	8	3.020	0.0045	0.0063	0.0005		
	Fe-C_{meso}	4	3.364	0.0044	0.0015	0.0004		
	Fe-NO	1	1.862	0.0108	0.0058	0.0013		
	Fe-C_β	8	4.446	0.0122	0.0066	0.0013		32.45%
6	Fe-N_p	5	2.037	0.0024	0.0050	0.0002	3.26	
	Fe-C_α	8	3.026	0.0041	0.0063	0.0004		
	Fe-C_{meso}	4	3.364	0.0041	0.0016	0.0004		
	Fe-NO	1	1.858	0.0117	0.0074	0.0015		
	Fe-C_β	16	4.334	0.0084	0.0006	0.0009		29.58%

Table 3.3. EXAFS simulations for cyt P460 5c $\{FeNO\}^7$ EXAFS data were fit using paths calculated by FEFF7. Distance and Debye-Waller factors were allowed to float while, coordination numbers were held constant. Goodness of fit is determined by F, defined as $[(\sum_i^n [k_i^3(\mathrm{EXAFS}_{\mathrm{obs}} - \mathrm{EXAFS}_{\mathrm{calc}})_i])^2 / n]^{1/2}$. Fe-$N_p$ denotes the pyrrole nitrogens of the porphyrin, Fe-C_α denotes the α carbons of the porphyrin, Fe-C_{meso} denotes the meso carbons of the porphyrin and Fe-C_β denotes the β carbons of the porphyrin.

Fit	Path	Coordination #	R(Å)	±	σ^2	±	E_0	F
1	Fe-N_p	4	2.020	0.0034	0.0028	0.0002	3.52	55.04%
2	Fe-N_p	4	2.023	0.0022	0.0028	0.0002	3.92	
	Fe-C_α	8	3.036	0.0052	0.0050	0.0005		41.28%
3	Fe-N_p	5	2.023	0.0025	0.0040	0.0002	4.50	
	Fe-C_α	8	3.033	0.0056	0.0050	0.0006		45.91%
4	Fe-N_p	4	2.022	0.0022	0.0027	0.0005	4.00	
	Fe-C_α	8	3.036	0.0050	0.0051	0.0005		
	Fe-NO	1	1.723	0.0233	0.0161	0.0042		38.05%
5	Fe-N_p	4	2.024	0.0021	0.0028	0.0002	4.36	
	Fe-C_α	8	3.039	0.0049	0.0052	0.0004		
	Fe-NO	1	1.715	0.0226	0.0171	0.0039		
	Fe-C_{meso}	4	3.389	0.0151	0.0053	0.0011		33.48%
6	Fe-N_p	4	2.025	0.0020	0.0028	0.0002	5.52	
	Fe-C_α	8	3.041	0.0047	0.0053	0.0004		
	Fe-NO	1	1.703	0.0181	0.0181	0.0041		
	Fe-C_{meso}	4	3.395	0.0048	0.0050	0.0011		
	Fe-Nhis	1	2.533	0.0137	0.0042	0.0015		32.42%
7	Fe-N_p	4	2.021	0.0020	0.0027	0.0001	6.57	
	Fe-C_α	8	3.032	0.0048	0.0054	0.0004		
	Fe-NO	1	1.742	0.0255	0.0189	0.0045		
	Fe-C_{meso}	4	3.382	0.0087	0.0043	0.0009		
	Fe-C_β	16	4.381	0.0200	0.0059	0.0027		
	Fe-Nhis	1	2.524	0.0125	0.0039	0.0013		31.23%
8	Fe-N_p	4	2.021	0.0020	0.0027	0.0002	4.32	
	Fe-C_α	8	3.028	0.0047	0.0053	0.0004		
	Fe-NO	0.75	1.735	0.0227	0.0129	0.0036		
	Fe-C_{meso}	4	3.384	0.0088	0.0044	0.0009		
	Fe-C_β	16	4.385	0.1995	0.0060	0.0028		
	Fe-N(His)	1	2.525	0.0124	0.0038	0.0013		30.25%

Cyt P460 6c {FeNO}^{7}, a NH_2OH oxidation intermediate.

The characterized 6c-to-5c {FeNO}^{7} conversion suggests that the 5c {FeNO}^{7} species observed in our previous work arises from the slow decay of the 6c {FeNO}^{7} intermediate generated during cyt P460 turnover. Our previous failure to observe the 6c {FeNO}^{7} suggests that this intermediate reacts with either an oxidant or NH_2OH, both present under turnover conditions, to form the {FeNO}^{6} intermediate.

To test whether the 6c {FeNO}^{7} species can be oxidized to the {FeNO}^{6} species, the former was allowed to react with an oxidant or NH_2OH. To generate the 6c {FeNO}^{7} species, we treated 15 μM Fe^{III} cyt P460 with 200 μM HNO in anaerobic pH 8.0 buffer at room temperature for 2 min to produce 15 μM of cyt P460 6c {FeNO}^{7}. The addition of 3 mM NH_2OH to this solution resulted in no changes to the UV/vis absorption spectrum or the rate of 6c-to-5c {FeNO}^{7} conversion (Fig. 7). These results suggest that NH_2OH is unreactive with the 6c {FeNO}^{7} species.

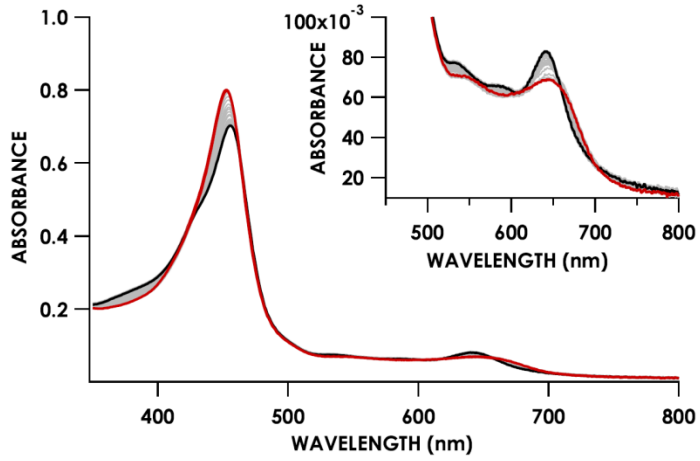

Figure 3.27. UV/vis absorption full-spectral scans of the reaction of 15μM 6c $\{FeNO\}^7$ and 10mM NH_2OH in 200mM HEPES pH 8.0. The solid red trace corresponds to the 6c $\{FeNO\}^7$ after addition of 10mM NH_2OH. Grey spectra are collected in 30s increments for 30 min and the black spectra is the final species corresponding to the 5c $\{FeNO\}^7$. Inset highlights the q band region after the addition of NH_2OH and corresponds to the transition from the 6c to 5c $\{FeNO\}^7$.

By contrast, oxidant addition promoted rapid changes in the UV/vis absorption spectrum. Anaerobic treatment of 15 μM cyt P460 6c $\{FeNO\}^7$ with 100 μM of PMS (E^o = +92 mV vs normal hydrogen electrode (NHE)], DCPIP (E^o = +224 mV vs NHE), or $[Ru(NH_3)_6]Cl_3$ (E^o = +51 mV vs NHE) effected 6c $\{FeNO\}^7$ decay within 30 s (Fig. 8). The product of this reaction had UV/vis absorption features identical to those assigned to the cyt P460 $\{FeNO\}^6$ species.[12] The results of previous experiments showed treating cyt P460 5c $\{FeNO\}^7$ with these oxidants afforded no evidence of $\{FeNO\}^6$ formation.[12] The only spectral changes observed were a minor decrease in the 455-nm Soret maximum and the appearance of a shoulder at 414 nm, which suggested cofactor degradation (Fig. 9). No conversion to $\{FeNO\}^6$ was observed even after treatment with the far more potent oxidant potassium hexachloroiridate $K_2[IrCl_6]$ (E^o = +892 mV vs NHE). Here again, only degradation occurred.

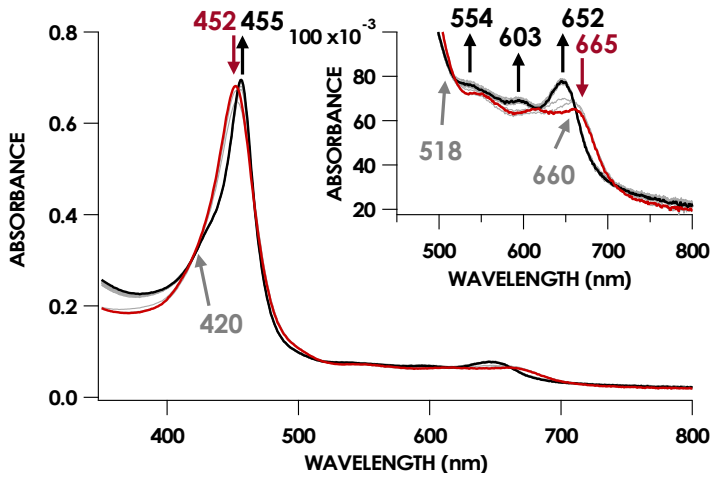

Figure 3.28 UV/vis absorption spectral time course of 15 µM 6c cyt P460 $\{FeNO\}^7$ treated with $Ru(NH_3)_6Cl_3$ in anaerobic 50 mM HEPES buffer (pH 8.0) at room temperature. The solid red trace is the absorbance spectrum collected 5 min after adding 10 equiv of the HNO donor $Na_2N_2O_3$ to 15 µM Fe^{III} cyt P460. The solid black trace shows the final spectrum collected after the addition of 15 equiv of $Ru(NH_3)_6Cl_3$ to these solutions and matches the previously reported spectrum of the cyt P460 $\{FeNO\}^6$ intermediate. Grey spectra were collected in 30 s increments. The inset highlights the time course in the Q band region.

.

EPR spectra obtained for cyt P460 6c and 5c $\{FeNO\}^7$ samples treated with oxidant (Fig. 10) corroborated the results of the UV/vis absorption experiments. Under anaerobic conditions, 600 µM PMS was added to a solution of 200 µM 6c cyt P460 $\{FeNO\}^7$ at pH 8.0 and 25 °C, and the mixture was immediately frozen in liquid N_2. The resulting EPR spectrum was dominated by a sharp signal at $g = 2.0$ attributed to PMS semiquinone. The spectrum lacks features assigned to the 6c $\{FeNO\}^7$ species and shows no evidence for any other Fe-based signals. This outcome suggests that most of the cyt P460 Fe is in an EPR-silent state, which is consistent with the oxidation of the 6c $\{FeNO\}^7$ species to the EPR-silent $\{FeNO\}^6$ form. Moreover, the EPR spectrum obtained after the addition of 600 µM PMS to 200 µM 5c cyt P460

{FeNO}^{7} at pH 8.0 and 25 °C shows EPR features consistent with those of the 5c {FeNO}^{7} species as well as the $g = 2.0$ signal assigned to PMS semiquinone. This PMS semiquinone spectrum is observed in samples of PMS in buffer, indicating that the semiquinone form is present even in the absence of protein or NH_2OH. The aggregate data are consistent with the 5c {FeNO}^{7} species being unreactive and off-pathway; however, the 6c {FeNO}^{7} species can be oxidized to {FeNO}^{6}. The 5c species therefore must have a more positive reduction potential than the 6c {FeNO}^{7}. This latter result suggests that 6c {FeNO}^{7} is an intermediate of NH_2OH oxidation by cyt P460.

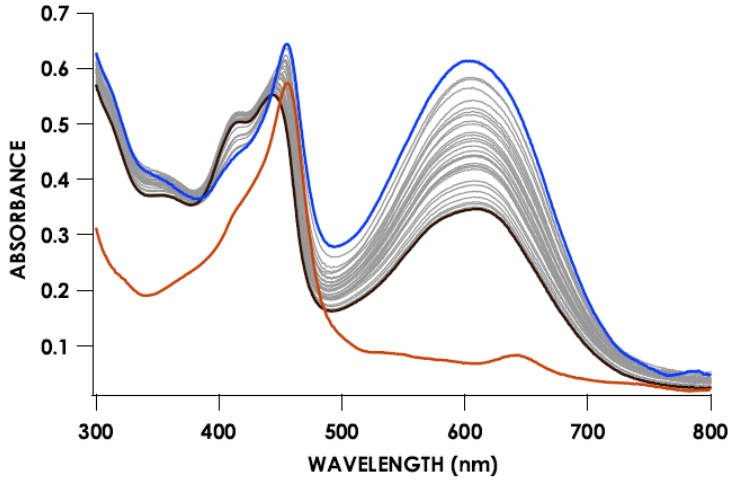

Figure 3.29. UV/vis absorption full-spectral scans of the reaction of 5c {FeNO}^{7} species formed by treatment of 15µM Fe^{III} and 100µM of the HNO donor $Na_2N_2O_3$ and allowed to react for 30 mins in 200mM HEPES pH 8.0. The solid red trace corresponds to the 5c {FeNO}^{7} prior to the addition of the oxidant dichloroindolphenol (DCPIP). The solid blue trace is immediately after addition of 1mM DCPIP. Grey spectra are collected in 30s increments for 20 min and the black spectra is the final species with a split soret max at 413 nm and 442 nm.

To demonstrate conclusively that cyt P460 6c $\{FeNO\}^7$ is a NH_2OH oxidation intermediate, we generated this species by oxidizing the Fe^{III}-NH_2OH species. The 6c-to-5c $\{FeNO\}^7$ conversion occurs on a minutes timescale, whereas oxidant rapidly converts this species to $\{FeNO\}^6$ on a seconds timescale. Therefore, if 6c $\{FeNO\}^7$ is generated as a catalytic intermediate, the presence of oxidant will kinetically favor its conversion to $\{FeNO\}^6$ over His dissociation to form the off-pathway 5c $\{FeNO\}^7$ species. Oxidation to $\{FeNO\}^6$ should be first-order with respect to oxidant concentration. Therefore, at low oxidant concentrations, the rate of the oxidation pathway will be slow enough for the His dissociation pathway to kinetically compete. By these rationales, the 6c $\{FeNO\}^7$ intermediate should accumulate immediately after the depletion of the oxidant.

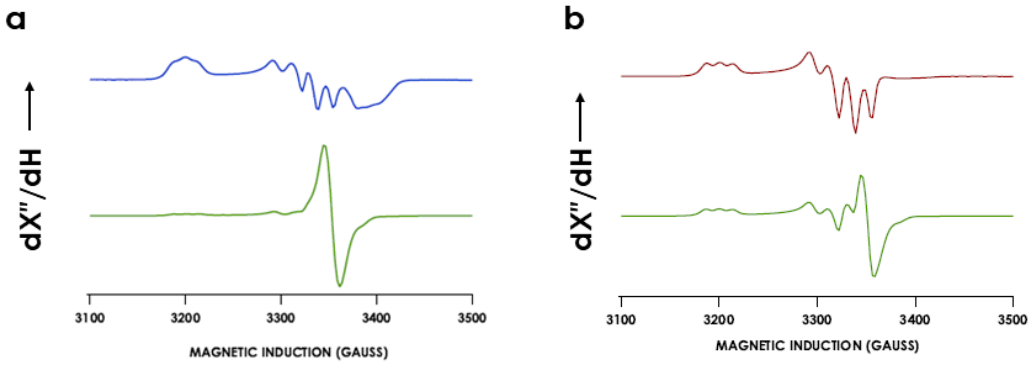

Figure 3.30. EPR spectra of 200 µM P460 Fe^{III} cyt P460 with the addition of 1 mM of the HNO donor $Na_2N_2O_3$ at room temperature for a) 2 min (blue trace) or b) 30 min (red trace) and subsequently reacted with 800 µM of the oxidant phenazine methosulfate (green traces).

To test this hypothesis, we allowed 200 µM cyt P460 to react with 1 mM DCPIP and 1 mM NH_2OH at pH 8.0 and room temperature. The sample was frozen in liquid N_2 within 2 min, immediately after the blue color of the DCPIP disappeared. The 20 K EPR spectrum of this sample exhibited one anisotropic $S = ½$ signal with features identical to those observed for 6c $\{FeNO\}^7$ (Fig. 11). The signal accounts for 40 µM or 20% of the Fe centers in the sample. In the absence of any other Fe-based signal, we accounted for the remainder of the iron (160 µM) as EPR-silent $\{FeNO\}^6$. Our inability to detect the 6c $\{FeNO\}^7$ species within UV/vis absorption time courses likely results from the low ratio of 6c $\{FeNO\}^7$ to $\{FeNO\}^6$ concentrations and the overlapping UV/vis absorption features of the two species. Nevertheless, the EPR spectra clearly show evidence for the formation of the 6c $\{FeNO\}^7$ species, and

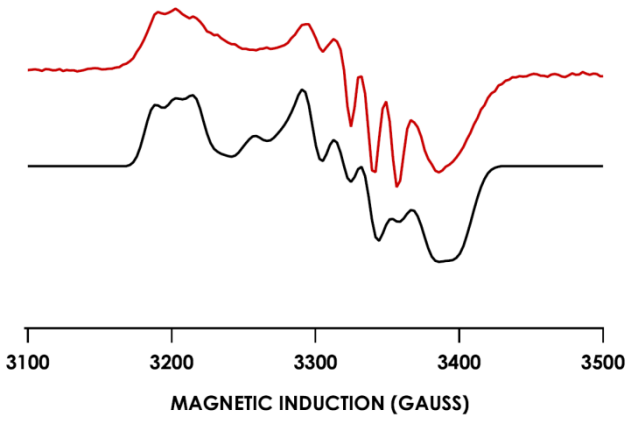

Figure 3.31 EPR spectrum shown in red of 200 µM P460 treated with 1 mM NH_2OH and 1 mM dicholorophenolindophenol (DCPIP) in 200 mM HEPES buffer (pH 8.0). The sample was frozen 2 min after the consumption of oxidant. The black spectrum is the corresponding simulation of the Fe^{III}-NH_2OH oxidized species and is consistent with the 6c $\{FeNO\}^7$ generated from either addition of HNO or NO to Fe^{III} and Fe^{II}, respectfully. Parameters for the black spectrum, corresponding to WT cyt P460 6c $\{FeNO\}^7$, are (g_1, g_2, g_3) = (2.10, 2.01, 1.98) and (^{14}N A_1, A_2, A_3) = (38, 54, 40 MHz).

therefore, we assigned 6c {FeNO}^{7} as an intermediate on the cyt P460 NH_2OH oxidation pathway.

NO-independent His140 dissociation from cyt P460 {FeNO}^{7}

NO promotes rapid (milliseconds to seconds) His dissociation in many heme proteins.[23,24] This phenomenon underlies the mechanism of signal transduction by H-NOX proteins and sGC in both eukaryotes and bacteria.[25] Given this common behavior by heme proteins, we sought to test if the rate of His dissociation from the cyt P460 6c {FeNO}^{7} is also promoted by NO.

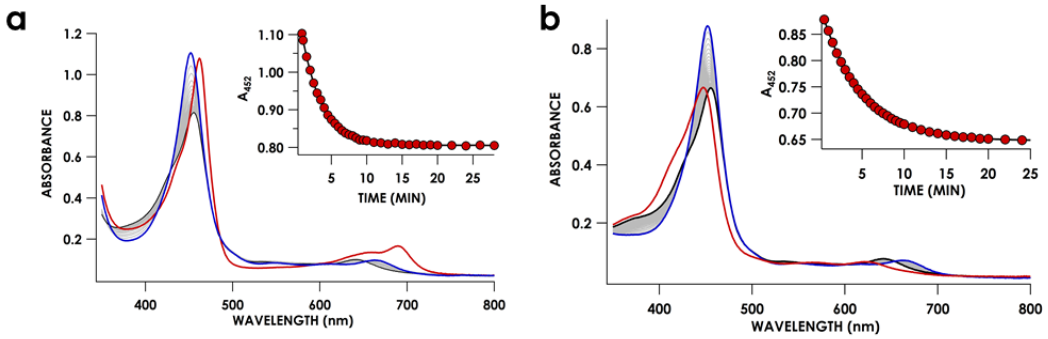

Figure 3.32. UV/vis absorption full-spectral scans of the reaction of cyt P460 15µM (a) Fe^{III} and 100µM of the HNO donor $Na_2N_2O_3$ or (b) Fe^{II} with 100µM NO (50µM Proli-NONOate). The red trace is the initial species of (a) Fe^{III} or (b) Fe^{II}. The blue trace is after the addition of (a) HNO or (b) NO and black is the final trace of the 5c {FeNO}^{7}. The insert is the corresponding single wavelength time course following the absorbance at 452 nm.

The cyt P460 6c {FeNO}^{7} species can be generated from the reaction of either Fe^{III} cyt P460 with HNO or Fe^{II} cyt P460 with NO (Fig. 12 and Fig. 13). The two independent methods allow for testing the reactivity of 6c {FeNO}^{7} in the absence or presence of a large excess of NO, respectively. Rate constants for 6c-to-5c {FeNO}^{7}

conversion were obtained from the reaction of 15 μM Fe^{II} cyt P460 with varying excess concentrations of NO ranging from 100–600 μM. The conversion was monitored by the decrease in absorbance of the 6c $\{FeNO\}^7$ Soret band at 452 nm. Single-exponential functions were fit to the 452 nm traces by nonlinear least-squares regression to determine k_{obs} under each condition. Plotting k_{obs} values versus NO concentration revealed that the 6c-to-5c $\{FeNO\}^7$ conversion is zeroth-order in NO with a His140 dissociation rate constant ($k_{His\text{-}off}$) of $5.7 \pm 0.2 \times 10^{-3}$ s^{-1}. A similar $k_{His\text{-}off}$ of $2.9 \pm 0.2 \times 10^{-3} \pm s^{-1}$ was obtained when Fe^{III} cyt P460 was treated with HNO (Fig. 13). The data clearly show that His140 dissociation for cyt P460 6c $\{FeNO\}^7$ proceeds via a mechanism that is independent of either NO or HNO. This behavior contrasts starkly with the behavior common to NO-sensing heme proteins. Furthermore, the His dissociation of cyt P460 is appreciably slower than that observed for other heme proteins, which dissociate their axial His on millisecond time scales. This slow His dissociation allows the oxidation of 6c $\{FeNO\}^7$ to $\{FeNO\}^6$ to

kinetically outcompete the formation of the off-pathway 5c $\{FeNO\}^7$ intermediate, and thus, appears essential to preserving active catalyst.

Characterization of $\{FeNO\}^7$ species on a cross-link variant, Lys70Tyr cyt P460

The lack of an NO-dependent $k_{His\text{-}off}$ for cyt P460 6c $\{FeNO\}^7$ is unusual compared with that for most NO signaling heme protein $\{FeNO\}^7$ units, prompting us to investigate how this anomalous behavior relates to the unique P460 cofactor structure. To this end, we hypothesized that the distinguishing Lys70 cross-link to the 13′ meso C of the P460 cofactor may influence $k_{His\text{-}off}$. Therefore, we generated a cross-link-deficient Lys70Tyr (K70Y) cyt P460 variant for a comparison of His140 dissociation kinetics. Purified Fe^{III} K70Y cyt P460 is a red protein with a UV/vis absorption Soret maximum at 406 nm and Q-bands at 500 nm and 632 nm (Fig. 14a). The continuous-wave X-band EPR spectra of the resting Fe^{III} exhibited an $S = {}^5/_2$ signal with *g*-values of 5.78 and 1.98 (Fig. 14b). These *g*-values are consistent with an

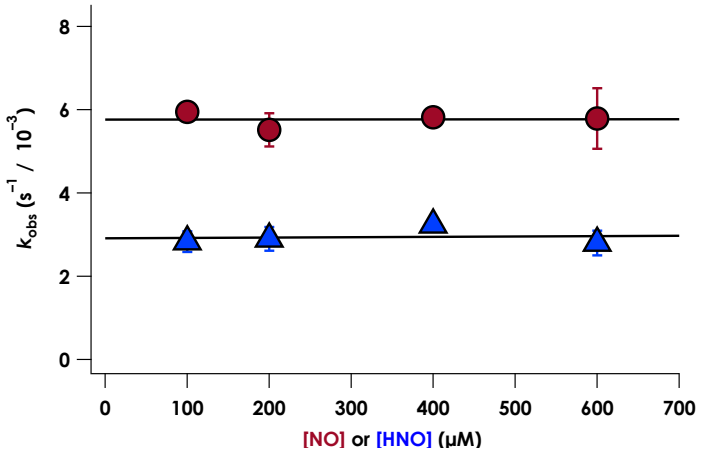

Figure 3.33. Plot of k_{obs} vs NO concentration (red circles) or HNO concentration (blue triangles) shows that His140 dissociation is zeroth-order in either reagent. The corresponding $k_{His\text{-}off}$ values are 2.9 ± 0.2 × 10^{-3} s^{-1} and 5.7 ± 0.2 × 10^{-3} s^{-1} for NO and HNO, respectively.

axial ($^{E}/_{D}$ = 0.00) signal and suggest an increased heme symmetry compared with the WT Fe^{III} cyt P460 $S = {}^{5}/_{2}$ spectrum with an $^{E}/_{D}$ of 0.03. This increased symmetry is consistent with the loss of the Lys cross-link in the variant.

To characterize the cofactor in the K70Y variant further, we obtained resonance Raman (rR) spectra via excitation near the Soret maxima of Fe^{III} WT (λ_{ex} = 457.8 nm) and Fe^{III} K70Y (λ_{ex} = 405.0 nm) cyt P460 (Fig. 14c). Detailed analysis of the Fe^{III} WT cyt P460 rR spectrum was beyond the scope of the present work; however, the increased number of observed bands relative to non-cross-linked hemes suggests that the cyt P460 cofactor has diminished symmetry. This increase in band count is consistent with the rR spectrum obtained for the HAO Fe^{II} heme P460 cofactor.[26] The rR spectrum obtained for Fe^{III} K70Y exhibited an oxidation state marker band (ν_4) at 1370 cm^{-1} but a spin-state marker band (ν_3) at 1501 cm^{-1}. Typically, ν_3 greater than 1500 cm^{-1} indicates a low spin 6-coordinate heme, however, 5-coordinate ferric cyt c′ proteins—verified by EPR spectroscopy and crystal structures—also exhibit $\nu_3 \approx 1500$ cm^{-1}.[27] The EPR spectrum of the Fe^{III} K70Y cyt P460 is also consistent with a high-spin ferric heme. To further characterize the coordination number of the variant cyt P460, we also obtained the rR spectrum obtained of Fe^{II} K70Y cyt P460 (λ_{ex} = 405.0 nm), which has the profile of a standard, effectively D_{4h} 5c high spin Fe^{II} *c*-heme with an oxidation state marker band (ν_4) at 1356 cm^{-1} and a spin-state marker band (ν_3) at 1473 cm^{-1}.[28,29] The aggregate

spectroscopic data are consistent with the restoration of a canonical *c*-heme due to loss of the 13′ cross-link.[30]

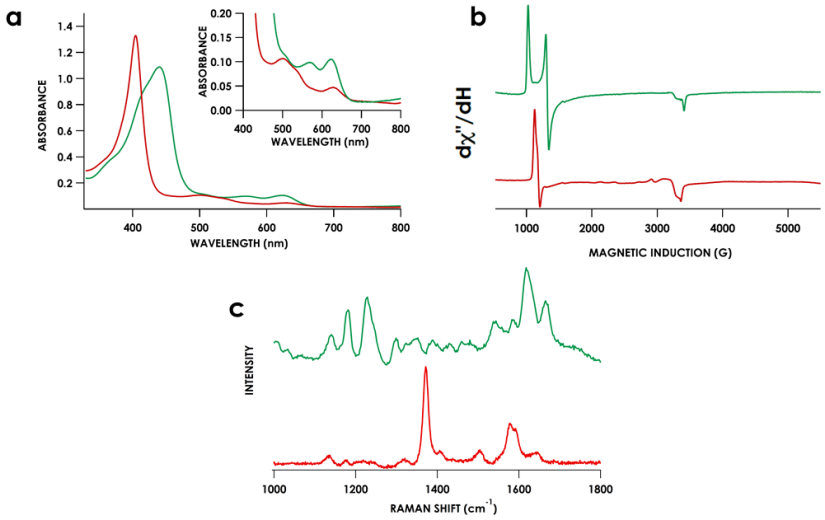

Figure 3.34. (a) UV/vis absorption (b) EPR, and (c) rR spectra of Fe^{III} WT (green) and K70Y Fe^{III} (red) cyt P460. Inset in panel (a) highlights the Q-band region. EPR *g*-values are 5.78 and 1.98; $^{E}/_{D} = 0.00$. EPR spectra were measured at 9.40 GHz and 12 K with 633 μW microwave power. The rR data were obtained via near-resonance excitation with Soret absorption bands: λ_{ex} = 458.7 nm (20 mW) and 405.0 nm (20 mW) for the WT and K70Y variant, respectively.

The Fe^{III} K70Y cyt P460 binds NH_2OH and NO to form the Fe^{III}-NH_2OH adduct or the $\{FeNO\}^6$ species, respectively (Ch.4). However, this variant protein is incapable of turnover, resulting from loss of the Fe^{III}-NH_2OH oxidation reactivity to form $\{FeNO\}^6$. Therefore, the cross-link is necessary for reactivity of the Fe^{III}-NH_2OH adduct. This lack of NH_2OH oxidation reactivity in the variant will be further discussed in the next chapter.

UV/vis absorption time courses of 6c $\{FeNO\}^7$ formation and decay were obtained to compare the His dissociation between WT and K70Y cyt P460. Anaerobic treatment of 10 μM K70Y Fe^{III} cyt P460 with 600 μM HNO resulted in the appearance

of a new species with an UV/vis absorption Soret maximum at 415 nm and Q-band maxima at 540 and 580 nm (Fig. 15**).** This species decayed slowly (within 80 min) to a species exhibiting a Soret peak at 413 nm with a shoulder at 396 nm and unshifted Q-bands at 540 and 580 nm. By contrast, no intermediate was observed when 10 μM K70Y Fe^{II} cyt P460 was treated with 600 μM NO. The UV/vis spectral time course showed the immediate formation of a stable species within the time of manual mixing. The absorption spectrum of this product matches that of the HNO reaction product, which suggests an identical Fe product for both reactions.

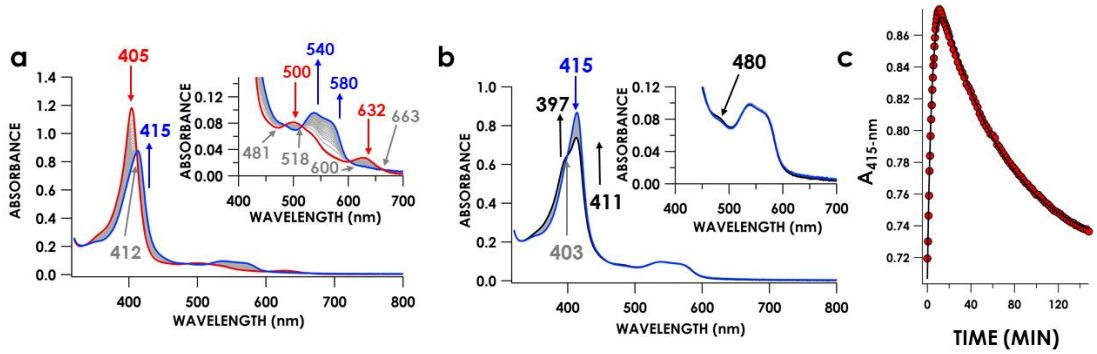

Figure 3.35. The 150-min UV/vis absorption (a,b) full-spectral and (c) single-wavelength (415 nm) time courses of the reaction of 10 μM Fe^{III} cyt P460 with 100 μM of HNO in 200 mM HEPES buffer (pH 8.0). In (a), the solid red trace corresponds to the time point spectrum collected immediately after mixing and represents K70Y Fe^{III} cyt P460. The solid blue trace is the spectrum collected after 10 min and represents K70Y cyt P460 6c $\{FeNO\}^7$. The spectra in (b) follow the 6c-to-5c $\{FeNO\}^7$ conversion, with the solid black trace representing K70Y cyt P460 5c $\{FeNO\}^7$. Grey spectra were collected in 1 min increments. The insets highlight the time courses in the Q-band region. Absorption maxima in nanometers are labeled with colors corresponding to each species. Isosbestic points are labeled in gray. In (c), the black trace is a double-exponential fit ($\boldsymbol{A_{415} = A_0 + A_1 \times e^{-k_{obs(1)} \times t} + A_2 \times e^{-k_{obs(2)} \times t}}$) to the data, yielding $k_{obs(1)}$ = 3.7 × 10^{-3} s^{-1} (6c $\{FeNO\}^7$ formation) and $k_{obs(2)}$ = 2.7 × 10^{-4} s^{-1} (6c-to-5c conversion).

EPR spectroscopic analyses afforded informative characterizations of the two-observed species. An anaerobic sample was prepared containing 150 μM K70Y Fe^{III} cyt P460 and 700 μM HNO at pH 8.0 and 25 °C. The sample was incubated for 3 min and frozen in liquid N_2. The EPR spectrum of this sample exhibited *g*-values of 2.09, 2.02, and 1.98 with corresponding ^{14}N hyperfine values of 45, 47, and 40 MHz, respectively. These parameters are characteristic of a heme 6c $\{FeNO\}^7$ species. A second sample was prepared by treating 150 μM K70Y Fe^{II} cyt P460 with 600 μM NO at pH 8.0 and 25 °C with immediate freezing in liquid N_2. The EPR spectrum of this sample exhibited *g*-values of 2.09, 2.03, and 2.01 with corresponding ^{14}N hyperfine values of 47, 41, and 49 MHz, respectively (Fig. 16). As with the WT experiments, the differences in the two EPR spectra are consistent with a conversion from a 6c to a

5c $\{FeNO\}^7$. The K70Y also does not exhibit a 9-line super hyperfine splitting in the 6c $\{FeNO\}^7$. Again, ENDOR spectroscopy would need to be attained in order to determine the degree Fe-N(His) hyperfine to compare to the WT, which is outside the scope of this paper. The correlated EPR and UV/vis absorption spectra indicate that the reaction of K70Y Fe^{III} cyt P460 with HNO forms a 6c $\{FeNO\}^7$, which decays slowly to a 5c $\{FeNO\}^7$.

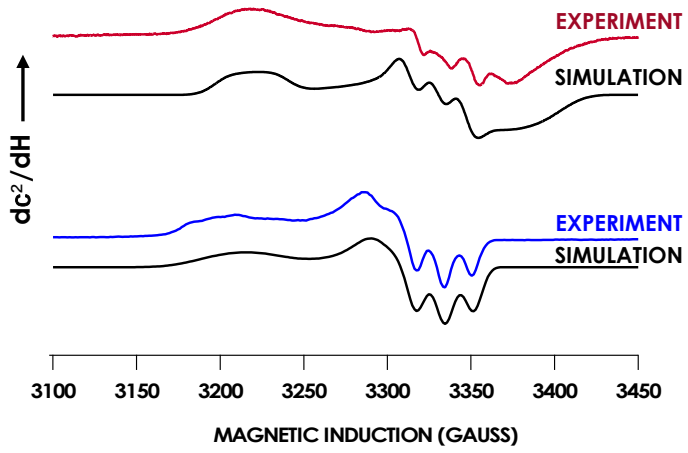

Figure 3.36. Continuous-wave X-band (9.40 GHz) EPR spectra measured at 8 K with 63 µW microwave power of 150 µM K70Y Fe^{III} cyt P460 treated with 750 µM HNO (red) and 150 µM K70Y Fe^{II} cyt P460 treated with 750 µM NO in 200 mM HEPES buffer pH 8.0 (blue). SpinCount simulations are shown in black for each spectrum. Spin Hamiltonian parameters for the red spectrum, corresponding to K70Y cyt P460 6c $\{FeNO\}^7$, are (g_1, g_2, g_3) = (2.09, 2.02, 1.98) and (^{14}N A_1, A_2, A_3) = (45, 47, 40 MHz). Parameters for the blue spectrum, corresponding to WT cyt P460 5c $\{FeNO\}^7$, are (g_1, g_2, g_3) = (2.09, 2.03, 2.01) and (^{14}N A_1, A_2, A_3) = (47, 41, 49 MHz).

Data for the Fe K-edge absorption near-edge regions and EXAFS region of the variant 5c $\{FeNO\}^7$ species were collected for comparison with that of the WT. The K70Y variant also exhibited a pre-edge feature near 7113 eV with intensity similar to that seen in the WT 5c $\{FeNO\}^7$ spectrum. This result is consistent with decreased centrosymmetry at the Fe center resulting from the decrease in coordination number

from the dissociation of the axial His (Fig. 17).[18] EXAFS data were collected to determine the bond distances of K70Y cyt P460 5c {FeNO}^{7}, and fits of the EXAFS region from a k of 2–14 Å^{-1} yielded a Fe–NO bond length of 1.80 Å. As with that of the WT 5c {FeNO}^{7}, the EXAFS data fit best with the addition of the axial His as a separate parameter, yielding a bond length of 2.48 Å, which is outside the range of coordination for an Fe–N(His) bond (Fig. 18 and Table 1).

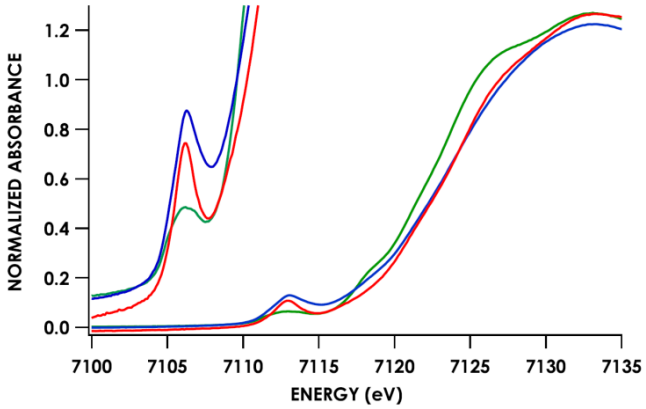

Figure 3. 17. Fe-K edge X-ray absorption spectra (XAS) obtained at 10 K of 1mM Fe^{II} K70Y treated with 10mM NO immediately frozen to form the K70Y 5c {FeNO}^{7} species (red trace). The K70Y 5c {FeNO}^{7} species is compared to the 6c (green trace) and 5c (blue trace) WT cyt P460 {FeNO}^{7} species. All samples were glassed in 200mM HEPES buffer pH 8.0 with 25% v/v glycerol. The 1s → 3d pre-edge feature is at 7113.3 eV

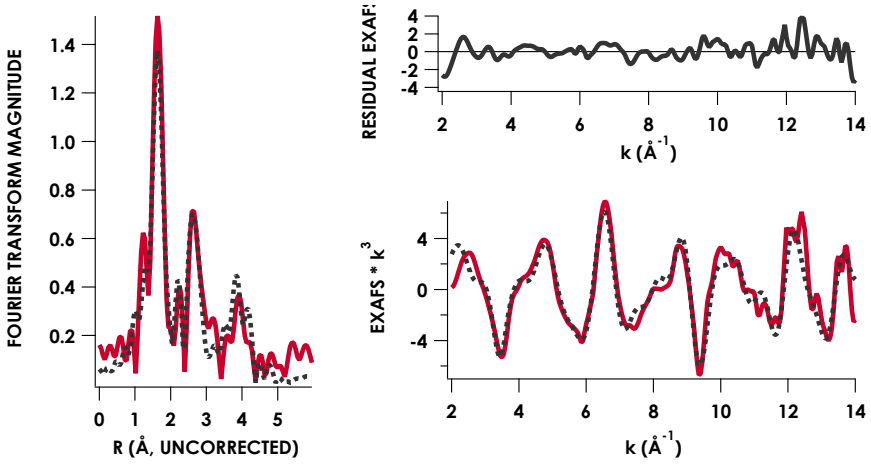

Figure 3.37. Fe K-edge EXAFS data obtained at 10 K for K70Y cyt P460 5c {FeNO}^{7} in glassed 200 mM HEPES buffer (pH 8.0) containing 25% v/v glycerol. Experimental data are plotted as solid lines; fits are dotted lines.

Table 3.4. EXAFS simulations for K70Y cyt P460 5c {FeNO}^{7} EXAFS data were fit with EXAFSPAK using paths calculated by FEFF7. Distance and Debye-Waller factors were allowed to float while, coordination numbers were held constant. Goodness of fit is determined by F, defined as $[(\sum_i^n [k_i^3(\mathrm{EXAFS}_{\mathrm{obs}} - \mathrm{EXAFS}_{\mathrm{calc}})_i])^2 / n]^{1/2}$. Fe-$N_p$ denotes the pyrrole nitrogens of the porphyrin, Fe-C_α denotes the α carbons of the porphyrin, Fe-MS denotes carbon nitrogen multiscatters and Fe-C_β denotes the β carbons of the porphyrin.

Fit	Path	Coordination #	R(Å)	±	σ^2	±	E_0	F
1	Fe-N_p	4	1.998	0.0038	0.0033	0.0003	11.75	60.54%
2	Fe-N_p	4	2.009	0.0029	0.0035	0.0003	10.95	
	Fe-C_α	8	2.977	0.0061	0.0039	0.0005		55.84%
3	Fe-N_p	5	2.009	0.0032	0.0050	0.0035	10.69	
	Fe-C_α	8	2.968	0.0066	0.0038	0.0006		61.34%
4	Fe-N_p	4	1.990	0.0038	0.0030	0.0003	10.62	
	Fe-C_α	8	3.002	0.0054	0.0039	0.0005		
	Fe-NO	1	1.776	0.0156	0.0056	0.0018		52.44%
5	Fe-N_p	4	1.992	0.0037	0.0030	0.0003	10.43	
	Fe-C_α	8	3.000	0.0055	0.0041	0.0006		
	Fe-NO	1	1.788	0.0194	0.0073	0.0025		
	Fe-N(His)	1	2.502	0.0156	0.0023	0.0016		51.01%
6	Fe-N_p	4	1.995	0.0030	0.0030	0.0003	9.59	
	Fe-C_α	8	3.000	0.0044	0.0037	0.0004		
	Fe-NO	1	1.807	0.0185	0.0086	0.0026		
	Fe-N(His)	1	2.490	0.0115	0.0019	0.0012		
	Fe-C-N (MS)	16	3.233	0.0132	0.0025	0.0017		40.66%
7	Fe-N_p	4	1.991	0.0025	0.0028	0.0002	8.45	
	Fe-C_α	8	2.997	0.0038	0.0038	0.0003		
	Fe-NO	1	1.805	0.0141	0.0069	0.0018		
	Fe-N(His)	8	2.483	0.0117	0.0026	0.0012		
	Fe-C-N (MS)	16	3.224	0.0114	0.0022	0.0014		
	Fe-C_β	8	4.341	0.0055	0.0020	0.0005		35.66%

Rapid, NO dependent His140 dissociation when cross-link removed

A 6c $\{FeNO\}^7$ species was observed when either WT or K70Y Fe^{III} cyt P460 was allowed to react with HNO. However, this species was not observed during the reaction of the Fe^{II} form of the b with NO, suggesting either the 6c $\{FeNO\}^7$ is never formed or it decays too fast for observation. To differentiate between these possibilities, we monitored the reaction of K70Y Fe^{II} cyt P460 with NO using stopped-flow UV/vis absorption spectroscopy. The spectral time course exhibited accumulation within 20 ms of absorption features attributed to K70Y cyt P460 6c $\{FeNO\}^7$ (Fig. 19). This spectrum decayed within 5 s to a new spectrum characteristic of the 5c $\{FeNO\}^7$ species. An isosbestic point at 400 nm suggests direct conversion from the 6c to the 5c $\{FeNO\}^7$ species. These results verify that the 6c $\{FeNO\}^7$ species is generated when Fe^{II} K70Y cyt P460 reacts with NO and its conversion to the 5c $\{FeNO\}^7$ species is rapid. This 6c-to-5c $\{FeNO\}^7$ conversion is orders of magnitude faster in the reaction when excess NO is present, suggesting that NO induces rapid His140 dissociation. Such rapid NO-dependent His dissociation from 6c heme $\{FeNO\}^7$ species has been previously characterized in several NO-sensing heme proteins.

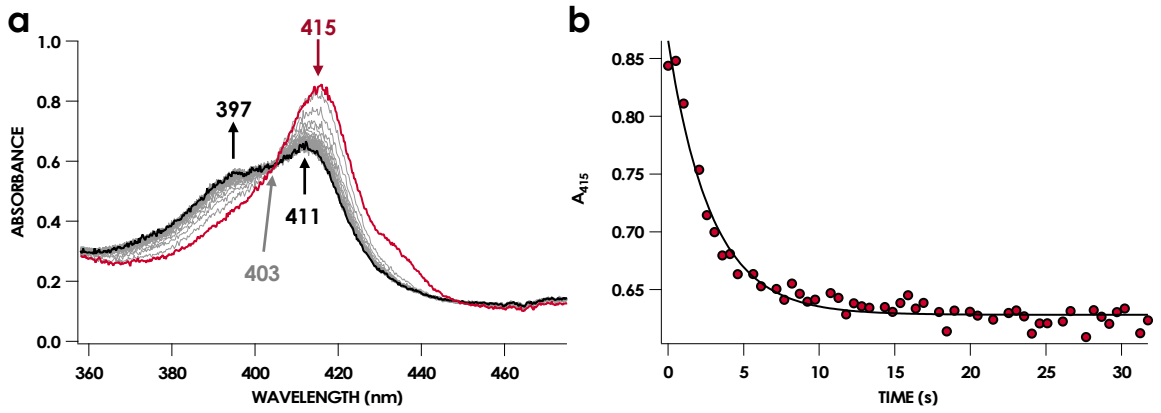

Figure 3. 38. The 32-s stopped-flow UV/vis absorption (a) full-spectral and (b) single-wavelength (415 nm) time courses of the reaction of 10 μM Fe^{II} cyt P460 with 100 μM NO in 200 mM HEPES buffer (pH 8.0). In (a), the solid red trace corresponds to the time point spectrum collected immediately after mixing and represents K70Y cyt P460 6c {FeNO}^{7}, and the solid black trace represents K70Y cyt P460 5c {FeNO}^{7}. Grey spectra were collected in ca. 0.5 s increments. Absorption maxima in nanometers are labeled with colors corresponding to each species. An isosbestic point is labeled in gray. In (c), the black trace is a single exponential ($\boldsymbol{A_{415} = y_0 + A \times e^{-k_{obs} \times t}}$) fit to the data, yielding k_{obs} = 0.40 s^{-1}.

Rate constants were determined for the NO-independent and NO-dependent His140 dissociation pathways ofK70Y cyt P460 6c {FeNO}^{7}. The NO-independent rate constant, $k_{His\text{-}off}$, was determined from the reactions of 10 μM K70Y Fe^{III} cyt P460 with HNO at various concentrations in the range of 100–600 μM. The accumulation and decay of 6c {FeNO}^{7} was monitored at 415 nm with UV/vis absorption spectroscopy. Double-exponential functions were fit to biphasic 415 nm traces. The k_{obs} for His140 dissociation was zeroth-order with respect to HNO **(**Fig. 20a). An averaging of the k_{obs} values at all HNO concentrations provided a $k_{His\text{-}off}$ of 3.8 ± 0.9 × 10^{-4} s^{-1}, which is an order of magnitude slower than the $k_{His\text{-}off}$ measured for WT cyt P460.

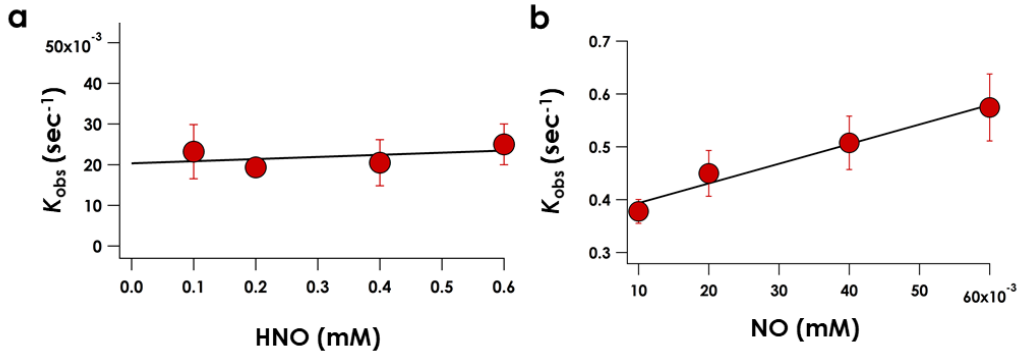

Figure 3.39. Plots of k_{obs} vs HNO concentration (a) and NO concentration (b) show that His140 dissociation is zeroth-order in HNO but first-order in NO for Lys70Tyr cyt P460 {FeNO}^{7}. The corresponding rate constants are $k_{His\text{-}off} = 3.8 \pm 0.9 \times 10^{-4}$ s^{-1} and $k_{His\text{-}off(NO)} = 790 \pm 80 \times$ M^{-1}s^{-1} for HNO and NO, respectively. Linear regression analysis with corresponding T-test for b is shown in the appendix.

The rate constant of the NO-dependent His140 dissociation pathway was measured using stopped-flow UV/vis absorption spectroscopy. The NO-dependent rate constant for His140 dissociation, $k_{\text{His-off(NO)}}$, was determined from the reactions of 10 μM K70Y Fe^{II} cyt P460 with 100–800 μM NO. These stopped-flow kinetics experiments were monitored at 415 nm. Because the 6c {FeNO}^{7} species formed completely within the stopped-flow mixing dead time, the kinetic traces were monophasic that were well fit by single exponentials. Extracted values of k_{obs} were fit to a linear regression with equation 3 (Fig. 20b):

$$k_{obs}=k_{His-off(NO)}[NO] + k_{app} \quad (3)$$

The best-fit parameters were a $k_{\text{His-off(NO)}}$ of 790 ± 80 M^{-1} s^{-1} with a y-intercept, or k_{app}, of 0.36 ± 0.04 s^{-1}. The first-order dependence of 6c-to-5 {FeNO}^{7} conversion has been used to support a mechanism involving a hypothetical *trans*-dinitrosyl {Fe(NO)$_2$}^{8} intermediate in other heme systems.[31] Our spectral time course is

inconsistent with formation of an intermediate during this conversion. Furthermore, it is unclear from our data what k_{app} represents. In our hands, the 6c-to-5c {FeNO}^{7} conversion is irreversible, thus the non-zero value for k_{app} likely reports the rate constant of an alternative pathway. One possibility is that this y-intercept represents the parallel NO-independent His dissociation pathway, $k_{His\text{-}off}$. However, this value was independently measured to be vastly slower: $3.7 \pm 0.4 \times 10^{-4}$ s^{-1}. Another possibility is that the range of NO concentrations surveyed was insufficient to observe saturating behavior; such behavior has been noted in other studies of heme {FeNO}^{7} 6c-to-5c conversion.[32] Our data clearly show that removal of the cross-link introduces an NO-dependent His140 dissociation pathway However, more detailed mechanistic work will be required to correctly interpret the observed non-zero y-intercept of the NO-dependent His dissociation pathway.

The kinetics thus revealed two distinct pathways for His140 dissociation from the K70Y cyt P460 6c {FeNO}^{7}. One pathway is independent of NO with a first-order rate constant similar to that observed for the WT cyt P460 6c {FeNO}^{7} species while the second pathway is absent in the WT cyt P460. The results of these experiments suggest that in the presence of excess NO, the Lys70 cross-link of the P460 cofactor is necessary to inhibit the NO-dependent pathway, thereby allowing the oxidation of 6c {FeNO}^{7} to {FeNO}^{6}. These results identify at least one function of the cross-link characteristic of P460 cofactors.

Activation analysis of His140 dissociation from WT and K70Y: Insight into the role of the cross-link in 6c-to-5c conversion.

Determination of activation enthalpies ($\Delta H^{\ddagger}$) and entropies ($\Delta S^{\ddagger}$) for the NO-independent pathways provided insight into how the Lys70 cross-link influences the His140 dissociation rate in the NO-dependent pathway. The results of the Eyring analysis of NO-independent and NO-dependent pathways for WT and K70Y cyt P460 are shown in Table 5. For both the WT and K70Y, the NO-independent pathway is dominated by the dissociation of His140. The 1 kcal mol^{-1} difference in $\Delta G^{\ddagger}$ between the variant and the WT proteins ($\Delta\Delta G^{\ddagger}$) accords with the 10-fold smaller rate constant for the NO-independent His dissociation of K70Ycyt P460 compared with that of the WT. The increased barrier to dissociation can largely be attributed to the increased $\Delta H^{\ddagger}$ of the variant dissociation reaction. The difference in $\Delta H^{\ddagger}$ of 11 kcal mol^{-1} between the K70Y and WT cyt P460 proteins implies an increased Fe–N(His) bond dissociation energy in the former. The relatively small $\Delta S^{\ddagger}$ of the WT (0.4 ± 0.3 cal mol^{-1} K^{-1}) is surprising for a dissociation mechanism, which would assume an overall gain in $\Delta S^{\ddagger}$ and therefore a larger $\Delta S^{\ddagger}$. This increase in $\Delta S^{\ddagger}$ of 27.3 cal mol^{-1} K^{-1} in the K70Y contributes to lowering the overall $\Delta G^{\ddagger}$ of the NO-independent pathway to account for a difference of 1 kcal mol^{-1} rather than the approximately 9 kcal mol^{-1} difference if the variant and WT shared a similar $\Delta S^{\ddagger}$. Therefore, this difference in $\Delta S^{\ddagger}$ suggests one functional contribution of the cross-link (See discussion).

The activation parameters were also obtained for the NO-dependent His140 dissociation in K70Y cyt P460. Both the NO-dependent and NO-independent pathways for K70Yr cyt P460 yield similar $\Delta H^{\ddagger}$ values. This is consistent with 6c-to-5c $\{FeNO\}^7$ conversion in either pathway is dominated by the Fe–His bond

dissociation energy. The entropic terms from the NO-dependent and NO-independent pathways differ by approximately 30 cal mol^{-1} K^{-1}, a value that commonly attends a unit change in reaction order.[33]

Table 3.5. His140 Dissociation Rate Constants and Activation Parameters.[a]

Temperature (°C)	Wild-Type NO-Independent ($k_{His\text{-}off}$)	K70Y NO-Independent ($k_{His\text{-}off}$)	K70Y NO-Dependent ($k_{His\text{-}off(NO)}$)
15	$0.9 \pm 0.1 \times 10^{-3}$ s^{-1}	$6.6 \pm 2.3 \times 10^{-5}$ s^{-1}	210 ± 20 $M^{-1}s^{-1}$
20	$1.86 \pm 0.03 \times 10^{-3}$ s^{-1}	$2.2 \pm 0.1 \times 10^{-4}$ s^{-1}	510 ± 40 $M^{-1}s^{-1}$
25	$2.9 \pm 0.2 \times 10^{-3}$ s^{-1}	$3.8 \pm 0.9 \times 10^{-4}$ s^{-1}	790 ± 80 $M^{-1}s^{-1}$
30	$6.26 \pm 0.14 \times 10^{-3}$ s^{-1}	$1.23 \pm 0.08 \times 10^{-3}$ s^{-1}	3190 ± 260 $M^{-1}s^{-1}$
35	$1.12 \pm 0.05 \times 10^{-2}$ s^{-1}	$2.80 \pm 0.03 \times 10^{-3}$ s^{-1}	6550 ± 270 $M^{-1}s^{-1}$
$\Delta H^{\ddagger}$ (kcal mol^{-1})	20.9 ± 0.3	30.2 ± 2.8	30.5 ± 0.7
$\Delta S^{\ddagger}$ (cal mol^{-1} K^{-1})	0.4 ± 0.3	27.6 ± 2.2	57.8 ± 2.4
$\Delta G^{\ddagger}$ (25 ºC) (kcal mol^{-1})	20.8 ± 0.1	21.9 ± 0.7	13.2 ± 0.7

[a]Errors in rate constants represent the standard deviation of three trials per reaction at each temperature. Eyring plots were weighted in Igor. A propagation of error analysis from the weighted errors of the linear regression fit in Igor was used to calculate the errors in the activation parameters.[35]

Conclusions

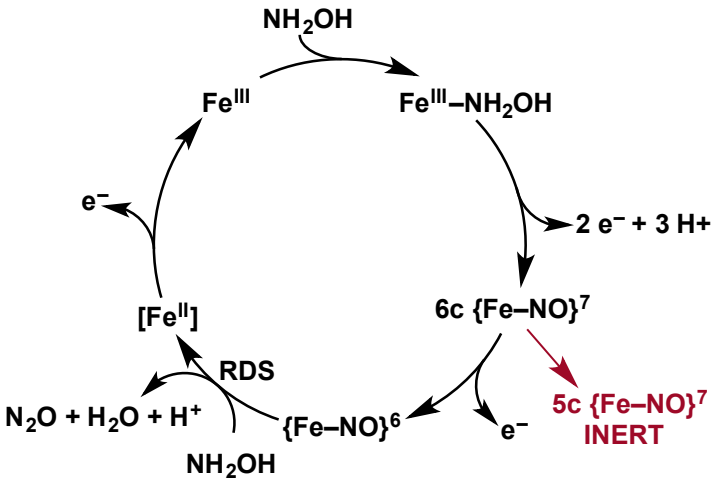

Figure 3.40. Revised mechanism of NH_2OH oxidation and formation of N_2O by cyt P460.

We have identified a 6c $\{FeNO\}^7$ intermediate on the cyt P460 NH_2OH oxidation pathway (Fig. 21). This species results from an apparent 2-electron oxidation of Fe^{III}-NH_2OH cyt P460. We suspect that Fe^{III}-NH_2OH conversion to 6c $\{FeNO\}^7$ occurs via two subsequent and rapid 1-electron oxidation steps with reduction potential inversion between these steps.[34] Possible 1-electron oxidized intermediates are either the Fe^{III}-$NH_2O^{\bullet}$, invoked as an intermediate for cyt P450 nitric oxide reductase catalysis, or a Fe^{II}-HNO species.[35] Future studies will pursue the trapping and characterization of these intermediates.

The oxidation of 6c $\{FeNO\}^7$ produces the $\{FeNO\}^6$ intermediate competent for electrophilic attack by NH_2OH, ultimately resulting in N_2O release. In the absence of oxidant, the 6c $\{FeNO\}^7$ decays to the inert, off-pathway 5c $\{FeNO\}^7$. However, with oxidant present, the oxidation of 6c $\{FeNO\}^7$ to $\{FeNO\}^6$ proceeds far more

swiftly than His dissociation to form the 5c $\{FeNO\}^7$ species. Thus, in the presence of oxidant, catalysis outpaces the formation of the irreversible, off-pathway 5c $\{FeNO\}^7$, thereby preserving active enzyme. From this result, we speculate that the in vivo lifetime of cyt P460 is partially dependent on steady-state oxidant concentrations, which should fluctuate with periplasmic O_2 concentrations. This mechanism could affect active cyt P460 concentrations when AOB transition from oxic to anoxic environments. The bulk enzyme could tolerate short periods of low O_2 concentration given that 6c-to-5c $\{FeNO\}^7$ conversion requires several minutes. Determining if HAO inactivates in a similar fashion upon oxidant depletion could determine whether our hypothesis also applies to energy-producing reactions in AOB. Indeed, a 5c $\{FeNO\}^7$ species of the HAO P460 cofactor has been observed when the enzyme is treated with NH_2OH and NO. However, it remains unclear whether this species is similarly unreactive, as observed for cyt P460 5c $\{FeNO\}^7$ intermediate.

Experiments with the K70Y cyt P460 showed how the Lys–heme cross-link, the defining characteristic of cyt P460s, is critical for avoiding the off-pathway 5c $\{FeNO\}^7$. This cross-link lengthens the lifetime of the 6c $\{FeNO\}^7$ intermediate ($k_{\text{His-off}} = 2.9 \times 10^{-3}$ s^{-1}) compared to that of the other heme proteins. As noted above, the lifetime of the 6c $\{FeNO\}^7$ is related to the *trans* influence exerted by the NO, which weakens the Fe–His140 bond. However, we noted that the $\Delta H^{\ddagger}$ for His dissociation is larger for the variant than the WT, implying the variant has a stronger Fe–N(His) bond strength. The stronger Fe–N(His) bond strength in K70Y is consistent with the loss of heme ruffling after the removal of the cross-link; the restoration of planarity allows

electron delocalization from Fe into the porphyrin π system.[36] Consequently, Fe becomes less electron-rich, strengthening the Fe–N(His) interaction while weakening the Fe–NO interaction. The elongated Fe–NO distance of the K70Y 5c $\{FeNO\}^7$ species relative to that of the WT (1.81 Å vs 1.74 Å, respectively) obtained from the EXAFS data could be interpreted as a consequence of the increased Fe–N(His) strength which weakens the σ-bonding donation of the NO to the Fe center thereby lengthening the Fe–N(O) bond.

The 6c $\{FeNO\}^7$ species of the K707Y variant exhibited a rapid His dissociation with a first-order dependence on NO [$k_{\text{His-off(NO)}}$ = 790 M^{-1} s^{-1}]. The combined data imply that the Lys–heme cross-link renders cyt P460 6c $\{FeNO\}^7$ insensitive to NO. We have proposed that NO_2^- produced during aerobic NH_2OH oxidation turnover by cyt P460 is a non-enzymatic product; NO dissociates from the $\{FeNO\}^6$ intermediate of the catalytic cycle and reacts with O_2 to generate the observed NO_2^-. In other words, one product of cyt P460 is NO. In the absence of an NO sink, cyt P460 could be surrounded by a local pocket of high NO concentration generated by its own turnover; thus, cyt P460 generates a potential poison to its own catalytic cycle. Furthermore, recent work from our laboratory has established NO as an obligate intermediate in the NH_3-oxidizing pathway through NH_2OH oxidation by HAO.[2] Thus, intracellular NO likely accumulates during oxic metabolism. The cross-link, therefore, appears to be necessary for avoiding cyt P460 catalysis inactivation under conditions with available NO.

NO-dependent 6c-to-5c $\{FeNO\}^7$ conversion is also characteristic of the human NO-sensing protein sGC.[24] Along with its bacterial counterparts, these NO sensors are collectively known as H-NOX (Heme NO/O_2 binding) proteins because they contain an H-NOX domain, a *b*-heme with an axially bound His. Downstream signaling is conferred through a partner protein, or in sGC, an attached guanylate cyclase domain. NO binds to the Fe^{II}-heme to form a 6c $\{FeNO\}^7$ species that rapidly converts to a 5c $\{FeNO\}^7$ species. The ensuing His dissociation induces a protein conformational change that activates the cyclase domain, thereby initiating the signaling cascade. Three hypotheses have been offered to explain the observed NO dependence on the rate of the 6c-to-5c $\{FeNO\}^7$ conversion: (1) NO binding at an allosteric site promotes His dissociation, (2) a second NO molecule replaces the axial His to form a *trans*-dinitrosyl intermediate, or (3) nucleophilic attack on the $\{FeNO\}^7$ intermediate by a second NO molecule results in N–N bond formation, which in turn results in His dissociation.[37] However, NO dependence on His dissociation has also been observed for our cyt P460 variant, cyt c′-α and an engineered heme/non-heme nitric oxide reductase, none of which are related to H-NOX proteins.[38,39] These non-H-NOX proteins are unlikely to contain the same allosteric site, therefore, we can rule out hypothesis 1 as a general mechanism. Biological N–N bond formation is preceded by diferrous-dinitrosyl ($[\{FeNO\}^7]_2$), Fe^{III}-$^{\bullet}NH_2OH$, or $\{FeNO\}^6$ intermediates.[35,40–43] Although we cannot rule out hypothesis 3, N–N bond formation via the nucleophilic attack of NO on an $\{FeNO\}^7$ species has not yet been observed in a biological system. In support of hypothesis 2, the crystal structure of a cyt c′-α protein from *Alcaligenes*

xylosoxidans, which also exhibits NO-dependent 6c-to-5c {FeNO}^{7}conversion, shows that NO is bound to the proximal side of the heme.[44] Furthermore, kinetic evidence exists for an intermediate species between the 6c and 5c {FeNO}^{7} of a *Nostoc* sp. H-NOX protein.[45] This intermediate was proposed to be *trans*-dinitrosyl. We saw no evidence for an intermediate in our experiments, which suggests that the mechanism for K70Y cyt P460 differs from those proposed for H-NOX. Therefore, to elucidate this NO-dependent mechanism, we will need to perform further kinetic and intermediate trapping studies. For the purpose of the current study, the relevant result is that the removal of the cross-link causes the rate of His dissociation to be dominated by a NO-dependent pathway that is absent in the native cyt P460.

The lack of a NO-dependent pathway for WT cyt P460 could be due to decreased accessibility at the proximal side of the heme, precluding the binding of the second NO molecule. For the NO-independent His140 dissociation pathway, the WT cyt P460 has a $\Delta S^{\ddagger}$ term (0.4 ± 0.3 cal mol^{-1} K^{-1}) that is smaller than that for K70Y cyt P460 (27.6 ± 2.2 cal mol^{-1} K^{-1}). A similarly large $\Delta S^{\ddagger}$ was found for His dissociation from *A. xylosoxidans* c′ {FeNO}^{7}.[46] We propose that the change in the $\Delta S^{\ddagger}$ term for the WT cyt P460 reflects the degrees of freedom of the His140 ligand. By this hypothesis, the discrepancy between the $\Delta S^{\ddagger}$ terms may indicate that the His140 pocket in WT cyt P460 is more rigid, which could decrease NO accessibility on the proximal side of the heme and preclude the NO-dependent His dissociation pathway. Thus, the cyt P460 cross-link "locks" the axial His of the 6c {FeNO}^{7}

species, thereby slowing its dissociation rate. This impediment allows the oxidation of 6c $\{FeNO\}^7$ to $\{FeNO\}^6$ to kinetically outcompete protein inactivation.

Our results suggest that the K70Y cyt P460 variant can be used as another model for signal transduction by H-NOX proteins. The increased $\Delta S^{\ddagger}$ term in the cyt P460 variant may reflect a less rigid pocket surrounding the axial His. In contrast, H-NOX proteins rely on protein conformational changes induced by the formation of the 5c $\{FeNO\}^7$ complex to activate signal transduction. Locking the protein conformation would be detrimental to the activation of cyclase activity or interactions with partner signaling proteins. Therefore, the increased degrees of motion in the His pocket may be necessary for signal transduction. To test this hypothesis, mutagenesis studies that perturb the Fe-His interaction will be carried out to explore the effects of His140 pocket alterations on the dissociation of the axial His on other cross-link deficient cyt P460 $\{FeNO\}^7$ variants.

Our results also show that the 6c $\{FeNO\}^7$ species can be independently generated by treating either Fe^{III} with HNO or Fe^{II} with NO. For the K70Y cyt P460, these treatments result in either a slow, HNO-concentration-independent His dissociation or a rapid, NO-concentration-dependent His dissociation, respectively. HNO and NO are known to exhibit orthologous physiological effects in humans.[47] The observed differences in the rate laws for the dissociation of axial His from 6c $\{FeNO\}^7$ in the presence of HNO or NO may provide insight into the divergent signaling pathways and orthologous physiological effects.

In summary, we have characterized a 6c $\{FeNO\}^7$ species on the NH_2OH oxidation pathway of cyt P460. This species can undergo axial His dissociation to yield an off-pathway 5c $\{FeNO\}^7$ species. Kinetic analysis of WT and K70Y cyt P460 proteins show that the Lys–heme cross-link of the WT protein eliminates a NO-dependent pathway toward 6c-to-5c $\{FeNO\}^7$ conversion. Avoidance of this pathway appears to be critical for preserving cyt P460 activity in the periplasmic space of AOB, which necessarily includes NO as an obligate nitrification intermediate. Eyring analyses of the 6c-to-5c $\{FeNO\}^7$ conversion were compared to gain insight into how the Lys–heme cross-link increases this activation barrier. Compared with the WT protein pathways, the NO-independent pathway of the cross-link deficient variant has a higher activation entropy. We interpret this observation as evidence that the Lys–heme cross-link confers rigidity to the pocket surrounding the axial His in the WT and propose that this rigidity decreases the number of possible His dissociation pathways. We contend that in addition to obviation of NO-dependent His dissociation, another role for the Lys–heme cross-link is protective: it disfavors 6c-to-5c $\{FeNO\}^7$ conversion and consequent inactivation of cyt P460.

Experimental

General considerations.

Milli-Q water (18.2 MΩ; Millipore) was used in all preparations of buffers and solutions. 1-(Hydroxyl-NNO-azoxy)-L-proline, disodium salt (Proli-NONOate) and disodium diazen-1-ium-1,2,2 triolate ($Na_2N_2O_3$, Angeli's salt) were purchased from Cayman Chemicals. Stock solutions of Proli-NONOate and $Na_2N_2O_3$ were prepared as described previously.[11] NH_2OH•HCl was purchased from Sigma-Aldrich. All other chemicals were purchased from VWR International and used as obtained. All reactions were prepared inside an MBraun Labstar glovebox under a N_2 atmosphere. All buffers were degassed with 3 cycles of vacuum for 20 min followed by sparging with N_2 for 20 min. Aliquots of protein were equilibrated in the glovebox for 2 h before the experiments. UV/vis absorption spectra were obtained using either a scanning Cary 60 UV/vis spectrometer or an Ocean Optics 2000+ high-resolution diode array spectrometer coupled to a KinTek SF-2004 stopped-flow apparatus. UV/vis scans using the Cary 60 UV/vis spectrometer spanned 200–800 nm with scan rates of 80 nm/s. Temperatures were controlled using a Peltier accessory. The Ocean Optics spectrometer spanned a usable range of 200–500 nm. The optical flow cell was 0.5 cm with a 3 ms mixing dead time. Before the experiments, the stopped-flow syringes were flushed with sodium dithionite ($Na_2S_2O_4$) for deoxygenation. The lines were then washed with deoxygenated buffer to rinse out the remaining $Na_2S_2O_4$. Temperatures were controlled by using a water jacket hooked to a recirculating water

bath. Kinetics data were fit using v6.37 of the IgorPro software package (Wavemetrics).

Protein expression and purification.

WT *N. europaea* cyt P460 was purified and expressed as previously described.[11] An expression system for K70Y cyt P460 was constructed via site-directed mutagenesis of the pET-22b+ vector bearing the gene for WT cyt P460. The K70Y expression plasmid was co-transformed with a pEC86 plasmid bearing the cyt c maturation genes ccmABCDFGH[18] (provided by H. B. Gray) into *Escherichia coli* strain BL21(DE3). A single colony was then used to inoculate a 3 mL starter culture of lysogeny broth supplemented with 100 μg mL^{-1} ampicillin and chloramphenicol. The starter culture was shaken at 200 rpm at 37 °C for 6 h. Then, 1.5 mL of starter culture was used to inoculate two 4 L Erlenmeyer flasks containing 1.5 L of Terrific Broth medium. The cells were grown with shaking at 200 rpm at 30 °C to an optical density at 600 nm of 0.7 ± 0.1. The temperature was then decreased to 20 °C, and protein expression was induced by adding isopropyl β-D-1-thiogalactopyranoside to a final concentration of 0.4 mM. The cells were harvested via centrifugation as a pink pellet after 24 h, resuspended in 20 mM Tris containing 150 mM NaCl and 0.01% Triton X (pH 8.0), and lysed via sonication. The pink soluble lysate fraction was separated from cellular debris via centrifugation for 45 min at 35,000 × *g*. The soluble pink lysate was purified with fast protein liquid chromatography as previously described for WT cyt P460.[11]

Reactions of WT cyt P460 to form {FeNO}^{7} species.

{FeNO}^{7} species were generated by either treating Fe^{III} cyt P460 with HNO generated by $Na_2N_2O_3$ or treating Fe^{II} cyt P460 with NO generated by Proli-NONOate. Fe^{III} cyt P460 (15 μM) in 2 mL of deoxygenated 200 mM 4-(2-hydroxyethyl)-1-piperazine-ethanesulphonic acid (HEPES; pH 8.0) buffer was prepared in a septum-sealed anaerobic cuvette in the glovebox. The reactions were initiated by adding the HNO donor $Na_2N_2O_3$ via gas-tight syringe (Hamilton) through the cuvette septum to a final concentration of 100 μM. The 6c-to-5c {FeNO}^{7} conversion was monitored using the full spectrum (200-800 nm) Cary 60 UV/vis spectrometer with scans at 0.5 min intervals from 0 to 10 min, 1 min intervals from 10 to 20 min, and 2 min intervals from 20 to 40 min and the decay trace was monitored at 452 nm. Alternatively, Fe^{III} cyt P460 (10 μM) in 2 mL of deoxygenated 200 mM HEPES buffer (pH 8.0) was reduced by treatment with 2 equiv of sodium dithionite ($Na_2S_2O_4$) in a septum-sealed anaerobic cuvette in the glovebox. The formation of the 6c {FeNO}^{7} species was initiated by adding 50 μM Proli-NONOate to generate 100 μM NO and monitored with UV/vis absorption scans as described above.

Reactions of the 6c and 5c {FeNO}^{7} species with NH_2OH or oxidant.

All {FeNO}^{7} samples were prepared in the glovebox as described above. Solid NH_2OH•HCl was equilibrated under a N_2 atmosphere in the glovebox overnight. Then, 1 M NH_2OH•HCl solutions were prepared by dissolving the equilibrated solid

into 1 mL of deoxygenated Milli-Q water. Solid $[Ru(NH_3)_6]Cl_3$ was equilibrated overnight in the glovebox and then dissolved in 1 mL of deoxygenated Milli-Q water to generate a 200 mM stock solution. The 6c $\{FeNO\}^7$ species was generated using HNO from Fe^{III} cyt P460 as described above. After the maximal formation (approximately 2 min) of the 6c $\{FeNO\}^7$ species, the reaction was monitored at 452 nm, NH_2OH•HCl or oxidant to concentrations listed in the figure captions were added via gas-tight syringe. The 5c $\{FeNO\}^7$ species was generated from the reaction of Fe^{III} cyt P460 (10 μM) with 50 μM HNO generated by $Na_2N_2O_3$ in 2 mL of deoxygenated 200 mM HEPES buffer (pH 8.0) in a septum-sealed anaerobic cuvette in the glovebox. The species was incubated in the glovebox for approximately 30 min to effect complete conversion to the 5c form. The reaction between the 5c $\{FeNO\}^7$ species and NH_2OH or oxidant was initiated similarly as described for the 6c $\{FeNO\}^7$ species and monitored at 455 nm. The alternative oxidants dichlorophenolindophenol (DCPIP), phenazine methosulfate (PMS), potassium hexachloroiridate, and potassium ferricyanide were also tested; stocks solutions were prepared as described above.

Kinetic measurements of 6c-to-5c {FeNO}^{7} conversion.

Kinetic studies of the 6c-to-5c$\{FeNO\}^7$ conversion for the WT cyt P460 were monitored by UV/vis absorption spectroscopy. Fe^{II} or Fe^{III} cyt P460 solutions were in a septum-sealed cuvette and reactions were initiated by adding Proli-NONOate or $Na_2N_2O_3$, respectively, via gas-tight syringe. NO and HNO concentrations were varied between 100 and 600 μM by adding appropriate volumes of Proli-NONOate or

$Na_2N_2O_3$ stock solutions. The reaction was monitored at 452 nm at 25 °C. A single-exponential equation was fit to the 452-nm kinetic traces. These fits provided observed rate constants (k_{obs}) at each NO and HNO concentration and were then plotted against these concentrations to evaluate order in either NO or HNO.

The kinetics of K70Y cyt P460 6c-to-5c $\{FeNO\}^7$ conversion with varying HNO or NO concentrations were monitored by UV/vis absorption spectroscopy or stopped-flow UV/vis absorption spectroscopy, respectively. Reactions of Fe^{III} K70Y cyt P460 with varying HNO concentrations were performed as described for the WT cyt P460. Faster reactions of the K70Y variant with NO were monitored using stopped-flow UV/vis absorption spectrophotometry. For stopped-flow experiments Proli-NONOate in 10mM NaOH was used as the NO generator and was shot against Fe^{II} K70Y in 200mM HEPES buffer pH 8.0 with final concentrations after mixing of 10 μM K70Y cyt P460, 50 μM $Na_2S_2O_4$, and varying NO in the range of 100–600 μM. All reactions were monitored at 415 nm at 25 °C. A single- or double-exponential equation was fit to the 415-nm kinetic traces. These fits provided observed rate constants ($k_{obs}=k$[NO]) at each NO concentration. The plots of k_{obs} versus NO concentration were fit with linear regression to obtain the rate constant k. Temperature-dependent kinetic studies were performed for all species as described above while varying the temperature between 15 °C and 35 °C at 5 °C increments. Data was analyzed by non-linear regression also decscribed above. Rate constants were plotted against the inverse of temperature (T) in K. Linear fits to these plots were

used to extract values for activation enthalpy ($\Delta H^{\ddagger}$) and activation entropy ($\Delta S^{\ddagger}$) according to the Eyring[19] equation (eq 1):

$$\ln\frac{k}{T} = \frac{-\Delta H^{\ddagger}}{R}\left(\frac{1}{\mathrm{T}}\right) + \ln\left(\frac{k_B}{h}\right) + \frac{\Delta S^{\ddagger}}{R} \quad (1)$$

where k_B is the Boltzmann constant, h is Planck's constant, and R is the gas constant.

EPR measurements.

Continuous-wave X-band (9.40 GHz) EPR spectra were recorded at the NIH Biomedical Center for Advanced ESR Technology (ACERT) using a Bruker Elexsys-II spectrometer equipped with a liquid He cryostat (Oxford Instruments). All samples were prepared in an anaerobic glovebox with deoxygenated solutions. The protein concentrations used were 0.15 mM in 200 mM HEPES buffer (pH 8.0) with 25% (v/v) glycerol. EPR data were simulated, and spin concentrations were determined with SpinCount.[20]

Fe K-edge X-ray absorption spectroscopy.

Samples for Fe K-edge X-ray absorption spectroscopy (XAS) were prepared in an anaerobic glovebox with 1 mM protein and 25% (v/v) glycerol, loaded into a Delrin sample cell, and sealed with 37 μm Kapton tape. The 5c WT cyt P460 $\{FeNO\}^7$ sample was prepared by allowing 1 mM Fe^{III} P460 to react with 8 mM $Na_2N_2O_3$ for 30 min. The sample was then frozen in liquid N_2 outside of the box. The K70Y cyt P460 5c $\{FeNO\}^7$ sample was prepared in the glovebox by treating 1 mM K70Y cyt P460 with 2 equiv of sodium dithionite and 10 mM Proli-NONOate. The sample was then

frozen outside the glovebox in liquid N_2. The formation of the WT cyt P460 6c $\{FeNO\}^7$ species was first monitored with UV/vis absorption spectroscopy to obtain a time course for maximum accumulation, which occurred within 3 min. In the glovebox, the K70Y cyt P460 6c $\{FeNO\}^7$ species was prepared by treating 1 mM Fe^{III} K70Y cyt P460 with 4 mM $Na_2N_2O_3$ and freezing the mixture outside the glovebox in liquid N_2 within 3 min.

Fe K-edge XAS data including extended X-ray absorption fine structure (EXAFS) data were obtained at the Stanford Synchrotron Lightsource Radiation (SSRL) at the 16-pole, 2 T wiggler beamline 9-3 under ring conditions of 3 GeV and 500 mA. A Si(220) double-crystal monochromator was used for energy selection, and a Rh-coated mirror (set to an energy cutoff of 13 keV) was used for harmonic rejection. Internal energy calibration was performed by assigning the first inflection point of an Fe foil spectrum to 7111.2 eV. Data were collected in fluorescence mode (windowed onto Fe $K\alpha_1$) using a Canberra 100-element Ge moonlight solid-state detector perpendicular to the incident beam. Elastic scatter into the detector was attenuated using a Soller slit with an upstream Mn filter. Data were collected from 6800 to 8000 eV (k = 14 $Å^{-1}$), and 16 scans were obtained for each sample. Multiple spots were collected per sample, although there was no evidence of photodamage. The scans were averaged and processed using the SIXPACK software package. A smooth pre-edge background was removed from each averaged spectrum by fitting a first-order polynomial to the pre-edge region and subtracting this polynomial from the entire spectrum. The post-edge region was fit to a polynomial spline, flattened below

7130 eV, and then subtracted from the entire spectrum. Data were then normalized to a value of 1.0 at 7130 eV. EXAFS data were fit using the OPT module of the EXAFSPAK software package with input scattering paths generated using FEFF7.

Resonance Raman measurements.

Resonance Raman (rR) spectra were obtained using a home-built spectrometer. Samples were prepared in J. Young NMR tubes in the glovebox. Samples were excited using either a SpectraPhysics Stabilite 1800 Ar/Kr mixed-gas laser or a 405 nm diffraction-limed Lepton IV diode laser (Microlaser Systems). Incident laser excitation was passed through Semrock MaxLine laser clean-up filters and focused to a ca. 2mm point using a spherical lens (ThorLabs). Samples were held in a 180º backscattering geometry and continuously spun at room temperature using an NMR tube spinner for power dissipation. Incident laser power at the sample was measured using a ThorLabs digital power meter. Scattered light was collected in a 180º backscattering geometry using a 50 mM Canon F/1.2 FD macro lens and focused through a 10 μm slit into an Princeton Instruments IsoPlane SCT320 spectrograph using an F-matched achromatic doublet lens. Semrock Razoredge long-pass filters were used to remove Rayleigh scattering. Scattered, filtered light was energy dispersed using either 1200 or 2400 g/mm gratings onto a Pixis 100B eXcelon digital CCD held thermoelectrically at –60 ºC. Data were recorded and processed using the Lightfield software package (Princeton Instruments). Acetaminophen was used as a Raman shift calibrant.

REFERENCES

1. Whittaker, M., Bergmann, D., Arciero, D. & Hooper, A. B. Electron transfer during the oxidation of ammonia by the chemolithotrophic bacterium *Nitrosomonas europaea*. *Biochim. Biophys. Acta* **1459,** 346–355 (2000).
2. Caranto, J. D. & Lancaster, K. M. Nitric oxide is an obligate bacterial nitrification intermediate produced by hydroxylamine oxidoreductase. *Proc. Natl. Acad. Sci.* 201704504 (2017). doi:10.1073/pnas.1704504114
3. Cedervall, P., Hooper, A. B. & Wilmot, C. M. Structural studies of hydroxylamine oxidoreductase reveal a unique heme cofactor and a previously unidentified interaction partner. *Biochemistry* **52,** 6211–6218 (2013).
4. Arciero, D. M., Golombek, A., Hendrich, M. P. & Hooper, A. B. Correlation of optical and EPR signals with the P460 heme of hydroxylamine oxidoreductase from Nitrosomonas europaea. *Biochemistry* **37,** 523–529 (1998).
5. Zahn, J. A., Duncan, C. & DiSpirito, A. A. Oxidation of hydroxylamine by cytochrome P-460 of the obligate methylotroph Methylococcus capsulatus Bath. *J. Bacteriol.* **176,** 5879–5887 (1994).
6. Maalcke, W. J. *et al.* Structural basis of biological no generation by octaheme oxidoreductases. *J. Biol. Chem.* **289,** 1228–1242 (2014).
7. Kartal, B. *et al.* Molecular mechanism of anaerobic ammonium oxidation. *Nature* **479,** 127–130 (2011).
8. Maalcke, W. J. *et al.* Characterization of anammox hydrazine dehydrogenase, a Key -producing enzyme in the global nitrogen cycle. *J. Biol. Chem.* **291,** 17077–17092 (2016).
9. Pearson, A. R. *et al.* The crystal structure of cytochrome P460 of Nitrosomonas europaea reveals a novel cytochrome fold and heme - Protein cross-link. *Biochemistry* **46,** 8340–8349 (2007).
10. Andersson, K. K., Kent, T. A. & Lipscomb, J. D. Mossbauer, EPR, and optical studies of the P-460 center of hydroxylamine oxidoreductase from Nitrosomonas. A ferrous heme with an unusually large quadrupole splitting. *J. Biol. Chem.* **259,** 6833–6840 (1984).
11. Numata, M., Saito, T., Yamazaki, T., Fukumori, Y. & Yamanaka, T. Cytochrome P-460 of Nitrosomonas europaea: Further purification and further characterization. *J. Biochem.* **108,** 1016–1021 (1990).
12. Caranto, J. D., Vilbert, A. C. & Lancaster, K. M. Nitrosomonas europaea cytochrome P460 is a direct link between nitrification and nitrous oxide emission. (2016). doi:10.1073/pnas.1611051113
13. Enemark, J. H. & Feltham, R. D. Principles of structure, bonding, and reactivity for metal nitrosyl complexes. *Coord. Chem. Rev.* **13,** 339–406 (1974).
14. Klotz, M. G. & Stein, L. Y. Nitrifier genomics and evolution of the nitrogen cycle. *FEMS Microbiol. Lett.* **278,** 146–156 (2008).
15. Hughes, M. N. Relationships between nitric oxide, nitroxyl ion, nitrosonium cation and peroxynitrite. *Biochim. Biophys. Acta - Bioenerg.* **1411,** 263–272

(1999).
16. Fernández, M. L., Estrin, D. A. & Bari, S. E. Theoretical insight into the hydroxylamine oxidoreductase mechanism. *J. Inorg. Biochem.* **102,** 1523–1530 (2008).
17. Berto, T. C., Praneeth, V. K. K., Goodrich, L. E. & Lehnert, N. Iron-porphyrin NO complexes with covalently attached N-donor ligands: Formation of a stable six-coordinate species in solution. *J. Am. Chem. Soc.* **131,** 17116–17126 (2009).
18. Hahn, J. E. *et al.* Observation of an electric quadrupole transition in the X-ray absorption spectrum of a Cu(II) complex. *Chem. Phys. Lett.* **88,** 595–598 (1982).
19. Wyllie, G. R. A. & Scheidt, W. R. Solid-State Structures of Metalloporphyrin NO x Compounds. *Chem. Rev.* **102,** 1067–1090 (2002).
20. Traylor, T. G. & Sharma, V. S. Why nitric oxide? *Biochemistry* **31,** 2847–2849 (1992).
21. Yu, A. E., Hu, S., Spiro, T. G. & Burstyn, J. N. Resonance Raman Spectroscopy of Soluble Guanylyl Cyclase Reveals Displacement of Distal and Proximal Heme Ligands by NO. *J. Am. Chem. Soc.* **116,** 4117–4118 (1994).
22. Derbyshire, E. R. & Marletta, M. A. Structure and Regulation of Soluble Guanylate Cyclase. *Annu. Rev. Biochem.* **81,** 533–559 (2012).
23. Deinum, G., Stone, J. R., Babcock, G. T. & Marletta, M. A. Binding of nitric oxide and carbon monoxide to soluble guanylate cyclase as observed with Resonance raman spectroscopy. *Biochemistry* **35,** 1540–7 (1996).
24. Guo, Y. *et al.* Regulation of nitric oxide signaling by formation of a distal receptor-ligand complex. *Nat. Chem. Biol.* **13,** 1216–1221 (2017).
25. Rao, M., Herzik, M. A., Iavarone, A. T. & Marletta, M. A. Nitric Oxide-Induced Conformational Changes Govern H-NOX and Histidine Kinase Interaction and Regulation in Shewanella oneidensis. *Biochemistry* **56,** 1274–1284 (2017).
26. Andersson, K. K., Babcock, G. T. & Hooper, A. B. P460 of hydroxylamine oxidoreductase of Nitrosomonas europaea: Soret resonance Raman evidence for a novel heme-like structure. *Biochem. Biophys. Res. Commun.* **174,** 358–363 (1991).
27. Andrew, C. R., Green, E. L., Lawson, D. M. & Eady, R. R. Resonance Raman studies of cytochrome c??? support the binding of NO and CO to opposite sides of the heme: Implications for ligand discrimination in heme-based sensors. *Biochemistry* **40,** 4115–4122 (2001).
28. Strekas, T. C. & Spiro, T. G. Resonance-Raman evidence for anomalous heme structures in cytochrome c′ from Rhodopseudomonas palustris. *BBA - Protein Struct.* **351,** 237–245 (1974).
29. Choi, S. & Spiro, T. G. Out-of-Plane Deformation Modes in the Resonance Raman Spectra of Metalloporphyrins and Heme Proteins. *J. Am. Chem. Soc.* **105,** 3683–3692 (1983).
30. Spiro, T. G. Resonance raman spectroscopic studies of heme proteins. *Biochim.*

Biophys. Acta - Rev. Bioenerg. **416,** 169–189 (1975).
31. Wu, G., Liu, W., Berka, V. & Tsai, A. L. The selectivity of vibrio cholerae h-nox for gaseous ligands follows the 'sliding Scale Rule' Hypothesis. Ligand interactions with both ferrous and ferric Vc H-NOX. *Biochemistry* **52,** 9432–9446 (2013).
32. Tsai, A. L. *et al.* Is nostoc H-NOX a no sensor or redox switch? *Biochemistry* **49,** 6587–6599 (2010).
33. Evans, D. H. One-Electron and Two-Electron Transfers in Electrochemistry and Homogeneous Solution Reactions. *Chem. Rev.* **108,** 2113–2144 (2008).
34. Attia, A. A. A. & Silaghi-Dumitrescu, R. Computational investigation of the initial two-electron, two-proton steps in the reaction mechanism of hydroxylamine oxidoreductase. *J. Phys. Chem. B* **118,** 12140–12145 (2014).
35. McQuarters, A. B., Wirgau, N. E. & Lehnert, N. Model complexes of key intermediates in fungal cytochrome P450 nitric oxide reductase (P450nor). *Curr. Opin. Chem. Biol.* **19,** 82–89 (2014).
36. Liptak, M. D., Wen, X. & Bren, K. L. NMR and DFT investigation of heme ruffling: Functional implications for cytochrome c. *J. Am. Chem. Soc.* **132,** 9753–9763 (2010).
37. Zhao, Y., Brandish, P., Ballou, D. & Marletta, M. A Molecular Basis for Nitric Oxide Sensing by Soluble Guanylate Cyclase. *Proc. Natl. Acad. Sci. U. S. A.* **96,** 14753–14758 (1999).
38. Andrew, C. R., George, S. J., Lawson, D. M. & Eady, R. R. Six- to five-coordinate heme-nitrosyl conversion in cytochrome c??? and its relevance to guanylate cyclase. *Biochemistry* **41,** 2353–2360 (2002).
39. Kruglik, S. G. *et al.* Molecular basis for nitric oxide dynamics and affinity with Alcaligenes xylosoxidans cytochrome c′. *J. Biol. Chem.* **282,** 5053–5062 (2007).
40. Vilbert, A. C., Caranto, J. D. & Lancaster, K. M. Influences of the heme-lysine crosslink in cytochrome P460 over redox catalysis and nitric oxide sensitivity. *Chem. Sci.* **00,** 1–12 (2018).
41. Jiang, Y. *et al.* Light-Induced N2O Production from a Non-heme Iron–Nitrosyl Dimer. *J. Am. Chem. Soc.* **136,** 12524–12527 (2014).
42. Averill, B. A. Dissimilatory Nitrite and Nitric Oxide Reductases. *Chem. Rev.* **96,** 2951–2964 (1996).
43. Wasser, I. M., de Vries, S., Moënne-Loccoz, P., Schröder, I. & Karlin, K. D. Nitric Oxide in Biological Denitrification: Fe/Cu Metalloenzyme and Metal Complex NOx Redox Chemistry. *Chem. Rev.* **102,** 1201–1234 (2002).
44. Lawson, D. M., Stevenson, C. E. M., Andrew, C. R., George, S. J. & Eady, R. R. A two-faced molecule offers NO explanation: the proximal binding of nitric oxide to haem. *Biochem. Soc. Trans.* **31,** 553–7 (2003).
45. Lawson, D. M., Stevenson, C. E., Andrew, C. R. & Eady, R. R. Unprecedented proximal binding of nitric oxide to heme: implications for guanylate cyclase. *EMBO J.* **19,** 5661–71 (2000).

46. Pixton, D. A. *et al.* Activation parameters for heme-NO binding in alcaligenes xylosoxidans cytochrome c': The putative dinitrosyl intermediate forms via a dissociative mechanism. *J. Am. Chem. Soc.* **131,** 4846–4853 (2009).
47. Irvine, J. C. *et al.* Nitroxyl (HNO): the Cinderella of the nitric oxide story. *Trends Pharmacol. Sci.* **29,** 601–608 (2008).

APPENDIX

Plasmid name: K70Y cytochrome P460 n.e

Parent plasmid: pET22 B^+ 6,020bp (with insert, 5,493bps without insert) insert is 527bps
Antibiotic resistance: Ampicillin
Expression inducer (if applicable): IPGT

Description: Variant K70Y from codon optimized Cytochrome P460 from *Nitrosomonas europeae* inserted into pET22B^+. Parent plasmid includes His-tag and pelB leader sequence

Cloning/mutagenesis primers:
5'-ATA AAC CGT CAC GGT ACC ATC ACG G-3' Reverse K70Y
5'-GAA CTG GTC AGT GTG GGT GAC C-3' Forward K70X
Around the Horn mutagenesis

Sequencing primers: T7 promoter
References: N/A
Sequence: K70Y

Sequence results:
>91_2261724__092.ab1
GAGAATTCCCTCNGAATATTTTGTTTACTTTAAGAAGGAGATATACATATGAAATACCTGC
TGCCCATTGCTGCTGCTGGTCTGCTGCTCCTCGCTGCCCAGCCGGCGATGGCCATGGCTGG
CGTCGCGGAATTTAACGATAAAGGTGAACTGCTGCTGCCGAAAAATTATCGTGAATGGGT
CATGGTGGGCACCCAGGTTACGCCGAACGAACTGAATGATGGTAAAGCTCCGTTTACCGA
AATTCGCACGGTTTATGTCGACCCGGAAAGCTACGCCCATTGGAAGAAAACCGGCGAATT
CCGTGATGGTACCGTGACGGTTTATGAACTGGTCAGTGTGGGTGACCGTAAAGGTCCGGGT
TCCGGTAACGGTTATTTTATGGGCGATTACATTGGTCTGGAAGCGAGCGTGAAAGACTCTC
AGCGTTTCGCCAACGAACCGGGTAATTGGGCATTTTATATCTTCTACGTTCCGGATACCCC
GCTGGTCGCGGCAGCAAAAAACCTGCCGACGGCCGAATGCGCTGCGTGTCACAAAGAAAA
TGCAAAAACCGACATGGTGTTTACGCAATTCTACCCGGTTCTGCGCGCCGCAAAAGCTACC
GGCGAAAGCGGTGTGGTTGCGCCGAAACTCGAGCACCACCACCACCACCACTGAGATCCG
GCTGCTAACAAAGCCCGAAAGGAAGCTGAGTTGGCTGCTGCCACCGCTGAGCAATAACTA
NCATAACCCCTTGGGGCCTCTAAACGGGTCTTGAGGGGTTTTTTGCTGAAAAGGAGGAACT
ATATCCCGGATTGGCGAATTGGAACGCGCCCTGTAGCGGGCGCATTAANCGCGGCGGGTG
TGGTGNTTACGCGCATCGTGANCGCTACANTGNCAGCGCCCTTACNGCCNCTCCTTTCCCT
TTNTTCCCTTCCNTTCTCGCCNCGTTNNGCCGNTTTTNCCCGTNAAGNTNCTAAATCGGGGG
CTCCCTTNAGGGGTCCNAATTTAGNGCTTTNNNGGCNCCTCNAACCCCAAAAACTTNNNTA
GGTNAAGTTTCANTAANGGNCATCCCCNNGANAAAGGTTTTTCCCCTTGNANNTTGGANN
CANNTTTTTATAGGGGANTTTNTTCCAANTGGAAAACNNNACCCTANNTCGNNCNTTTTTT
GTTTTAAAGAATTTNCCNTTTNNGCNTTGGTTAAAATNNNNTNTTNNAANTTACCNAATTT
ANANANTAACTTNNTTTNNGGCTCTTCGGGAANGNCNGACCCNTTTTTTTTAAAANNTNAA
TTTCCCCTANAAAAN

Translation Results:

Met A G V A E F N D K G E L L L P K N Y R E W V **Met** V G T Q V T P N E L N D G K A P F T E I R T V Y V D P E S Y A H W K K T G E F R D G T V T V Y E L V S V G D R K G P G S G N G Y F **Met** G D Y I G L E A S V K D S Q R F A N E P G N W A F Y I F Y V P D T P L V A A A K N L P T A E C A A C H K E N A K T D **Met** V F T Q F Y P V L R A A K A T G E S G V V A P K L E H H H H H H **Stop**

CytP460: T V T V K E L V S V G D R K G
K70Y: T V T V Y E L V S V G D R K G

pEt22-b MCS region

ggcgtagaggatcgagatctcgatcccgcgaaattaatacgactcactataggggaattgtgagcggataacaattcccctc
tagaaataattttgtttaactttaagaaggagatatacat**atg**aaatacctgctgccgaccgctgctgctggtctgctgctcctc
gctgcccagccggcgatggcc*atg*gatatcggaattaattcggatccgaattcgagctccgtcgacaagcttgcggccgca
ctcgagcaccaccaccaccaccactgagatccggctgctaacaaagcccgaaaggaagctgagttggctgctgccaccg
ctgagcaataactagcataaccccttggggcctctaaacgggtcttgaggggttttttgctgaaaggaggaactatatccgga
t

Appendix 3.2. Linear regression analysis of the first order reaction in NO for Lys70Tyr cyt P460 His dissociation. Note Linear regression analysis done by excel rather than igor as in paper. Slope and intercept from excel and igor do not match but t-stat will always remain the same.

Regression Statistics	
Multiple R	0.87
R Square	0.76
Adjusted R Square	0.75
Standard Error	0.06
Observations	25.00

ANOVA

	df	*SS*	*MS*	*F*	*Significance F*
Regression	1	0.24	0.24	73.51	1.28E-08
Residual	23	0.08	0.00		
Total	24	0.32			

	Coefficients	*Standard Error*	*t Stat*	*P-value*	*Lower 95%*	*Upper 95%*	*Lower 90.0%*	*Upper 90.0%*
Intercept	0.23	0.02	9.84	1.03E-09	0.18	0.28	0.19	0.27
X Variable 1	515.34	60.11	8.57	1.28E-08	391.01	639.68	412.33	618.36

H_0: null hypothesis β_1 (slope) = 0
H_1: alternative hypothesis β_1 (slope) $\neq$ 0 at a significant value (α) of 0.05

Reject null hypothesis that slope is equal to zero since the p-value (1.028×10^{-9}) is less than the significant value of 0.05.

CHAPTER 4

SIGNIFICANT RUFFLING OF THE CYT P460 COFACTOR IS NOT ENTIRELY ATTRIBUTABLE TO THE HEME-LYS CROSS-LINK

Introduction

Heme proteins carry out diverse biological functions. It is believed that macrocyle structural distortions away from planarity contribute to the functional versatility of these ubiquitous cofactors. The biological functions of heme proteins span O_2 transport (hemoglobin) and storage (myoglobin), electron transfer (cytochromes), and oxidative reactions catalyzed by peroxidases, catalases and cytochrome P450. Out-of-plane (OOP) distortions are conserved within each functionally related class of protein.[1] The most common OOP distortions in biology are ruffling (B_{1u}), saddling (B_{2u}) and doming (A_{2u}), where each distortion resembles the corresponding lowest-frequency of these symmetry types within the D_{4h} point group (Fig.1).[2,3]

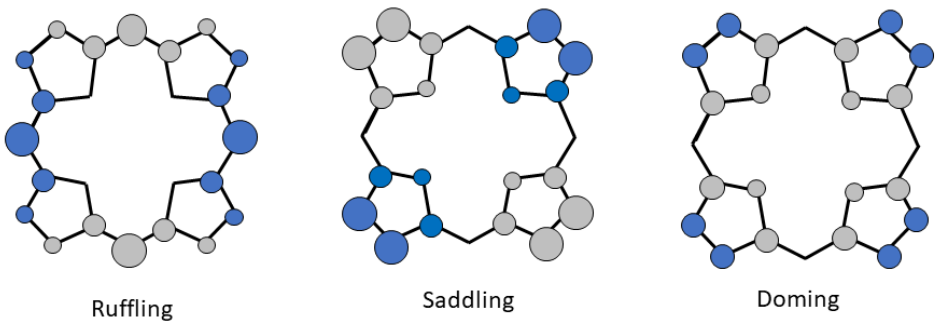

Figure 4.41. Representative deformation modes of the 3 major OOP distortions seen in heme proteins. Grey circles represent the atoms above the porphyrin plane and blue circles represent atoms below the porphyrin plan. Figure adapted from reference 3.

Ruffling is an OOP distortion where the *meso*-carbon atoms alternate up and down from the mean porphyrin plane (Fig. 1).[3] This type of distortion is commonly found in cyt *c* electron transfer proteins, enzyme-substrate complexes of heme oxygenases, and NO-carrier proteins such as nitrophorins and heme nitric oxide/ oxygen binding (H-NOX) proteins.[4] Saddling is the prominent distortion in peroxidases, and doming is typically found in heme proteins that function in oxygen storage or transport like myoglobin and hemoglobin, respectfully (Fig. 1).[2] Both saddling and doming have been implicated in spin state changes, whereas ruffling has been proposed to modulate heme reduction potential.[4]

The degree of OOP distortion is quantified by using the normal-coordinate structural decomposition (NSD) procedure. This process sets a scale where a 1-Å deformation is equal to some degree of distortion from planarity. For example, a 1-Å ruffling deformation is consistent with a dihedral angle of 22.0° between the planes of the pyrroles of the porphyrin ring.[5] Whereas, a 1-Å saddling deformation lowers the tilt angle of the N(pyrrole)-Fe-N(pyrrole) by about 4.2° from 180°.[1] Analysis of the heme deformation by NSD of cyt P460 *N. europaea* (Fig. 2b) revealed that the heme is composed of equal contributions from saddled (0.78 Å) and ruffled (-0.76 Å) deformations.[6] The crystal structure of cyt P460 from *Nitrosomonas* sp. AL212[7] also exhibited equal contribution of both saddling and ruffling. This differs from the P460 cofactor in HAO (Fig. 2a) which exhibits almost no contribution of saddling deformation (0.14 Å) but displays a large degree of ruffling (2.36 Å).[8] It is proposed

that the large degree of ruffling conserved by the P460 cofactor in cytochrome P460 directs its reactivity.

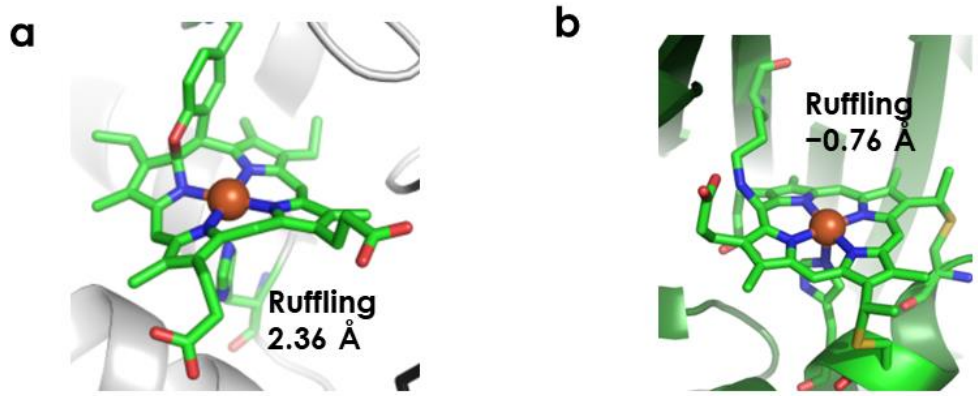

Figure 4.42. Fe^{III} P460 cofactors HAO (PDB: 4FAS, resolution 2.1 Å) (a) and cyt P460 (PDB: 2JE3, resolution 1.8 Å) (b) with their corresponding NSD ruffling.

The previous chapter established the importance of the heme-Lys cross-link in avoiding a 5-coordinate $\{FeNO\}^7$ sink in the cyt P460 catalytic cycle.[9] In addition to preserving 6-coordination of $\{FeNO\}^7$, removal of the cross-link has an additional, profound effect: cross-link deficient cyt P460 lacks NH_2OH oxidase reactivity. Monitoring the reaction of 10 μM Lys70Tyr variant (K70Y) with 15 mM NH_2OH and with 100 μM DCPIP by UV/vis absorption spectroscopy (Fig. 3a) showed no shift in the Soret maximum as seen with wild-type (WT) cyt P460. Monitoring the consumption of oxidant at 605 nm is more indicative of the lack of reactivity (Fig. 3b). In either the presence or absence of protein, the rate of consumption of oxidant remains the same. Therefore, the presence of the cross-link necessarily impacts redox reactivity. One hypothesis for the difference in reactivity between cyt P460 and the

cross-link deficient variants relates to the large degree of distortion (ruffling) that cyt P460 exhibits.

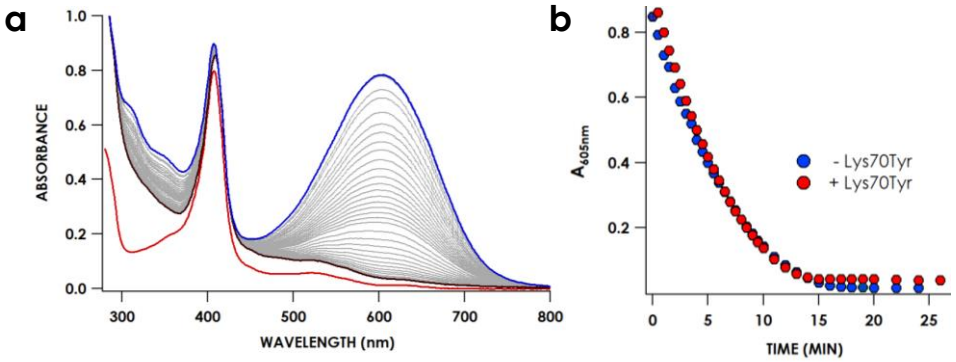

Figure 4.43. UV-vis absorption spectrum (a) of 10 μM K70Y with 15 mM NH_2OH and the addition of 100 μM DCPIP in 200 mM HEPES buffer pH 8.0 and (b) the corresponding single wavelength time course following the consumption of DCPIP with conditions of 100 μM DCPIP and 15 mM NH_2OH either in the presence or absence of 10 μM K70Y.

Ruffling has been proposed to influence heme reactivity in many ways, with a significant effect manifesting as modulation of reduction potential.[10] Another effect of ruffling has been associated with lower O_2 affinity in H-NOX proteins. A mutation in the heme site of an H-NOX protein degenerated a more planar heme and resulted in a lower dissociation constant for O_2 than the WT.[11] Ruffling has profound effects over the function of nitrophorins, which are NO carrying proteins found in the saliva of the blood sucking insects such as *Rhodnius prolixus*.[12] Nitrophorins are unique proteins in that they form a stable heme $\{FeNO\}^6$ units. Ruffling is thought to play a role in dictating the properties of these $\{FeNO\}^6$ units, in particular via influence over NO binding geometry and stability of $\{FeNO\}^6$ to reductive nitrosylation.[10] The stability of the $\{FeNO\}^6$ complex in nitrophorins has been proposed to be due to the large degree of ruffling which stabilizes the Fe^{III} oxidation state over the Fe^{II}.[13]

One possibility for the lack of redox reactivity in the cross-link deficient variants is that the heme-Lys cross-link locks the heme in a ruffled geometry and that removal of the cross-link generates a more planar heme. The majority of investigation on heme ruffling has been carried out via X-ray crystallography, NMR, EPR and vibrational spectroscopy[14,15] in tandem with density functional calculations (DFT).[4] Following suit, investigation of the degree of heme ruffling in the cross-link deficient cyt P460 variants is described below.

Cross-link deficient variants exhibit characteristics of cytochrome c′ proteins

Cytochrome (cyt) *c′* proteins comprise a class of periplasmic, *c*-type heme proteins with axial His ligation. These proteins are found in numerous bacterial species including sulfur oxidizing, photosynthetic, denitrifying, methanotropic and nitrogen-fixing bacteria, however, their function remains unknown.[16] Elmore et al[17] established that there are two families of cyt *c′* proteins; one that have a secondary structure that is predominately α-helical termed cyt *c′*-α and the other that is predominately β-sheet in structure (cyt *c′*-β). While there are many protein structures available for cyt *c′*-α proteins, cyt *c′*-β proteins have yet to be crystalized. The two families of cyt *c′* proteins also differ in their respective Fe^{II}/Fe^{III} reduction potentials. Cyt *c′*-α proteins have reduction potentials between −10 mV to 200 mV[18] whereas a cyt *c′*-β from *Methylococcus capsulatus* Bath was found to have a much lower reduction potential of −200 mV.[19] Protein sequence similarity[19] between *N. europaea* cyt P460, *M. capsulatus* Bath cyt P460 and cyt *c′*-β suggest a common ancestry

between cyts *c′*-β and cyts P460. These two proteins only differ from one another in that cyt *c′*-β lacks the third additional attachment to the heme center.[17,19]

Two cross-link deficient cyt P460 variants were studied, one with a tyrosine in the lysine position and the other with an alanine. The K70A variant was generated to remove any possible interaction between an amino acid sidechain at position 70 and the heme. Both cross-link deficient variants are red proteins exhibitng large blue-shifts in their Soret absorption maxima relative to WT cyt P460. These maxima are at 407 nm and 403 nm in K70Y and K70A, respectively. Both K70Y and K70A exhibit the same Q band region with a broad band at 501 nm accompanied by shoulders at 535 nm and a sharp band at 635 nm (Fig 4a). Fe^{II} K70Y cyt P460 exhibits a split Soret with a λ_{max} located at 421 nm with a shoulder at 433 nm and sharpening of the Q bands at 524 nm and 553 nm (Fig 4b). Interestingly, Fe^{II} K70A does not exhibit a split Soret instead it produces a λ_{max} at 431 nm with a broader Q band region with a maximum at 553 nm and a shoulder at 579 nm (Fig 4b). K70Y and K70A both show similarities in their UV/vis absorption spectra to other cyt *c′* proteins. In particular the split Soret in Fe^{II} K70Y is a hallmark of other cyt *c′* proteins and has been attributed to a nondegenerate Soret electronic transition involving what is formulated as a doubly-

degenerate e_g set of orbitals invoked in Gouterman's four-orbital model for porphryinoid electronic structure.[20,21]

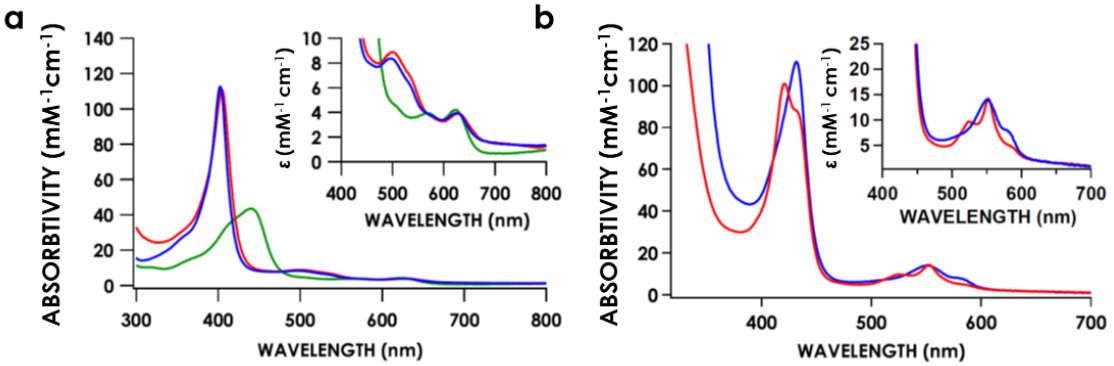

Figure 4.44. UV/vis absorption spectra (a) of Fe^{III}-OH_2 cyt P460 (green trace), Fe^{III} K70Y (red trace) and Fe^{III} K70A (blue trace) and (a) of Fe^{II} K70Y and K70A. The inset magnifies the Q-bands. Electron Paramagnetic Resonance spectra (b) of Fe^{III}-OH_2 cyt P460 (green trace), Fe^{III} K70Y (red trace) and Fe^{III} K70A (blue trace).

To confirm that modulation of the amino acid at position 70 between the propionate groups did not drastically alter the heme site, the resting Fe^{III} states of the two proteins were spectroscopically characterized. Interestingly, the identity of the amino acid in the position between the propionate groups is important in defining the Fe^{III} spin state of the heme center. The EPR spectrum of Fe^{III} K70Y cyt P460 exhibited an axial ($^{E}/_{D}$ = 0.00) high spin $S = {}^{5}/_{2}$ signal with *g*-values of 5.78 and 1.98 (Fig. 5). However, the EPR spectrum of Fe^{III} K70A cyt P460 exhibited a low spin (LS) $S = {}^{1}/_{2}$ signal with g values of 2.91, 2.29 and 1.54 (Fig. 5).

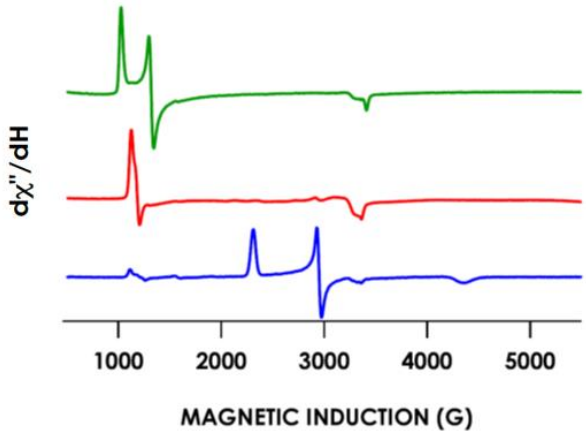

Figure 4.45. Electron Paramagnetic Resonance spectra (b) of Fe^{III}-OH_2 cyt P460 (green trace), Fe^{III} K70Y (red trace) and Fe^{III} K70A (blue trace). EPR measurements were collected at 12 K and 6 μW microwave power.

Since the above examination of the spin state was probed by EPR at 12 K; investigation on whether K70A exhibited a spin crossover state was investigated by room temperature resonance Raman (rR) spectroscopy (Fig. 6). The rR spectra were obtained via excitation near the Soret maxima of Fe^{III} K70Y and K70A (λ_{ex} = 405.0 nm) (Fig. 6). The rR spectrum of Fe^{III} K70Y exhibited an oxidation state marker band (ν_4) at 1370 cm^{-1} but a spin-state marker band (ν_3) at 1501 cm^{-1}. As stated in Chapter 3, typically a spin state marker band greater than 1500 cm^{-1} indicates a LS 6-coordinate heme. However, a Fe^{III} cyt *c*′-α protein was also identified to have a spin state marker band at approximately 1500 cm^{1} similar to K70Y. The Fe^{III} cyt *c*′-α exhibited an EPR spectrum consistent with a high spin $S = {}^5/_2$ and according to its crystal structure was 5-coordinate.[22] Therefore, similar to the Fe^{III} cyt *c*′-α's corresponding EPR and rR data, K70Y also exhibits this ambiguity in spin state marker band as seen previously for high spin c-type hemes.[21]

The rR spectrum obtained for Fe^{III} K70A cyt P460 exhibited an oxidation state marker band (ν_4) at 1370 cm^{-1}, again typical of Fe^{III} heme protein (Fig 6). However, this variant exhibited two spin-state marker bands (ν_3) of equal intensity at 1486 cm^{-1} and 1506 cm^{-1}, the former more consistent with a high spin (HS) $S = {}^5/_2$ and the latter more consistent with a LS $S = {}^1/_2$.[23] The combination of both spin states at room temperature indicates the presence of either a spin admixture or spin crossover state in the K70A variant. This has been seen previously with other heme proteins[18] in particular with other cyt *c′* proteins[18] as well as in nitrophorin.[24] The percentage of spin-mixed character can vary in cyt *c′* proteins from 90% HS and 10% LS in proteobacteria *A. xylosoxidans* to 60% HS and 40% LS in photosynthetic bacteria.[25] The degrees of saddling and/or ruffling deformations have been shown to correlate with the percentage of spin admixtures character,[18,25] where the amount of LS character reflects the degree of Fe displacement in the heme site.[25] Regardless of the cause of the spin admixture character of K70A, removal of the cross-link produces a cyt *c′*-β-like protein where the identity of the amino acid between the propionate groups directs the resting spin state of the heme protein. For the remainder of this chapter direct comparisons will be drawn between WT cyt P460 and K70Y rather than K70A due to the complicating presence of its spin admixture state.

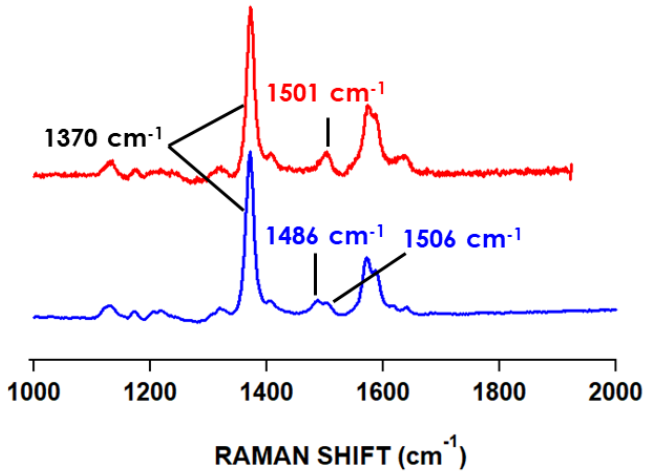

Figure 4.46. The rR spectra obtained via near-resonance excitation with Soret absorption band: λ_{ex} = 405.0 nm (20 mW) for K70Y Fe^{III} (red) and K70A Fe^{III} (blue) the ν(4) and ν(3) are labeled above.

The $Fe^{II/III}$ reduction potentials were also measured for the cross-link deficient variants. As mentioned above, the large degree of ruffling on the heme center has been proposed to modulate reduction potential. Removal of the cross-link therefore should increase the Fe^{III}/Fe^{II} reduction potential couple as compared to the WT cyt P460. The reduction potential of cyt P460 has been measured previously to be −405 mV vs NHE.[26] In the experiments shown below, a potential was applied stepwise beginning from −50 mV to −625 mV vs NHE at 50 mV intervals and were performed in 50 mM phosphate, 150 mM NaCl buffer at pH 8.0. The spectral changes as a function of applied potential are shown below (Fig. 7). Experiments were first performed on WT cyt P460 which confirmed its previously measured reduction potential (−400 mV ± 6 mV vs NHE). The reduction potentials of the $Fe^{II/III}$ couple for K70Y and K70A cyt P460 are −350 ± 5 mV and −290 ± 8 mV, respectively.

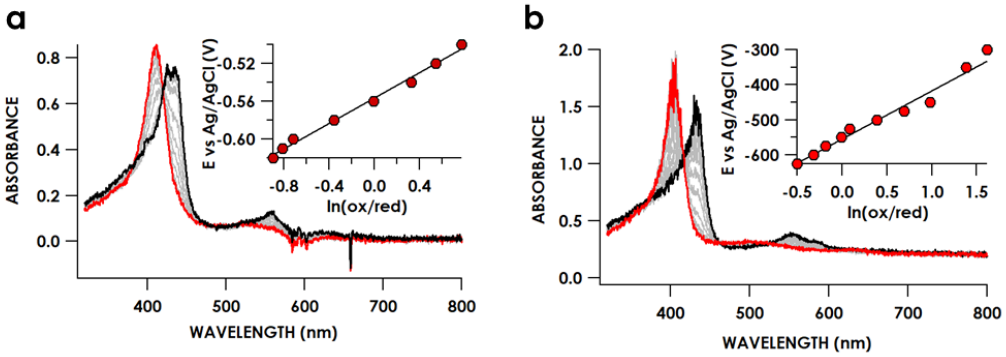

Figure 4.47. UV/vis absortption spectra of K70Y (a) and K70A at pH 8.0 as a function of applied potential. No potenial was applied in the red spectrum and the following spectrums in gray are in increments of −50 mV from −50 mV to −625 mV vs Ag/AgCl. The inset is the Nernst plot of the spectroelectrochemical data.

The heme-Lys Cross-link deficient variant exhibits a rhombic low spin Fe^{III} EPR spectrum

Cyt *c* heme proteins are coordinatively saturated *c*-type hemes that function in electron transfer and exhibit a conserved large degree of ruffling at the heme site.[14] It is proposed that the large degree of ruffling exhibited by cyt *c* proteins aids in the function of electron transfer.[14] LS Fe^{III} *c*-type heme sites (as well as synthetic models) have been extensively characterized by their spectroscopic (EPR, NMR etc)[2,27] profiles to correlate the degree of ruffling by NSD procedure to the spectrum exhibited by the LS Fe^{III} heme site. Therefore, to correlate both the degree of ruffling with

reactivity of the cross-link deficient variants NH_2OH binding experiments were conducted to enforce LS $S = {}^1/_2$ configurations.

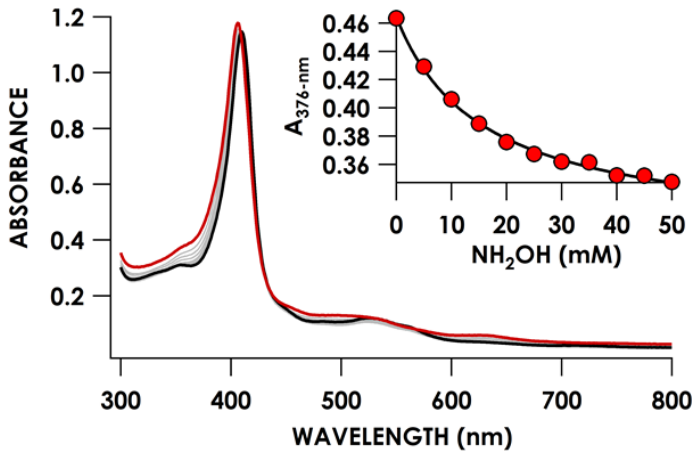

Figure 4.48. NH_2OH titration curve of K70Y monitored by UV/vis absorption spectroscopy. UV-vis traces of 10 µM K70Y titrated against various amounts of NH_2OH in anaerobic 200 mM HEPES, pH 8.0, at room temperature. Inset shows a plot of $A_{376\text{-nm}}$ versus NH_2OH concentration. This was fit to the following hyperbolic equation: $\mathbf{A_{376nm}} = \frac{\Delta \mathbf{A_{414}}[\mathbf{NH_2}OH]_0}{K_d + [\mathbf{NH_2}OH]_0}$.

NH_2OH binding was measured by monitoring the changes in the UV/vis absorption spectrum during NH_2OH titration. Treatment of 10 µM Fe^{III} K70Y cyt P460 with 20 mM NH_2OH results in a shift in the Soret maximum from 407 nm to 411 nm with a concomitant shift in the Q band region to a sharp Q band at 527 nm with a shoulder at 561 nm. The formation of this species was monitored more clearly by analyzing the UV/vis absorption spectrum during the titration of K70Y with NH_2OH (Fig. 8). The resulting series of spectra produced an isobestic point at 409 nm again consistent with the conversion from the Fe^{III} species to the proposed Fe^{III}-NH_2OH adduct. The NH_2OH dissociation constant [$K_{d(NH_2OH)}$] was determined by plotting the

decrease in absorption at 376 nm (A_{376}) against NH_2OH concentration (Fig. 8). Fitting the data to a hyperbolic binding curve resulted in a slightly higher [$K_{d(NH_2OH)}$] of 17 ± 2 mM than determined previously for the WT cyt P460 which was 9 ± 1 mM.

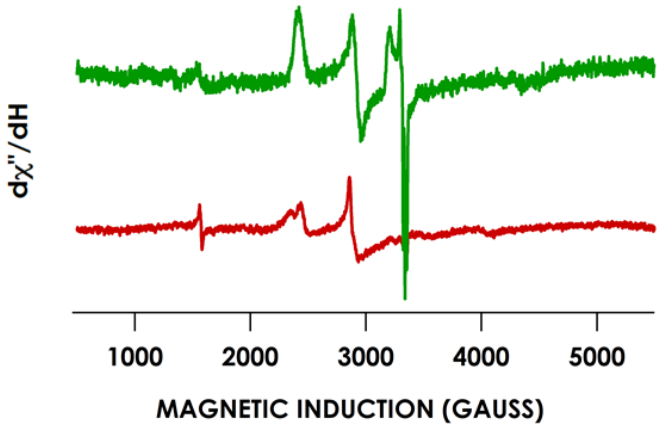

Figure 4.49. Electron Paramagnetic spectra of the NH_2OH adducts of WT cyt P460 (green trace), K70Y (red trace) and K70A (blue trace). Samples were prepared by reacting 150 μM protein with 100 mM NH_2OH in 200 mM HEPES buffer, pH 8.0. The spectra were collected at 12 K with 6 μW microwave power.

The NH_2OH adducts of K70Y were analyzed by EPR and rR spectroscopy. Addition of 100 mM NH_2OH to 150 μM K70Y produced an EPR spectrum consistent with a LS Fe^{III} species similar to Fe^{III}-NH_2OH WT cyt P460 (Fig. 9). However, this species had slightly different g values of 2.85, 2.34 and 1.64. The change in the EPR spectrum upon addition of NH_2OH from HS to LS is consistent with substrate binding to the Fe center. The NH_2OH adduct of K70Y was also analyzed by rR spectroscopy via Soret band excitation at 405 nm (Fig. 10). In the spectrum of Fe^{III}-NH_2OH K70Y, the oxidation state marker band (ν_4) shifts from 1370 cm^{-1} to 1375 cm^{-1} with a shift in the spin state marker band from 1501 to 1506 cm^{-1} consistent with low-spin 6-

coordinate heme. The shift in the oxidation state marker band (ν_4) in K70Y is surprising and consistent with a more reduced Fe center. However, this is inconsistent with the EPR spectrum which indicates a LS $S = {}^1/_2$ system more consistent with a Fe^{III}-NH_2OH adduct.

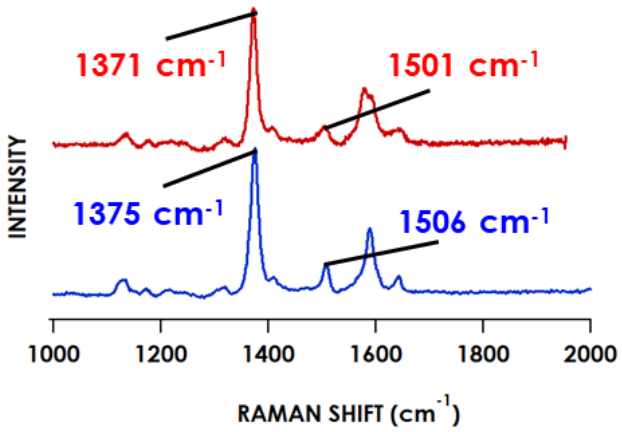

Figure 4.50. The rR spectra obtained via near-resonance excitation with Soret absorption band: λ_{ex} = 405.0 nm (20 mW) for K70Y Fe^{III} (red trace) and Fe^{III}-NH_2OH (blue trace). The porphyrin band markers (ν (4) and ν (3)) are labeled above.

The correlation between the degree of ruffling of a heme and its corresponding LS Fe^{III} EPR spectrum has been extensively discussed.[4,14,27] Previous work has shown that a more rhombic LS EPR spectrum correlates with a more ruffled heme geometry.[28] The EPR spectra of LS heme proteins with the ground state electronic configuration of $(d_{xy})^2$ $(d_{xz}, d_{yz})^3$ can be classified into two groups: either type I with highly anisotropic LS spectra (HALS) or type II, which exhibit rhombic spectra.[4,27] A HALS spectrum is characterized by large g anisotropy with $g_{max} > 3.3$ and small, broad g_{mid} and g_{min}. The g_{min} in most cases is often too weak to resolve from background. This large g_{max} signal is indicative of near-degenerate d_{xz} and d_{yz} orbital manifold (Fig.

11).[27] Type II low-spin Fe^{III} hemes are characterized by a large energy gap between the d_{xz} and d_{yz} orbitals (Fig. 11).[14] Their EPR signals exhibit small g anisotropies with $g_{max} < 3.2$. Therefore, these two types of signals are characterized by either a large axial (Δ) strain (HALS, type I) or a large rhombic (*V*) strain (type II). The degree of axial or rhombic strain can be correlated to the relative ΔE between the d_{xz} and d_{yz}. Depending on the heme site, the strength of the rhombic versus axial field (*V*/ Δ) can produce either a HALS signal with V = 0 due to near-degenerate d_{xz} and d_{yz} or a highly rhombic signal with *V*/Δ = 0.67 and a large energy gap between the d_{xz} and d_{yz}.

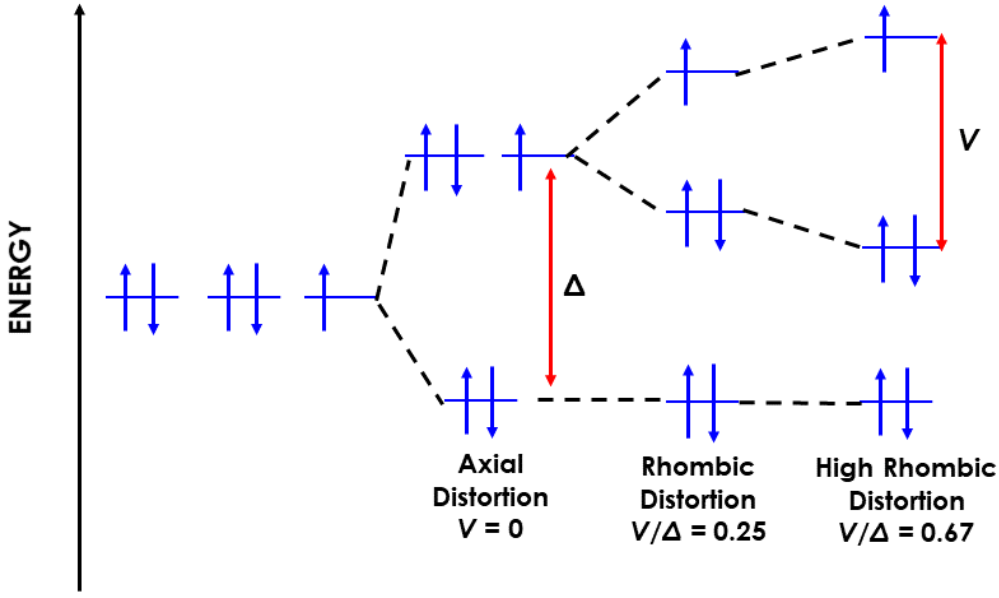

Figure 4.51. Energy diagram of the d-orbital levels for LS Fe^{III} with $(d_{xy})^2$ $(d_{xz}, d_{xz})^3$ electron configuration in reference to the Taylor analysis. The Δ (axial strain) and *V* (rhombic strain) on the system is labeled above. The $\boldsymbol{d_{z^2}}$ and $\boldsymbol{d_{x^2-y^2}}$ orbitals are not pictured, and the figure is adapted from reference 13.

The degree of axial and rhombic strain can be computed by using Taylor's method.[27,29] Through this analysis, the difference in the degree of ruffling between the WT cyt P460 and its cross-link deficient variants can be determined. The rhombicity parameters can be calculated using the g-values obtained from the EPR spectrum.[30] Lubitz et al[28] demonstrated a correlation between the degree of ruffling calculated by NSD procedure via crystal structures of multiple nitrophorin proteins with the degree of rhombicity in the LS Fe^{III} EPR spectrum. Lubitz et al[31] were able to show that an EPR spectrum with more contribution from a HALS signal resulted in a more planar heme structure, whereas a rhombic LS Fe^{III} heme resulted in a more distorted geometry, in particular a larger degree of ruffling.

Table 4.6. Taylor analysis of the low spin Fe^{III} WT, K70Y and K70A cyt P460.[a]

	g_1	g_2	g_3	V/ζ	V/Δ
WT-NH_2OH	2.75	2.28	1.54	2.19	0.73
K70Y-NH_2OH	2.85	2.34	1.64	2.25	0.68
K70A	2.91	2.29	1.54	1.97	0.63
Ht cyt c_{552}	3.20	2.08	1.20	1.3	0.39
Nitrphororin	2.95	2.23	1.41	1.72	0.59

[a]The spin orbit coupling constant (ζ) is estimated to be 400 cm^{-1} for Fe^{III} heme complexes from reference 13 and 27. See appendix.

The rhombicity of the Fe^{III} LS EPR spectrum of WT, K70Y and K70A were calculated, the two formers from their respective NH_2OH adducts whereas the latter from the Fe^{III} as isolated. The LS Fe^{III}-NH_2OH adducts of WT cyt P460, K70Y and Fe^{III} K70A all exhibited rhombic LS Fe^{III} EPR signals with g_{max} values less than 3.2

(Table 1). Taylor analysis of the LS Fe^{III} WT, K70Y and K70A demonstrate that all of these complexes exhibit a large degree of rhombicity with V/Δ values of 0.73, 0.68 and 0.63, for WT cyt P460, K70Y and K70A, respectfully. Interestingly, cyt P460 and its variants produce a highly rhombic LS Fe^{III} EPR signal, indicating a large ΔE between the d_{xz} and d_{yz} orbitals. Nitrophorin proteins which display a large degree of ruffling also exhibit a large rhombic LS Fe^{III} EPR signal with a V/Δ of 0.59.

Cross-link deficient variant also forms a stable {FeNO}^{6} unit to reductive nitrosylation

The formation of the $\{FeNO\}^6$ is essential in the NH_2OH oxidation cycle of cyt P460. Most heme proteins upon binding NO in the Fe^{III} state will undergo reductive nitrosylation and form the Fe^{II} product or under excess NO will form the $\{FeNO\}^7$ species.[32] Nitrophorin exhibits a highly ruffled heme site and is the only known heme protein other than cyt P460 to exhibit a stable $\{FeNO\}^6$ species[13].[33] It is proposed that the large degree of ruffling increases the stability of the $\{FeNO\}^6$ complex.[34] The above characterization of the cross-link deficient variants suggest that these hemes remain significantly ruffled. Therefore, shunt experiments to generate a $\{FeNO\}^6$ intermediate were performed to probe the cross-link deficient variant for formation of a long lived $\{FeNO\}^6$.

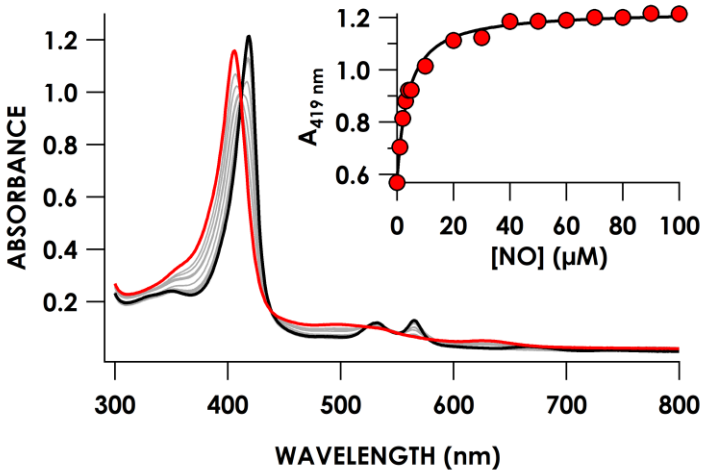

Figure 4.52. NO titration curve of K70Y monitored by UV/vis absorption spectroscopy. UV-vis traces of 10 μM K70Y titrated against various amounts of NO in anaerobic 200 mM HEPES, pH 8.0, at room temperature. Inset shows a plot of $A_{419\text{-nm}}$ versus NO concentration. This was fit to the following hyperbolic equation: $\mathbf{A_{419nm}} = \frac{\Delta \mathbf{A_{419}}[\boldsymbol{NO}]_0}{K_d + [\boldsymbol{NO}]_0}$.

Formation of the $\{FeNO\}^6$ species of the cross-link deficient variants was monitored by both UV/vis absorption spectroscopy and EPR. Treatment of 10 μM Fe^{III} K70Y cyt P460 with 10 equiv. of Proli-NONOate produced a UV/vis absorption spectrum with a Soret λ_{max} of 419 nm with corresponding sharp Q bands at 532 nm and 565 nm (Fig. 12). This species is stable under anaerobic conditions for 12 hours. The dissociation constant $[K_{d(NO)}]$ was also measured for NO binding to Fe^{III} K70Y. Titration of NO by the NO generator Proli-NONOate to 10 μM Fe^{III} K70Y was monitored by UV/vis absorption spectroscopy (Fig. 12). Upon addition of increasing NO concentrations a concomitant decrease at 407 nm with an increase at 419 nm was observed with isobestic points at 411 nm, 524 nm and 578 nm (Fig. 12). Fitting the rise in the absorbance at 419 nm against NO concentration to a hyperbolic binding curve produced a $[K_{d(NO)}]$ of 6 ± 1.5 μM, which is similar to WT cyt P460 with a

[$K_{d(NO)}$] of 10 ± 2 μM. EPR measurements confirmed (Fig. 13) the formation of a {FeNO}^{6} species. Treatment of 150 μM K70Y with 10 mM NO resulted in an EPR silent species. The species at around g = 2.0 is consistent with excess NO in the sample.

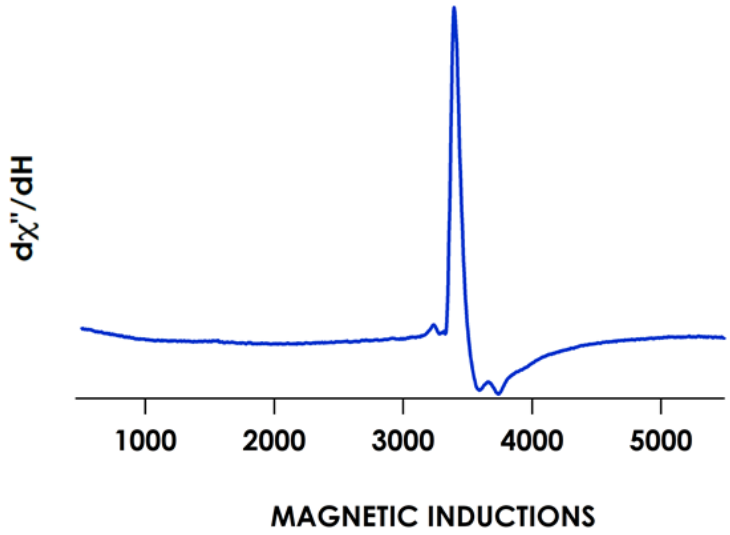

Figure 4.53. Electron Paramagnetic Spectra of 150 μM K70Y (blue trace) with 10 mM NO in 50 mM phosphate buffer, pH 8.0. Spectra were collected at 12 K and with 633 μW microwave power.

Conclusions

The combined analysis demonstrates that the removal of the cross-link does not generate a planar heme but instead the cross-link deficient variant still exhibits similar characteristics of other highly ruffled hemes. The low reduction potential, the rhombic LS Fe^{III} EPR spectrum as well as the stability of the {FeNO}^{6} complex all are characteristics of highly ruffled heme centers. Further analysis of the cross-link deficient variants by x-ray crystallography will be necessary in order to measure the exact degree of ruffling via NSD procedure. However, even with lack of a crystal

structure, the above results propose that the heme site remains quite distorted even with removal of the cross-link.

First identification of the low $Fe^{II/III}$ reduction potential couple exhibited by both K70Y and K70A hinted at the possibility that the cross-link deficient variants still exhibit a degree of ruffling. Low reduction potentials are hallmarks of highly ruffled heme centers, where a larger ruffled distortion produces a lower reduction potential.[10] WT exhibits the lowest reduction potential consistent with the highest degree of ruffling. As expected, K70Y has a lower reduction potential then K70A as a tyrosine residue between the propionate groups would contribute to more of a distortion in the heme site than an alanine. Therefore, K70A has the highest reduction potential of −290 mV versus NHE pH 8.0. However, this change in reduction potential between the WT and its variants is not nearly as drastic as expected. The tyrosine variant only differs in reduction potential from the WT by 50 mV. Therefore, removal of the cross-link does not considerably modulate the reduction potential of the $Fe^{II/III}$ heme site since the cross-link deficient variants still exhibit very negative reduction potentials as compared to cyt *c*′-α proteins (−10 to 200 mV).[18]

This low reduction potential seen in the cross-link deficient variants was exhibited by another class of cyt *c*′ proteins termed cyt *c*′-β where the reduction potential of cyt *c*′-β from *M. capsulatus* Bath is −200 mV versus NHE at pH 7.0. [19] The heme site of the cyt *c*′-α protein is fairly planar with a moderate saddling

distortion of −0.25 Å and little contribution of ruffling (0.12 Å).[1] This could indicate that cyt *c*′-β proteins have a larger degree of ruffling at the heme site than cyt *c*′-α proteins. Nevertheless, the above analysis thus suggests that these variants exhibit low reduction potentials similar to other highly ruffled hemes centers

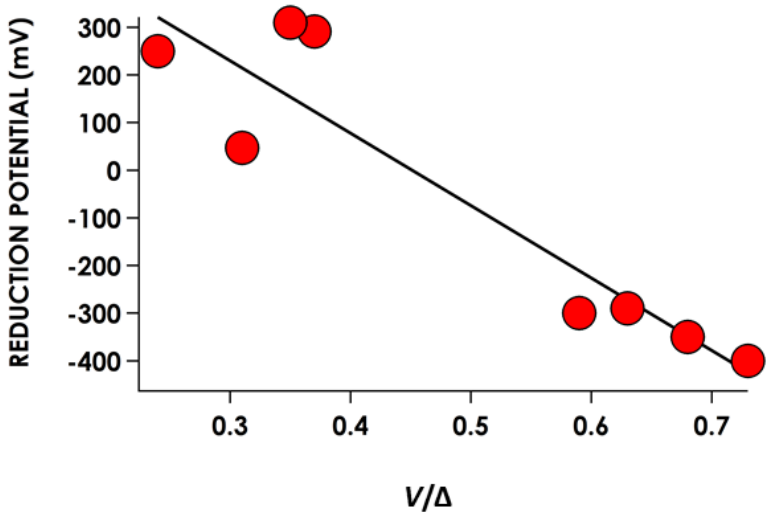

Figure 4.54. Correlation between reduction potential of a select group of heme proteins and the degree of rhombicity (*V*/Δ) calculated from Taylor analysis (Refence 13 and 29).

The EPR analysis comparing the LS Fe^{III}-NH_2OH adducts of the WT cyt P460, K70Y and Fe^{III} K70A also suggest a highly ruffled heme site. The resulting LS Fe^{III} EPR spectrum obtained for WT and its cross-link deficient variants all exhibit highly rhombic EPR signals indicating a large ΔE between the d_{xz} and d_{yz}. Therefore, removal of the cross-link does not give rise to a HALS signal which would be consistent with a more planar heme and thus degenerate (d_{xz}, d_{yz}) manifold. The highly

[1] Analysis through online version of the normal-mode structural decomposition procedure http://mliptak.w3.uvm.edu/scripts/hemeDistortion/finalDraft.pl

rhombic LS Fe^{III} EPR spectrum produced by the cross-link deficient variants is similar to the EPR spectra of a series of LS Fe^{III}-NO_2^- adducts.[31] This study demonstrated that the degree of ruffling via NSD analysis of crystal structures corresponds with the percentage of HALS signal, where the smaller the percentage of HALS signal correlates with a more ruffled heme site.[28] To further compare the rhombicity of the EPR spectrum with the degree of ruffling, a correlation between the rhombicity (V/Δ) parameter and the reduction potential of a group of *c*-type hemes were analyzed (Fig. 14) (Table 2). From the correlation graph above, the trend fits nicely where a lower reduction potential is expected for a larger degree of rhombicity in the EPR LS Fe^{III} spectrum. Both qualities of the large rhombicity (V/Δ) value and the low reduction potentials have been shown to be characteristics of highly ruffled hemes.[4,28] Therefore, if the cross-link's role was to generate a highly ruffled heme site, then removal of the cross-link would generate both a LS Fe^{III} EPR spectrum consistent with a HALS signal and a more positive reduction potential. This analysis demonstrates that the cross-link does not solely direct the large degree of distortion in the heme site as removal of the cross-link did not generate a Fe^{III} EPR spectrum consistent with a more planar heme site. Therefore, there must be another characteristic of the protein scaffold that directs this degree of ruffling.

Table 4.7. Correlation between rhombicity parameters (V/Δ) and reduction potential. Table adapted from reference 13. .[a]Reduction potential collected at pH 8.0, [b] pH 7.5, [c] pH 7.0

Protein	V/Δ	E (mV)
N. europaea cyt P460	0.73	-400 [a]
N. europaea c-552	0.24	250 [c]
Pa c-551	0.37	291 [c]
R. rubrum c_2	0.35	310 [c]
B. pasteurii c-553	0.31	47 [c]
N. europaea K70Y	0.68	-350[a]
N. europaea K70A	0.63	-290[a]
Nitrophorin	0.69	-300[b]

Both cross-link deficient proteins were able to produce a stable $\{FeNO\}^6$ species similar to WT (see appendix). Nitrophorin is the only other known heme protein to produce a stable $\{FeNO\}^6$ unit. The binding of NO to the Fe^{III} heme center in nitrophorin is important in establishing its reactivity as a NO transport protein.[12] The equilibrium binding constants (K_{eq}) of NO to the Fe^{III} heme are in the range of 10^3-10^5 M^{-1} whereas the K_{eq} of NO binding to the Fe^{II} heme are several orders of magnitude higher (10^{10}-10^{12} M^{-1}), therefore in order to effectively deliver NO, the protein must maintain a Fe^{III} oxidation state and be stable against reductive nitrosylation.[34] The increased stability in the Fe^{III} oxidation in nitrophorin was believed to be the result of the increased ruffling in the heme site.

NSD analysis of nitrophorin indicates that this protein in the resting state exhibits a large degree of ruffling (-0.55 Å) with minor saddling distortion of 0.30 Å.[35] The increased ruffling of the heme allows the nitrogen p_z orbitals of the porphyrin ring to now interact with the d_{xy} orbital. This interaction now creates a porphyrin with an electronic ground state of $(d_{xz}, d_{yz})^4 (d_{xy})^1$.[13] This ground state according to Walker et al[13], stabilizes the Fe^{III} oxidation state upon binding NO because the unpaired electron on NO would be located in an orbital that is orthogonal to the metal d_{xy} and therefore reduction into the metal d orbital is blocked.[13] The stability of the $\{FeNO\}^6$ species of both WT and the cross-link deficient variants could also be due to the increased ruffling of the heme that leads to this change in the ground state electron configuration. Further analysis of the $\{FeNO\}^6$ unit will be addressed in the following chapter. Nevertheless, both cross-link deficient variants produce $\{FeNO\}^6$ complexes that are stable towards reductive nitrosylation which is characteristic of highly ruffled heme sites.

Therefore, the role of the cross-link must not be to lock the heme in a ruffling geometry in order to modulate reduction potential and NO binding abilities as the cross-link deficient variants display both of these characteristics. The degree of ruffling at the heme site could be the result of the inherent protein scaffold that influences the heme distortion. Walker et al[15], demonstrated the importance of the amino acids around the heme and how those amino acids impact the heme conformation. In particular, mutations in the proximal heme pocket in nitrophorins drastically altered the degree of heme ruffling.[36] Therefore, perhaps it is the amino

acid composition in the proximal heme pocket that modulates the degree of ruffling on the heme site more so than the cross-link.

UV/vis characteristics of the cross-link deficient variants resemble other cyt *c′* proteins. As discussed above, cyt *c′*-β from *M. capsulatus* Bath share little sequence similarities with other cyt *c′*-α but share considerable sequence similarity with cyt P460s. As cyt P460 and cyt *c′*-β proteins are closely related and without a crystal structure of a cyt *c′*-β protein, analogies can be drawn from the information gained by the cross-link deficient variants towards understanding the properties of the cyt *c′*-β protein. The reduction potential of the cross-link deficient variants is much lower than other cyt *c′*-α proteins and more closely echos the reduction potential of the cyt *c′*-β from *M. capsulatus* Bath which has a reduction potential of −200 mV at pH 7.0.[16] Cyt *c′*-β proteins have not been analyzed for their degree of ruffling in the heme site but analysis of the cross-link deficient variants suggests that the heme site of cyt *c′*- β proteins is more ruffled than the cyt *c′*-α proteins.

Knowledge from the cross-link deficient variants suggest that the amino acids on the proximal side of the heme could be directing the degree of ruffling at the heme center and therefore important in maintaining the properties (e.g reduction potential, $\{FeNO\}^6$ stability) in the cross-link deficient variants. In fact, there is a conserved arginine residue[17] in *N. europaea* cyt P460, *M. capsulatus* Bath cyt P460 and cyt *c′*-β that is believed to hydrogen bond with a propionate group of the heme. This interaction could be a cause of the large degree of ruffling at the heme center in the cross-link deficient variants. Therefore, the properties of NO binding ability and low

reduction potential could be maintained via this interaction between the arginine residue and the propionate group of the heme. This could be one example of many that direct the degree of ruffling at the heme center in the cyt P460 and in the cross-link deficient variants. By extension perhaps analysis of the characteristics in cyt *c′*-β proteins (e.g reduction potential) also arises from these interactions between the heme site and the amino acids on the proximal side of the heme. Therefore, the cross-link does not solely direct the large degree of ruffling at the heme site, that perhaps this large degree of ruffling is due to the inherent protein scaffold of cyt P460. Further analysis must be done on a cyt *c′*- β to compare with the cross-link deficient variants to see if this unique primarily β structure produces a more ruffled heme site than the heme site of cyt *c′*-α.

Thus, the hypothesis that the large degree of ruffling imposed on the heme site by the cross-link directs its NH_2OH oxidase reactivity is not valid. The heme site of cyt P460 without the cross-link remains quite distorted. However, the question remains on why the cross-link deficient variants lack NH_2OH oxidase reactivity. While the function of cyt *c′*- β from *M. capsulatus* Bath is unknown, the gene is upregulated in the presence of ammonia and copurifies in a complex with cyt P460 from purification of the native organism.[19] Zahn et al[16] by EPR spectroscopy were able to show that cyt *c′*- β was reduced by cyt P460 in the presence of NH_2OH suggesting that cyt *c′*-β could act as an electron acceptor to cyt P460. Therefore, removal of the cross-link could change the role of the heme site from NH_2OH oxidase reactivity to an electron transfer agent. Analysis described herein also points to a role

in cyt *c′*- β proteins as a NO sequestering/transport agent as the cross-link deficient variants demonstrate similar stability of the $\{FeNO\}^6$ as nitrophorin. Further analysis on the cyt *c′*- β from *M. capsulatus* Bath is needed in order to understand the role of this β protein scaffold on its reactivity.

Experimental

General Considerations

Milli-Q water (18.2 MΩ; Millipore) was used in all preparations of buffers and solutions. All reactions were prepared inside an MBraun Labstar glovebox under a N_2 atmosphere. 1-(Hydroxyl-NNO-azoxy)-L-proline, disodium salt (Proli-NONOate) was purchased from Cayman Chemicals and stock solutions of Proli-NONOate were prepared as described previously.[9] NH_2OH•HCl was purchased from Sigma-Aldrich. All other chemicals were purchased from VWR International and used as obtained. All buffers were degassed with 3 cycles of vacuum for 20 min followed by sparging with N_2 for 20 min. Aliquots of protein were equilibrated in the glovebox for 2 h before the experiments. UV/vis absorption spectra were obtained using either a scanning Cary 60 UV/vis spectrometer or an Ocean Optics 2000+ high-resolution diode array spectrometer. Resonance raman spectra and Electron Paramagnetic Resonance were collected as previously described.[9]

Protein Expression and purification

WT and K70Y *N. europaea* cyt P460 and K70A was purified and expressed as previously described.[9] K70A was constructed via site-directed mutagenesis of the pET-22b+ vector bearing the gene for WT cyt P460 (see appendix). The K70A

expression plasmid was co-transformed into *Escherichia coli* with a pEC86 plasmid, which bears the cyt *c* maturation genes ccmABCDFGH. This plasmid was provided by H.B gray. The transformed cells were then plated onto lysogeny broth (LB) agar plates supplemented with 100 μg mL^{-1} ampicillin and chloroamphenicol. A single colony was then used to inoculate a 3 mL LB starter culture and grown at 200 rpm at at 37 °C for 6 h. 1.5 mL of starter culture was used to inoculate two 4 L Erlenmeyer flasks containing 1.5 L of Terrific Broth (TB) medium. The cells were grown under similar conditions as WT cyt P460, which is grown overnight at 30 °C then induced by the addition of isopropyl β-D-1-thiogalactopyranoside to a final concentration of 0.4 mM. The cells were harvested after 6hrs and produced a pink pellet that was then resuspended in 20 mM Tris, 150 mM NaCl and 0.01% Triton X at pH 8.0. The cells were lysed via sonication and the pink soluble lysate fraction was separated from cellular debris via centrifugation for 45 min at 16,000 rpm. The pink soluble lysate fraction was purified via benchtop nickel affinity column.

Spectroelectrochemical Potentiometric Titrations of WT and cross-link deficient variants

The spectroelectrochemical titrations were performed in a N_2 wet box using a 1 mm pathlength Basi cell with a mesh Pt working electrode, Pt counter and Ag/AgCl reference electrode. The protein solution consisted of a total volume of 500 μL of 200 μM protein (WT, K70Y or K70A) in 50 mM phosphate, 100 mM NaCl pH 8.0. The addition of methyl viologen (20 μM) to the solution was used as a mediator to ensure

electrochemical communication between the protein and the electrode. Bulk electrolysis experiments were conducted and monitored using a WaveNow potentiostat, Pine Research instrument. A potential was applied between -500 mV to -620 mV in 50 mV increments. Following each addition of a potential the solution was allowed to equilibrate for approximately 10 mins then a UV/vis absorption spectrum was collected over the range of 200-800 nm. The resulting full wavelength spectra were analyzed and fit to the linearized Nernst equation.

Reactions of cross-link deficient variants

The NH_2OH binding experiments were prepared in the glovebox and analyzed by UV/vis absorption spectroscopy using a Cary UV/vis spectrometer. The cross-link deficient variants and solid NH_2OH•HCl were allowed to equilibrate in the glovebox for approximately 2 hrs prior to use. All solutions were degassed prior to being brought into the glovebox. Solutions of (10 μM) K70Y or K70A were prepared by placing the correct amount of K70Y or K70A into anaerobic cuvette with 200 mM HEPES buffer pH 8.0. Solid NH_2OH•HCl (345 mg) were allowed dissolved into 1 mL of deoxygenated Milli-Q H_2O to produce a 5 M solution. This solution was placed into a 5 mL gas chromatography (GC) vial and stoppered with a spectrum seal. The titration experiments were initiated by the addition of NH_2OH via a gas-tight Hamiltonian syringe through the cuvette septum to a final concentration of 1 mM.

The formation of the $\{FeNO\}^6$ species was generated via addition of Proli-NONOate to the Fe^{III} cross-link deficient variant. Concentration of Proli-NONOate

was performed as previously described.[9] Solutions of Fe^{III} K70A or K70Y were prepared in the glovebox by addition of protein to a concentration of 10 μM into degassed 200 mM HEPES buffer. Solution of diluted NO were prepared in the glovebox into 0.1 M NaOH after the addition of Proli-NONOate to a final concentration of 1 mM. The NO titration experiments were analyzed by the Cary UV/vis spectrometer. The titration was initiated by addition of Proli-NONOate through a gas-tight syringe (Hamilton). The reaction was allowed to equilibrate for approximately 1 min then full wavelength spectra were collected between 200 to 800 nm.

EPR Spectroscopy and Taylor Analysis for rhombicity parameters

Samples were prepared anaerobically in a Mbraun glovebox. Solid NH_2OH•HCl (345 mg) were allowed dissolved into 1 mL of deoxygenated Milli-Q H_2O to produce a 5 M solution. The proper amount of 5 M NH_2OH was then added to produce 50 mM NH_2OH to a solution of K70Y (150 μM) in 200 mM HEPES buffer pH 8.0. The samples were then capped in an EPR tube in the glovebox and brought out of the glovebox to be immediately frozen in LN2. The samples were collected at 12 K as previously described.[33] The Taylor analysis was calculated as previously described (see appendix).[4]

REFERENCES

1. Jentzen, W., Ma, J.-G. & Shelnutt, J. A. Conservation of the Conformation of the Porphyrin Macrocycle in Hemoproteins. *Biophys. J.* **74,** 753–763 (1998).
2. Sun, Y. *et al.* Investigations of heme distortion, low-frequency vibrational excitations, and electron transfer in cytochrome c. *Proc. Natl. Acad. Sci.* **111,** 6570–6575 (2014).
3. Ikezaki, A., Ohgo, Y. & Nakamura, M. NMR studies on the electronic structure of one-electron oxidized complexes of iron(III) porphyrinates. *Coord. Chem. Rev.* **253,** 2056–2069 (2009).
4. Liptak, M. D., Wen, X. & Bren, K. L. NMR and DFT investigation of heme ruffling: Functional implications for cytochrome c. *J. Am. Chem. Soc.* **132,** 9753–9763 (2010).
5. Jentzen, W., Song, X.-Z. & Shelnutt, J. A. Structural Characterization of Synthetic and Protein-Bound Porphyrins in Terms of the Lowest-Frequency Normal Coordinates of the Macrocycle. *J. Phys. Chem. B* **101,** 1684–1699 (1997).
6. Pearson, A. R. *et al.* The crystal structure of cytochrome P460 of Nitrosomonas europaea reveals a novel cytochrome fold and heme - Protein cross-link. *Biochemistry* **46,** 8340–8349 (2007).
7. Smith, M. A. & Lancaster, K. M. The Eponymous Cofactors in Cytochrome P460s from Ammonia-Oxidizing Bacteria Are Iron Porphyrinoids Whose Macrocycles Are Dibasic. *Biochemistry* **57,** 334–343 (2018).
8. Igarashi, N., Moriyama, H., Fujiwara, T., Fukumori, Y. & Tanaka, N. The 2.8 Å structure of hydroxylamine oxidoreductase from a nitrifying chemoautotrophic bacterium, Nitrosomonas europaea. *Nat. Struct. Biol.* **4,** 276–284 (1997).
9. Vilbert, A. C., Caranto, J. D. & Lancaster, K. M. Influences of the heme-lysine crosslink in cytochrome P460 over redox catalysis and nitric oxide sensitivity. *Chem. Sci.* **00,** 1–12 (2018).
10. Bowman, S. E. J. & Bren, K. L. NIH Public Access. **25,** 1118–1130 (2009).
11. Olea, C., Boon, E. M., Pellicena, P., Kuriyan, J. & Marletta, M. A. A RTICLE. **3,** 703–710 (2008).
12. Ding, X. D. *et al.* Nitric oxide binding to the ferri- and ferroheme states of nitrophorin 1, a reversible NO-binding heme protein from the saliva of the blood-sucking insect, Rhodnius prolixus. *J. Am. Chem. Soc.* **121,** 128–138 (1999).
13. Walker, F. A. Nitric oxide interaction with insect nitrophorins and thoughts on the electron configuration of the {FeNO}6complex. *J. Inorg. Biochem.* **99,** 216–236 (2005).
14. Zoppellaro, G. *et al.* Modulation of the Ligand-Field Anisotropy in a Series of Ferric Low-Spin Cytochrome c Mutants derived from Pseudomonas aeruginosa Cytochrome c -551 and Nitrosomonas europaea Cytochrome c -552: A Nuclear Magnetic Resonance and Electron Paramagnetic Resonan. *J. Am. Chem. Soc.* **130,** 15348–15360 (2008).
15. Shokhireva, T. K., Shokhirev, N. V. & Walker, F. A. Assignment of heme resonances and determination of the electronic structures of high- and low-spin nitrophorin 2 by 1H and 13C NMR spectroscopy: An explanation of the order of heme methyl resonances in high-spin ferriheme proteins. *Biochemistry* **42,** 679–693 (2003).
16. Zahn, J. A., Arcier, D. M., Hooper, A. B. & Dispirito, A. A. Cytochrome c ’ of

Methy lococcus capsulatus Bath. **691,** 684–691 (1996).
17. Elmore, B. O., Bergmann, D. J., Klotz, M. G. & Hooper, A. B. Cytochromes P460 and c′-beta; A new family of high-spin cytochromes c. *FEBS Lett.* **581,** 911–916 (2007).
18. Weiss, R. *et al.* Cytochromes c ′ : Biological Models for the S) 3 / 2 , 5 / 2 Spin-State Admixture ? 2550–2579 (2006). doi:10.1021/cr040416l
19. Bergmann, D. J., Zahn, J. A. & Dispirito, A. A. Primary structure of cytochrome c ′ of Methylococcus capsulatus Bath : evidence of a phylogenetic link between P460 and c ′ -type cytochromes. 29–34 (2000).
20. Gouterman, M. Spectra of porphyrins. *J. Mol. Spectrosc.* **6,** 138–163 (1961).
21. Strekas, T. C. & Spiro, T. G. Resonance-Raman evidence for anomalous heme structures in cytochrome c′ from Rhodopseudomonas palustris. *BBA - Protein Struct.* **351,** 237–245 (1974).
22. Andrew, C. R., Green, E. L., Lawson, D. M. & Eady, R. R. Resonance Raman studies of cytochrome c??? support the binding of NO and CO to opposite sides of the heme: Implications for ligand discrimination in heme-based sensors. *Biochemistry* **40,** 4115–4122 (2001).
23. Spiro, T. G. & Czernuszewicz, R. S. [18] Resonance Raman spectroscopy of metalloproteins. *Biochem. Spectrosc.* **246,** 416–460 (1995).
24. He, C. *et al.* Nitrite dismutase reaction mechanism: Kinetic and spectroscopic investigation of the interaction between nitrophorin and nitrite. *J. Am. Chem. Soc.* **137,** 4141–4150 (2015).
25. Fujii, M. Spectroscopic and Kinetic Studies on Reaction of Cytochrome P450nor with Nitric Oxide. *Journal of Biological Chemistry* **270,** 1617–1623 (1995).
26. Collins, M. J., Arciero, D. M. & Hooper, A. B. Optical spectropotentiometric resolution of the hemes of hydroxylamine oxidoreductase. Heme quantitation and pH dependence of E(m). *J. Biol. Chem.* **268,** 14655–14662 (1993).
27. Walker, F. A. Magnetic spectroscopic (EPR, ESEEM, Mössbauer, MCD and NMR) studies of low-spin ferriheme centers and their corresponding heme proteins. *Coord. Chem. Rev.* **185–186,** 471–534 (1999).
28. He, C., Ogata, H. & Lubitz, W. Elucidation of the heme active site electronic structure affecting the unprecedented nitrite dismutase activity of the ferriheme b proteins, the nitrophorins. *Chem. Sci.* **7,** 5332–5340 (2016).
29. Taylor, C. P. S. (Received August 5th, 1976). **491,** (1977).
30. Que, L. *Physical Methods in Bioinorganic Chemistry: Spectroscopy and Magnetism*. (University Science Books, 2000).
31. He, C., Ogata, H. & Lubitz, W. Elucidation of the heme active site electronic structure affecting the unprecedented nitrite dismutase activity of the ferriheme b proteins, the nitrophorins. *Chem. Sci.* **7,** 5332–5340 (2016).
32. Hoshino, M., Maeda, M., Konishi, R., Seki, H. & Ford, P. C. Studies on the reaction mechanism for reductive nitrosylation of ferrihemoproteins in buffer solutions. *J. Am. Chem. Soc.* **118,** 5702–5707 (1996).
33. Caranto, J. D., Vilbert, A. C. & Lancaster, K. M. Nitrosomonas europaea cytochrome P460 is a direct link between nitrification and nitrous oxide emission. (2016). doi:10.1073/pnas.1611051113
34. Andersen, J. F. *et al.* Kinetics and equilibria in ligand binding by nitrophorins 1-4: Evidence for stabilization of a nitric oxide-ferriheme complex through a ligand-induced conformational trap. *Biochemistry* **39,** 10118–10131 (2000).
35. Maes, E. M., Roberts, S. A., Weichsel, A. & Montfort, W. R. Ultrahigh resolution structures of nitrophorin 4: Heme distortion in ferrous CO and NO complexes. *Biochemistry* **44,** 12690–12699 (2005).

36. Shokhireva, T. K. *et al.* Electrochemical and NMR spectroscopic studies of distal pocket mutants of nitrophorin 2: Stability, structure, and dynamics of axial ligand complexes. *Proc. Natl. Acad. Sci.* **100,** 3778–3783 (2003).

APPENDIX

K70A NH_2OH binding

Upon addition of NH_2OH, a similar shift in the Soret maximum was also seen in K70A. Monitoring the titration of NH_2OH to Fe^{III} K70A by UV/vis absorption spectroscopy showed a shift in the Soret maximum from 403 nm to 408 nm with an isobestic point at 406 nm and similar Q band as seen with K70Y. The [$K_{d(NH_2OH)}$] of K70A was determined as described above and fit to a hyperbolic binding curve to produce a much higher [$K_{d(NH_2OH)}$] of 31 ± 5 mM.

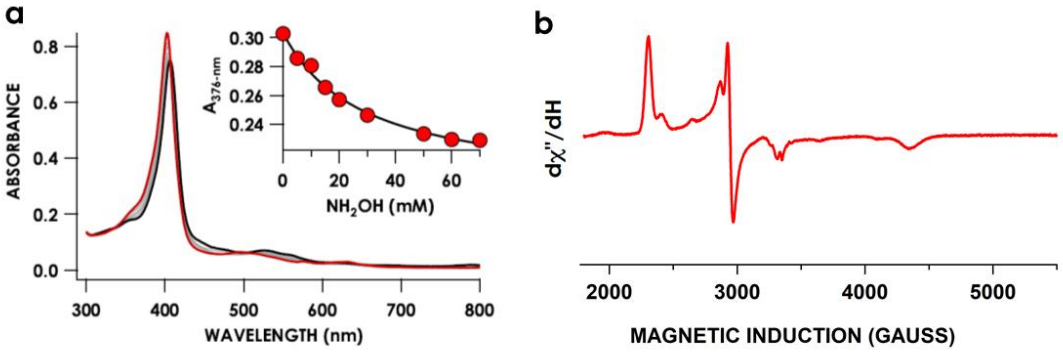

Appendix 4.3. NH_2OH titration curve of K70A monitored by UV/vis absorption spectroscopy. UV-vis traces of 10 µM K70A titrated against various amounts of NH_2OH in anaerobic 200 mM HEPES, pH 8.0, at room temperature. Inset shows a plot of $A_{419\text{-nm}}$ versus NO concentration. This was fit to the following hyperbolic equation: $\mathbf{A_{419nm}} = \frac{\Delta \mathbf{A_{419}}[\boldsymbol{NH_2OH}]_0}{K_d + [\boldsymbol{NH_2OH}]_0}$. Electron Paramagnetic Spectra (b) of 150 µM K70A (red trace) with 100 mM NH_2OH in 50 mM phosphate buffer, pH 8.0. Spectra were collected at 12 K 633 µW microwave power.

Due to the spin admixture state that exists in K70A, analysis of K70A Fe^{III}-NH_2OH species by EPR did not show major changes in the spectrum since this species is LS at cryogenic temperatures. Therefore, K70A was analyzed at room temperature via rR spectroscopy (Fig 5a). Samples were excited near Soret maximum at 405 nm. The spectrum of K70A exhibited an oxidation state marker band (ν_4) at 1370 cm^{-1}

consistent with a Fe^{III} oxidation state. However, upon binding NH_2OH the spin state marker band (ν_3) resolves into one peak at 1506 cm^{-1} consistent with a 6-coordinate LS species. Therefore, binding of NH_2OH to K70A also induces a spin state change from high spin to LS.

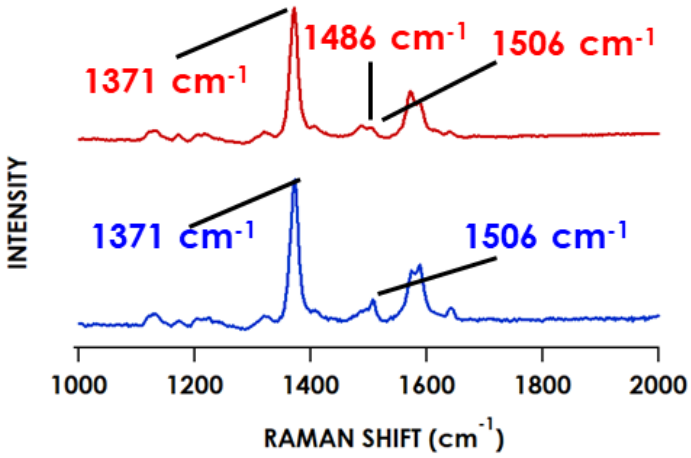

Appendix 4.4. The rR spectra obtained via near-resonance excitation with Soret absorption band: λ_{ex} = 405.0 nm (20 mW) for K70Y Fe^{III} (red trace) and Fe^{III}-NH_2OH (blue trace). The porphyrin band markers (ν (4) and ν (3)) are labeled above.

Fe^{III} NO Binding

Addition of NO to Fe^{III} K70A also produced a shift in the UV/vis absorption spectrum to 417 nm with similar sharp Q bands at 532 nm and 565 nm as seen in K70Y (Fig. 9b). The [$K_{d(NO)}$] was also measured by monitoring the increase in absorbance at 417 nm with increasing NO concentration. Fitting the data to a hypernolic binding curve produced a [$K_{d(NO)}$] of 6 ± 0.8 μM. This species was also stable under anaerobic conditions for 12 hours. EPR analysis confirmed the formation of a $\{FeNO\}^6$ species by formation of an EPR silent spectrum with the species at around g = 2 consistent with excess NO in solution. Therefore, similar to nitrophorin, these cross-link deficient variants also produce a long lived $\{FeNO\}^6$ species.

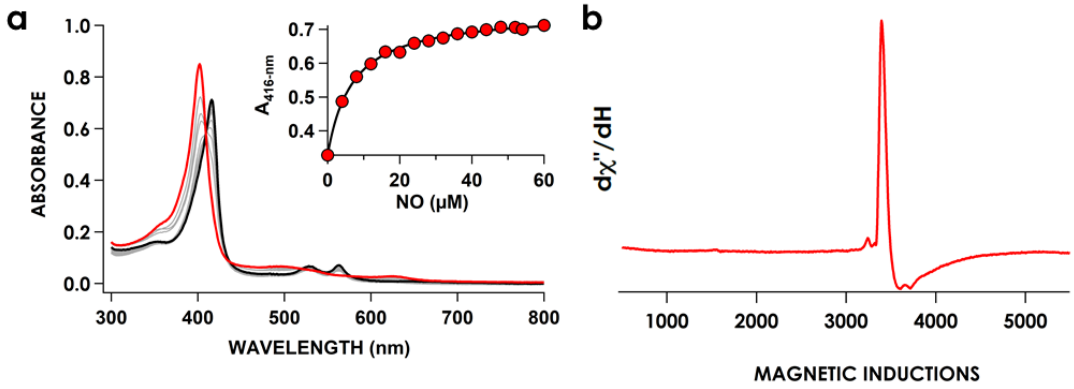

Appendix 4.5. NO titration curve (a) of K70A monitored by UV/vis absorption spectroscopy. UV-vis traces of 10 μM K70A titrated against various amounts of NO in anaerobic 200 mM HEPES, pH 8.0, at room temperature. Inset shows a plot of $A_{419\text{-nm}}$ versus NO concentration. This was fit to the following hyperbolic equation: $\mathbf{A_{419nm}} = \frac{\Delta \mathbf{A_{419}}[\boldsymbol{NO}]_0}{K_d + [NO]_0}$. Electron Paramagnetic Spectra (b) of 150 μM K70A (red trace) with 10 mM NO in 50 mM phosphate buffer, pH 8.0. Spectra were collected at 12 K 633 μW microwave power.

Taylor method: Summary

For more detailed analysis please see references 4, 27, 29, 30

$$V/\zeta = \frac{g_x}{(g_z+g_y)} + \frac{g_y}{(g_z-g_x)}$$

$$\Delta/\zeta = \frac{g_x}{(g_z+g_y)} + \frac{g_z}{(g_y-g_x)} - \frac{2V}{\zeta}$$

ζ = the spin-orbit coupling constant which is estimated to be 400 cm^{-1} for Fe^{III} heme complexes

K70A Plasmid

Plasmid name: K70A cytochrome P460 n.e

Parent plasmid: pET22 B^+ 6,020bp (with insert, 5,493bps without insert) insert is 527bps
Antibiotic resistance: Ampicillin
Expression inducer (if applicable): IPGT

Description: Variant K70A from codon optimized Cytochrome P460 from *Nitrosomonas europeae* inserted into pET22B^+. Parent plasmid includes His-tag and pelB leader sequence

Cloning/mutagenesis primers:
5'-AGC AAC CGT CAC GGT ACC ATC ACG G-3'Reverse K70A
5'-GAA CTG GTC AGT GTG GGT GAC C-3' Forward K70X
Around the Horn mutagenesis

Cyt P460 AA sequence
MAGVAEFNDKGELLLPKNYREWVMVGTQVTPNELNDGKAPFTEIRTVYVDPESYAHWKKTG
EFRDGTVTVKELVSVGDRKGPGSGNGYFMGDYIGLEASVKDSQRFANEPGNWAFYIFYVPDT
PLVAAAKNLPTAECAACHKENAKTDMVFTQYPVLRAAKATGESGVVAPKKLAAALEHHHHH
H

Order Number: 10384461

Sample Name: K70A2

Sequence:
>54_2572676__053.ab1
TGAGNAAATTCCCTCTAGAATATTTTGTTTAACTTTAAGAAGGAGATATACATATGAAATA
CCTGCTGCCGACCGCTGCTGCTGGTCTGCTGCTCCTCGCTGCCCAGCCGGCGATGGCCATG
GCTGGCGTCGCGGAATTTAACGATAAAGGTGAACTGCTGCTGCCGAAAAATTATCGTGAA
TGGGTCATGGTGGGCACCCAGGTTACGCCGAACGAACTGAATGATGGTAAAGCTCCGTTT
ACCGAAATTCGCACGGTTTATGTCGACCCGGAAAGCTACGCCCATTGGAAGAAAACCGGC
GAATTCCGTGATGGTACCGTGACGGTTGCTGAACTGGTCAGTGTGGGTGACCGTAAAGGTC
CGGGTTCCGGTAACGGTTATTTTATGGGCGATTACATTGGTCTGGAAGCGAGCGTGAAAGA
CTCTCAGCGTTTCGCCAACGAACCGGGTAATTGGGCATTTTATATCTTCTACGTTCCGGATA
CCCCGCTGGTCGCGGCAGCAAAAAACCTGCCGACGGCCGAATGCGCTGCGTGTCACAAAG
AAAATGCAAAAACCGACATGGTGTTTACGCAATTCTACCCGGTTCTGCGCGCCGCAAAAG
CTACCGGCGAAAGCGGTGTGGTTGCGCCGAAACTCGAGCACCACCACCACCACCACTGAG
ATCCGGCTGCTAACAAAGCCCGAAAGGAAGCTGAGTTGGCTGCTGCCACCGCTGAGCAAT
AACTAGCATAACCCCTTGGGGCCTCTAAACGGGTCTTGAGGGGTTTTTTGCTGAAAGGAGG
AACTATATCCGGATTGGCGAATGGGACGCGCCCTGTAGCGGCGCATTAAGCGCGGCGGGT
GTGGTGGTTACGCGCAGCGTGACCGCTACACTTGCCAGCGCCCTAGCGCCCGCTCCTTTCG
CTTTCTTCCCTCCTTTCTCGCCACGTTCGCCGGCTTTCCCCGTCANGCTCTAAATCGGGGGC
TCCCTTTAGGGTTCCNATTAGTGCTTACGGCACTCGACCCNAAAAACTTGATAGGGGAGGT
TCNGTANTGGGCCATCCCCTGAANACGNTTTNCGTCCTTGACGTGGATCCACGTCTTAAAG
TGACTTTGTCCNANCTGGACACATCACCTATNCGTCTNTTTTNATTAAAGGATTGCCATTCG
CNATGTNAAATGACGATTANAAATTANCGATTACAAATTANCTNAATTAGGGCCTTTCGGA
NGGN

CHAPTER 5

DIFFERENCES IN REACTIVITY BETWEEN WILD-TYPE *N. EUROPAEA* CYT P460 AND ITS CROSS-LINK DEFICIENT VARIANTS

Introduction

Heme proteins can catalyze numerous varied oxidative reactions that require the binding and activation of either O_2 or H_2O_2 as key components of the catalysis. In either peroxidase or cyt P450 enzymes, the function of binding O_2 or H_2O_2 is to generate the reactive ferryl-porphryin radical intermediate, compound I, which then proceeds to hydroxylate C–H bonds.[1–3] These oxidative reactions have been extensively studied due to the critical functions in mammalian metabolism, including biosynthesis of steroids, detoxification of xenobiotics and drug metabolism.[4] Heme P460-containing enzymes are unique among oxidative enzymes in that their catalytic mechanisms invokes direct substrate binding to the Fe center of the cofactor,[5–7] and thus redox requires no intercession of a reactive Fe-O species.

NO reductases invoke similar $\{FeNO\}^x$ intermediates to those related to P460 chemistry, but as the name implies, such enzymes mediate reductive chemistry.[8,9] The fungal NOR is a member of the P450 family and is involved in fungal denitrification which catalyzes the reduction of NO to N_2O.[10] This enzyme catalyzes a non-standard P450 type reaction which is initiated by binding of NO to the Fe^{III} heme. This protein is unusual in that it undergoes reductase activity rather than monooxygenase reactivity as in most P450 isozymes.[11] It is proposed that following binding of NO to the Fe^{III} heme, NADH reduces the Fe^{III} heme-NO adduct to some unknown intermediate. This

intermediate has been hypothesized as a formal Fe^{II}–NHOH species.[9,12,13] It is still unknown if the 2 proton additions occur in one step or in sequential additions, however, this intermediate then is proposed to react with a second molecule of NO to then ultimately generate the Fe^{III} heme, N_2O, and H_2O. Therefore, similar to other P450 enzymes the catalytically reactive species is first formed via binding of a diatomic ligand (in this case NO) to the Fe heme center. However, in cyt P450nor, the second NO acts as a substrate for the active species to produce N_2O. The catalytic mechanism of cyt P460 provides a new oxidative pathway for formation of N_2O.[5] Slight analogies can be draw between the catalytic mechanism of P450nor and cyt P460 in that both mechanisms invoke attack of a second molecule of its substrate (NO as in cyt P450nor or NH_2OH as in cyt P460) to produce N_2O.

However, the significance of the heme-Lys cross-link remains a persistent question of this thesis, and this question is further complicated by the aforementioned information: N_2O can also be generated via a thiolate-coordinated P450 type heme—a heme that lacks both cross-links and Cys thioether linkages. Thus, there are two classes of $\{FeNO\}^6$ heme protein species to consider in N_2O formation: one that is His ligated (cyt P460) and the other that is thiolate ligated (P450nor). In His ligated $\{FeNO\}^6$ complexes, the Fe-NO bond distance is approximately 1.65 Å with ν(N-O) of 1930 cm^{-1} and ν(Fe-NO) of 580-600 cm^{-1}. Thiolate coordination to the Fe^{III} heme has profound effects on the geometry of the bound NO. In particular, the Fe-N-O unit becomes bent in the presence of an axial thiolate ligand and consequently both the Fe–NO and N–O bonds become weaker. The Fe-NO bond distance remains the same as other His ligated heme $\{FeNO\}^6$ with typical bond distances of 1.66-1.70 Å, but these

species exhibit an observed lower ν(Fe-NO) of 530-550 cm^{-1} and ν(N-O) of approximately 1850 cm^{-1}. This weakening of the Fe-NO bond is proposed to be due to a σ-back-bonding interaction into a fully antibonding Fe-N-O σ^*orbital. The strength of this back-bonding is proportional to the donor strength of the anionic axial ligand trans to NO.[14,15] Therefore, perhaps the purpose of the cross-link is to generate a $\{FeNO\}^6$ that is unique from the typical His coordinated or thiolate coordinated systems.

The analysis in the previous chapter demonstrated that the cross-link's role in catalysis is not purely based on the degree of ruffling at the heme site. Upon removal of the cross-link, the heme still exhibits a low negative reduction potential and forms a $\{FeNO\}^6$ that is stable towards reductive nitrosylation. However, the question remains how the cross-link endows the heme with NH_2OH oxidase reactivity. The previous analysis in chapter 3 demonstrated that the cross-link is necessary for avoiding the 5-coordinate $\{FeNO\}^7$ sink[6] but the cross-link does not aid in formation of the $\{FeNO\}^6$ or in NH_2OH binding. This chapter will compare the reactive intermediate species formed along the NH_2OH oxidation pathway to analogous species formed by the cross-link deficient variant. This will help to understand how the cross-link activates each intermediate towards NH_2OH oxidation.

Increased spin density at Fe center of WT cyt P460 could activate NH_2OH adduct towards oxidation

The previous chapter demonstrated that the cross-link does not aid in NH_2OH binding. Each cross-link deficient variant can bind NH_2OH with similar affinity as the WT. The measured [$K_{d(NH_2OH)}$] changes little between the WT cyt P460 and its cross-link deficient variants. The WT does in fact have the lowest $K_{d(NH_2OH)}$, but all species have dissociation constants in the mM range signifying low affinity of NH_2OH to the Fe center. While the cross-link deficient variants cannot oxidize NH_2OH, they can still form stable NH_2OH adducts. It is not surprising that the cross-link deficient variants are able to bind NH_2OH, since there is precedent in formation of a stable NH_2OH adduct in heme peroxidases.[16] As NH_2OH is isoelectronic with H_2O_2, NH_2OH has been used previously as a model for H_2O_2 binding in a cytochrome *c* peroxidase. Addition of NH_2OH to the heme peroxidase from *Arthromyces ramosus* results in a similar UV/vis absorption shift in the Soret maximum from 403 nm to 414 nm accompanied by a similar [$K_{d(NH_2OH)}$] of 6.2 ± 0.1 mM at pH 7.0.[16] Wariishi et al[16], also analyzed the Fe^{III}-NH_2OH by rR spectroscopy with excitation into the Soret (405 nm). Addition of NH_2OH shifts the spin state marker band (ν_3) to 1504 cm^{-1}, while the heme protein remains Fe^{III} with an oxidation state marker (ν_4) at 1371 cm^{-1}.[16] Therefore, NH_2OH binds to the heme peroxidase and produces a spin state change similar to the previous results with the cross-link deficient variants.

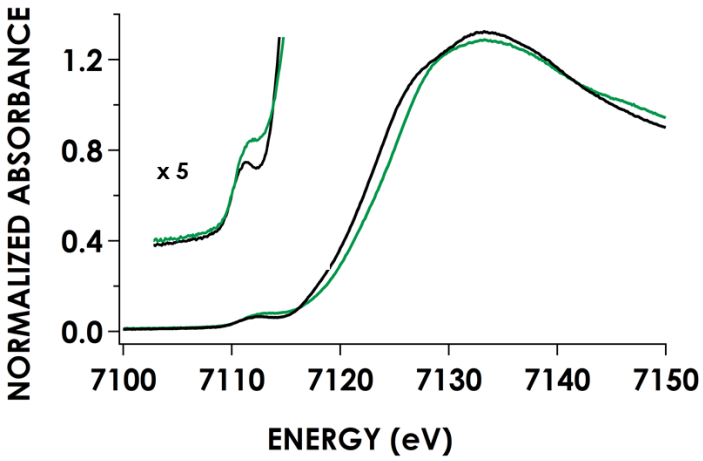

Figure 5.55. Fe K-edge XAS data obtained at 10 K for 1 mM WT cyt P460 (black) and 1 mM WT cyt P460 Fe^{III}-NH_2OH (green) species in glassed 200 mM HEPES buffer (pH 8.0) containing 25% v/v glycerol. Note the 1s → 3d pre-edge feature at 7112.4 eV.

X-ray absorption spectroscopy (XAS) data obtained for WT cyt P460 aided in determining structural characteristics of the NH_2OH adduct. The rising edge inflection point shifts to higher energy than in the Fe^{III} (resting) cyt P460: it shifts from 7129.7 to 7130.4 eV. There is slight pre-edge intensity change, with the Fe^{III} WT cyt P460 having weaker intensity relative to the Fe^{III}-NH_2OH adduct, but the transition energy itself has an identical value of 7112.8 eV for both species. Fits of the extended X-ray absorption fine structure (EXAFS) region from k values of 2–11 $Å^{-1}$ of the Fe^{III}-NH_2OH cyt P460 revealed a Fe-N(NH_2OH) bond distance similar to the NH_2OH adduct of cytochrome *c* peroxidase: the fit best of the WT cyt P460 Fe^{III}-NH_2OH corresponded to a coordination number of 6 N attached to the Fe center all at 1.98 Å, which includes the 4 N(pyrroles), the N(His) as well as NH_2OH. This bond distance of the Fe^{III}-NH_2OH of the peroxidase and cyt P460 is proposed to be similar to the cross-link deficient variants.

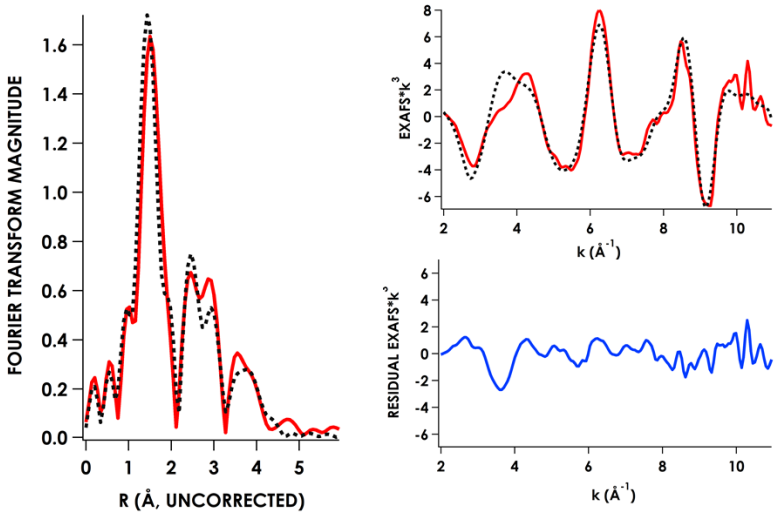

Figure 5.56. Fe K-edge EXAFS data obtained at 10 K for Fe^{III}-NH_2OH adduct in 200 mM HEPES (pH 8.0) containing 25% v/v glycerol. Experimental data are plotted as solid lines; fits are dotted lines.

The NH_2OH adduct of the cross-link deficient variants differs from WT cyt P460 in that the Fe^{III}-NH_2OH WT cyt P460 undergoes facile oxidation, whereas the NH_2OH adduct of the cross-link deficient variants are stable to addition of even potent oxidants. In previous EPR measurements (Ch. 2) the NH_2OH adduct of WT cyt P460 exhibited a spectrum composed of both the NH_2OH adduct as well as the 5-coordinate $\{FeNO\}^7$ species even under sub-stochiometric O_2 concentrations. Isotope labeling experiments confirmed that the NO in the 5-coordinate $\{FeNO\}^7$ species originated from NH_2OH (Fig. 3). Treatment of 150 μM cyt P460 with 50 mM $^{15}NH_2OH$ resulted in the characteristic 3-line super hyperfine of ^{14}N to collapse into a 2-line super hyperfine splitting due to interaction with the I = $^1/_2$ ^{15}N nucleus (Fig. 3). Neither EPR spectrum of the NH_2OH adducts of the cross-link deficient variants prepared aerobically evidenced production of an $\{FeNO\}^7$. Therefore, the NH_2OH adduct of the

WT cyt P460 is uniquely reactive compared to the NH_2OH adduct of the cross-link deficient variants.

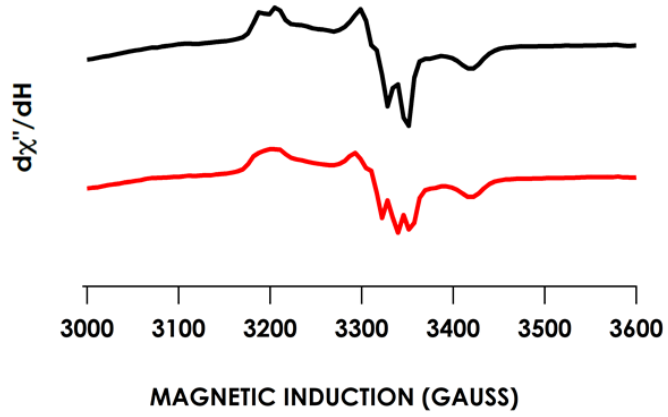

Figure 5.57. Electron Paramagnetic Resonance (EPR) spectra of 200 μM cyt P460 either treated with 50 mM $^{14}NH_2OH$ (red) or $^{15}NH_2OH$ (black).

The cross-link must aid in activating the NH_2OH adduct towards oxidation. Employing density functional theory (DFT) calculations presented a different view of the NH_2OH adduct of cyt P460. Spin density calculations of the Fe^{III}-NH_2OH cyt P460 species demonstrated that the spin density resides on the Fe^{III} center, with equal spin density on the bound His and NH_2OH rather than on the porphyrin ligand (Fig. 4). This in is contrast to other low spin Fe^{III} heme proteins where the electron spin density is delocalized over the heme porphyrin.[17] This creates two radically different Fe heme centers: one that is electron deficient (K70Y) and the other that is electron rich (WT cyt P460).

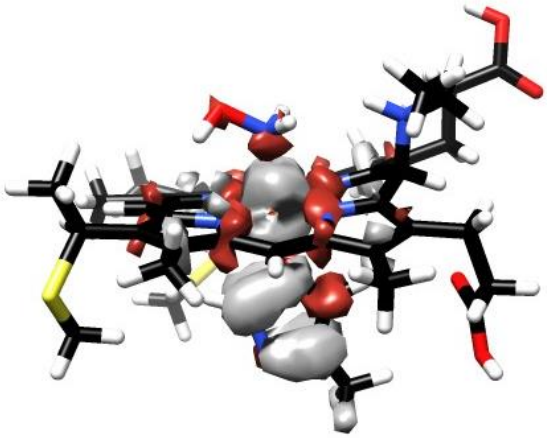

Figure 5.58. DFT geometry optimized structure of cyt P460 Fe^{III}–NH_2OH, with spin density plotted. Calculations employed the BP86 functional with a CP (PPP) basis set on the Fe atom and the def2-TZVP/J ZORA basis set on all atoms. Isovalue 0.03.

Cross-link deficient variant exhibits peroxidase activity whereas WT Cyt P460 does not

The above hypothesis suggests that the crosslink aids in creating an electron rich Fe center. Oxidation reactions of other heme proteins undergo formation of compound I, a strong oxidant rather than oxidation of a bound substrate to the Fe center. Compound I is described as a oxo-Fe^{IV}-radical (ferryl-radical) complex and has been characterized by UV/vis absorption, rR, EPR and Mossbauer.[18–20] Compound I can be formed by either thiolate ligated hemes or His-ligated hemes as in cyt P450 and peroxidases, respectfully. The thiolate ligated heme is proposed to stabilize the high valent Fe center via increased election donation to the Fe.[20,21] A similar mechanism is employed in peroxidases where a conserved Arg residue near the axial His is proposed to create more imidozolate character, which in turn increases the electron donation to the Fe center.[2,22] Therefore, increased donation from the axial residue is necessary in

order to stabilize this high valent reactive intermediate. Cyt *c* peroxidases are peroxidase enzymes that utilize *c*-type hemes similar to cyt P460 and K70Y. Cyt *c* peroxidases are also able to form compound I species by the reaction of the H_2O_2 with the Fe^{III} heme. Heme peroxidases are able to catalyze the oxidation of a large range of substrates including guaiacol ,ρ-anisidine, o-phenylenediamine and luminol.[23] Nitrophorin[24] as well as other engineered 5-coordinate *c*-type heme proteins have been shown to have peroxidase reactivity.[23]

The hypothesis that the crosslink increases the electron density at the Fe center should therefore create a heme that is also able to carry out peroxidase like activity. Interestingly, the results do not accord with this hypothesis. Treatment of 5 μM K70Y with 100 μM H_2O_2 and 1 mM guaiacol results in the formation of tetraguaiacol (Fig. 5b). However, treatment of 5 μM WT cyt P460 with 100 μM H_2O_2 and 1 mM guaiacol does not result in the production of the oxidized product but instead only results in heme degradation (Fig. 5a). K70Y was also able to perform oxidative dehalogenation of the peroxidase substrate trichlorophenol (TCP). Initiating the reaction with 100 μM H_2O_2, treatment of 10 μM K70Y with 1 mM TCP resulted in the immediate formation of the purple product 3-hydroxy-2,6-dichloroquione. However, addition of H_2O_2 to WT and TCP again only resulted in heme degradation with no isolation of the product.

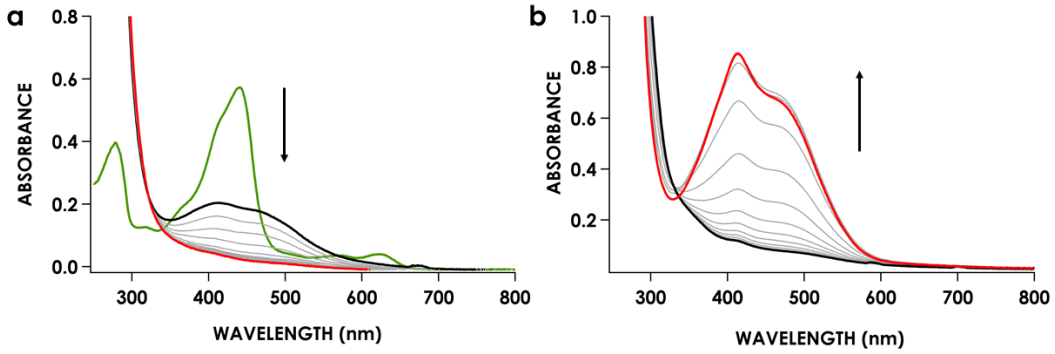

Figure 5.59. UV/vis absorption spectra of the reaction of 100 µM H_2O_2 and 1 mM guaiacol with 5 µM WT (a) or K70Y (b). The traces were taken every 5 secs for 2 mins. The initial trace is shown in red and the final trace is shown in black.

Cross-link deficient variants exhibit similar elongated Fe-NO bond distances of the {FeNO}^{6} species

Heme {FeNO}^{6} complexes that are stable to reductive nitrosylation are rare in proteins. Nitrophorin is the only other known protein that is able to form a stable {FeNO}^{6} species.[25] The previous chapter touched on the importance of heme ruffling on stability of the {FeNO}^{6} and suggested that the cross-link deficient variants also exhibit a large degree of ruffling. Walker et al,[26] addressed that the stable {FeNO}^{6} complex is due to a change in the ground state electron configuration from $(d_{xy})^2(d_{xz}, d_{yz})^3$ to $(d_{xz}, d_{yz})^4 (d_{xy})^1$ that stabilizes the Fe^{III} oxidation state over the Fe^{II} upon binding NO in the Fe^{III} state. This ground state change produces a strict Fe^{III}–$NO^{\bullet}$ configuration where the unpaired electrons are antiferromagntically coupled to produce the perceived diamagnetic species.

The exact electronic configuration of an $\{FeNO\}^6$: that is, Fe^{III}–$NO^{\bullet}$ vs. Fe^{II}–NO^+, has been offered as an explanation for diverging reactivities.[25] Lehnert et al[27], calculated the potential energy surfaces (PESs) for the Fe^{II}–NO^+ (S = 0) ground state, Fe^{III}–$NO^{\bullet}$ (S =0) and the corresponding high spin Fe^{III}–$NO^{\bullet}$ state (S = 2). The Fe^{II}-NO^+ configuration crosses over to the Fe^{III}–$NO^{\bullet}$ ground state at a Fe–NO bond distance of 1.70-1.76 Å.[9] This elongation of the Fe–NO bond is proposed to be due to the transfer of one electron from the Fe^{II} back to the NO^+. Therefore, the low spin Fe^{III}–$NO^{\bullet}$ has a weaker (longer) Fe–NO bond and consequently a lower Fe–NO stretching frequency. The high spin Fe^{III}–$NO^{\bullet}$ ground state occurs upon further elongation to approximately 1.9 Å, where eventually the NO dissociates to produce the 5-coordinate Fe^{III} heme product.[27]

Thus far, all heme $\{FeNO\}^6$ complexes that have been characterized exhibit a Fe^{II}-NO^+ ground state rather than a low spin Fe^{III}–$NO^{\bullet}$ configuration. Even the experimental data of nitrophorin, which has been proposed to adopt the Fe^{III}–$NO^{\bullet}$ configuration, has a similar N–O bond stretching frequency to well-characterized Fe^{II}-NO^+ species.[28,29] This suggests that the $\{FeNO\}^6$ species of nitrophorin does not differ in electronic configuration from other $\{FeNO\}^6$ complexes that all have the corresponding Fe^{II}-NO^+ configuration.[27] Both cyt P460 and the cross-link deficient variants exhibit stable $\{FeNO\}^6$ species. The experimental data presented herein in will investigate whether the cross-link directs this change in ground state configuration from a Fe^{II}-NO^+ in other heme proteins to the Fe^{III}-$NO^{\bullet}$.

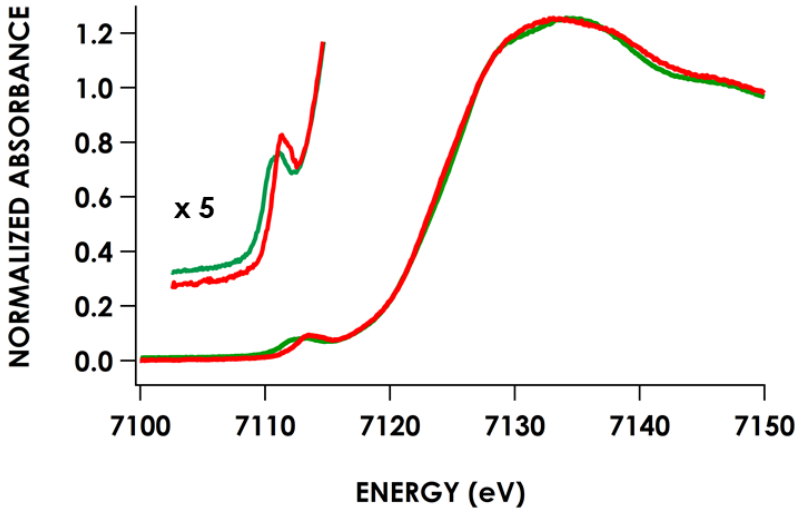

Figure 5.60. Fe K-edge X-ray Absorption (XAS) spectra of 1 mM WT Fe^{III} cyt P460 (green) and Fe^{III} K70Y (red) treated with 10 mM NO. The samples were glassed in 200 mM HEPES buffer pH 8.0.

XAS was employed for structural characterization of the $\{FeNO\}^6$ unit in the WT cyt P460 and the K70Y. The energies of the rising edge inflection points of the $\{FeNO\}^6$ complexes generated from the WT or K70Y are identical, appearing at 7130.5 eV (Fig. 6). There is a slight shift in the pre-edge feature in Fe K-edge of the $\{FeNO\}^6$ WT cyt P460 and K70Y which shifts from 7112.9 eV in WT to 7113.7 eV in K70Y $\{FeNO\}^6$. However, the two species remain 6-coordinate as there is no increase in the intensity of the pre-edge feature upon formation of the $\{FeNO\}^6$ species in the WT and K70Y.

Fitting the EXAFS region of the WT and K70Y $\{FeNO\}^6$ complexes afforded Fe-NO bond distances of the $\{FeNO]^6$ heme (Fig. 7). The best fit for the WT $\{FeNO\}^6$ included 5 Fe-N(pyrrole) at a bond distance of 2.00 Å and a Fe–NO bond distance of 1.77 Å (Table 1). The fit drastically improved upon the addition of an Fe–O scatter at 2.67 Å consistent with a bent NO (See Appendix Fig. 2). The EXAFS of the $\{FeNO\}^6$

K70Y afforded similar Fe-NO bond distances as the WT cyt P460. The best fit for the K70Y $\{FeNO\}^6$ included 5 Fe-N(pyrrole) at a bond distance of 1.99 Å and a slightly longer Fe-NO bond distance of 1.78 Å (Table 1). The fit also improved upon addition of the Fe-N-O multiple scattering path at 2.89 Å (See Appendix Fig. 3). The Fe-NO bond distance of the $\{FeNO\}^6$ in either WT cyt P460 or K70Y is severely elongated compared to other heme $\{FeNO\}^6$ species, which typically exhibit a bond distance of 1.64 to 1.68 Å.[9] The elongated Fe-NO bond and inclusion of the Fe-N-O multiple scattering path suggests that both the WT and K70Y $\{FeNO\}^6$ species exhibits a bent NO adduct which is consistent with a Fe^{III}-$NO^{\bullet}$ configuration.

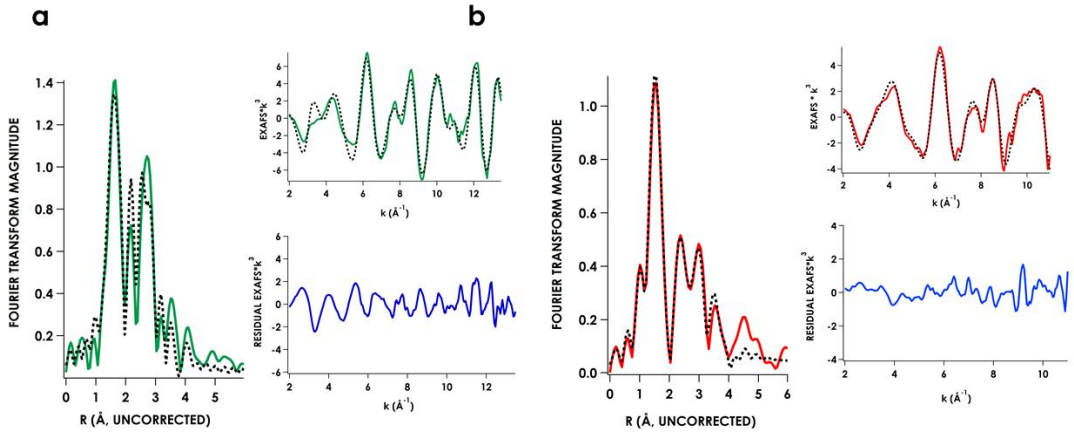

Figure 5.61. Fe K-edge EXAFS data obtained at 10 K for the 6c (a) and 5c (b) cyt P460 $\{FeNO\}^7$ intermediates in glassed 200 mM HEPES buffer (pH 8.0) containing 25% v/v glycerol. Experimental data are plotted as solid lines; fits are dotted lines.

Table 5.8. Best Fits to Fe K-Edge EXAFS Data Obtained for WT Cyt P460 {FeNO}^{6} and K70Y {FeNO}^{6}.[a]

	Scattering Path	Coordination Number	R(Å)	ΔR(Å)	σ^2	$\Delta\sigma^2$	F (%)
WT {FeNO}^{6}	Fe–N(pyrrole)	5	2.000	0.002	0.0003	0.0002	29.8
	Fe–N(NO)	1	1.772	0.026	0.012	0.0034	
K70Y {FeNO}^{6}	Fe–N(pyrrole)	5	1.992	0.005	0.005	0.0004	26.6
	Fe–N(NO)	1	1.781	0.01	0.003	0.0012	

[a]EXAFS data were fit in OPT using paths calculated by FEFF7. Coordination numbers were held constant, whereas distances (R) and Debye-Waller factors (σ^2) were allowed to float. Errors in coordination numbers are estimated to be on the order of 25%. Fits were performed over the entire Fourier transform window (0–6.0 Å). Goodness of fit was measured with F, which was defined as $[(\sum_i^n [k_i^3(\mathrm{EXAFS_{obs}} - \mathrm{EXAFS_{calc}})_i])^2 / n]^{1/2}$.

Resonance Raman (rR) spectroscopy was employed to confirm the elongated Fe-NO bond that is seen in these proteins. First rR spectroscopy was performed on the WT cyt P460 {FeNO}^{6} via excitation into the near Soret maximum at 458 nm. The decrease in symmetry and resulting increase of the porphyrin band markers make it difficult to analyze all the vibrational data without detailed calculation. Thus, analysis of WT cyt P460{FeNO}^{6} was examined by addition of ^{14}NO and its isotopically

labeled analog ^{15}NO to Fe^{III} protein (Fig. 8). The ν (Fe-NO) vibration was identified from subtraction of the $\{Fe^{14}NO\}^6$ from $\{Fe^{15}NO\}^6$ that revealed an isotope-sensitive band at 563 cm^{-1}. This ν(Fe-NO) is much weaker than the previously analyzed ν(Fe-NO) stretches of other His-ligated heme $\{FeNO\}^6$ complexes.[30] The ν(Fe-NO) of cyt P460 is however not as weak as thiolate-ligated hemes which exhibit a ν(Fe-NO) between 530 and 550 cm^{-1}.[14] The ν (N-O) was too weak and broad to identify fully, which is consistent with other $\{FeNO\}^6$ complexes where the ν(N-O) is not Raman enhanced. Therefore, further analysis of the ν(Fe-NO) from the WT cyt P460 $\{FeNO\}^6$ must be carried out and the ν(N-O) obtained via Fourier transform infrared (FTIR) spectroscopy.

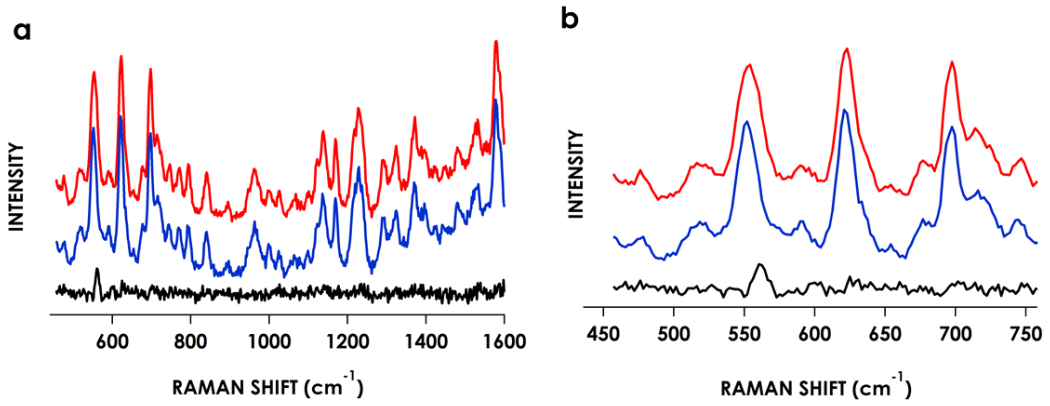

Figure 5.62. Resonance Raman spectra of WT Cyt P460 $\{FeNO\}^6$. The spectra were collected at room temperature with near Soret maximum excitation at 458 nm. Full spectrum (a) or low frequency region (b) of Fe^{III} WT cyt P460 (75 μM) treated with either 5 mM ^{14}NO (red) or 5 mM ^{15}NO (blue). The ^{14}N-^{15}N difference spectrum is shown in black.

The rR spectrum of $\{FeNO\}^6$ K70Y was collected at cryogenic temperatures via excitation of near Soret maximum at 405 nm and resulted in a similar spectrum to the $\{FeNO\}^6$ from nitrophorin.[31] The rR spectrum of K70Y $\{FeNO\}^6$ produced an oxidation state marker band ν(4) at 1375 cm^{-1} with a spin state marker band at 1506

cm^{-1} consistent with a 6-coordinate low spin heme (Fig.10).[32] Compared to the Fe^{III} K70Y rR spectrum a new band at 602 cm^{-1} arose upon treatment of the Fe^{III} heme with NO. This peak is different from the nitrophorin species which exhibited a new band at 591 cm^{-1}. Walker at al from $^{14}N/^{15}NO$ difference spectrum saw a shift in the 591 cm^{-1} to 587 cm^{-1} upon isotopic substitution of ^{15}NO. A 4 cm^{-1} shift has been observed previously for the ν(Fe-NO) vibrational mode in Fe^{III} metMB(NO) at 595 cm^{-1}.[30] Unfortunately, the peak at 602 cm^{-1} was too broad in the K70Y $\{FeNO\}^6$ spectrum to unambiguously identify an isotope sensitive band marker for the $^{14}N/^{15}N$ ν(Fe-NO). The ν(Fe-NO) are weak bands that are usually analyzed by substitution of $^{15}N^{18}O$ which produces a larger isotope shift. Further analysis by FTIR spectroscopy to obtain the ν(N-O) of the K70Y $\{FeNO\}^6$ will be needed to confirm the ν(Fe-NO) and Fe-NO bond distance. The tentative ν(Fe-NO) at 602 cm^{-1} for the K70Y $\{FeNO\}^6$ is not consistent with the elongated Fe-NO bond distance measured by EXAFS. However, without the (N-O) stretch to directly compare or the $^{15}N^{18}O$ isotopic difference this stretch cannot be explicitly defined.

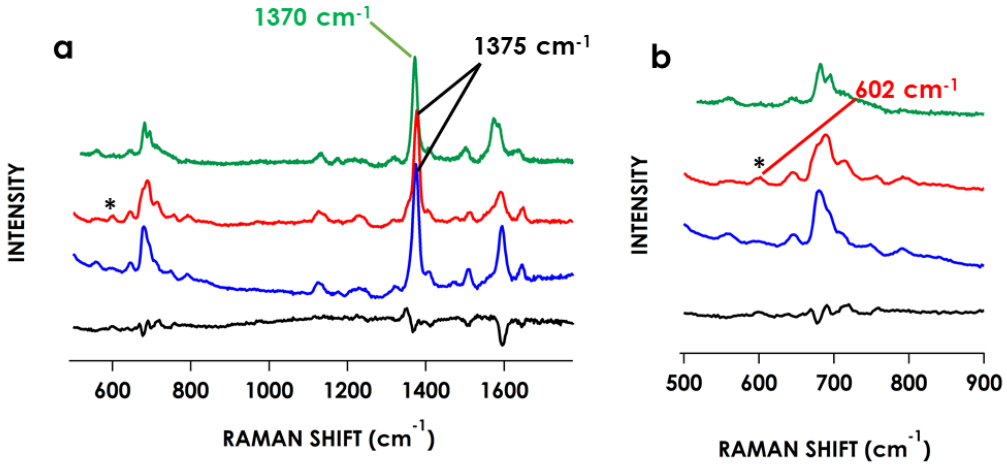

Figure 5.63. Resonance Raman spectra of K70Y {FeNO}^{6}. The spectra were collected at cryogenic temperatures with near Soret maximum excitation at 405 nm. Full spectrum (a) or low frequency region (b) of Fe^{III} K70Y (300 μM) (green) treated with either 10 mM ^{14}NO (red) or 10 mM ^{15}NO (blue). The ^{14}N-^{15}N difference spectrum is shown in black and the asterisk (*) denotes the new band that arises from the Fe^{III} spectrum to the {FeNO}^{6}.

To our knowledge, there are no protein {FeNO}^{6} complexes that exhibit this elongated Fe-NO bond distance and here we have shown that there are two proteins that each produce a lengthened Fe-NO bond. The Fe-NO bond distance is more consistent with a bent Fe-NO geometry rather than a linear Fe-NO as in the Fe^{II}–NO^+ configuration. Bond distances from a crystal structure of nitrophorin complexed with NO to form the {FeNO}^{6} heme produced shorten Fe-NO bond distances of 1.66 Å consistent with a Fe^{II}–NO^+ configuration.[33] The only other {FeNO}^{6} protein that was structurally characterized was the nitrosyl adduct of soybean leghemoglobin which was analyzed by EXAFS.[34] This produced a Fe-NO bond distance of 1.68 Å, with an unusually short Fe–N(His) bond distance of 1.89 Å.

As stated above, Lehnert et al[9] demonstrated that the Fe^{II}-NO^+ ground state configuration crosses over at a bond distance of 1.70-1.76 Å to the Fe^{III}–$NO^{\bullet}$ via calculation of the PES of the Fe-NO unit in {FeNO}^{6}. Therefore, by Lehnert's

calculations the bond distances of the Fe-NO from cyt P460 and K70Y more closely resemble that of the Fe^{III}–$NO^{\bullet}$ configuration. Also, the fits of the EXAFS from both WT cyt P460 and K70Y improve when the Fe-N-O multiple scattering path is included, which is again consistent with a bent NO. Thus, the EXAFS suggest that both WT cyt P460 and K70Y display the Fe^{III}–$NO^{\bullet}$ configuration unlike other heme $\{FeNO\}^6$ complexes. Therefore, the cross-link does not seem to direct the proposed configuration change from Fe^{II}–NO^{+} to the Fe^{III}–$NO^{\bullet}$ as K70Y $\{FeNO\}^6$ also displays an elongated Fe-NO bond distance.

Treatment of cross-link deficient variant $\{FeNO\}^6$ with NH_2OH produces a $\{FeNO\}^7$ species rather than a Fe^{III} species as in WT cyt P460

The above analysis of the $\{FeNO\}^6$ species of WT cyt P460 and the cross-link deficient variant suggest that both species form similar Fe^{III}-NO adducts. The $\{FeNO\}^6$ species in WT cyt P460 reacts with an additional molecule of NH_2OH to produce N_2O. Therefore, as these two $\{FeNO\}^6$ species are similar by EXAFS, the cross-link deficient variants should also be active towards NH_2OH to produced N_2O. Initial experiments were monitored by UV/vis absorption spectroscopy of 5 μM K70Y and 4 equivalents of NO generated from Proli-NONOate to form the $\{FeNO\}^6$ species. The reaction was then initiated by the addition of 10 mM NH_2OH to the $\{FeNO\}^6$. The addition of NH_2OH resulted in the immediate decay of the $\{FeNO\}^6$ species and formation of a Soret maximum at 415 nm consistent with formation of the 6-coordinate $\{FeNO\}^7$ species (Fig. 10). As seen previously, the 6-coordinate $\{FeNO\}^7$ species will then decay to the 5-coordinate $\{FeNO\}^7$ as evidenced by the Soret at 411

nm and shoulder at 397 nm. Therefore, K70Y $\{FeNO\}^6$ does seem to react with NH_2OH, however, unlike WT $\{FeNO\}^6$, the reaction between K70Y $\{FeNO\}^6$ and NH_2OH produces a $\{FeNO\}^7$ species rather than the Fe^{III} species as in WT.

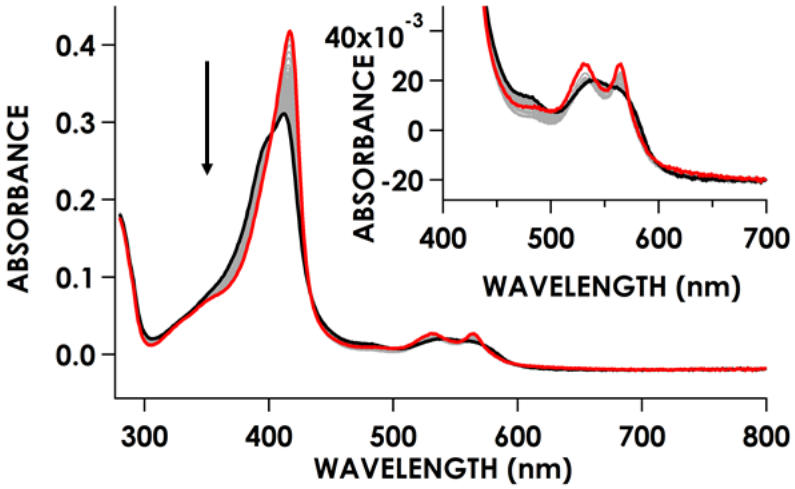

Figure 5.64. UV/vis absorption spectra monitoring the reaction of 5 µM K70Y $\{FeNO\}^6$ with 10 mM NH_2OH in 200 mM HEPES pH 8.0. The spectrum in red corresponds to the initial $\{FeNO\}^6$ K70Y immediately after the addition of NH_2OH, the gray spectra was taken every 30sec for 30 mins. The final species is shown in black.

Conclusions

Comparison between cyt P460 and K70Y demonstrated stark differences in reactivity between the intermediates formed along the NH_2OH oxidation pathway. The formation of a stable NH_2OH adduct in K70Y in the presence of external oxidants is in direct contrast to the facile oxidation of the NH_2OH adduct of WT cyt P460. The data above from DFT analysis of WT cyt P460 NH_2OH adduct suggests that the cross-link could aid in formation of an electron rich Fe center, where the electron density is located on the Fe rather than delocalized about the porphyrin ring.

This notion of an electron rich Fe center in WT cyt P460 was experimentally determined previously by comparison of the Fe-N(His) bond strength. The relative Fe-N(His) bond strength of WT cyt P460 and K70Y was determined through Erying analysis from the His dissociation mechanism.[6] The calculated $\Delta H^{\ddagger}$ of K70Y NO independent and dependent reaction mechanism for His dissociation confirmed that the $\Delta H^{\ddagger}$ is dominated by the strength of the Fe-N(His) bond as both produced similar $\Delta H^{\ddagger}$ of 30.2 ± 2.8 and 30.5 ± 0.7 kcal mol^{-1}, respectively.[6] The calculated $\Delta H^{\ddagger}$ for the WT cyt P460 was drastically lower than the cross-link deficient variants with a $\Delta H^{\ddagger}$ of 20.9 ± 0.3 kcal mol^{-1}. This difference in Fe-N(His) bond strength can be attributed to more electron density on the Fe center in the WT which weakens the Fe-N(His) bond. Removal of the cross-link creates electron delocalization about the porphyrin ring and as a consequence a more electron deficient Fe center, which in turn strengthens the Fe-N(His) bond. Therefore, perhaps the more electron rich Fe center in cyt P460 Fe^{III}-NH_2OH adduct activates the NH_2OH for oxidation and that the consequence of the cross-link is to create a Fe rich center that creates facile oxidation of the bound NH_2OH. Further spectroscopic analysis (i.e. ^{57}Fe Mössbauer) of the electron density at the Fe center of the Fe^{III}-NH_2OH adduct in the cross-link deficient variant compared to WT cyt P460 will be needed to further test this hypothesis.

This change in the electron density of the heme center in cyt P460 could directs its reactivity towards oxidation of a bound substrate rather than oxidation of a substrate via formation of a reactive oxidant (i.e compound I). It is interesting that removal of the crosslink creates a major change in reactivity from a typical heme oxidation type pathway with K70Y to the direct substrate-bound oxidation pathway in

WT cyt P460. From the above hypothesis, increased electron density at the Fe center in WT cyt P460 should aid in stabilizing the high valent Fe center of compound I. Therefore, with the increased electron density to the Fe center, WT cyt P460 should be able to carry out peroxidase reactivity. However, instead the results are reversed, where the cross-link deficient variant is able to undergo peroxidase activity whereas addition of H_2O_2 to Fe^{III} cyt P460 only results in heme degradation.

A possible reason for the lack of peroxidase reactivity in WT cyt P460 came from analysis of the heme degradation pathway. In particular, Isdl, a heme degrading protein from *Staphylococcus aureus,* binds hemes in such a way to generate a highly ruffled heme site (NSD value of 2.1 Å), which is proposed to aid in heme degradation.[35] From the combination of ^{13}C-NMR and ^{1}H-NMR, the electronic ground state of the heme bound by Isdl was identified as $(d_{xz}d_{yz})^4(d_{xy})^1$.[35,36] This is important in catalysis in that this ground state puts electron density on the meso carbon positions, which is proposed to increase the susceptibility of oxidative attack at that position.[37] Heme degradation begins with oxidative attack at the meso carbon position to produce α-hydroxyheme.[38] Therefore, perhaps the existence of the Lys-heme cross-link makes the other meso positions even more susceptible for oxidation attack. In fact, a hydroxylated meso-carbon was seen in the crystal structure of cytochrome P460 *N. europaea*.[39,40] The lack of reactivity seen in WT cyt P460 could be due to the increased activation of the meso carbons which promote oxidative attack of H_2O_2 at the other meso carbon position resulting in heme degradation.

Next, comparison between the $\{FeNO\}^6$ species of WT and K70Y cyt P460 was analyzed to further understand how the crosslink aids in activating the heme

towards NH_2OH oxidation. Interestingly, the unique configuration of the $\{FeNO\}^6$ species is not dependent on the presence of the cross-link. Both WT cyt P460 and K70Y $\{FeNO\}^6$ exhibit an elongated Fe-NO bond (1.77 and 1.78 Å) from EXAFS analysis, which is unusual for any heme protein $\{FeNO\}^6$ that has been characterized thus far.[9,41,42] The weak ν(Fe-NO) from the rR data of the WT cyt P460 $\{FeNO\}^6$ is consistent with the elongated Fe-NO bond. The ν(Fe-NO) of K70Y is not consistent with the elongated Fe-NO bond distance and will need further confirmation by other spectroscopic techniques. As suggested earlier further analysis either by $^{15}N^{18}O$ or FTIR will be needed for confirmation for either the WT cyt P460 or K70Y $\{FeNO\}^6$.

Even though WT and K70Y cyt P460 exhibit the similar elongated Fe-NO bond of the $\{FeNO\}^6$ species, the reactivity of K70Y $\{FeNO\}^6$ with NH_2OH differs from the WT. Addition of NH_2OH to K70Y $\{FeNO\}^6$ results in decay of the $\{FeNO\}^6$ species with a concomitant formation of the $\{FeNO\}^7$ rather than formation of the Fe^{III} species as in WT cyt P460. The proposed mechanism of N_2O formation from the WT cyt P460 $\{FeNO\}^6$ invokes nucleophilic attack of the NH_2OH to the Fe^{II}–NO^+ center of the $\{FeNO\}^6$ unit.[5,6] Therefore, this mechanism is similar to the mechanism of reductive nitrosylation. The mechanism of reductive nitrosylation is first order with respect to Fe^{III}–NO and hydroxide.[26,43] Attack of the hydroxide ion on the coordinated NO^+ of the Fe^{II}–NO^+ species is the rate determining step in the autoreduction process and is followed by dissociation of HNO_2 and production of a Fe^{II} species. In conditions of excess NO, the Fe^{II} species binds NO to produce the resulting $\{FeNO\}^7$ species.[44]

There was no identification of a Fe^{II} species in the WT cyt P460 experiments, which was attributed to both the fast oxidation rate of the Fe^{II} center as well as the fast reaction of the Fe^{II} center with NH_2OH.[5] The formation of the $\{FeNO\}^7$ center in K70Y upon addition of NH_2OH suggests that NH_2OH could be reacting with the $\{FeNO\}^6$ center similar to the previously proposed mechanism of WT cyt P460. The production of the $\{FeNO\}^7$ from the reaction between K70Y $\{FeNO\}^6$ and NH_2OH suggests this reaction could be producing a Fe^{II} center and in the presence of excess NO forms the $\{FeNO\}^7$ species. Therefore, again the cross-link seems to aid in avoiding the formation of the $\{FeNO\}^7$ dead end species. Further kinetic and GC analysis will have to be done to confirm if K70Y $\{FeNO\}^6$ produces N_2O and if the mechanism of $\{FeNO\}^7$ formation is dependent on NH_2OH.

Analysis of the cross-link in the previous chapter illustrated that the degree of ruffling of the heme site does not direct its unique reactivity. Therefore, this chapter sought to understand how the cross-link aids in activating the heme towards oxidation of the bound substrate NH_2OH. The cross-link does not change the electronic structure of the $\{FeNO\}^6$ species as both K70Y and WT cyt P460 exhibit elongated Fe-NO bond distances and EXAFS analysis is more consistent with a bent $\{FeNO\}^6$ species. Applying simple trigonometry from the Fe-NO distance calculated by EXAFS (for either K70Y or WT, 1.77 and 178, respectfully), a Fe-N-O bond angle can be calculated by applying a standard N-O distance of 1.14 Å. From this simple calculation a bond angle of 147° is calculated which deviates from 180° consistent with a bent NO.

However, the differences in reactivity between WT and K70Y $\{FeNO\}^6$ with NH_2OH suggest the cross-link seems to aid in avoiding the formation of the $\{FeNO\}^7$ species. This follows the proposed hypothesis that the cross-link generates a radically different heme center, which allows for two different types of oxidation reactions to occur. With increased spin density on the Fe center, the heme site is now able to undergo direct oxidation of a bound substrate. However, removal of the cross-link creates electron delocalization about the porphyrin ring creating a more electron deficient Fe center, which in turn strengthens the Fe-N(His) bond.[6] Even with removal of the crosslink, there is still enough donation from the axial His to stabilize a compound I type species to allow for the exhibited peroxidase activity in K70Y. Therefore, the heme cofactor is selectively tuned to carry out a specific function. This has been demonstrated in this chapter via the radically different reactivities seen in K70Y and WT cyt P460. Further spectroscopic studies are required to test the hypothesis that the degree of electron delocalization about the ring in the P460 heme site directs its reactivity.

Further Considerations: Implications for the Fe^{III}-$NO^{\bullet}$ electronic configuration in catalysis

As stated above, the production of N_2O was proposed to be due to nucleophilic attack of a second molecule of NH_2OH to the Fe^{II}-NO^+ or $\{FeNO\}^6$ center. However, the data represented herein for the electronic structure of the WT cyt $\{FeNO\}^6$ is more consistent with a Fe^{III}–$NO^{\bullet}$ configuration from EXAFS and rR spectroscopy. This change in electronic structure of the $\{FeNO\}^6$ unit differs from the proposed reactivity

of the $\{FeNO\}^6$ in the NH_2OH oxidation pathway. Therefore, this raises the question of the mechanism of N_2O formation from the $\{FeNO\}^6$ unit.

It is well accepted that the amino acids around an active site are specifically tuned for a particular function. The active site of cyt P460 is not immune to this case. Recent work in our lab has shown the importance of the glutamate residue above the heme site in *N. europaea* cyt P460. A cytochrome P460 from *Nitrosomonas* sp. AL212 does not possess the glutamate residue as seen in *N. europaea* but still exhibits similar spectroscopic characteristics to cyt P460 *N. europaea*.[45] However, this variant of cyt P460 neither possesses NH_2OH oxidase reactivity nor does it possess N_2O production via the shunted reaction of $\{FeNO\}^6$ with NH_2OH. Substitution of the alanine residue with a glutamate as in *N. europeae* restores the NH_2OH oxidase reactivity. It is suggested that the glutamate aids in proton coupled oxidation of the Fe^{III}–NH_2OH adduct. The glutamate also restores the reactivity of the shunted $\{FeNO\}^6$ species with NH_2OH, where the cyt P460 AL212 Ala131Glu variant produces N_2O and a Fe^{III} species upon reaction of the $\{FeNO\}^6$ and NH_2OH. NH_2OH is an interesting substrate in that it can act as either an oxidizing or a reducing agent.[46] In the previous mechanism, NH_2OH acted as a nucleophile to attack the positively charge NO adduct. However, if the analysis of the $\{FeNO\}^6$ electronic configuration is correct, then this proposes that another mechanism could be occurring for N_2O production. Further analysis must be done on how the glutamate activates the second molecule of NH_2OH towards attack of the Fe^{III}–$NO^{\bullet}$ species.

Experimental

General Considerations

Milli-Q water (18.2 MΩ; Millipore) was used in all preparations of buffers and solutions. All reactions were prepared inside an MBraun Labstar glovebox under a N_2 atmosphere and all buffers were degassed prior to being brought into the box as previously described.[5,6] 1-(Hydroxyl-NNO-azoxy)-L-proline, disodium salt (Proli-NONOate) was purchased from Cayman Chemicals and stock solutions of Proli-NONOate were prepared as described previously.[6] NH_2OH•HCl was purchased from Sigma-Aldrich. All other chemicals were purchased from VWR International and used as obtained. Aliquots of protein were equilibrated in the glovebox for 2 h before the experiments. UV/vis absorption spectra were obtained using either a scanning Cary 60 UV/vis spectrometer or an Ocean Optics 2000+ high-resolution diode array spectrometer. Purification and expression of WT cyt P460, K70Y and K70A were performed as previously described.[5,6,39] Resonance raman spectra and electron paramagnetic resonance were collected as previously described.[6]

Fe K-edge X-ray absorption spectroscopy.

Samples for Fe K-edge X-ray absorption spectroscopy (XAS) were prepared in an anaerobic glovebox with 1 mM protein and 25% (v/v) glycerol, loaded into a Delrin sample cell, and sealed with 37 μm Kapton tape. The WT cyt P460 NH_2OH adduct sample was prepared by allowing 1 mM Fe^{III} P460 to react with 100 mM NH_2OH. The sample was then frozen in liquid N_2 outside of the box. The $\{FeNO\}^6$ samples of WT

and K70Y were prepared in the glovebox by treating 1 mM protein with 10 mM Proli-NONOate. The sample was identified by the Q-band region in a 1mm cuvette in the glovebox prior to freezing outside the glovebox in liquid N_2. Collection of the XAS data analysis of the EXAFS data was performed as previously described.[6] The inflection points of the rising edge were fit using IgorPro wavemetrics peak fitting analysis, which allowed for unambiguous determination of energies.

Resonance Raman Spectroscopy

Samples for rR spectroscopy were prepared in an anaerobic glovebox. Samples were excited using either a SpectraPhysics Stabilite 1800 Ar/Kr mixed-gas laser or a 405 nm diffraction-limed Lepton IV diode laser (Microlaser Systems). All samples used acetaminophen as a Raman shift calibrant. Generation of the isotopically labeled ^{15}NO and ^{14}NO were prepared as described previously via the reaction of 1 to 1 sodium ascorbate and NO_2^-. Addition of 100 mM sodium ascorbate to 100 mM NO_2^- produces immediate bubbling and the formation of NO. The concentration of NO was determined as previously described.[5] The WT cyt P460 $\{FeNO\}^6$ samples were prepared by treatment of 80 μM of protein with either 5 mM ^{15}NO/^{14}NO generated from the reaction as described above. The WT $\{FeNO\}^6$ sample was collected at room temperature with near Soret maximum excitation at 458 nm generated. The samples were collected in an NMR spinning setup to reduce any photodamage on the protein sample. The samples were collected with 30 sec exposure time for 2 min and the scans were summed to produce the resulting spectrum.

The {FeNO}^{6} K70Y samples were prepared in an anaerobic glovebox. The $^{15}NO/^{14}NO$ was generated as described above. The {FeNO}^{6} K70Y samples were prepared by treatment of 300 μM protein with 5 mM $^{15}NO/^{14}NO$. The {FeNO}^{6} K70Y samples were collected at cryogenic temperatures. The samples were held in a 180° backscattering geometry in an EPR finger dewar. The sample was collected with a near Soret maximum excitation at 405 nm with a 30 sec exposure time for 1 min. The scans were summed to produce the resulting spectrum.

Reactivity studies of K70Y {FeNO}^{6} and NH_2OH

The reactivity of K70Y {FeNO}6 and NH_2OH was monitored by UV/vis absorption spectroscopy. The samples were prepared in an anaerobic glovebox using deoxygenated buffers. The {FeNO}^{6} K70Y species was prepared by treatment of 5 μM K70Y with 10 μM PROLI-NONOATE (20μM NO) were combined with 2mL of deoxygenated 200mM HEPES buffer (pH 8.0) in the coy chamber in an aerobic cuvette. Solid (345 mg) of $NH_2OH•Cl$ was brought into the glovebox and allowed to equilibrate for 2 hrs prior to conducting experiments. A 5 M solution of NH_2OH was prepared by addition of 1 mL of deoxygenated buffer to 345 mg of $NH_2OH•Cl$. The reaction between the shunted {FeNO}^{6} and NH_2OH was initiated by using a gas-tight Hamilton syringe and adding the appropriate volume of $NH_2OH•Cl$ to the anaerobic cuvette. Measurements were carried out with 10 mM NH_2OH. The decay of the {FeNO}^{6} species was monitored with full-wavelength kinetic UV/vis absorption scans at intervals of 0.5 min for 10min, 1 min for 20 min and 2 min for 40 min.

Peroxidase reactivity experiments of WT and K70Y

The peroxidase activity of WT and K70Y was measured by monitoring the reaction by UV/vis absorption spectroscopy. Experiments were performed aerobically due to the generation of O_2 after H_2O_2 decomposition and were temperature controlled at 20°C using a peltier temperature control system. The concentration of 30% H_2O_2 was measured spectroscopically by the λ_{max} at 240 nm with extinction coefficient of 43.6 M^{-1} cm^{-1}. Stock solutions of H_2O_2 were then prepared and placed on ice. Experiments were done in 50 mM phosphate buffer pH 8.0. The reaction was initiated via manual mix by the addition of 100 μM H_2O_2 to either 5 μM WT or K70Y and 1mM guaiacol. Scans were collected every 5sec for 2 min. Experiments with 1 mM trichlorophenol (TCP) wereconducted with the same procedure as described above.

DFT calculations

Geometry optimized structures and spin density calculations were carried out using ORCA 3.03 quantum chemical computation suite. Geometry optimized structures for the NH_2OH bound P460 center were performed on the cofactor from coordinates obtained from the crystal structure (PDB: 2je3) while restricting movement of the thiolate linkages and propionate groups. Amino acids in the second and outer sphere were excluded in the calculations. The optimized structure and spin density calculations used BP86 functional with a CP (PPP) basis set on the Fe atom and the def2-TZVP/J ZORA basis set on all atoms. The solvation was modeled using COSMO and RIJCOSX procedure was used to accelerate DFT calculations.

REFERENCES

1. Green, M. T., Dawson, J. H. & Gray, H. B. Oxoiron(IV) in chloroperoxidase compound II is basic: Implications for P450 chemistry. *Science (80-.).* **304,** 1653–1656 (2004).
2. Green, M. T. Imidazole-ligated compound I intermediates: The effects of hydrogen bonding. *J. Am. Chem. Soc.* **122,** 9495–9499 (2000).
3. Kellner, D. G., Hung, S. C., Weiss, K. E. & Sligar, S. G. Kinetic characterization of Compound I formation in the thermostable cytochrome P450 CYP119. *J. Biol. Chem.* **277,** 9641–9644 (2002).
4. Bertini, I. & Gray, H. B. *Bioinorganic chemistry*.
5. Caranto, J. D., Vilbert, A. C. & Lancaster, K. M. Nitrosomonas europaea cytochrome P460 is a direct link between nitrification and nitrous oxide emission. (2016). doi:10.1073/pnas.1611051113
6. Vilbert, A. C., Caranto, J. D. & Lancaster, K. M. Influences of the heme-lysine crosslink in cytochrome P460 over redox catalysis and nitric oxide sensitivity. *Chem. Sci.* **00,** 1–12 (2018).
7. Fernández, M. L., Estrin, D. A. & Bari, S. E. Theoretical insight into the hydroxylamine oxidoreductase mechanism. *J. Inorg. Biochem.* **102,** 1523–1530 (2008).
8. Obayashi, E., Takahashi, S. & Shiro, Y. Electronic Structure of Reaction Intermediate of Cytochrome P450nor in Its Nitric Oxide Reduction. **3,** 12964–12965 (1998).
9. Goodrich, L. E., Paulat, F., Praneeth, V. K. K. & Lehnert, N. Electronic structure of heme-nitrosyls and its significance for nitric oxide reactivity, sensing, transport, and toxicity in biological systems. *Inorg. Chem.* **49,** 6293–6316 (2010).
10. Obayashi, E., Tsukamoto, K., Adachi, S. & Takahashi, S. Unique Binding of Nitric Oxide to Ferric Nitric Oxide Reductase from Fusarium oxysporum Elucidated with Infrared , Resonance Raman , and X-ray Absorption Spectroscopies. **7863,** 7807–7816 (1997).
11. Harris, D. L. Cytochrome P450nor: A nitric oxide reductase - Structure, spectra, and mechanism. *Int. J. Quantum Chem.* **88,** 183–200 (2002).
12. Fujii, M. Spectroscopic and Kinetic Studies on Reaction of Cytochrome P450nor with Nitric Oxide. *Journal of Biological Chemistry* **270,** 1617–1623 (1995).
13. Daiber, A. *et al.* Isotope effects and intermediates in the reduction of NO by P450NOR. *J. Inorg. Biochem.* **88,** 343–352 (2002).
14. Praneeth, V. K. K., Haupt, E. & Lehnert, N. Thiolate coordination to Fe(II)-porphyrin NO centers. *J. Inorg. Biochem.* **99,** 940–948 (2005).
15. Hunt, A. P. & Lehnert, N. Heme-Nitrosyls: Electronic Structure Implications for Function in Biology. *Acc. Chem. Res.* **48,** 2117–2125 (2015).
16. Wariishi, H. *et al.* Direct binding of hydroxylamine to the heme iron of Arthromyces ramosus peroxidase. Substrate analogue that inhibits compound I formation in a competitive manner. *J. Biol. Chem.* **275,** 32919–32924 (2000).
17. Liptak, M. D., Wen, X. & Bren, K. L. NMR and DFT investigation of heme ruffling: Functional implications for cytochrome c. *J. Am. Chem. Soc.* **132,** 9753–9763 (2010).
18. Rittle, J. & Green, M. T. Cytochrome P450 compound I: Capture,

characterization, and C-H bond activation kinetics. *Science (80-.).* **330,** 933–937 (2010).
19. Sligar, S. G. Coupling of spin, substrate, and redox equilibria in cytochrome P450. *Biochemistry* **15,** 5399–5406 (1976).
20. Green, M. T. The structure and spin coupling of catalase compound I: A study of noncovalent effects [3]. *J. Am. Chem. Soc.* **123,** 9218–9219 (2001).
21. Cheesman, M. R. *et al.* Two enzymes with a common function but different heme ligands in the forms as isolated. Optical and magnetic properties of the heme groups in the oxidized forms of nitrite reductase, cytochrome cd1, from Pseudomonas stutzeri and Thiosphaera pantotropha. *Biochemistry* **36,** 16267–16276 (1997).
22. Rydberg, P., Sigfridsson, E. & Ryde, U. On the role of the axial ligand in heme proteins : a theoretical study. 203–223 (2004). doi:10.1007/s00775-003-0515-y
23. Watkins, D. W. *et al.* Construction and in vivo assembly of a catalytically proficient and hyperthermostable de novo enzyme. *Nat. Commun.* **8,** 1–9 (2017).
24. Singh, R. *et al.* Unprecedented peroxidase-like activity of rhodnius prolixus nitrophorin 2: Identification of the [FeIV=O Por•]+ and [FeIV=O Por](Tyr38•) intermediates and their role(s) in substrate oxidation. *Biochemistry* **49,** 8857–8872 (2010).
25. Andersen, J. F. *et al.* Kinetics and equilibria in ligand binding by nitrophorins 1-4: Evidence for stabilization of a nitric oxide-ferriheme complex through a ligand-induced conformational trap. *Biochemistry* **39,** 10118–10131 (2000).
26. Walker, F. A. Nitric oxide interaction with insect nitrophorins and thoughts on the electron configuration of the {FeNO}6complex. *J. Inorg. Biochem.* **99,** 216–236 (2005).
27. Nicolai, L., K., P. V. K. & Florian, P. Electronic structure of iron(II)–porphyrin nitroxyl complexes: Molecular mechanism of fungal nitric oxide reductase (P450nor). *J. Comput. Chem.* **27,** 1338–1351 (2006).
28. Ellison, M. K., Schulz, C. E. & Scheidt, W. R. Nitrosyliron(III) porphyrinates: Porphyrin core conformation and FeNO geometry. Any correlation? *J. Am. Chem. Soc.* **124,** 13833–13841 (2002).
29. Spiro, T. G. & Czernuszewicz, R. S. [18] Resonance Raman spectroscopy of metalloproteins. *Biochem. Spectrosc.* **246,** 416–460 (1995).
30. Benko, B. & Yu, N. T. Resonance Raman studies of nitric oxide binding to ferric and ferrous hemoproteins: detection of Fe(III)--NO stretching, Fe(III)--N--O bending, and Fe(II)--N--O bending vibrations. *Proc. Natl. Acad. Sci. U. S. A.* **80,** 7042–6 (1983).
31. Maes, E. M., Walker, F. A., Montfort, W. R. & Czernuszewicz, R. S. Resonance Raman spectroscopic study of nitrophorin 1, a nitric oxide-binding heme protein from Rhodnius prolixus, and its nitrosyl and cyano adducts. *J. Am. Chem. Soc.* **123,** 11664–11672 (2001).
32. Spiro, T. G. Resonance raman spectroscopic studies of heme proteins. *Biochim. Biophys. Acta - Rev. Bioenerg.* **416,** 169–189 (1975).
33. Maes, E. M., Roberts, S. A., Weichsel, A. & Montfort, W. R. Ultrahigh resolution structures of nitrophorin 4: Heme distortion in ferrous CO and NO complexes. *Biochemistry* **44,** 12690–12699 (2005).
34. Wyllie, G. R. A. & Scheidt, W. R. Solid-State Structures of Metalloporphyrin NO x Compounds. *Chem. Rev.* **102,** 1067–1090 (2002).
35. Takayama, S. -i. J., Ukpabi, G., Murphy, M. E. P. & Mauk, A. G. Electronic properties of the highly ruffled heme bound to the heme degrading enzyme IsdI. *Proc. Natl. Acad. Sci.* **108,** 13071–13076 (2011).

36. Wu, J. *et al.* 1H NMR Study of the Solution Molecular and Electronic Structure of Escherichia coli Ferricytochrome b562: Evidence for S = 1/2 Reversible 5/2 Spin Equilibrium for Intact His/Met Ligation. *Biochemistry* **30,** 2156–2165 (1991).
37. Rivera, M. *et al.* Models of the Low-Spin Iron (III) Hydroperoxide Intermediate of Heme Oxygenase : Magnetic Resonance Evidence for Thermodynamic Stabilization of the d xy Electronic State at Ambient Temperatures. 6077–6089 (2002). doi:10.1021/ja017334o
38. Kikuchi, G., Yoshida, T. & Noguchi, M. Heme oxygenase and heme degradation. *Biochem. Biophys. Res. Commun.* **338,** 558–567 (2005).
39. Pearson, A. R. *et al.* The crystal structure of cytochrome P460 of Nitrosomonas europaea reveals a novel cytochrome fold and heme - Protein cross-link. *Biochemistry* **46,** 8340–8349 (2007).
40. Elmore, B. O., Pearson, A. R., Wilmot, C. M. & Hooper, A. B. Expression, purification, crystallization and preliminary X-ray diffraction of a novel Nitrosomonas europaea cytochrome, cytochrome P460. *Acta Crystallogr. Sect. F Struct. Biol. Cryst. Commun.* **62,** 395–398 (2006).
41. McQuarters, A. B. *et al.* Ferric Heme-Nitrosyl Complexes: Kinetically Robust or Unstable Intermediates? *Inorg. Chem.* **56,** 10513–10528 (2017).
42. Speelman, A. L., Zhang, B., Krebs, C. & Lehnert, N. Structural and Spectroscopic Characterization of a High-Spin {FeNO}6 Complex with an Iron(IV)-NO- Electronic Structure. *Angew. Chemie - Int. Ed.* **55,** 6685–6688 (2016).
43. Bartberger, M. D. *et al.* The reduction potential of nitric oxide (NO) and its importance to NO biochemistry. *Proc. Natl. Acad. Sci.* **99,** 10958–10963 (2002).
44. Ford, P. C., Fernandez, B. O. & Lim, M. D. Mechanisms of reductive nitrosylation in iron and copper models relevant to biological systems. *Chem. Rev.* **105,** 2439–2455 (2005).
45. Smith, M. A. & Lancaster, K. M. The Eponymous Cofactors in Cytochrome P460s from Ammonia-Oxidizing Bacteria Are Iron Porphyrinoids Whose Macrocycles Are Dibasic. *Biochemistry* **57,** 334–343 (2018).
46. Einsle, O., Messerschmidt, A., Huber, R., Kroneck, P. M. H. & Neese, F. Mechanism of the six-electron reduction of nitrite to ammonia by cytochrome c nitrite reductase. *J. Am. Chem. Soc.* **124,** 11737–11745 (2002).

APPENDIX

Appendix 5.6. EXAFS simulations for cyt P460 WT and NH_2OH EXAFS data were fit with EXAFSPAK using paths calculated by FEFF7. Distance and Debye-Waller factors were allowed to float while, coordination numbers were held constant. Goodness of fit is determined by F, defined as $[(EXAFS_{abs} - EXAFS_{calc})_i)^2/n]^{1/2}$. Fe-$N_p$ denotes the pyrrole nitrogens of the porphyrin, Fe-C_α denotes the α carbons of the porphyrin, Fe-C_{meso} denotes the meso carbons of the porphyrin and Fe-C_β denotes the β carbons of the porphyrin.

Fit	Path	Coordination #	R(Å)	±	σ^2	±	E0	F
1	Fe-N_p	6	2.00	0.005	0.005	0.0004	-5.78	54.99%
2	Fe-N_p	6	1.99	0.003	0.005	0.0003	-7.38	
	Fe-C_α	8	3.01	0.005	0.004	0.0005		41.69%
3	Fe-N_p	6	1.99	0.003	0.005	0.0003	-8.01	
	Fe-C_α	8	3.01	0.005	0.004	0.0005		
	Fe-C_β	8	4.39	0.010	0.002	0.0011		36.81%
4	Fe-N_p	5	1.99	0.003	0.003	0.0003	-7.78	
	Fe-C_α	8	3.01	0.005	0.004	0.0004		
	Fe-C_β	8	4.39	0.010	0.002	0.0011		35.71%
5	Fe-N_p	5	1.99	0.003	0.005	0.0003	-8.82	
	Fe-C_α	8	3.01	0.005	0.004	0.0005		
	Fe-Cb	8	4.39	0.010	0.002	0.0011		
	Fe-NH_2OH	1	1.80	0.027	0.013	0.0053		34.96%
7	Fe-N_p	6	1.99	0.002	0.005	0.0002	-8.35	
	Fe-C_α	8	3.02	0.007	0.008	0.0010		
	Fe-C_β	8	4.39	0.007	0.001	0.0008		
	Fe-C_{meso}	4	3.35	0.005	-0.001	0.0007		29.65%
8	Fe-N_p	6	1.99	0.002	0.005	0.0002	-8.21	
	Fe-C_α	8	3.04	0.006	0.006	0.0010		
	Fe-C_β	8	4.39	0.008	0.001	0.0008		
	Fe-C-N (MS)	8	3.34	0.008	0.001	0.0008		28.73%

Appendix 5.7. EXAFS simulations for cyt P460 WT {FeNO}^{6} EXAFS data were fit with EXAFSPAK using paths calculated by FEFF7. Distance and Debye-Waller factors were allowed to float while, coordination numbers were held constant. Goodness of fit is determined by F, defined as $[(EXAFS_{abs} - EXAFS_{calc})_i)^2/n]^{1/2}$. Fe-$N_p$ denotes the pyrrole nitrogens of the porphyrin, Fe-C_α denotes the α carbons of the porphyrin, Fe-C_{meso} denotes the meso carbons of the porphyrin and Fe-C_β denotes the β carbons of the porphyrin.

Fit	Path	Coordination #	R(Å)	±	σ^2	±	E0	F
1	Fe-N_p	5	2.01	0.005	0.003	0.0004	-1.92	71.16%
2	Fe-N_p	5	2.01	0.003	0.003	0.0002	-0.65	
	Fe-C_α	8	3.02	0.003	0.000	0.0002		42.25%
3	Fe-Np	5	2.01	0.003	0.003	0.0002	-0.68	
	Fe-C_α	10	3.02	0.003	0.002	0.0002		
	Fe-NO	1	1.75	0.031	0.014	0.0052		39.33%
4	Fe-N_p	5	2.01	0.002	0.003	0.0002	-1.51	
	Fe-C_α	10	3.01	0.002	0.001	0.0002		
	Fe-NO	1	1.74	0.025	0.013	0.0041		
	Fe-O	1	2.67	0.005	0.001	0.0004		31.07%
5	Fe-N_p	5	2.00	0.002	0.003	0.0002	-2.34	
	Fe-C_α	9	3.02	0.002	0.000	0.0002		
	Fe-NO	1	1.77	0.026	0.012	0.0034		
	Fe-O	1	2.67	0.004	0.001	0.0004		
	Fe-C-N (MS)	16	4.35	0.017	0.003	0.0022		29.83%

Appendix 5.8. EXAFS simulations for cyt P460 K70Y {FeNO}^{6} EXAFS data were fit with EXAFSPAK using paths calculated by FEFF7. Distance and Debye-Waller factors were allowed to float while, coordination numbers were held constant. Goodness of fit is determined by F, defined as $[(EXAFS_{abs} - EXAFS_{calc})_i)^2/n]^{1/2}$. Fe-$N_p$ denotes the pyrrole nitrogens of the porphyrin, Fe-C_α denotes the α carbons of the porphyrin, Fe-C_{meso} denotes the meso carbons of the porphyrin and Fe-C_β denotes the β carbons of the porphyrin.

Fit	Path	Coordination #	R(Å)	±	σ^2	±	E0	F
1	Fe-N_p	5	2.00	0.007	0.007	0.0006	-5.82	66.66%
2	Fe-N_p	5	2.01	0.005	0.007	0.0005	-3.62	
	Fe-C_α	8	3.00	0.010	0.008	0.0012		56.31%
3	Fe-N_p	5	2.01	0.006	0.007	0.0006	-3.63	
	Fe-C_α	8	3.00	0.010	0.008	0.0011		
	Fe-NO	1	1.74	0.025	0.011	0.0036		52.93%
4	Fe-N_p	5	2.01	0.006	0.006	0.0005	-4.97	
	Fe-C_α	8	2.99	0.010	0.008	0.0010		
	Fe-NO	1	1.75	0.024	0.009	0.0031		
	Fe-C_β	8	4.46	0.028	0.009	0.0035		51.01%
5	Fe-N_p	5	1.97	0.005	0.005	0.0039	-10.36	
	Fe-C_α	8	2.96	0.009	0.011	0.0014		
	Fe-NO	1	1.76	0.009	0.002	0.0010		
	Fe-C_β	8	4.40	0.017	0.007	0.0018		
	Fe-C-N (MS)	12	3.38	0.007	0.003	0.0005		35.48%
6	Fe-N_p	5	1.99	0.005	0.005	0.0004	-10.41	
	Fe-C_α	8	3.13	0.009	0.001	0.0007		
	Fe-NO	1	1.78	0.010	0.003	0.0012		
	Fe-C_β	8	4.42	0.011	0.004	0.0010		
	Fe-C-N (MS)	12	3.35	0.006	0.002	0.0004		
	Fe-N-O (MS)	4	2.89	0.006	0.003	0.0006		26.57%